

Université Fédérale



Toulouse Midi-Pyrénées

# THÈSE

En vue de l'obtention du

## DOCTORAT DE L'UNIVERSITÉ DE TOULOUSE

Délivré par :

Université Toulouse 3 Paul Sabatier (UT3 Paul Sabatier)

---

**Présentée et soutenue par :**

**Guillaume BELIJAR**

le lundi 5 décembre 2016

**Titre :**

Anisotropic composite elaboration and modeling:  
toward materials adapted to systems

---

**École doctorale et discipline ou spécialité :**

ED GEET : Génie Electrique

**Unité de recherche :**

UMR 5213

**Directeur/trice(s) de Thèse :**

Thierry LEBEY

Sombel DIAHAM et Zarel VALDEZ NAVA

Lionel LAUDEBAT

Directeur de thèse :

Co-directeurs :

Encadrant :

**Jury :**

**M. Lionel FLANDIN**

**M. Masayuki HIKITA**

**M. Christophe LOUSTE**

**Mme. Séverine LE ROY**

**M. Eric DAVID**

Professeur à l'Université de Savoie

Professeur au KIT, Japon

Maître de Conférence, Université de Poitiers

Chargée de Recherche, Université de Toulouse III

Professeur à l'ETS, Canada

Président

Rapporteur

Rapporteur

Examinatrice

Examinateur



# Remerciements

Je souhaite tout d'abord remercier Sombel Diahm qui a su m'insuffler la passion de la recherche lors de mon stage de recherche, me donnant la conviction nécessaire pour me lancer dans l'aventure de la thèse. J'ai apprécié tout au long de ces presque quatre années ton écoute, nos longues discussions et tout ce tu as pu m'apporter en tant qu'encadrant.

Cette thèse n'aurait sûrement pas été ce qu'elle est sans la présence de Zarel Valdez Nava. Sans lui pour me pousser toujours plus loin je n'aurais pas vécu bien des choses (les USA...). Si je ne devais retenir qu'une chose de ton encadrement, ce serait très certainement la touche de philosophie que tu m'as transmis. Pour tout cela, merci.

Même si son suivi n'est arrivé qu'un peu plus tard, je tiens à exprimer mes sincères remerciements à Lionel Laudebat, tu m'as fait me sentir bien moins seul avec mes simulations.

Je ne saurai parler de ma thèse sans citer Thierry Lebey, ta rigueur scientifique et tes remarques m'ont toujours poussé à me remettre en question, ce qui m'a toujours poussé à me surpasser. Je tiens aussi à t'exprimer ma gratitude pour l'attention particulière que tu as porté une fois ma thèse terminée.

Pour votre confiance et votre soutien à tous les quatre, je vous remercie très chaleureusement.

I would like to make a small break in English to sincerely thank Thomas Jones for having shared his dielectrophoretic passion with me. It was a great honor for me to work with you, I will always remind your kindness and what you brought to my work.

Je tiens à remercier sincèrement les membres de mon jury pour leur présence ainsi que pour les discussions autour de ma thèse.

Vous le savez déjà certainement, mais c'est avec regret que je vous ai quitté, merci à tous les membres du groupe MDCE pour votre gentillesse et la bonne humeur qui fait le cadre de ces années. Pour essayer d'être exhaustif, merci à Jean-Pascal, Marie-Laure, David, Nadine, Philippe, Sorin, Pierre, Vincent et Céline. Et bien sûr tous les docs passés et présents, François Trung, Thomas, Hélène, Lumeï, Zenjebil, Mateusz, Laurent, Thibaut, Louis, Cyril, Ana.

Un grand merci aux personnels techniques qui m'ont aidés lors de cette thèse, une pensée particulière pour les Stéphane et les Benoits.

J'ai comme l'impression d'oublier des gens... Ah oui ! Simon et Cedric, je ne sais pas comment vous remercier pour toutes ces années, les pauses, les déconnades et le Mulligans ? Peut-être en vous disant à très bientôt et bon courage pour vos thèses. (PS : supprimez les photos svp)

Pour tous ceux qui ne sont pas du labo mais qui ont entourés ma vie pendant ces années, merci à vous, ç'aurait été vraiment plus dure sans vous. Max, Yow, les copines, John, Pinpin, Alice, Mélanie, Quentin, les potes du foot, merci encore.

Pour mon frère, merci pour tout, et surtout pour la belle surprise le jour J. A très bientôt à vous trois.

Je profite de ce moment pour remercier tous ceux qui sont venu me soutenir le jour de la soutenance, votre présence m'a fait chaud au cœur.

Je voudrais maintenant remercier ceux sans qui cette thèse n'aurait jamais vu le jour (et moi non plus), papa, maman, je vous exprime ma gratitude et mon amour pour tout ce que vous avez fait pour m'emmener là où j'en suis. Sans votre soutien et votre affection, rien de tout cela n'aurait été possible.

A tout ceux que je n'ai pas cité, famille, amis, collègues mais à qui je pense, merci.

*Enfin, pour celle à qui ce manuscrit est dédié, merci d'être ce qui est le plus cher dans ma vie.*





# Foreword

The phenomenon of electric-field-induced particle chaining, and the analogous behavior of magnetic particle in a magnetic field, have intrigued and challenged physicists for many years. The literature contains experimental and theoretical contributions to this topic going back many years. On the experimental front, Muth, reporting the phenomenon in 1927, called the formations “pearl chains”. This highly descriptive term is still in today. On the theoretical front, modeling the chaining force presents difficulty, because as particles in an electric field approach each other, their electrostatic interactions become very rapidly stronger. Mathematical solutions must rely on cumbersome, slowly-converging series expressions.

Why should we be interested in the problem of particle chaining? One important application, the one that Guillaume Belijar has addressed, stems from the technology of smart, structured materials. For composites formulated from particulate dispensed in a matrix, critically important physico-chemical properties can be made strongly anisotropic by forming the particles into oriented chains. Examples include thermal and electrical conductivities and the dielectric constant. The potential significance of anisotropic media created via chaining was recognized long ago; more recently, with the explosion of interest in microscale systems, the range of applicability for such smart materials has burgeoned. Exploiting such enhancements requires a flexible, predictive tool placed in the hands of the engineers who wish to design composites for new applications.

Belijar has performed extensive simulations of the dynamics of dielectric particle chain formation, and has then employed the results to extract chain formation times and to predict the final (quasi)equilibrium morphologies of the chains. He has succeeded in this challenging endeavor by exploiting the *effective moment method* to calculate the interparticle forces that draw the particles together. The method works because, while interparticle force calculations are very computational resource-intensive when the particles in a large ensemble are touching or very close together, the far simpler dipole-dipole approximation suffices to represent the interactions during most of the time required for the particles to approach each other. A useful analogy might be comparing the time spent by an airplane in flight as the pilot responds to air traffic control instructions (tens of minutes) to the time needed to land the aircraft and bring it to a stop (tens of seconds).

This thesis opens doors for materials scientists and engineers who wish to design and create new, structured composites in a large range of applications. There remains much to learn about the fine details of electric-field-driven particle chain morphology and how it might subtly influence bulk properties, particularly conductivity; the simulation tool Belijar presents to us will assist in this work.

T. B. Jones

Rochester, New York (USA)

November, 2016



# Table of Contents

## INTRODUCTION

### I. MATERIALS IN ELECTRICAL ENGINEERING, CURRENT LIMITATIONS AND PROSPECTIVE DEVELOPMENTS

- I.1. Today’s materials..... 7
  - I.1.a. Materials in systems ..... 7
  - I.1.b. Isotropic materials..... 11
    - I.1.b.1 Polymers (as matrix) ..... 11*
    - I.1.b.2 Composites ..... 12*
    - I.1.b.3 Ceramic fillers..... 13*
    - I.1.b.4 Metallic fillers ..... 14*
    - I.1.b.5 Allotropes of carbon fillers..... 15*
  - I.1.c. Intermediate conclusion..... 16
- I.2. Emerging materials: anisotropic composites..... 17
  - I.2.a. Benefits of anisotropy ..... 17
  - I.2.b. Methods for anisotropic composite processing..... 19
    - I.2.b.1 Mechanical/acoustical constraint..... 19*
    - I.2.b.2 Electrical constraint..... 21*
    - I.2.b.3 Magnetic constraint ..... 26*
  - I.2.a. Terminology..... 27
- I.3. Conclusion ..... 28

### II. DIELECTROPHORESIS: THEORETICAL DESCRIPTION

- II.1. Dielectrophoresis: a brief survey..... 33
  - II.1.a. Early descriptions ..... 33

II.1.b.	Development of the theory and applications .....	34
II.2.	Physical phenomenon .....	39
II.2.a.	Polarization .....	39
II.2.b.	DEP induced by the electrodes geometry .....	40
II.2.c.	DEP in chain formation .....	41
II.3.	Mathematical description .....	43
II.3.a.	General form .....	43
II.3.b.	Method of the effective dipole moment.....	45
II.3.c.	Negative and positive DEP .....	46
II.4.	Modeling of chain formation under electric field.....	47
II.4.a.	Description of the existing ways to model particle chaining .....	48
II.4.b.	Developed model.....	49
II.5.	Conclusion .....	53
 <b>III. CHARACTERIZATION OF THE COMPOUNDS</b>		
III.1.	Measurement of the liquid properties.....	57
III.1.a.	Principle of dielectric spectroscopy.....	57
III.1.b.	Experimental setup.....	58
III.1.c.	Dielectric spectroscopy on liquids .....	60
III.1.d.	Measurement of the polymer resin viscosity.....	64
III.2.	Measurement of the powders properties.....	65
III.2.a.	Estimation from bulk permittivity .....	65
III.2.b.	Estimation from mixing rules .....	68
III.2.c.	Theoretical description of the crossover frequency.....	71
III.2.d.	Method and experimental results.....	72

III.3. Perspectives ..... 76

**IV. EXPERIMENTAL STUDY OF ANISOTROPIC COMPOSITE FORMATION: ALIGNED FILLERS**

IV.1. Description of the setups and protocols..... 81

- IV.1.a. Preparation of the epoxy/ceramic powder mixtures ..... 81
- IV.1.b. Experimental setup and protocol for optical observations ..... 82
- IV.1.c. Experimental setup and protocol for dielectric monitoring of the chaining ..... 85

IV.2. Monitoring the chain formation..... 87

- IV.2.a. Evolution of the dielectric properties of the neat epoxy ..... 87
- IV.2.a. Combined optical and dielectric monitoring of particle chaining at low filler content 87
- IV.2.b. Dielectric monitoring at high filler contents ..... 89

IV.3. Characterization of the impact of the chaining..... 92

- IV.3.a. Influence of the process on the dielectric properties ..... 92
- IV.3.b. Influence of the filler content on the dielectric properties..... 94
- IV.3.c. Observation of the composite structures..... 95

IV.4. Conclusions and perspective ..... 97

**V. MODELING THE CHAIN FORMATION AND THE STRUCTURE IMPACT ON THE COMPOSITE PROPERTIES**

V.1. Dynamics of particle chaining..... 101

- V.1.a. Study of the chain structure as a function of the filler content ..... 101

V.2. Computation of the composite dielectric properties: comparison with the experimental measurements ..... 107

- V.2.a. Method to compute the composites dielectric properties ..... 107
- V.2.b. Normalization of the permittivity ..... 108

V.2.c.	Impact of the volume fraction of particles.....	109
V.2.d.	Impact of the particle properties.....	110
V.2.e.	Impact of the resin properties .....	111
V.2.f.	Impact of the electric field magnitude and waveform.....	113
V.3.	Conclusion and perspectives .....	114
<b>VI. PROSPECTIVE STUDY OF ANISOTROPIC COMPOSITE WITH PERPENDICULARLY ORIENTED FILLERS</b>		
VI.1.	Context, theory and numerical study.....	119
VI.1.a.	Context .....	119
VI.1.b.	Mathematical model .....	121
VI.1.c.	Determination of the experimental parameters through simulation .....	123
VI.2.	Formation of the composites .....	126
VI.2.a.	Perpendicular orientation in liquid state .....	126
VI.2.b.	Epoxy-Alumina composite .....	129
VI.2.c.	Epoxy-Alumina-BaTiO <sub>3</sub> three phase composite.....	131
VI.3.	Conclusion .....	133
VI.4.	Perspectives .....	133
VI.4.a.	Perspectives for anisotropic composite with perpendicular orientation .....	133
VI.4.b.	General Perspective.....	134

## **CONCLUSION**

## **REFERENCES**

**Appendix A: Method to compute the impact of the dipoles on the electric field**

**Appendix B: Measurements of the electric losses of composites**

**Appendix C: Measurements of the dielectric strength of composites**







## NOMENCLATURE

Symbol	Description
ac	Alternating current
$C$	Capacity [ <b>F</b> ]
$D$	Electric displacement field [ <b>C/m<sup>2</sup></b> ]
DEP	Dielectrophoresis / Dielectrophoretic
$E_0$	Amplitude (rms) of the external electric field [ <b>V/m</b> ]
$\underline{\varepsilon}$	Permittivity tensor
$\varepsilon_0$	Vacuum permittivity ( $8.854 \cdot 10^{-12}$ ) [ <b>F/m</b> ]
$\varepsilon_m$	Medium dielectric constant
$\varepsilon_p$	Particle dielectric constant
EHD	ElectroHydroDynamic
ER	Electrorheology / Electrorheological
$\Phi$	Electrostatic potential
$F_{DEP}$	Dielectrophoretic force
FEM	Finite Element Method
$\nabla$	Gradient operator
$k$	Spring constant
$K$	Clausius-Mossoti functions
MST	Maxwell Stress-Tensor
nDEP	Negative Dielectrophoresis
$p$	Dipole moment
$p_{eff}$	Effective dipole moment
pDEP	Positive Dielectrophoresis
$R$	Spherical particle radius
$\omega$	Pulsation of the electric field [ <b>rad/s</b> ]
$W$	Energy [ <b>J</b> ]



# Introduction

## INTRODUCTION

Materials in electrical engineering are characterized by the very wide variety of their nature and applications. Among them one finds polymers, ceramics, metals, and more. The range of properties, depending on the application, is also quite large, including electrical and thermal conductivity, permittivity, permeability, mechanical characteristics, and optical properties. The systems in which those materials operate can be the transportation of people and goods (cars, aircrafts, and trains), the transport of energy, but also smaller systems such as embedded systems and portable electronics. All of these systems are characterized by their own specific constraints, and material environments can present extreme temperatures (from very low in deep space to very high in aeronautics and power electronics), very high electric fields (in electronic devices at very small scales), extreme pressure (from very low in space to very high in petroleum exploration), reactive chemicals, etc. In almost all applications, the current trend is characterized by the rise of power densities that leads to ever-more severe constraints and smaller devices. This results in demand for increasingly robust materials featuring enhanced properties.

In the field of polymers, different strategies are explored to achieve such enhancements: research on new polymers and copolymers and the study of composites. Regarding the latter materials, the aim is to overcome matrix weaknesses by adding one or several types of fillers. The obtained composite presents a tradeoff between the matrix and filler properties. The types of properties that can be strengthened by the addition of fillers is almost unlimited, notably thermal, electrical, magnetic, mechanical, etc., depending on particle nature. Significant effort has been made to study the impact of particle nature, properties, size, aspect ratio, and dispersion on composite properties. Moreover, a complementary approach related to composites is to control the filler structure to adjust material properties. This is the rise of anisotropic composites.

Fiber-reinforced plastics are a well-known example of anisotropic composites with a polymeric matrix, in which glass or carbon fibers are arranged in specific directions to modify the composite's mechanical properties. The fibers in these materials provide the stiffness lacked by the polymers. New materials have been developed to create anisotropic composites with properties other than mechanical properties. Perhaps the more relevant example is that of conductive materials made of a polymer matrix blended with carbon nanotubes.

The way to induce anisotropy is not unique, but generally implies one crucial step: the application of an external constraint before or during matrix polymerization. The nature of this constraint can be mechanical, magnetic, or electrical. The latter constraint has proven to be highly promising: easy to use, the ability to address many types of filler, harmless for the matrix, etc. However, among the large number studies, some issues still need to be addressed. The general methodology to elaborate anisotropic

---

composite relies on empirical studies, leading to a lack of knowledge regarding the impact of several parameters on material tailoring. Among those studies treating electric field structuring numerically, to the best of the author's knowledge, none involve experimental validation directly.

The purpose of this thesis is to address the issues presented in the last paragraph, and more generally to propose strategies to elaborate anisotropic composites with fine control of material properties, in the intended directions.

This thesis dissertation is organized into six chapters. Each chapter is summarized below.

### **Chapter I**

This chapter provides an overview of existing materials, focusing on polymeric materials (pure and as a matrix for the composite). The purpose of this chapter is to define the main properties of materials already used in electrical engineering, as well as their limitations. The first part is dedicated to pure and isotropic composites, with the second part exploring emerging anisotropic composites. Different methods to obtain anisotropy are presented, along with a discussion about their pros and cons.

### **Chapter II**

The phenomenon of dielectrophoresis is presented in this chapter. First, a chronological review of the treatment of this force is addressed, followed by the main developments of theory and applications, not related only to the field of electrical engineering. A study of the physical phenomenon inherent to dielectrophoresis is then proposed. Lastly, the mathematical description of the DEP force is studied, as well as a numerical model of the structuration induced by this force.

### **Chapter III**

Chapter III is dedicated to the characterization of the compounds used to elaborate the composites. In the first part, polymer matrices are characterized by dielectric spectroscopy. In the second part, high permittivity ceramic powders are studied. We explored a new way to characterize the intrinsic permittivity of ceramic particles, as the permittivity value is critical for implementing any model that uses DEP force.

### **Chapter IV**

The experimental treatment of electric field-induced chaining is studied in chapter IV. The experimental setups and protocols are described in the first part. The second part presents the results for both optical and electrical monitoring of the structuration. Lastly, the materials are characterized electrically with a study on the impact of the process and filler concentration.

### **Chapter V**

This chapter offers a numerical simulation of the chain formation under an electric field. The obtained structures and structure changes are compared with both experimental and theoretical studies. Lastly, the evolution of permittivity, as a marker of composite structure, is discussed with respect to the impact of several parameters, and compared to experimental results.

## **Chapter VI**

The last chapter is dedicated to studying a novel way to achieve anisotropy in the direction perpendicular to the electric field by aligning fillers. A theoretical explanation of the phenomenon is proposed and compared with experimental results. Several experimental implementations are then presented, emphasizing the possibilities offered by these new types of materials.

Lastly, a general conclusion summarizes the work performed and contributions to this thesis. Perspectives and impact of this work are also discussed.







# Chapter I

Materials In Electrical Engineering,  
Current Limitations And Prospective Developments

# I. MATERIALS IN ELECTRICAL ENGINEERING, CURRENT LIMITATIONS AND PROSPECTIVE DEVELOPMENTS

The range of materials in electrical engineering applications is very wide, from conductors to insulators, and with materials presenting very specific properties (piezoelectric, pyroelectric, etc.), to others requiring basic functions such as electrical or thermal conductivity, permittivity, permeability, and more. The nature of these materials spans the entire spectrum, including polymers, ceramics, and metals. These materials can be either pure or composite, isotropic or anisotropic. Many advances have been made to obtain materials with enhanced properties to meet expectations for future technologies (increased power densities, severe external constraints, etc.). For their ease of use, implementation, and versatile properties, this study focuses on materials with a polymeric matrix (either pure or composite material), implementations, work in progress, and perspectives.

## I.1. Today's materials

### I.1.a. Materials in systems

As mentioned above, the range of materials present in electrical engineering as well as the constraints they must endure, is very wide. This diversity is illustrated here through three conventional systems: power modules, power cables, and film capacitors.

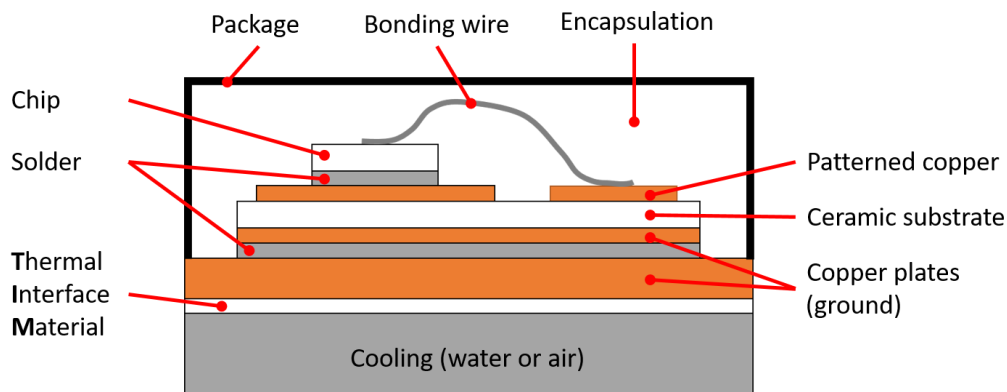


Figure I-1: Power module scheme.

Power modules are an assembly of active components (chips), interconnections, and insulating layers. The assembly is encapsulated by gels and polymer resins. The purpose of this encapsulation is to ensure the electrical insulation between metallic parts, as well as to provide the assembly with a level of mechanical resistance. Current materials are not used for cooling because of the one-side cooling design adopted and the poor thermal conductivity of the gels/polymers. Generally, the chips are soldered to DBC (Direct Bonded Copper) substrates composed of a ceramic (generally alumina) with copper plates

---

on both sides. The ceramic serves several purposes: to withstand the electric field and to extract heat generated by the chips. Key issues for ceramics are their CTE (Coefficient of Thermal Expansion) mismatch with the copper, and their brittleness [1]. Another key layer is the TIM (Thermal Interface Material), which corresponds to a viscous liquid composite made of a polymeric matrix and high thermal conductivity fillers [2]. The purpose of the TIM is to decrease thermal resistance at the interface between the sink and the copper plate. Current TIM still presents relatively low thermal conductivity (i.e. under  $4 \text{ W}\cdot\text{m}^{-1}\text{K}^{-1}$ ). Another known issue is the possible drying of the TIM during ageing. It should be noted that TIM is not supposed to ensure insulation, meaning that it is possible to use conductive fillers. Lastly, the power module enclosure corresponds to a hard plastic case, whose main purpose is to provide mechanical strength and allow electrical connections.

Throughout this first example, many different materials have been described with very specific functions. In addition to their intended purposes, all of these materials must be compatible with their environment. In order to minimize the risks of mechanical failure (such as those caused by thermal cycling), all the constituents should present a CTE as compatible as possible. The chips are the locations where heat is produced, so their surroundings can be subject to high operating temperatures (which are expected to increase due to the rise in power densities [3]). A very high electric field can be present locally in the area surrounding the chips and patterned copper (due to triple points and sharp edges). The encapsulating material and ceramic plate should therefore have high breakdown strength.

The second example of a system to be described is a power cable. Many varieties of this energy transport device can be found, from medium voltages to very high voltages (up to hundreds of kV), operating in AC or DC, and in many environments, in the air, ground, or underwater. Given the wide diversity, we will focus here on the example of a 3-phase high voltage cable.

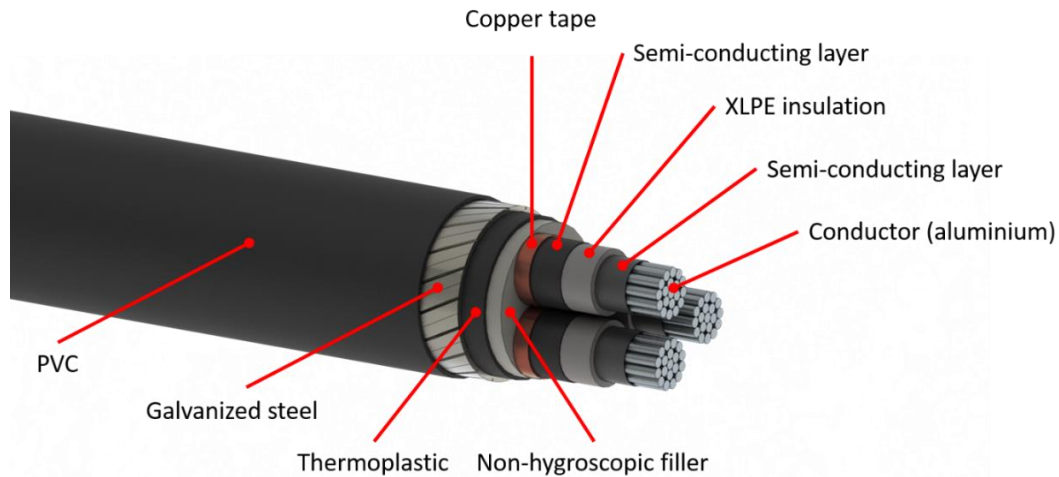


Figure I-2: Example of the composition of a 3-phase high voltage AC cable.

The main purpose of the cable (i.e. transporting energy) is fulfilled by the three conductors (one for each phase), generally made of aluminum (light weight and low cost) or copper (higher conductivity). Three consecutive layers are found directly surrounding the conductors: a sandwich of XLPE between semi-conducting layers. The role of the XLPE is to ensure insulation while the semi-conducting layers are present for electric field grading purposes to prevent partial discharges and reduce stress. The semi-conducting layer is generally made of polymers filled with carbon black. The insulating system must present the lowest losses possible. The outer PVC layer function is to protect the cable from external aggression, such as humidity and dust.

The materials in power cables are subjected to highly diverse constraints: they are in close contact with very high voltage; they are designed to withstand moderate temperature (up to 130 °C for a very short time). The most challenging aspect in cables is that, due to their high cost and the difficulty of maintenance, they are often designed to be in service for 40 years or more. The material aging in these conditions is quite complex to figure out due to water absorption, space charge formation (mostly in HVDC applications [4]), etc. Therefore, the materials used must be very stable over time. Examples of current research focus on understanding the space charge formation and on the replacement of carbon black fillers by carbon nanotubes to improve mechanical properties.

The final example is that of the capacitors. Here, we focused on film capacitors, i.e. where the dielectric material is a polymeric film. As polymers have low dielectric constants, capacity is increased by using large surface areas. The typical way to handle this large surface is with interdigitated electrodes as shown in Figure I-3.

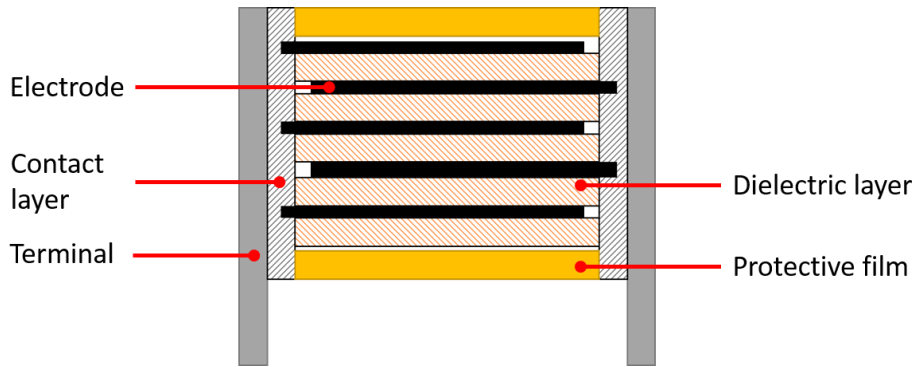


Figure I-3: Scheme of interdigitated film capacitor.

Each electrode is separated from neighboring electrodes by a thin dielectric layer. The capacitance being directly proportional to the distance between electrodes, thinner dielectric layers lead to increased capacity but lower breakdown voltage. Many different polymers are used as dielectrics (polypropylene, polyethylene etc.), depending on parameters such as the operating voltage, temperature, the environment, and others.

Although this kind of capacitor design is common, many other designs exist according to the intended function (embedded capacitors, filtering, energy storage, electromechanical transducers, etc.). The nature of the constraints differs greatly, as capacitors can be operated under a variety of conditions, from low to high voltage, high temperature, in stationary or portable systems, etc. Current developments are related to developing materials presenting higher permittivity and lower losses. Many ongoing research projects are based on polymer/ferroelectric ceramic and polymer/conductive filler composites [5].

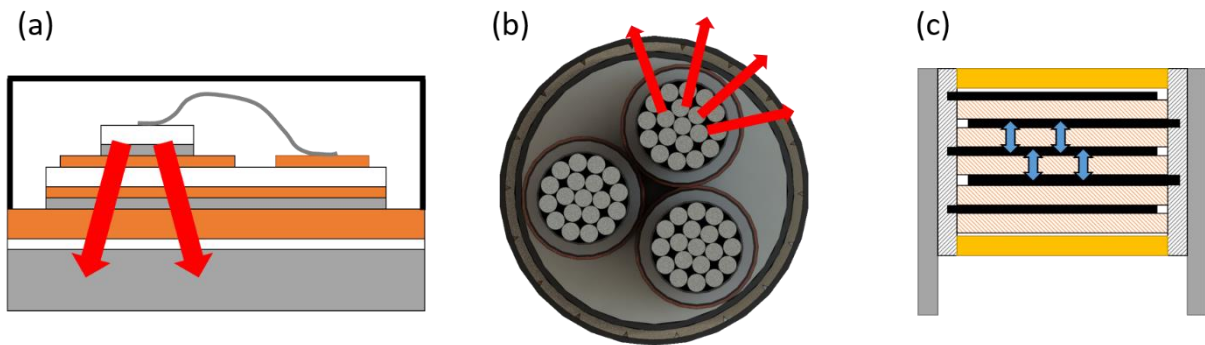


Figure I-4: Scheme of the heat flux (red arrows) and electric field (blue arrows) in (a) power module, (b) power cable, and (c) capacitor.

As a concluding remark, let us add that the systems presented have at least one point in common: all the materials used (pure or composite) have isotropic properties. However, the designs used often lead to flux directed preferentially in a single direction. For instance, the electric field is directed toward the electrodes in the capacitors; the heat flux is directed from the hot source (chip or conductor) to the cold source (sink or outer part of the cable) in power modules and cables (Figure I-4). This mismatch between material properties, and the direction of flux, open the possibility to enhance material properties by

better adapting them to their systems. In order to study this, today's isotropic materials (pure and composite) are examined in the next section. Then we address anisotropic materials and the ways to induce anisotropy.

*1.1.b. Isotropic materials*

*1.1.b.1 Polymers (as matrix)*

Polymers are used in electrical engineering for a wide range of applications that can generally be divided into two categories: insulation and dielectrics. The first category implies preventing the current from flowing between two electrodes with different electric potentials. Related applications include cable insulation (electrical transport, motors, busbar), passivation and packaging of electronic component, and printed circuit boards (PCB). The second category also implies low electrical conduction, this time for the purpose of energy storage. Generally, this term is also related to high polarizability, but polymers present a low dielectric constant. The associated application is for capacitors (energy storage, filtering). The lack of polarizability of polymers is compensated by their high dielectric strength. If large capacitance is required, it can be attained by implementing a large surface. Another application for polymers is their use as a chemical barrier. The range of properties for polymer materials is very broad. A partial summary is provided below in Table I-1.

Table I-1: Some general properties of polymers

	<b>Property</b>	<b>General behavior</b>	<b>Range</b>	<b>Ref.</b>
	Density [g.cm <sup>-3</sup> ]	Very low to low	0.84 – 2.35	[6]
<b>Mechanical</b>	Young's modulus [GPa]	Very soft to hard	1e-3 – 2.59	[7], [8]
	Conductivity [W.m <sup>-1</sup> .K <sup>-1</sup> ]	Very low	0.1 – 1	[8]
<b>Thermal</b>	Operating temperature [°C]	Very low to moderate	-269 – 400	[9]
	Glass transition [°C]	Very low to moderate	-128 – 400	[9], [10]
	Resistivity [Ω.m]	High to very high	10 <sup>-3</sup> – 10 <sup>16</sup>	[11], [12]
<b>Electrical</b>	Dielectric strength [kV.cm <sup>-1</sup> ]	High to extremely high	up to 10000	[13]
	Permittivity	Very low to moderate	2 – 45	[14], [15]

---

Some values in Table I-1 may seem unusual, but this is because more than just “conventional” polymers are taken into account. For example, very low values of resistivity are found in the case of conductive polymers, and higher values for permittivity in the case of copolymers.

The advantages of polymers include their ease of implementation (extrusion, molding, doctor blade, spin-coating, dip-coating etc.), high dielectric strength, low loss factor, chemical resistance, mechanical properties (compatibility with the substrate, shock resistance), and ability to serve as a barrier to moisture. Some resins are photosensitive, which allow using photolithographic techniques.

On the other hand, their disadvantages include their low thermal conductivity, relatively low operating temperature, and low permittivity (which actually can be advantageous in some applications). Also, the polymerization reaction is exothermic and can lead to thermal runaway.

Even if polymers present very interesting properties, some of their disadvantages are an obstacle for their use. That is one of the reasons why intense research has been conducted on composite materials with a polymeric matrix, to improve material performance or extend the range of polymer properties and applications.

### *1.1.b.2 Composites*

A composite is a material comprising at least two distinct phases. The purpose of the composite is to compensate a weakness in one of its constituents by adding other compounds. Wood is an example of natural composite with a polymer matrix (lignin) conferring resistance in compression filled with cellulose resisting traction. There are numerous examples of artificial composites, such as concrete, fiber reinforced plastics, TIM, to name a few.

In the field of electrical engineering, most composites are made with a polymer as the matrix. There are few other materials that use other matrices, such as ceramic-metal (cermet) for resistor and capacitor applications.

When it comes to elaborating a composite, the strategy is to define the specifications related to the intended application and then choose the matrix and filler according to their properties. The matrix must be compatible with the processing method, while presenting properties approaching the intended requirements. The filler is then chosen according to the property to be enhanced/introduced. Various fillers are available, depending on the material nature (ceramic, polymer, metal etc.), size, and shape. Generally, the size of the filler ranges from a few nanometers to 100  $\mu\text{m}$ , with the particle being spheroidal, ellipsoidal (needle, platelet), or fibrous. The size and shape of the particle are very important and must not be overlooked.

The following paragraphs present the general properties of different types of filler, along with examples of composite implementations.

### 1.1.b.3 Ceramic fillers

The variety of ceramic powders is very wide, from nanoscale to microscale. Almost all shapes are available. General properties of ceramics are presented in Table I-2.

The advantages of ceramic powders include high thermal conductivity as compared to polymers (ex. AlN), high permittivity (ex. BaTiO<sub>3</sub>), and support for very high operating temperatures. Ceramics can also present properties almost entirely absent from polymers, such as piezoelectric (ex. PZT), pyroelectric (ex. PZT), non-linear resistivity (varistor effect) (ex. ZnO), and magnetic properties (ex. Fe<sub>2</sub>O<sub>3</sub>).

The disadvantages of ceramic powders include their density mismatch with polymers (sometimes leading to sedimentation) and lower dielectric strength than polymers.

Table I-2: Some general properties of ceramics.

	Property	General behavior	Range	Ref.
	Density [g.cm <sup>-3</sup> ]	Moderate to high	2.5 – 15.6	[16]
<b>Mechanical</b>	Young's modulus [GPa]	Very Hard	73 – 500	[16], [17]
<b>Thermal</b>	Conductivity [W.m <sup>-1</sup> .K <sup>-1</sup> ]	Relatively high to extremely high	1 – 290	[17], [18]
	Operating temperature [°C]	Very high	500 – 1700	[16]
<b>Electrical</b>	Resistivity [Ω.m]	Low to high	10 <sup>-7</sup> – 10 <sup>12</sup>	[16]
	Dielec. strength [kV.mm <sup>-1</sup> ]	Medium to high	1 – 40	[16]
	Permittivity	Low to very high	4.1 – > 10 <sup>5</sup>	[16], [19], [20]

Some polymer/ceramic composites with very interesting properties have been elaborated. For example, Xu *et al.* reported an epoxy/AlN (60 vol%) with thermal conductivity of 11 W.m<sup>-1</sup>.K<sup>-1</sup> [21]; Ishida *et al.* reported a value of 32.5 W.m<sup>-1</sup>.K<sup>-1</sup> for polybenzoxazine/BN (78.5 vol%) composite [22]. As for the dielectric constant, 53.9 in permittivity at 1 kHz for PVDF/BaTiO<sub>3</sub> (50 vol%) was achieved by Yu *et al.* [23], but with relatively low dielectric strength, while Li *et al.* reported a P(VDF-CTFE)/ZrO<sub>2</sub> (9.1 weight % ≈ 2 vol%) composite with relatively low permittivity but high dielectric strength, allowing them to reach high energy density (11.2 J.cm<sup>-3</sup>) [24]. Higher permittivity (738 at 100 Hz) can be



---

obtained, but at the cost of increased losses (1.8 at 100 Hz) [13]. A PVDF/PZT composite (50 vol%) reached a piezoelectric coefficient value of  $13.8 \text{ pC}\cdot\text{N}^{-1}$  [25].

Xie *et al.* presented an interesting result: they managed to obtain a poly(vinyl alcohol)/BN composite with  $3.9 \text{ W}\cdot\text{m}^{-1}\cdot\text{K}^{-1}$  thermal conductivity at only 5.9 vol% [26]. This rather good result at such a low filler concentration was attributed to the aspect ratio of the particles (platelet shape) and a partial orientation of the fillers due to the deposition method.

Another aspect of composite that is studied intensively is the ability to improve materials' electrical performance. The major body of these works focuses on polymer/silica ( $\text{SiO}_2$ ) nanocomposites. It has been shown that these materials can present increased dielectric strength [27], PD resistance [28], [29], and decreased leakage current density [30]. The dependence of the dielectric strength results appears to be very sensitive to particle size. The general trend is a higher dielectric strength with nanoparticles than with microparticles [31]. However, the addition of nanoparticles does not ensure an increase in the dielectric strength compared to the neat polymer.

It is important to note that most of the composites cited above present very high volume fraction of fillers, and in some cases, additional treatments such as surface modification of particles were used.

#### *1.1.b.4 Metallic fillers*

Some examples of polymer/metal nanocomposites can be found in literature. Silver nanoparticles were used with poly(o-toluidine) to obtain a composite with an electric conductivity of  $1.28 \text{ S/cm}$  [32]. Another application is the increase of thermal conductivity: Serkan Tekce *et al.* made a polyamide/copper (60 vol%) microcomposite reaching  $11.57 \text{ W}\cdot\text{m}^{-1}\cdot\text{K}^{-1}$  [33]. This article also emphasizes the importance of particle shape. Measurement of thermal conductivity (Figure I-5) showed that particles with a higher aspect ratio had greater influence on composite properties.

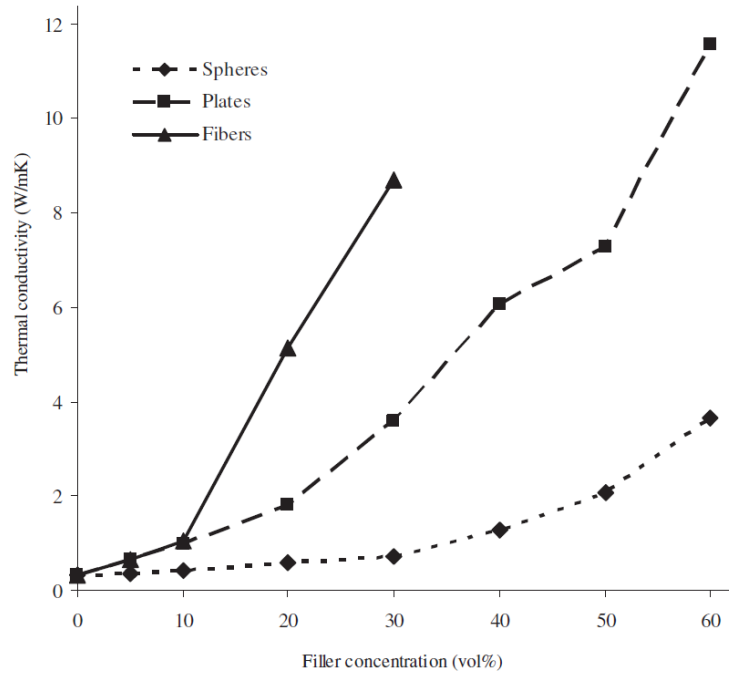


Figure I-5: Thermal conductivity of polyamide/copper composite as a function of filler concentration [33].

### 1.1.b.5 Allotropes of carbon fillers

The allotropic forms of carbon have met with great success in recent research with the development of carbon nanotubes (CNT) – single wall SWCNT and multi-wall MWCNT – and graphene (or graphene nanoplatelet GNP).

These nanoparticles with extraordinary properties are expected to lead to a breakthrough in composite materials. They also open the path to high-performance composites with low filler concentrations.

Table I-3 Some general properties of CNT and graphene monolayer.

	Property	CNT	Ref.	Graphene	Ref.
	Density [g.cm <sup>-3</sup> ]	1.33 – 1.4	[34]	2.0	[34]
<b>Mechanical</b>	Young's modulus [GPa]	640	[35]	1000 - 2400	[36], [37]
<b>Thermal</b>	Conductivity [W.m <sup>-1</sup> .K <sup>-1</sup> ]	1750 - 5800	[38]	3000	[34]
	Thermal stability [°C]	750 air 2800 vacuum	[34]	650 air	[39]
<b>Electrical</b>	Resistivity [Ω.m]	0.9×10 <sup>-6</sup>	[40]	50×10 <sup>-6</sup>	[34]

---

Among the numerous examples of composites made with CNT or graphene, we can mention PMMA/MWCNT (4 weight %  $\approx$  3.5 vol%) reaching  $4.4 \text{ W}\cdot\text{m}^{-1}\cdot\text{K}^{-1}$  [41], and polystyrene/graphene (2.4 vol%) nanocomposite with  $1 \text{ S}\cdot\text{m}^{-1}$  [42]. These materials are representative of the strong impact of CNT and graphene on material properties, even at very low filler content.

Carbon allotropes have numerous advantages: they are light in weight, and exhibit excellent mechanical, thermal, and electrical properties. Also, they are composed only of carbon, which is not a rare resource. However, many challenges make them complex to use. They are difficult to disperse and to stabilize in solution; their production is expensive; and the desired quality is not always achieved.

In parallel to graphene, many 2D particles are being developed, such as silicone [43] or monolayer  $\text{MoS}_2$  [44, p. 2].

### *1.1.c. Intermediate conclusion*

The list of materials mentioned in the previous paragraphs is merely a quick overview of the composites and properties that can be obtained. The materials were limited to two-phase composite, however, multiple phase composites can be found. In literature, other particles have seen growing interest, such as core-shell and Janus particles. The purpose of our review is to understand the general strategy for choosing the components used in a composite. The first step is to define the properties and their expected values needed for the intended application. The matrix should then be chosen according to its properties and the processing method. The choice of the particle is rather complex, as many types, sizes, and shapes are available. The first aspect to consider is the matrix property that needs to be enhanced, in order to determine what particle characteristics should be. Particle dimension is not a parameter to be neglected. Indeed, the effect of particle size can be extremely different, whether the particles are nanoscale or microscale. The example of dielectric strength is relevant to this extent; where microparticles tend to lower dielectric strength while nanoparticles can increase it. But it is important to note that nanoparticles are not always better than microparticles. Thus, one of the clues for obtaining suitable size is to determine whether the property to be enhanced relies on volume or on the surface properties of the particle. Tanaka attempted to give the general impact of nanoparticles on materials' electrical properties (dielectric strength, permittivity etc.) [45]. An alternative choice can be a distribution of particle size, with distribution being used to reach a high filler concentration. The last parameter to choose is the particle shape (or aspect ratio). In many cases, particles exhibiting a high aspect ratio lead to better performance, as they reduce the quantity of interfaces, which are generally detrimental. In that respect, many recent studies focus on the modification of these polymer/particle interfaces through chemical treatment.

Although materials with very interesting properties were presented here, there are still some outstanding issues related to these kinds of composites. In many cases, the volume fraction of filler needed to obtain a material with the desired properties is very high (up to 80 or 90 vol%). This is a major drawback because at these filler concentrations, some of the matrix properties are modified radically. The viscosity of the mixture before being cured can be very high, which makes implementation impractical. When cured, mechanical flexibility is drastically reduced, which is not a good option for many applications. Thus, in order to improve composite performance again, it will be necessary to lower the volume fraction of filler without degrading the properties. This is one of the promises held by anisotropic composites.

## I.2. Emerging materials: anisotropic composites

Many applications require a given property mainly in one direction as demonstrated in section I.1.a. Despite that, all the materials mentioned in the section I.1 have something in common: their properties are isotropic, meaning that they present the same properties in every direction. This means that current materials and composites are not fully optimized for the systems in which they are used. One way of working towards matching materials to systems would be to make them anisotropic, that is, tailoring the material to obtain the appropriate property in the appropriate direction for a given application.

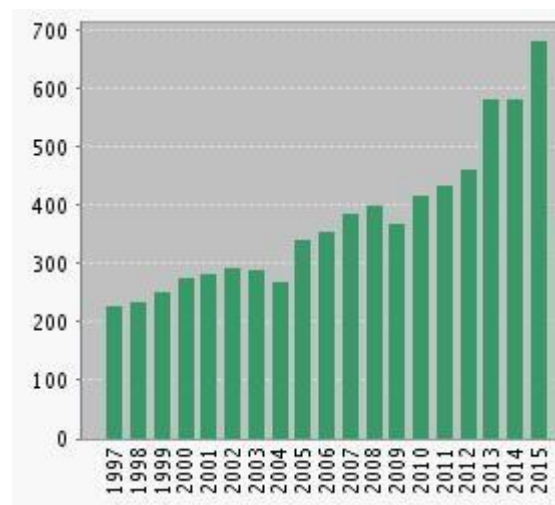


Figure I-6: Published items each year over the past 20 years with the keywords “anisotropic composite” [46].

The topic of anisotropic material has raised a growing interest over recent years, as can be seen in Figure I-6 (figure from [46]), reaching nearly 700 publications in 2015.

### I.2.a. Benefits of anisotropy

A simple example to explain the inherent benefit of anisotropy is the case of the capacitor. Let us consider a 1 mm side cube of permittivity 4. Inside the cube are placed 8 particles of permittivity 1000. Two different cases are studied, shown in Figure I-7. Numerical simulation performed using FEM [47]

allows computing capacitance in every direction. The computation method is described in detail in section V.2.a. The results are summarized in Table I-1.

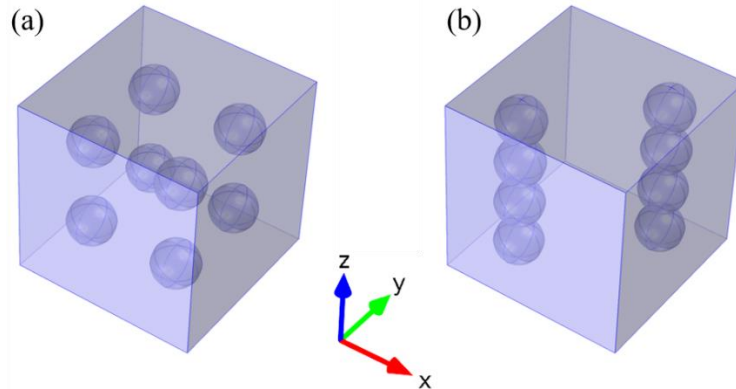


Figure I-7: Geometry simulated for (a) isotropic composite and (b) anisotropic composite.

The result shows a clear enhancement of material capacity in the direction of the aligned spheres for the material in Figure I-7 (b). In the other directions, the capacity value is smaller than with the isotropic composite. Numerical evidence of this is also reported by Wang *et al.* [48].

Table I-4: Calculated capacitance of isotropic and anisotropic composite

Material \ Axis	(a) [fF]	(b) [fF]
	X	43
Y	43	41
Z	43	84

The first interest of anisotropy is therefore to improve a property in one direction compared to an isotropic composite at the same filler content, or to obtain the same property but at lower filler concentration. This example is a good illustration of the concept of a material matched to a system. In a capacitor, the high permittivity of the dielectric material is needed only in the direction of the applied field, making the material in Figure I-7 (b) more adapted for a capacitor application as long as the dielectric strength remains the same. The slight decrease in X and Y permittivity has no impact on material performance (capacitance) because the electric field should not be directed in these directions.

Another key aspect of this material was also reported by Wang *et al* and can be observed in Figure I-8. From this numerical simulation, the dielectric susceptibility of the isotropic composite tends to saturate when filler susceptibility equals 20 times that of the matrix. On the contrary, no saturation is observed for the anisotropic composite due to the continuous path of high permittivity phase in the direction of the electric field. This means, for example, that there is no interest of using particles with very high

permittivity for an isotropic composite, since the impact becomes negligible above 20 times the permittivity of the matrix. For an anisotropic composite, there is still an interest in using particles with very high permittivity.

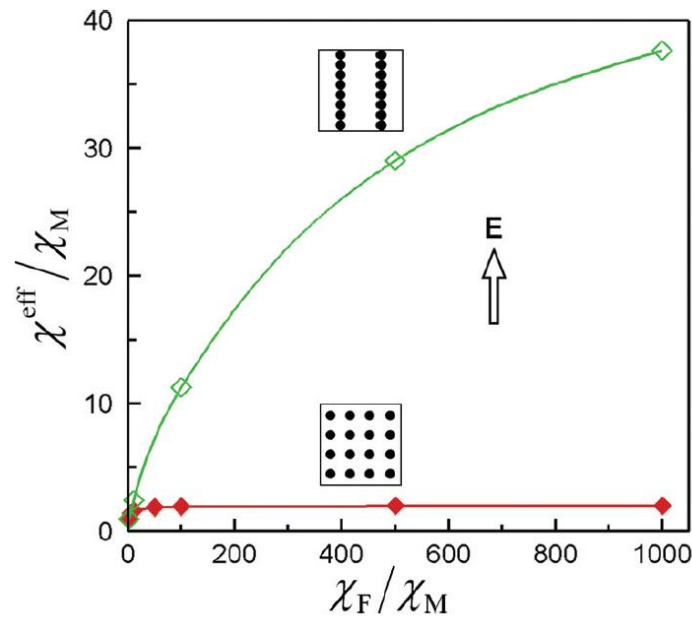


Figure I-8: Reduced composite dielectric susceptibility as a function of the filler reduced dielectric susceptibility [48].

Of course, the real structures of composite materials are much more complex than these simulated structures.

### *1.2.b. Methods for anisotropic composite processing*

There are several ways to induce anisotropy in composites, each of them having its own advantages and disadvantages. The common point to all these methods is the application of an external constraint prior to, or during, matrix processing.

#### *1.2.b.1 Mechanical/acoustic constraint*

Several methods have been developed to elaborate an anisotropic composite by applying a mechanical constraint. It should be noted that the mechanical constraint does not lead to the assembly of particles in chains, but rather to the alignment of non-spherical particles in a preferential direction.

The examples of methods found in literature are extrusion [49] and uniaxial strain [50]. The obtained structures are shown in Figure I-9.

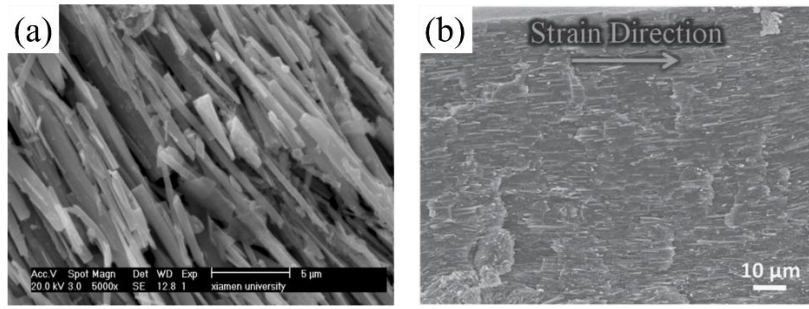


Figure I-9: Composite with mechanically aligned fillers. (a) BaTiO<sub>3</sub> whiskers after heat removal of the polymer, (b) PVDF/PZT (10 vol%) composite.

The use of acoustic waves to develop an anisotropic composite allows obtaining periodical structures and complex orientational behavior (Figure I-10). This method was demonstrated to work on a relatively large scale with the use of ultrasound. Contrary to mechanical methods, the use of spherical particles is not prohibited. Solid and liquid composites such as acrylic/polysiloxane, water/mica, water/polystyrene [51], water/polystyrene fiber [52], epoxy, polyester, silicone, and agar/glass [53] were obtained. To the best of the author's knowledge, only the mechanical properties of the obtained composites were studied, demonstrating an improvement.

Table I-5: Mechanically-structured composite properties

Method	Matrix	Filler	Filler content (vol%)	Property	Value	Increase (%)	Ref.
Extrusion	PVDF	BaTiO <sub>3</sub>	30	permittivity	90,72	104	[49]
Extrusion	PVDF	BaTiO <sub>3</sub>	30	piezo. coef.	13,7 [pm/V]	29	[49]
Strain release	PVDF	PZT	40	permittivity	45	80	[50]
Acoustic	Polymer	Glass	9.0 ± 2.0	mechanical failure	45 [MPa]	43	[53]

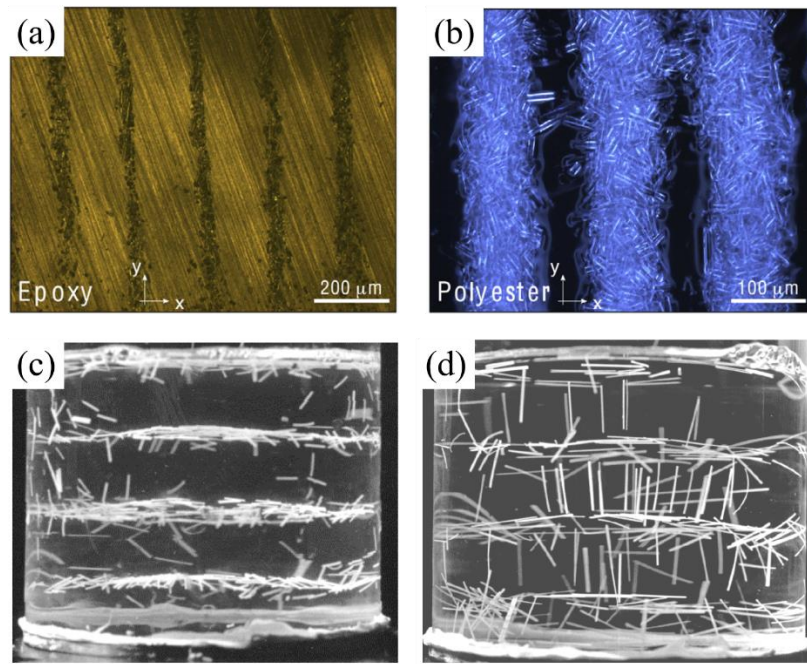


Figure I-10: Ultrasonically patterned composites. (a) epoxy/glass [53], (b) polyester/glass [53], (c) and (d) polystyrene fiber in water sugar solution [52].

The properties of anisotropic composites obtained with mechanical/acoustic constraints and the relative enhancement are summarized in Table I-5. The enhancements are compared to isotropic composite or anisotropic composite with perpendicular alignment.

The main advantage of mechanical constraints is their ability to work for large pieces.

Nevertheless, there is at least one disadvantage related to applying a mechanical constraint: it is often not compatible with in-situ tailoring of the material, as it would not be possible to apply a mechanical constraint in complex systems.

### 1.2.b.2 Electrical constraint

Tailoring composites under an electric field has been studied intensively over the past several decades. The terminology used is rather diverse and must be divided into two categories: assembly and alignment. The first term corresponds to particles connecting into chains in the direction of the applied electric field under dielectrophoretic force. The assembly phenomenon has several denominations, such as dielectrophoretic or electric field driven/assisted/induced assembly, chaining or pearl-chaining etc. The alignment of a particle corresponds to a non-spherical particle exhibiting a stable orientation (in the case of an ellipsoidal particle, one of its axes is aligned with the direction of the electric field) under the application of an external electric field. The alignment phenomenon also has several denominations, such as electro-orientation, electric field assisted/directed alignment/orientation. These two phenomena can be observed in AC and DC electric fields. For alignment, the use of DC leads to the long axis of the particle being parallel to the direction of the electric field.



---

Table I-6 summarizes a review of some developed anisotropic composites. The range of impacted properties is very wide: including permittivity, electrical and thermal conductivity, elastic modulus, optical transmittance. The range of matrix and fillers is also diverse. Several comments can be expressed regarding the data in this table. With respect to permittivity, the highest value is obtained with carbon nanofibers (CNF) as filler [54]. However, care should be taken regarding this result; CNFs are a conducting material, so even if the permittivity reaches very high value, the losses also increase dramatically. For the other materials, polydimethylsiloxane (PDMS) might not be the best choice as a matrix for energy density related applications, due to its very low permittivity (between 2.3 - 2.8) [55]. Matrices such as PVDF or copolymer can present higher permittivity. However, dielectric strength also needs to be high for such applications.

The electrical conductivity of anisotropic materials exhibits the most impressive results obtained [56]. More importantly, these results are reached at a very low filler concentration. The type of filler used is mostly CNT, GNP, or carbon fiber as conductive materials [56]–[58]. These particles also have the benefit of a high aspect ratio. Another interesting property of the obtained composites is their relatively high optical transmittance that is sometimes needed in some applications (e.g. solar panels).

It is important to note that the results of dielectric strength values presented in the Table I-6 [59], [60] are not representative of the typical properties of anisotropic materials. This is certainly due to the fact that here for the breakdown test the electric field is directed normally to the direction of the chains.

The thermal conductivity results are still rather limited [61], [62], certainly due to the interface of polymer between particles acting as a thermal resistance.

This table is clearly non-exhaustive, and many other particles (e.g. Janus [63], gold nanoparticles [64]) and properties (pyroelectricity [65]) have been studied. Another type of composite that is important to mention is electrorheological fluid [66]. This composite is unusual in the sense that the matrix remains liquid. However, the same principle acts in these fluids, with the application of an electric field leading to the formation of chains in its direction, modifying the viscosity and mechanical properties of the liquid composite. This phenomenon has been studied intensively both experimentally and numerically [67], [68].

Table I-6: Review of anisotropic composites with associated properties. The increase is compared to isotropic composites at the same volume fraction.

Property	Matrix	Filler	Filler content (vol%)	Value	Increase	Ref.	Comment
Permittivity	PDMS	BaTiO <sub>3</sub>	25	12.7	65 %	[55]	
	PDMS	BaTiO <sub>3</sub>	≈ 11	9	41 %	[69]	
	Epoxy	CNF	≈ 3	≈ 500	×50	[54]	High permittivity but increased losses
Electrical Conductivity [S/m]	Acrylate	SWCNT	≈ 0.03	10 <sup>-4</sup>	×10 <sup>3</sup>	[57]	
	PSU	MWCNT	≈ 0.5	10 <sup>-1</sup>	×10 <sup>14</sup>	[58]	Increase compared to pure polymer
	Epoxy	MWCNT	≈ 0.01	3.10 <sup>-4</sup>	×5.10 <sup>6</sup>	[70]	
	Epoxy	CNF	≈ 2	3.10 <sup>-2</sup>	×3	[56]	
	GNP	≈ 2	10 <sup>-5</sup>	×5.10 <sup>3</sup>			
Dielectric Strength [kV/mm]	PDMS	BaTiO <sub>3</sub>	25	128	25 %	[59]	In the direction perpendicular to the chains
	PE	o-MMT	6 (wt%)	370	23 %	[60]	In the direction perpendicular to the chains
Thermal conductivity [W.m <sup>-1</sup> .K <sup>-1</sup> ]	Epoxy	GNP	≈ 0.54	0.41	26 %	[61]	
	Epoxy	Aluminum	9.4	0.39	34 %	[62]	Particle are coated with Al <sub>2</sub> O <sub>3</sub>
Elastic modulus [GPa]	UDMA /HDDMA	SiO <sub>2</sub> + ZrO <sub>2</sub>	57	8.3	12 %	[71]	
Optical Transmittance	Epoxy	MWCNT	≈ 0.01	65 %	×2.6	[70]	

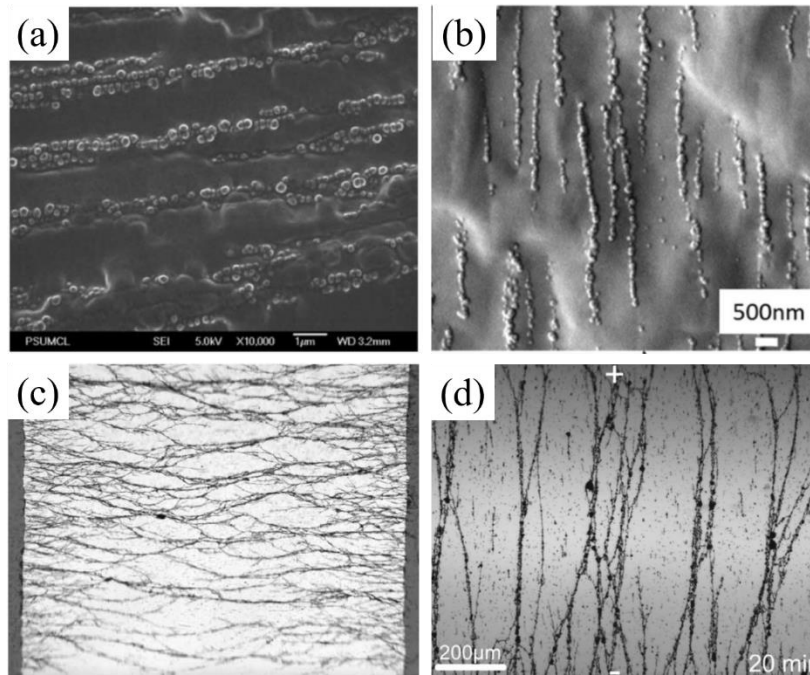


Figure I-11: Electric field structured composites. (a) PDMS/BaTiO<sub>3</sub> [55], (b) PDMS/BaTiO<sub>3</sub> [69], (c) epoxy/CNF [54], and (d) epoxy/GNP [61].

Images of some anisotropic composite presented in Table I-6 can be observed in Figure I-11. The difference in the structures between insulating (Figure I-11 (a) and (b)) and conductive (Figure I-11 (c) and (d)) particles is clear. As the electric potential is displaced at the end of the wires for conductive particles, it can lead to a very intense electric field locally resulting in tree formation.

The evolution of permittivity, and permittivity *increase*, as a function of filler concentration for two different composites, is shown in Figure I-12. The first observation is that permittivity increases with filler content, which seems logical. The second observation is that the permittivity *increase* compared to the isotropic composite starts by increasing at low filler content, reaching a maximum and then decreasing with filler content.

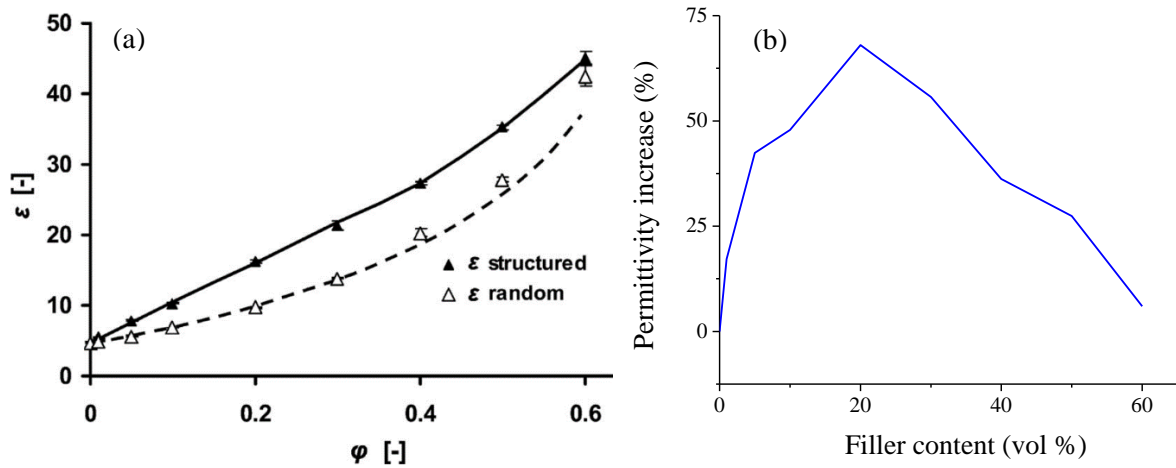


Figure I-12: (a) Permittivity of anisotropic (structured) and isotropic (random) epoxy/PZT composite and (b) permittivity increase compared to isotropic composite, as a function of the volume fraction of filler ( $\phi$ ) [72].

The same observations can be made for other properties, such as the piezoelectric coefficient (Figure I-13). The difference in the piezoelectric coefficient *increase* is even larger, but no evidence of increase at low filler content was observed.

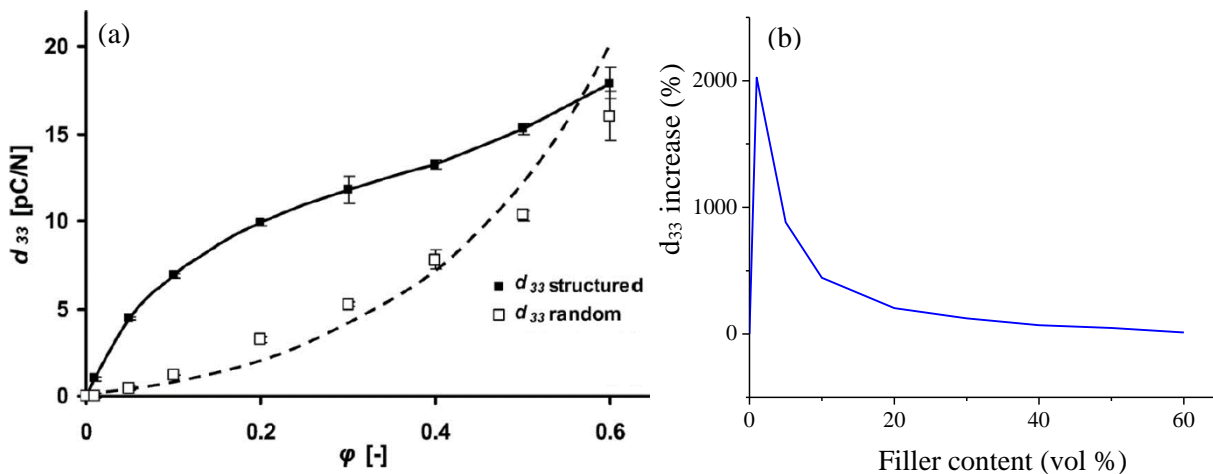


Figure I-13: (a) piezoelectric coefficient ( $d_{33}$ ) and (b) piezoelectric coefficient increase compared to isotropic composite as a function of the volume fraction of filler. Epoxy/PZT composite from ref. [72].

The behavior can be understood partially (at least concerning permittivity) from a circuit point of view. The simplest model for ideal anisotropic composite is two capacitors in parallel. For the isotropic composite, permittivity can be estimated thanks to a mixing law (more detailed explanation and study of mixing laws is provided in section III.2.b). The Lichtenecker equation was chosen here to model permittivity. The results are plotted in Figure I-14.

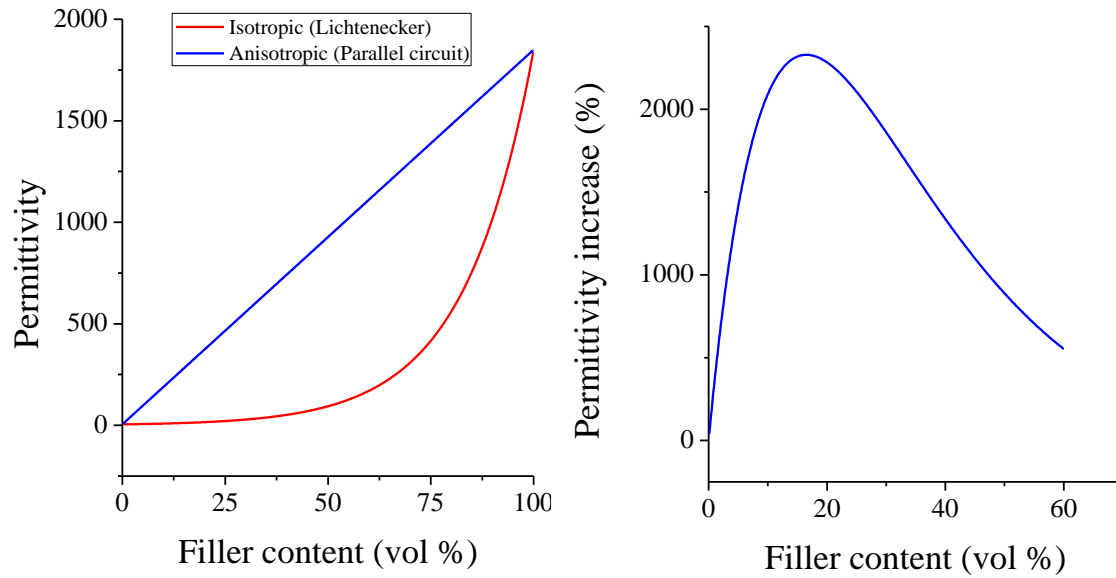


Figure I-14: Theoretical prediction of permittivity, and permittivity increase, for ideal anisotropic and isotropic composite as a function of filler content.

A numerical estimation of the permittivity *increase* predicts a maximum of around 18 vol%, which is in good agreement with experimental measurements. This specific behavior is very important, as it reflects the fact that the beneficial impact of the anisotropic composite is preponderant at low filler concentration.

The advantage of the electric field structuring method is the ease of applying the voltage. Electrodes are already present in many systems, allowing “in situ” tailoring of the composite. With the only condition for chaining or alignment being a difference in the complex permittivity between the particle and matrix, this approach works for almost every matrix/particle pair.

The disadvantage of this method is the need for high voltages when the sample is thick, hence limiting the maximum possible thickness. Electrohydrodynamic flow induced by the electric field can also restrict the operating frequency range to chain/align. The obtained properties are sometimes small compared to that which can be expected, probably due to particle/matrix interface. This is well illustrated by comparing the experimental results in Figure I-12 to the theoretical results in Figure I-14. Another limitation is that the chaining/alignment is restricted to the direction of the applied electric field.

### 1.2.b.3 Magnetic constraint

Tailoring under electrical constraint was described in the previous section. A strong analogy exists between magnetic and electrical constraints. The equivalent of dielectrophoresis is magnetophoresis, and the equivalent for electro-orientation is magneto-orientation. The analogy between these mechanisms was addressed extensively by [73]. However, some differences are still encountered in magnetic tailoring, with the presence of a permanent magnet more frequently than its electric equivalent (electret) and the phenomenon of saturation.

Examples of composites structured using a magnetic field are summarized in Table I-7.

Table I-7: Magnetically structured composite properties

Matrix	Filler	Filler content	Property	Value	Increase	Ref.
Silicone	Ni silver coated	0.75 vol%	Electrical conductivity	$2.5 \times 10^{-2}$ [S/m]	-	[74]
			Optical transmittance	> 90 %	-	
PMMA	Cobalt nanowire	1 vol%	Electrical conductivity	2 [S/m]	×4	[75]
Epoxy	CNT	3 weight %	Thermal conductivity	$6.6$ [W.m <sup>-1</sup> .K <sup>-1</sup> ]	10 %	[76]
PDMS	Fe <sub>3</sub> O <sub>4</sub>	30 weight %	Elastic modulus	10 [kPa]	×2.5	[77]

Most studies available in literature deal with CNT alignment. Transparent conductive materials seem to be the most frequent item.

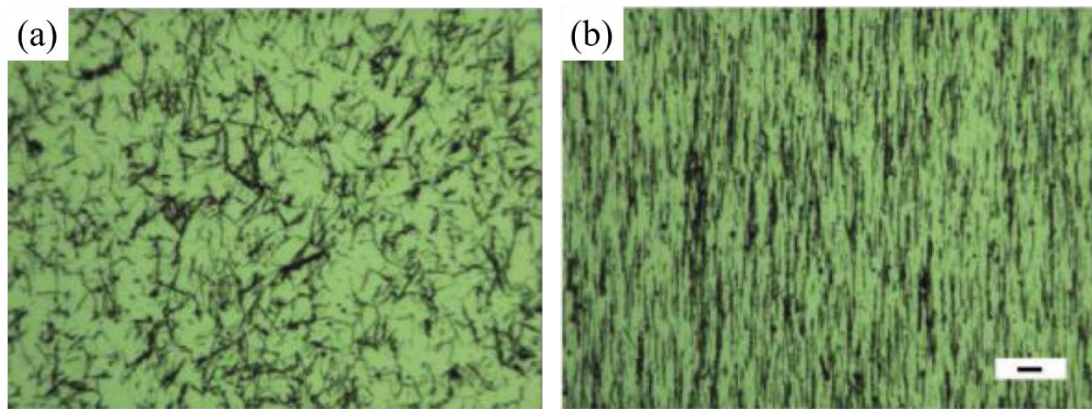


Figure I-15: PMMA/Cobalt nanowire composite (a) isotropic and (b) magnetically chained/aligned [75].

The advantage of magnetic field structuring is that very good results are obtained with CNT-based particles.

However, the use of a magnetic field drastically restricts the possible type of particles, as compared to an electric field. In addition, the application of a magnetic field is more complex and in-situ structuration is almost impossible.

### *1.2.c. Terminology*

As used to present the above materials, the term *anisotropic* is commonly accepted to describe composites presenting different properties in different orthogonal directions. However, a more exact designation of the composites obtained under external constraint should be *orthotropic* composite: a subgroup of anisotropic composites. Indeed, the composites described in this section of the manuscript

present three orthogonal symmetry planes. The impact on the permittivity tensor is described in Table I-8.

Table I-8: Permittivity tensor of different material types

Anisotropic	Orthotropic	Isotropic
$\underline{\underline{\varepsilon}} = \begin{bmatrix} \varepsilon_{xx} & \varepsilon_{xy} & \varepsilon_{xz} \\ \varepsilon_{yx} & \varepsilon_{yy} & \varepsilon_{yz} \\ \varepsilon_{zx} & \varepsilon_{zy} & \varepsilon_{zz} \end{bmatrix}$	$\underline{\underline{\varepsilon}} = \begin{bmatrix} \varepsilon_{xx} & 0 & 0 \\ 0 & \varepsilon_{yy} & 0 \\ 0 & 0 & \varepsilon_{zz} \end{bmatrix}$	$\underline{\underline{\varepsilon}} = \begin{bmatrix} \varepsilon & 0 & 0 \\ 0 & \varepsilon & 0 \\ 0 & 0 & \varepsilon \end{bmatrix} = \varepsilon$

However, since the term anisotropic is widely accepted by the scientific community, that term will continue to be used in this thesis dissertation to describe orthotropic composites.

### I.3. Conclusion

The main characteristics of the polymer-based materials used in electrical engineering have been presented throughout this first chapter. The properties of pure, isotropic, and anisotropic composites have been summarized. The latter materials have seen a growing interest over the past years. Among the three possible constraints to induce anisotropy in composites (mechanical, magnetic, and electrical), the tailoring of material by means of an electric field present some advantages. The most valuable assets are perhaps the possibility of in-situ tailoring, and being able to be adapt to systems without intrinsic modification (addition of electrodes). Taking into account these considerations, the electric field was selected in this work as the means to tailor composites.

However, regardless of its benefits, this tailoring method is not mature at this time. The enhancement of properties is proven, but somehow those properties fail to reach full expectations, far from the theoretical gain. An overview of the publications on electric field-structured materials shows that, currently, these materials are exclusively developed empirically. The typical method is to make the composite, vary some parameters (filler content, electric field magnitude and frequency), and characterize the obtained composites. While showing interesting outcome, this method is limited in terms of understanding the phenomena involved. Very few examples of monitoring the formation of anisotropic composites can be found in literature, whereas that aspect offers significant knowledge about the structuring phenomenon. Of course, some authors have tackled chaining/alignment theoretically and numerically, but without correlating it with the predictive elaboration of composite materials.

With these considerations in mind, the hypothesis of this work is that it should be possible, based on a predictive approach, to tailor the structure of a composite from isotropic to anisotropic when applying an electric field. To achieve this accurate control of material properties, several challenges first need to be addressed, as summarized in the following roadmap:

- Based on the theoretical study of the phenomena leading to filler structuration, the forces and parameters involved will be determined. A theoretical study should lead to the development of a structuration model.
- Once the physical parameters of the system are identified, their values need to be fully measured. This knowledge is essential both for experimental (to target experimental parameters) and numerical (as inputs of the model) investigation.
- The materials then need to be elaborated with online monitoring during their structuration. The physical parameter monitored must be related quantitatively to the numerical simulation in order to allow the comprehensive comparison between the model and the experiment.
- The obtained material will be characterized to confirm the accurate control of composite properties.
- Lastly, the model and the experiment results will be compared, while varying as many parameters as possible to reach a conclusion regarding the validity of the simulation.

Each of these points is addressed in this manuscript.

As a first step, we present in the next chapter, a survey of the force induced by the electric field, leading to the tailoring of filler structure, from historical development to theoretical and numerical description.







# Chapter II

Dielectrophoresis:  
Theoretical Description

## II. DIELECTROPHORESIS: THEORETICAL DESCRIPTION

A dielectric particle immersed in a dielectric medium, subject to a non-uniform electric field, will undergo a force: the dielectrophoretic (DEP) force. This force is the starting point of the formation of anisotropic composites under electric field. This phenomenon is studied in this chapter to understand the interaction between a particle and a non-uniform electric field, and to identify the key parameters involved.

### II.1. Dielectrophoresis: a brief survey

#### II.1.a. *Early descriptions*

The first tracks of dielectrophoretic phenomena are generally attributed to Thales of Miletus, around 600 B.C. The trading routes brought a material called “*electron*” ( $\eta\lambda\epsilon\tau\rho\theta\nu$ ), known today as amber. Even if the original text is missing, further documents report [78] that Thales succeeded in attracting fluff and other materials with a rod of amber rubbed with fur. The conclusion of this very early experiment was that a “magnet” (confusion was made between electrical and magnetic effects) had a soul because it was able to cause motion. The conclusion may seem amusing to us now, but behind this experiment lies the discovery of electrostatics and triboelectricity.



Figure 0-1: A piece of amber and fur [79].

Much later, in the 17<sup>th</sup> century, William Gilbert showed the interactions between drops of water and electrified amber in his book “*De Magnete*” [80]. The distinction between magnetism and electrostatic was an important step forward of his work.

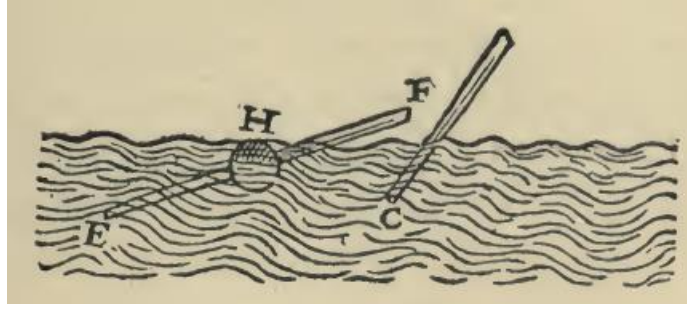


Figure 0-2: Drop of water attracted by amber rods [80].

In the middle of that same century, Winckler [81] and Priestley [82] studied the attractive forces acting upon organic matter. They are considered as the first people to describe the chaining of particles. The first step in the theoretical treatment of DEP followed Maxwell's theories with a description of the equation of the force acting on a dielectric sphere subject to a non-uniform electric field [83].

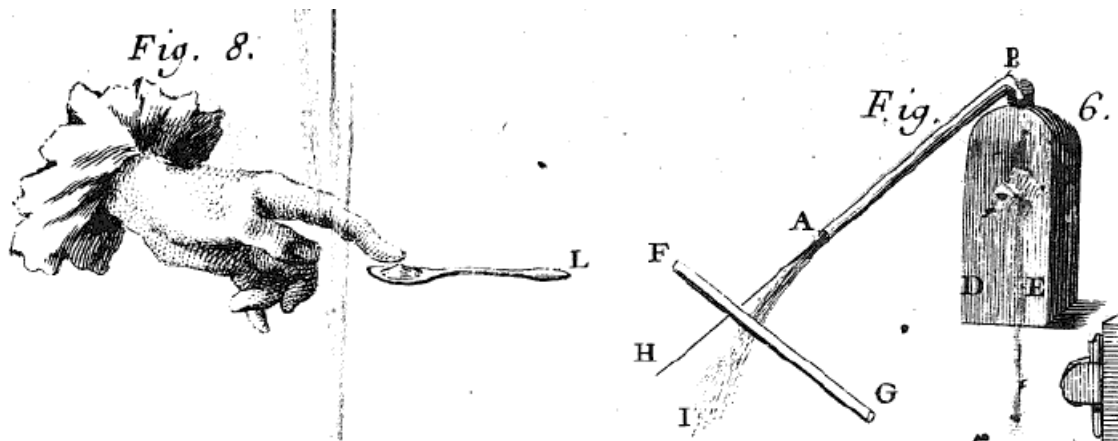


Figure 0-3: (Left) elevation of a liquid in presence of a charged body. (Right) deviation of a water stream by charged rod [81].

### *II.1.b. Development of the theory and applications*

The first industrial application of DEP was attributed to Hatfield, with a patent application in 1921 and published in 1924, about the separation of substances through the use of an electrostatic field (Figure 0-4) [84].

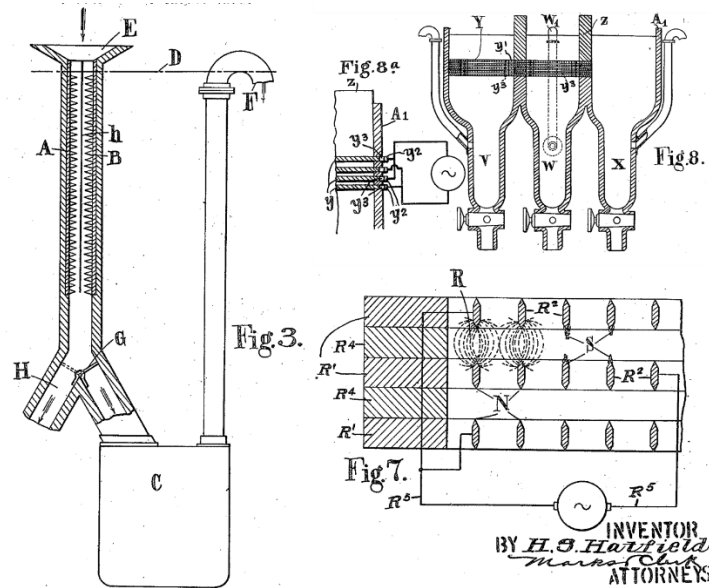


Figure 0-4: Illustration from a patent of different devices for particle sorting [84].

The word “dielectrophoresis” was coined by Herbert Pohl in an article published in 1951, in which he described the successful removal of carbon black from polyvinyl chloride [85]. Twenty-seven years later, in his book “*Dielectrophoresis, the behavior of neutral matter in nonuniform electric fields*” [86], he gave the following definition of the phenomenon: “the translational motion of neutral matter caused by polarization effects in a non-uniform electric field”. While Pohl’s first interests were concerned with liquid filtration, he rapidly began to study dielectrophoresis with biological cells and particles. The early interest in the behavior of cells and living matter subject to an electric field (chains of fat particles [87], biological cells and bacteria [88], [89]) led to intensive study and use of DEP in biomedical sciences in the second half of the 20<sup>th</sup> century. The ability to sort biological cells without killing them has proven to be of great interest. Among the numerous examples of how DEP is employed in this field, we can mention cell sorting and counting, driving and positioning single cells, cell characterization, etc. [90].

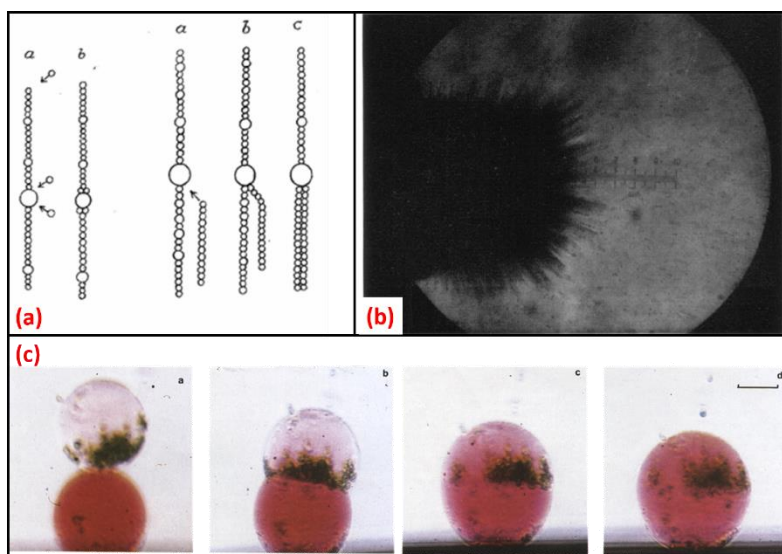


Figure 0-5: Examples of DEP applied to biological cells. (a) chaining [87], (b) yeast cell collection [91], (c) electrofusion [92].

From a theoretical point of view, the study of biological materials leads to the development of multipole corrections and to the elaboration of a core-shell model to describe the living cells.

In parallel with the growing interest of DEP in the biomedical field, the discovery by Willis Winslow of electrorheological (ER) fluids at the end of the 1940's (patent application in 1947 [93] and publication in 1949 [94]) opened the way for a new set of applications, such as clutches, shock absorbers, and valves. The ER effect corresponds to a fast change in a fluid's apparent viscosity (typically in milliseconds) by chaining particles through the application of an electric field. It is noteworthy to mention that great effort was made in this field on modeling the particle chaining.

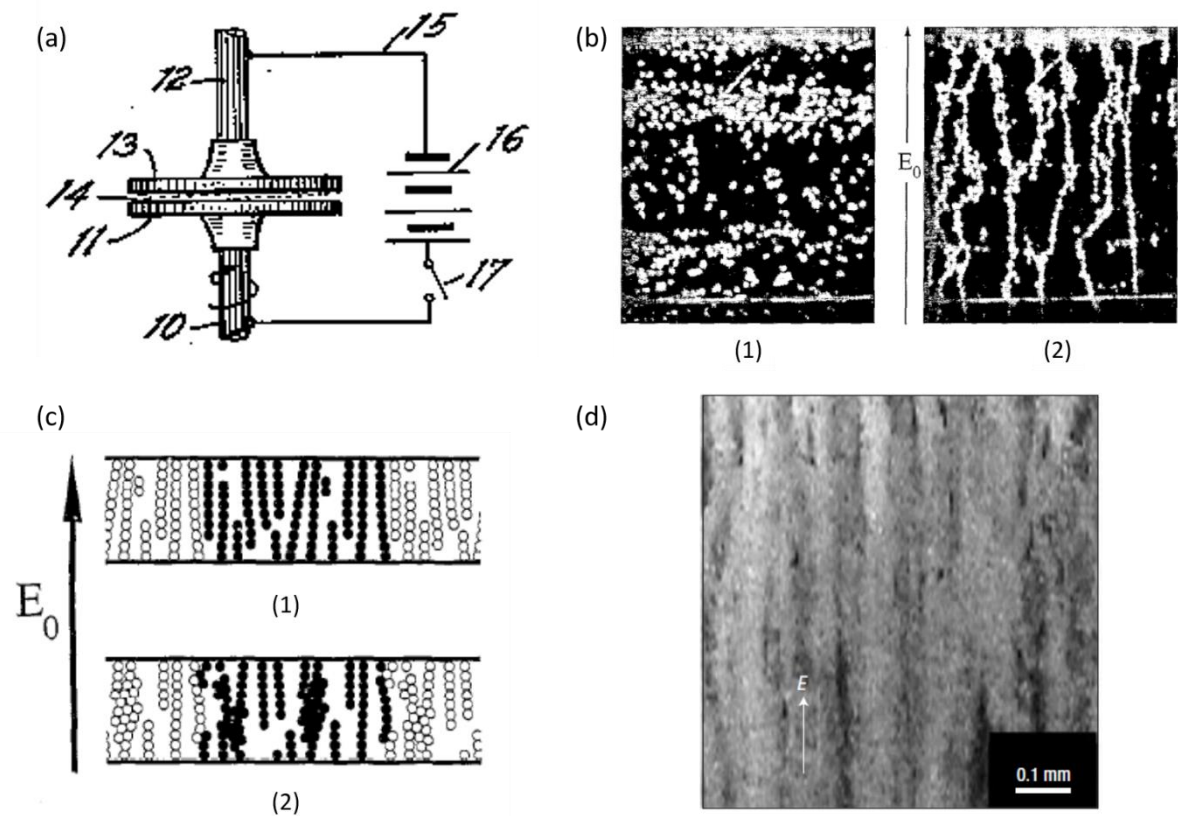


Figure 0-6: Examples of ER fluid studies and patents in literature. (a) clutch application [93], (b) suspension of silicon oil/alumina particles (2 wt.%) with diameter between 63-90  $\mu\text{m}$  before (1) and after (2) electric field application [68], (c) simulation of chain formation, (1) and (2) show the impact of different collision handling strategies on the chain structure [68], (d) optical microscopy image of columns of urea-coated nanoparticles in epoxy for giant ER effect [67].

Alongside biomedical and ER fluids, a new interest appeared in the mid-1990's in material science, and more specifically in the elaboration of anisotropic composites. This topic was first highlighted by Randall in a review [95] of the potential applications of anisotropic composites in the field of electronic components and devices. These potential applications are summarized in the chart shown in Figure 0-7.





Figure 0-8: Dielectrophoretically assembled nanomaterials. (a) and (b) nanoelectromechanical relays made by deposited carbon nanotubes [96], (c) crossed carbon nanotube junction [97], (d) junction of two electrodes by 3 to 10 layers of graphene oxide [98].

All of the experiments presented up until now share a common trait: the particle is in a solid state. However, DEP can also be applied to fluid (and gas [99]) particles with surprising results. Similarly to experiments with solid particles, fluid particles are either attracted or repulsed from the high electric field region, but the electric field also changes its shape.

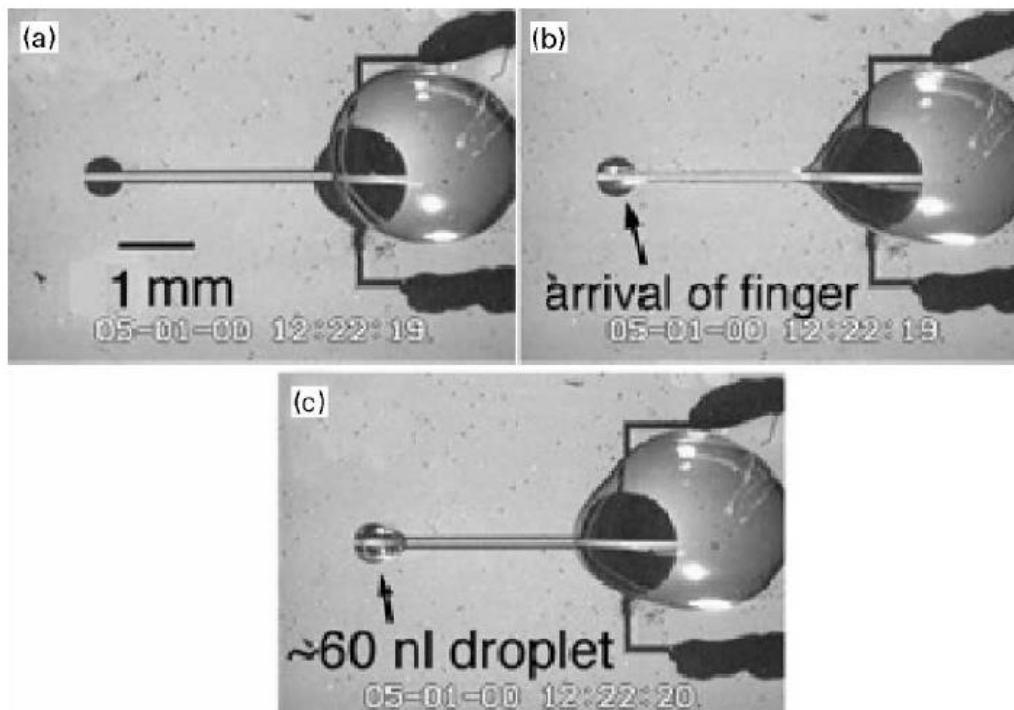


Figure 0-9: Geometry for droplet formation. Initially, a large droplet is deposited in the right sitting (a), the application of voltage drives part of the fluid to the left part in less than 0.1 s (b), after the voltage is removed, isolated droplet remains [100].

The intended applications of liquid DEP include liquid actuation (up to microscale), droplet dispensing, pumping, lab-on-a-chip, etc.

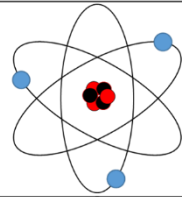
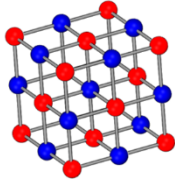
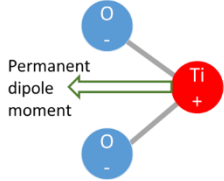
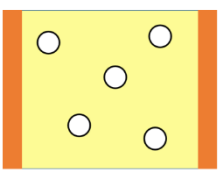
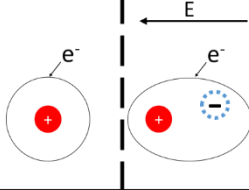
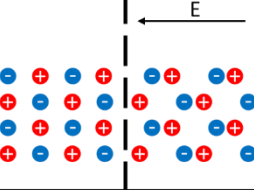
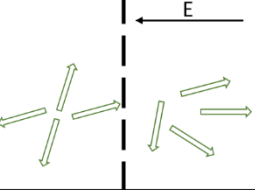
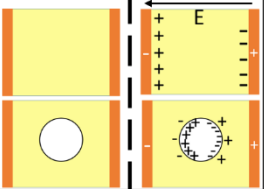
Hence, DEP has been observed for a while and it is now well described from a theoretical point of view. Its range of applications is very wide, making it possible to filter, sort, characterize, drive, position, pump, elaborate materials, and more. The range of materials involved is also very large, from living cell to inorganic particles, including solid, liquid, and gaseous particles. In the next section, we focus on the physical explanation of DEP, from a dipole representation to a mathematical description of the force.

## II.2. Physical phenomenon

### II.2.a. Polarization

Dielectrics (or insulating materials) subject to an electric field acquire a net dipole moment called *induced dipole* (the presence of permanent dipole will not be discussed here). In contrast with conductive materials, dielectrics present almost no free charges (i.e. electrons not associated with any particular nucleus, as in conductors) but bounded charges that can move slightly. Three kinds of polarization mechanisms are linked with these bounded charges: electronic, atomic (or ionic), and orientation polarization (or dipole). In addition, the presence of electric charge carriers that can migrate over some distance within the dielectric, leads to a fourth polarization mechanism called *space charge* (or interfacial) polarization. One of the first descriptions of these mechanisms was given by Von Hippel in “*Dielectric and Waves*” [101]. These four mechanisms are described in Table 0-1.

Table 0-1: Description of polarization mechanisms (adapted from [101])

Polarization mechanism	Electronic polarization	Atomic polarization	Orientation polarization	Space charge polarization
Matter state				
Effect of the electric field				
Physical description	The electric field distorts the electron cloud, leading to unbalanced charges positions	The equilibrium position of positively and negatively charged atoms inside molecules move in opposite directions	The electric field induces a torque aligning the permanent dipoles in it's direction	Carriers move toward electric field lines and get trapped at material interfaces such as medium/particle or electrode/material boundaries

The range of the charge separation distance involved in these different mechanisms is very wide, from subatomic to the length of the system. Their time constant therefore greatly differs one from another. The dependence of the mechanisms over frequency is shown in Figure 0-10. For the frequency range in which we are interested ( $10^{-1}$  to  $10^6$  Hz), atomic and electronic polarizations are quasi-instantaneous.

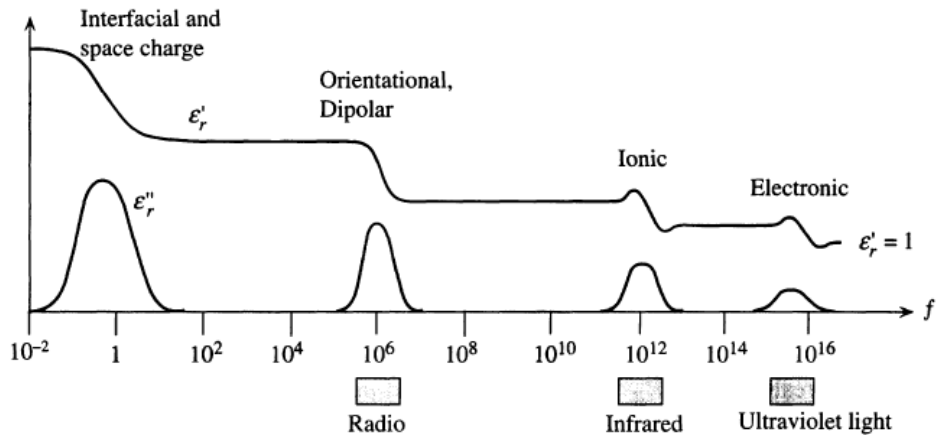


Figure 0-10: Frequency dependence of the real and imaginary parts of permittivity and their relationship with polarization mechanisms [102].

Through polarization mechanisms, the electric field induces a dipole moment in dielectric materials. When subject to non-uniform electric fields, these dipoles give rise to DEP forces and electromechanical torques. To explain the principle of dielectrophoresis, we examine the non-uniform electric field and its impact on particle displacement in the following sections.

### II.2.b. DEP induced by electrode geometry

The DEP phenomenon is generally divided into two categories, *imposed field* and *mutual particle* interactions, according to T.B. Jones' designation [73]. The first rises from the external electric field, whereas the second comes from interactions between the dipoles. A schematic description of the phenomenon is proposed in Figure 0-11.

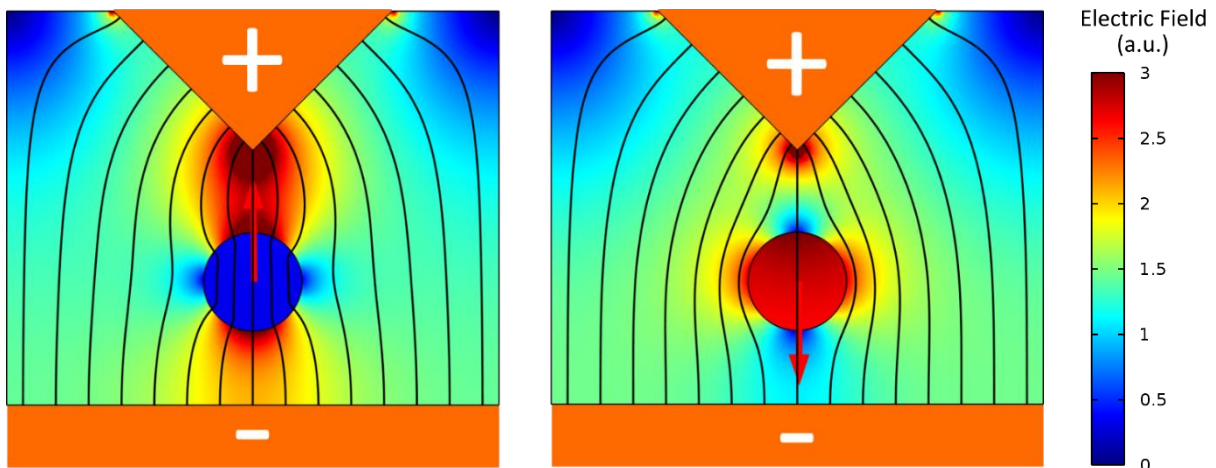


Figure 0-11: Neutral particles inside a non-uniform electric field. From left to right, particle more and less polarizable than the medium, respectively. The red arrows represent the direction of the DEP force. Black lines are the electric field lines. Colors represent the electric field magnitude. Blue corresponds to low electric field values, red to high values.

The behavior of neutral particles is shown in Figure 0-11: particles less polarizable than the medium are repelled from the area of high electric field (right particle), whereas the more polarizable particles are attracted (left particle). Particles are considered as being more polarizable than the medium when their permittivity is higher than that of the matrix. Many geometries have been derived based on this phenomenon to characterize particles, drive particles to specific areas, and sort them according to their size or properties. The electrode schemes in Figure 0-12 are representative of the technique involved. Numerous geometries can actually be found in literature [103]. However, they all rely on the same physical basis. A non-exhaustive list of electrode examples found in literature is presented in Figure 0-12.

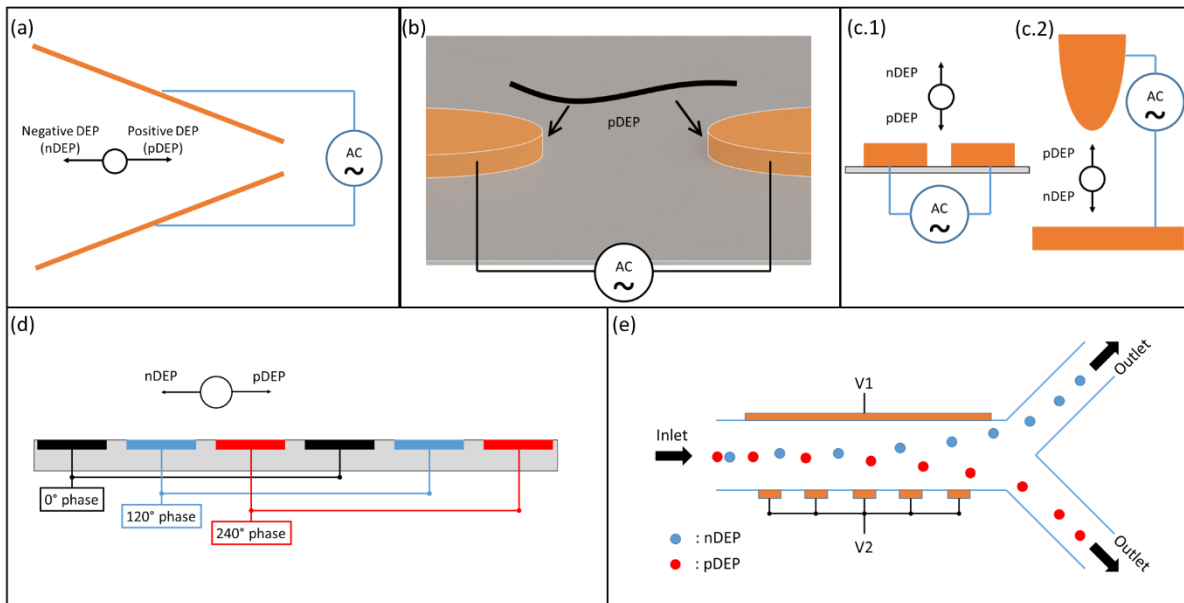


Figure 0-12: *Imposed field* geometries for different purposes: (a) particle sorting and/or driving, (b) assembly of nanoscale objects, (c) particle characterization by levitation, (d) particle driving by traveling wave dielectrophoresis, (e) particle sorting.

### II.2.c. DEP in chain formation

In the previous section, the particles undergo DEP forces rising from the electrode geometry. However, the difference between the medium and particle permittivity also induces electric field non-uniformity, even if the external electric field applied is uniform. This specific case is shown in Figure 0-13. When the particle is more polarizable than the medium (Figure 0-13 (a)), the high electric field regions are perpendicular to the electrodes and parallel for the low electric field region. The opposite occurs (Figure 0-13 (b)) when the medium is more polarizable than the particles. This implies that whenever the particles have a permittivity different than the medium, the DEP force leads to chaining, regardless of the DEP sign. There are two ways to describe this phenomenon, either with respect to the electric field distribution or to the dipole. From the electric field distribution point of view (Figure 0-14 (a) and (b)), when the particles undergo positive DEP (pDEP) ((a), they are driven to the high electric field region which is between them, and chaining occurs. The same behavior is observed for the negative DEP

(nDEP) case (b); the particles are attracted to the low electric field region, which is the space between them. From the dipole point of view (Figure 0-14 (c) and (d)), the change from pDEP (c) to nDEP (d) results in a change in the direction of effective dipole moment. However, as negative and positive charges attract each other, the resulting forces always lead to particle chaining.

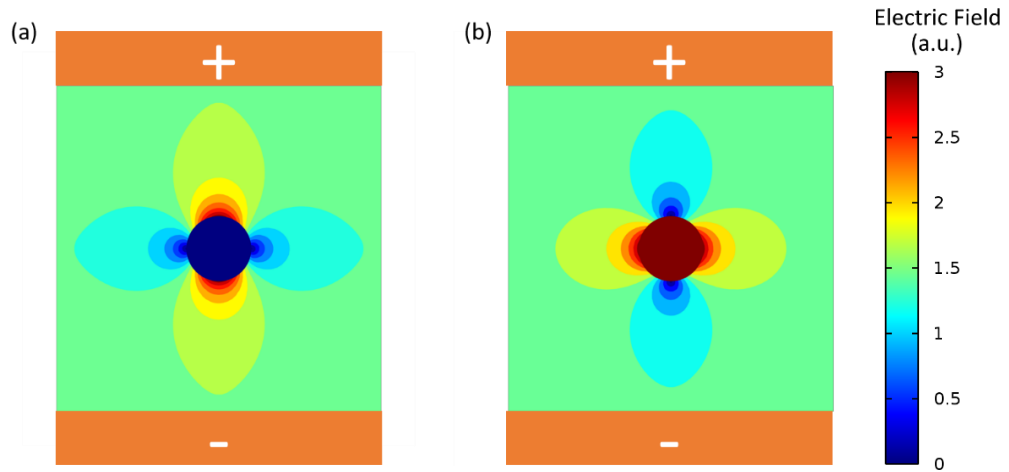
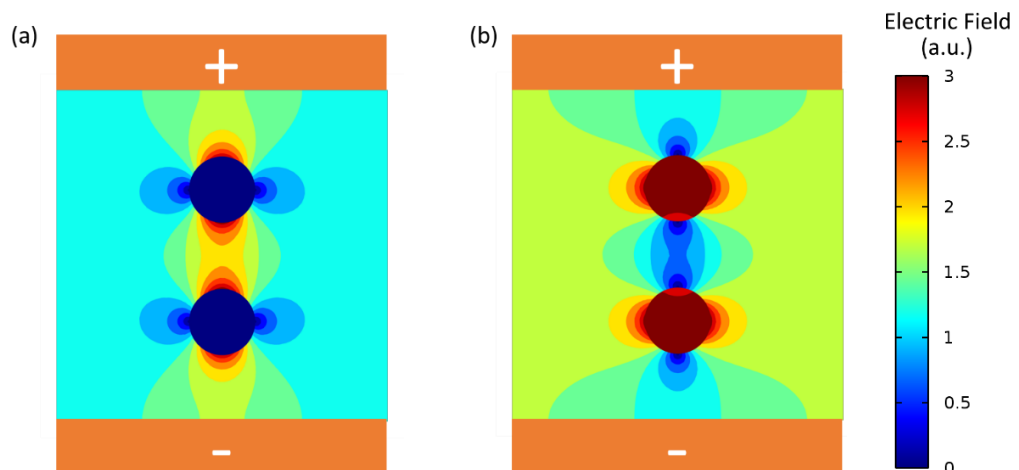


Figure 0-13: Distribution of the electric field induced by a particle in a parallel plane configuration. (a) particle more polarizable than the medium, (b) medium more polarizable than the particle.



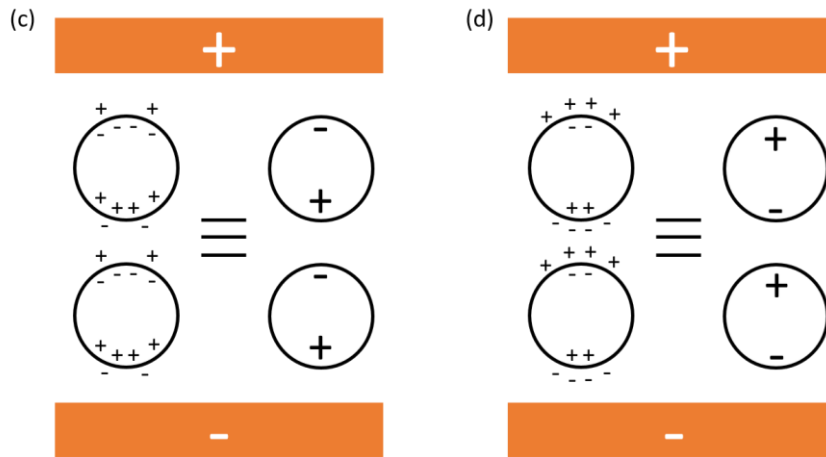


Figure 0-14: Electric field and charge distribution for particle chaining. (a) and (c) Particles more polarizable than the medium, (b) and (d) particles less polarizable than the medium. In (c) and (d) the image on the left corresponds to a scheme of charge distribution, the image on the right corresponds to the dipole representation.

### II.3. Mathematical description

Providing a mathematical description of the DEP force can be quite challenging if one wants to describe this phenomenon precisely in a real case. However, considering several hypotheses (particle shape, dipole approximation, etc.), the system can be reduced to simple equations which make it possible to determine the key parameters leading the DEP phenomenon. The way to obtain the equations for DEP force are described in the next section, as well as the assumptions made and their limitations. In a second step, a particle chaining model is developed based on the effective dipole moment. By describing this model, the necessary input parameters are determined, enabling us to define the ones that must be measured experimentally.

#### II.3.a. General form

The typical expression for describing DEP force is given by [73]:

$$\mathbf{F}_{DEP} = 2\pi\epsilon_0\epsilon_m KR^3\nabla E^2 \quad (1)$$

This equation must be explained carefully, as it implies several non-trivial hypotheses. The force in this equation corresponds to the time-average DEP force acting on a spherical particle. Both the medium and the particle are lossless dielectrics.  $K$  corresponds to the Clausius-Mossotti function and is given by the equation:

$$K = \frac{\epsilon_p - \epsilon_m}{\epsilon_p + 2\epsilon_m} \quad (2)$$

From eq. 1 and eq. 2, it is possible to identify the parameters that will impact the DEP force. The DEP force is proportional to the particle volume, with a larger electric field gradient leading to increased force. The dependence on particle permittivity is less direct. The Clausius-Mossotti function varies between -0.5 and 1, depending on the matrix and filler permittivity, but matrix permittivity is also found

outside the Clausius-Mossotti equation. Eq. (1) can be derived from Coulombic interactions. As it can be seen in Figure 0-15, a dipole in a non-uniform electric field undergoes unequal Coulombic forces, resulting in a net force: the DEP force.

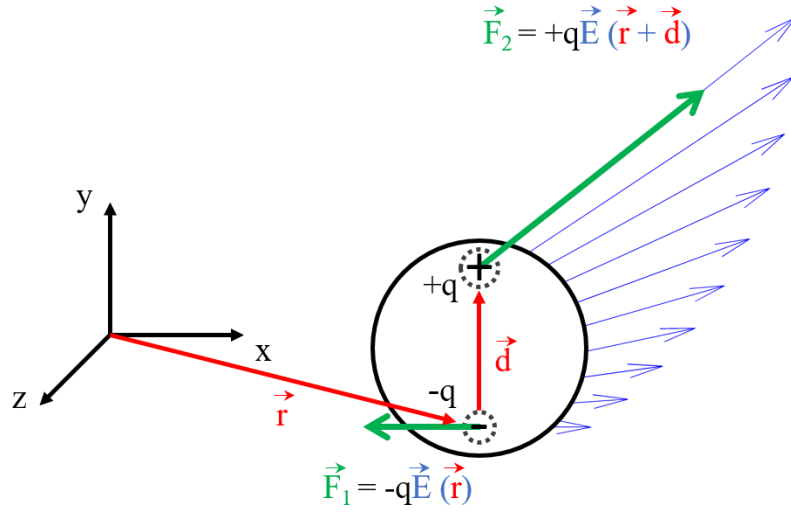


Figure 0-15: Coulombic forces acting on a small dipole in a non-uniform electric field.

From this description, the DEP force is then equal to:

$$\mathbf{F}_{DEP} = \mathbf{F}_1 + \mathbf{F}_2 = q\mathbf{E}(\mathbf{r} + \mathbf{d}) - q\mathbf{E}(\mathbf{r}) \quad (3)$$

with  $\mathbf{r}$  the position vector of the charge  $-q$ . When the norm of  $\mathbf{d}$  is small compared to the characteristic dimensions of the electric field, the electric field can be expanded about position  $\mathbf{r}$  using a vector Taylor series expansion:

$$\mathbf{E}(\mathbf{r} + \mathbf{d}) = \mathbf{E}(\mathbf{r}) + \mathbf{d} \cdot \nabla \mathbf{E}(\mathbf{r}) \quad (4)$$

Here, the terms of order higher than 1 (higher than dipolar term) have been neglected. Replacing eq. 4 in eq. 3 we obtain:

$$\mathbf{F}_{DEP} = q(\mathbf{E} + \mathbf{d} \cdot \nabla \mathbf{E} - \mathbf{E}) \quad (5)$$

which can be simplified as:

$$\mathbf{F}_{DEP} = q\mathbf{d} \cdot \nabla \mathbf{E} = \mathbf{p} \cdot \nabla \mathbf{E} \quad (6)$$

The fact that the higher order terms were neglected in eq. 4 implies that the derived equation of the DEP force only includes the dipole force. The real formulation (including all higher order terms) would lead to the addition of multipolar terms. The impact of this approximation can be understood in the case of two interacting spheres. The interaction force between two dipoles (multipole of order 1) is proportional to  $\frac{1}{distance^4}$  while the interaction force between quadrupoles (multipole of order 2) is proportional to  $\frac{1}{distance^6}$  with the general equation being:

$$F_{m,n} \propto \frac{1}{\text{distance}^{m+n+2}} \quad (7)$$

where  $m$  and  $n$  are the order of the two particle multipoles. The influence of the multipoles is rapidly negligible in comparison with the dipolar terms when the particles are not close to each other.

### II.3.b. Effective dipole moment method

Here, we briefly introduce the method of the effective dipole moment [73]. This method provides a useful tool for evaluating electromechanical force (DEP) and torque (electrorotation, electroorientation). The purpose of the method is to evaluate the quantity  $\mathbf{p}$  of a particle, induced by the external imposed electric field and by mutual field contribution (i.e. electric field due to neighboring particles). The study is restricted to the evaluation of the multipole of order 1 (dipolar term). This restriction is consistent for particles that are not close to each other and/or not subject to a high electric field gradient.

The principle of this method is to determine the moment of an equivalent point dipole which, positioned at the center of a particle, would produce the same electrostatic potential. The electrostatic potential ( $\Phi_{dipole}$ ) produced by a point dipole of moment  $p_{eff}$  in a medium with dielectric constant  $\epsilon_m$  is given by:

$$\Phi_{dipole} = \frac{p_{eff} \cos \theta}{4 \pi \epsilon_0 \epsilon_m r^2} \quad (8)$$

where  $\theta$  and  $r$  correspond to the polar angle and the radial position at which the electrostatic potential is evaluated. The demonstration of eq. 8 is fully described elsewhere [104]. The dipole moment is then determined by solving the boundary value problem. The potential inside and outside the particle are given by:

$$\begin{cases} \Phi_{out}(r, \theta) = -E(r)r \cos \theta + \frac{A \cos \theta}{r^2}, & r > R & (a) \\ \Phi_{in}(r, \theta) = -Br \cos \theta & , r < R & (b) \end{cases} \quad (9)$$

with the first term on the right side of eq. 9 (a) being the contribution of the external electric field, and the second term, the contribution of the point dipole. In the above equations, A and B are the coefficients to be determined. This system of equations can be solved with the appropriate boundary conditions, i.e. the continuity of the potential and of the normal component of the displacement across the particle boundary. These conditions are described by the following equations:

$$\begin{cases} \Phi_{in}(r = R, \theta) = \Phi_{out}(r = R, \theta) & (a) \\ \epsilon_p E_{np}(r = R, \theta) = \epsilon_m E_{nm}(r = R, \theta) & (b) \end{cases} \quad (10)$$

where  $E_{np} = \partial \Phi_{in} / \partial r$  and  $E_{nm} = \partial \Phi_{out} / \partial r$  are the normal components of the electric field inside the particle and the medium, respectively. From eqs. 9 (a) and (b) we obtain:



---


$$-BR \cos \theta = -ER \cos \theta + \frac{A \cos \theta}{R^2} \quad (11)$$

which can be rewritten as:

$$A = R^3(E - B) \quad (12)$$

From eq. 10 (b) and the derivatives of eqs. 9 (a) and (b) we obtain:

$$-\varepsilon_p B \cos \theta = -\varepsilon_m \left( E \cos \theta + 2 \frac{A \cos \theta}{R^3} \right) \quad (13)$$

$A$  and  $B$  can be determined by combining eqs. 12 and 13:

$$A = R^3 E \left( \frac{\varepsilon_p - \varepsilon_m}{\varepsilon_p + 2\varepsilon_m} \right), B = 3E \frac{\varepsilon_m}{\varepsilon_p + 2\varepsilon_m} \quad (14)$$

As mentioned earlier, the second term on the right side of eq. 9 (a) corresponds to the potential induced by the particle. The effective dipole moment can then be determined from eq. (8):

$$p_{eff} = 4 \pi \varepsilon_0 \varepsilon_m R^3 \left( \frac{\varepsilon_p - \varepsilon_m}{\varepsilon_p + 2\varepsilon_m} \right) E = 4 \pi \varepsilon_0 \varepsilon_m R^3 K E \quad (15)$$

It is worth noting that by combining the last equation with eq. 6 we obtain:

$$\mathbf{F}_{DEP} = 4 \pi \varepsilon_0 \varepsilon_m R^3 K E \nabla E = 2 \pi \varepsilon_0 \varepsilon_m R^3 K \nabla E^2 \quad (16)$$

which is indeed eq. 1.

As a conclusion of this mathematical development of the effective dipole moment method and of the DEP force, we can summarize several important points regarding eq. 1. Once again, this equation does not take into account higher order terms, so an error will rise in the presence of a strongly divergent electric field. Detailed multipolar expansion of the DEP force can be found elsewhere [105]. The described particle is a lossless spherical dielectric. The effective dipole moment method provides a tool to determine the point dipole equivalent of a particle by solving the appropriate boundary conditions problem.

### II.3.c. Negative and positive DEP

Equation 1 contains interesting information concerning the DEP phenomenon, and all the behavior described in the following sections III.2.b and III.2.c can be described by it. The direction of the DEP force is determined by  $\nabla E_0^2$  which is the gradient of the squared electric field norm. This implies that the DEP force is directed towards the region with the highest electric field gradient. nDEP and pDEP behavior is driven by the sign of the Clausius-Mossotti function. Its sign can be analyzed by rewriting eq. 2 as:

$$K = \frac{\frac{\varepsilon_p}{\varepsilon_m} - 1}{\frac{\varepsilon_p}{\varepsilon_m} + 2} \quad (17)$$

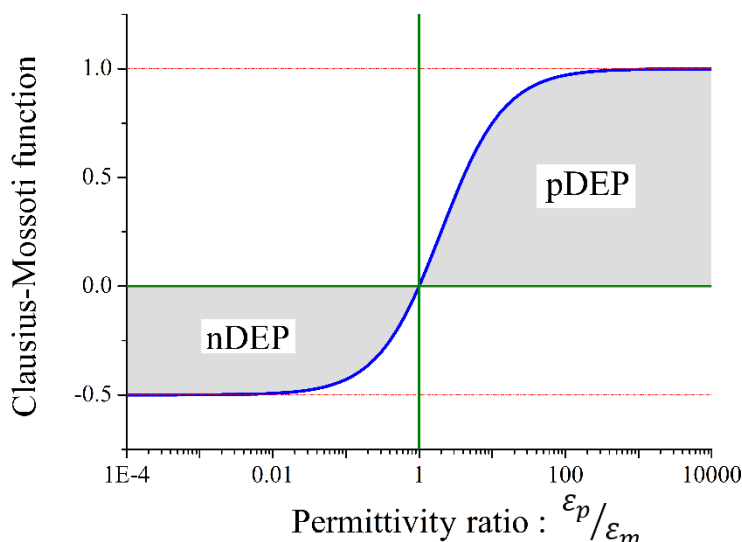


Figure 0-16: Clausius-Mossotti function plotted as a function of the permittivity ratio.

The evolution of the Clausius-Mossotti function is plotted in Figure 0-16. The theoretical change from nDEP to pDEP occurs when the particle becomes more polarizable than the medium. The minimum value of the function in nDEP is -0.5 while its maximum in pDEP is 1.

This selectivity of the DEP force regarding the particle permittivity against the medium has been used intensively for trapping and characterizing particles. This is the simplest case, as the particle is assumed to be a simple body without losses. However, particles can have losses because of their bulk conductive nature and their surface conductivity. Moreover, they can be composed of a core and a shell, such as in biological particles, coated particles [106], core-shell particles [107], and Janus particles [63], [108].

This chapter discussed the origin of the dipole leading to DEP force when subject to a non-uniform electric field. Two different kinds of electric field non-uniformity were depicted: the first rising from electrode geometry and the second from the particles themselves. All of the experiments conducted within the framework of this thesis correspond to the second case, where the effective dipole moment method for evaluating DEP force is described by lossless dielectric materials (except in the last chapter). This method is the starting point for the model that we develop in the next section. The difference between nDEP and pDEP was introduced briefly. This phenomenon is used in chapter III when attempting to characterize the permittivities of the studied particles.

#### II.4. Modeling chain formation under an electric field

There are two purposes for modeling the formation of chains due to DEP forces. The first is to establish the key parameters directing the chaining; the second is to provide a predictive tool for the formation of anisotropic composites.

---

#### *II.4.a. Description of the existing ways to model particle chaining*

The numerical treatment of DEP phenomena has been widely investigated. Authors have focused on several aspects, such as estimating DEP force, designing DEP experimental cells assisted by simulations, and modeling the filler structures. The latter topic has been studied intensively, especially for the case of electrorheological fluids.

Different approaches have been studied to compute the forces involved, which rely on two distinct methods. The first is known as the Maxwell Stress-Tensor (MST) method, the second as the effective dipole moment method. These methods may be used in several ways, which are discussed briefly.

The first method is pointed out as the more rigorous way to compute field-induced forces [109]–[113]. It is often used to study the effectiveness and accuracy of other developed methods. For the first method, the electric field needs to be computed over the surface of the particle. This can be computed either analytically or numerically (for example by FEM). The first case is very limited, as analytical expressions for the electric field are very complex to obtain and restricted to simple cases. The second case was proven to be efficient for low numbers of particles, but the number of triangles (2D) or tetrahedrons (3D) increases dramatically with the number of particles, and the domain needs to be re-meshed at every time step, making it impractical to use for a large number of particles (i.e. more than few tens). This method can be used to follow particle behavior as a function of time.

The second method relies on the approximation of the particle as a point dipole which, when placed at the location of the particle, produces the same electrostatic potential, as described by Jones [73]. This method has the advantage of being computationally efficient despite being less accurate than the MST method. However, accuracy can be improved by adding multipole correcting terms [114]–[116], thus approaching the accuracy of the MST method, but at the cost of model complexity and time consumption. Two different ways to use this method have been investigated: Monte-Carlo resolution of energy equations [117], [118] and resolution of the equation of motion (dipole [119], [120] and multipole).

The Monte-Carlo approach relies on minimization of the system's global energy. The particles' position at each iteration is estimated thanks to the Monte-Carlo method, taking the position of particles for which global energy is minimized. This step is repeated until the system reaches a steady state. This method was successfully used to model the chaining of numerous particles. However, it does not enable obtaining the time dependence of the phenomenon, but only the path and the steady state position of the particles.

The last approach, i.e. resolution of the equation of motion associated with effective dipole moment method, can be implemented easily with a numerical method (Euler; Runge-Kutta, etc.) taking fixed or variable time steps. At each time step, the forces involved are computed and the particles are then moved

to their new positions. This scheme is repeated for the duration of the computation. This approach is not time-consuming, at least for the dipolar estimation of DEP forces. Nevertheless, the addition of multipolar terms (to improve its accuracy) can drastically increase the computational cost. This method, relying on dipolar interactions, was used successfully to model a large number of particles.

In order to summarize the different methods presented in this section, their pros and cons are depicted in Table 0-2.

Table 0-2: Advantages and disadvantages of the different technics for modeling particle chaining.

Computational method	Variation	Number of particles	Accuracy at close contact	Computational cost	Temporal	
MST	Analytical	---	+++	++	YES	
	FEM	-	++	--	YES	
Effective Dipole Moment	Monte-Carlo	Dipole	++	-	+++	NO
		Multipole	+	+	-	NO
Equation of motion	Equation of motion	Dipole	++	-	++	YES
		Multipole	+	+	--	YES

Works presenting particle chaining models often focus on the values of the dielectrophoretic forces or particle trajectories, but very few of them deal with the link between the filler structure and a given composite property. Only a few examples of extracting a physical parameter related to the structure are found in the field of electrorheological fluids [68], [121]. A similar approach should enhance our understanding of the process involved while elaborating materials.

#### II.4.b. *Developed model*

Many methods have been developed to study the dielectrophoretic interactions between particles [109]–[112], [114]–[120]. The choice of the modeling method depends intrinsically on the studied system.

Since the purpose of our study is to understand the impact of chain formation on the physical properties of composites, and to predict the chaining dynamics, it is necessary: i) to describe both microscopic and macroscopic effects; and thus, ii) to be able to handle a large number of particles.

The Maxwell stress-tensor method gives the most accurate results on DEP force computation, but is limited to very few particles and simple systems. The relevant choice is therefore that of effective dipole moment methods. Monte-Carlo resolution of minimum energy state equations allows handling

---

numerous particles but, to the best of the author's knowledge, no study is available on time-dependent evaluation of particle trajectories. In order to be able to compare simulations to experimental results, it is necessary to know the time-dependence of the phenomenon. Our choice was therefore to use the resolution of the equation of motion. This turned out to be a fair choice, as detailed in chapter V. Within the framework of this work, up to 4,600 particles were simulated, 9 hours of computation were necessary to simulate 25 seconds of real-time using a laptop computer while the approach was still "brute force" (i.e. the interaction between every particle was taken into account, even if the impact of long-range interaction is negligible).

The question was still open as to whether the multipolar terms were necessary or not. If we consider that particles are sufficiently far apart during most of the time taken to find each other and form chains, the simple dipole approximation would be quite accurate. The comparison between experimental and simulation results confirmed this hypothesis. Limsimarat *et al.* compared DEP force and particle chaining trajectories using dipolar and multipolar terms. The results showed a slight difference in the trajectories, but large difference in the computational cost (300 ms of real time in 45 hours with multipole up to 5 and 20 particles) [122]. However, their results proved a clear difference for particles in contact. The dipole moment is assumed to be only due to the external electric field. Thus, the influence of the particle dipole moment on the electric field is neglected. The impact of this assumption was nonetheless evaluated to ensure its validity. The computation method to obtain the influence of the effective dipole on the electric field are developed in Appendix A.

The system is a three-dimensional Cartesian coordinate system and the experimental cell is composed of two parallel electrodes. The external electric field was assumed to be uniform, with only one component on the Z axis (cf. Figure 0-17). The particles are spheres with equal radii, are neutral and the particle and the host liquid electrical conductivities are neglected. The dipole moment of a particle is then [73]:

$$p = 4\pi\epsilon_0\epsilon_m R^3 K E_0 \quad (18)$$

According to the assumption made on conductivities, the Clausius-Mossoti factor is:

$$K = \frac{\epsilon_p - \epsilon_m}{\epsilon_p + 2\epsilon_m} \quad (19)$$

The DEP force exerted by particle  $j$  on particle  $i$  is:

$$\mathbf{F}_{DEP,ij} = \frac{1}{4\pi\epsilon_0\epsilon_m} \frac{3p^2}{d_{ij}^5} (\mathbf{d}_{ij} + 2d_{ij,z}\mathbf{e}_z - \frac{5}{d_{ij}^2} d_{ij,z}^2 \mathbf{d}_{ij}) \quad (20)$$

as described by Kadaksham [120]. Here,  $\mathbf{d}_{ij}$  is the vector formed by the particle centers,  $d_{ij}$  is the distance between the particles centers and  $\mathbf{e}_z$  the z coordinate unit vector. The amplitude and direction of the DEP forces in a two-particle system is plotted in Figure 0-17. The dipole approximation predicts a change

from attractive to repulsive force at about  $55^\circ$  for the angle formed by the electric field and the particle centers.

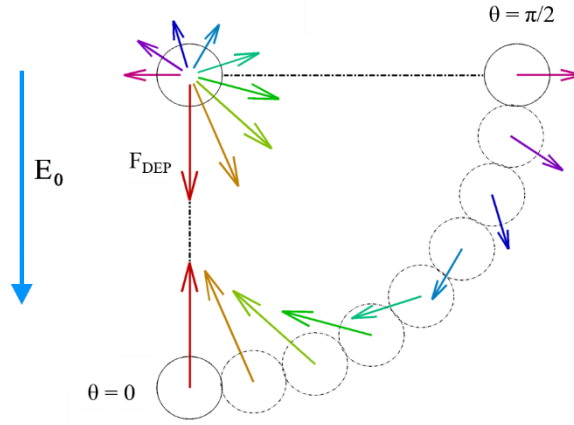


Figure 0-17: DEP forces acting on two particles as a function of the angle formed by the particle centers and the external electric field.

The total force acting on a particle is then:

$$\mathbf{F}_{D,i} = \sum_{\substack{j=1 \\ j \neq i}}^n \mathbf{F}_{D,ij} \quad (21)$$

Particle trajectories are determined by the following equation of motion:

$$m\mathbf{a}_i = \mathbf{F}_{D,i} - 6\pi\nu R\mathbf{V}_i - mg\mathbf{e}_z + \mathbf{F}_{coll-particles} + \mathbf{F}_{coll-walls} \quad (22)$$

where  $m$  is the particle mass,  $\mathbf{a}_i$  the particle acceleration,  $\nu$  the medium viscosity,  $\mathbf{V}_i$  the particle speed, and  $g$  the standard gravity. The equation of motion gives information about the particles' behavior: higher viscosity leads to slower displacement, but also slows down the sedimentation process driven by particle weight.

The second term on the right-hand side of eq. 22 is the well-known viscous drag force. This approximation for handling fluid interaction is justified by the very small Reynolds number of our system ( $Re \ll 1$ ). The fluid movement are not taken into account. The two last terms  $\mathbf{F}_{coll-particle}$  and  $\mathbf{F}_{coll-walls}$  are the forces representing the collision between particles and walls, respectively. The walls are necessary here to ensure that the volume fraction of particles is constant during chaining. However, these walls are unphysical. The two walls perpendicular to the direction of the electric field are not considered as electrodes. That is why no image particles were taken into account. The distribution of the different forces is described in Figure 0-18.

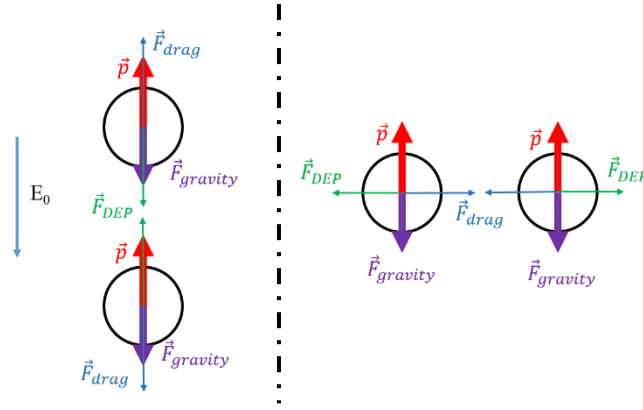


Figure 0-18: Schematic representation of the forces acting on the particles aligned in the direction of the electric field (left side) and perpendicular (right side). The red vector  $p$  represents the particle dipole.

The collision force between particles corresponds to a spring force given by the following equation:

$$\mathbf{F}_{coll\_particle} = k(d_{ij} - 2R) \frac{\mathbf{d}_{ij}}{d_{ij}} \quad (23)$$

The spring constant was not deduced from physical parameters, but was adjusted with simulation parameters. The collision force is set to 0, except when a neighboring particle is very close ( $d_{ij} \leq 2 \times R + 20 \times 10^{-9}$ ). The issue of handling particle collision is far more complex than it may seem. From the simulation point of view, collision behavior has a strong impact on model stiffness: the higher the spring constant, the stiffer the model. The particles interpenetrate if the spring constant is low, which is not physically possible, but the computation cost is minimized. On the other hand, a very high spring constant fixes the distance between particle surfaces at  $d_{ij} = 2 \times R + 20 \times 10^{-9}$ . It also results in a need for very small time steps. In addition to these considerations, not much is known from a physical point of view, even if the authors have pointed out that a small layer of matrix remains between particles (estimated at 20 nm for BaTiO<sub>3</sub> nanoparticles with 0.2 μm median particle size [55]). However, the thickness of the matrix layer between particles probably depends on several parameters, such as matrix viscosity, particle sizes and shapes, electric field strength, etc. In our simulations, we decided to fix the spring constant to obtain a layer thickness of around a few tens of nm. It is important to note that this is probably a key point for evaluating the composite permittivity value accurately. However, it should not have much impact on the permittivity change dynamics, as it does not affect movement.

The handling of the collision between particles and walls is implemented with the same kind of force as the collision between particles.

Runge-Kutta methods with variable time steps were used to solve the equation of motions. All the computations were performed using a commercial numerical computing environment [123]. The computation of 25 seconds of real time for 500 particles took approximately 500 seconds, and 9 hours for 4,600 particles on an Intel® Core™ i7-4810MQ processor.

The 3D rendering of particle structures was done using an open-source platform [124].

## II.5. Conclusion

This chapter studied the dielectrophoretic force, from its first description, from its physical cause, to its mathematical description. This study allowed us to identify the parameters involved and their impact on force (direction and magnitude).

From the theoretical treatment of the DEP force, a model of particle chaining under an electric field was developed. The method for modeling particle chaining was chosen carefully according to the following specifications: the need for a large number of particles, time-dependent study, and reasonable computational times. The effective moment method associated with the resolution of the equation of motion was chosen, as it fulfilled all required criteria.

In light of the model equations (i.e. eqs. 18, 19 and 22), the need for the characterization of the different compounds (matrix and filler) is clear. This is the focus of the next chapter.







# Chapter III

Characterization Of The Compounds

### III. CHARACTERIZATION OF THE COMPOUNDS

There are several reasons why it is important to know about compound properties. These properties affect the process, final composite properties, and they are required as inputs for numerical modeling. It is therefore necessary to characterize both the filler and the matrix prior to any elaboration and modeling of the composites.

While some properties are simple to obtain, either because they are provided by the supplier or are easy to measure (e.g. viscosity, density), others are more complex. For example, measuring particle permittivity is quite challenging, and the methods proposed in literature are not entirely satisfactory. Measuring matrix permittivity, on the other hand, is not difficult experimentally, but it requires a fine analysis of the results to identify phenomena such as electrode polarization.

A method adapted from biomedical science is examined here to address the issue of characterizing particle properties. Directly related to the measurement of a physical parameter (i.e. frequency crossover), this method is expected to overcome problems related to the conventional use of mixing rules or bulk properties.

#### III.1. Measurement of the liquid properties

##### III.1.a. Principle of dielectric spectroscopy

The essence of the impedance spectroscopy is to measure the current, the voltage and the phase shift on a given frequency range while applying a voltage. The dielectric properties of the sample (permittivity and losses) are then derived from these measurements by adopting a specific model for the sample (R-C parallel in the present case)

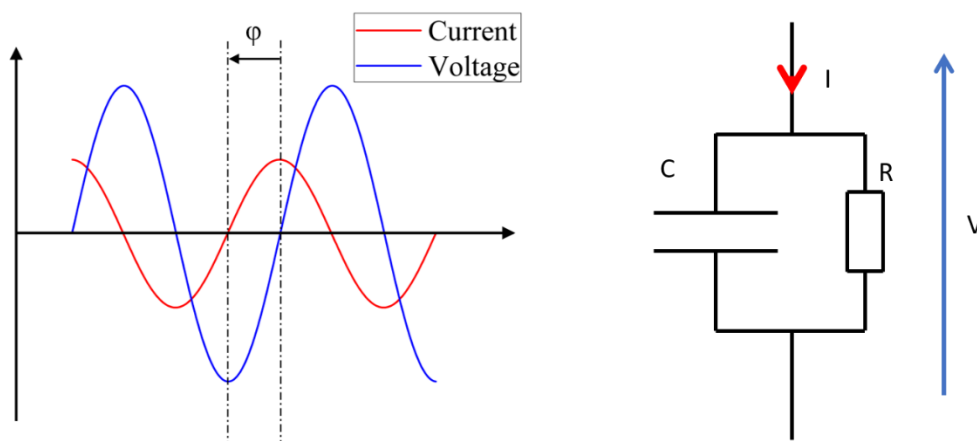


Figure III-1: Current, voltage amplitude and phase shift measurement (left), parallel R-C model is assumed to estimate the sample properties.

$$Y^*(\omega) = \frac{I^*(\omega)}{V^*(\omega)} = \frac{|V^*(\omega)|}{|I^*(\omega)|} \cdot e^{j\phi} = Y(\omega) \cos \phi + jY(\omega) \sin \phi \quad (24)$$

The admittance of the sample can be deduced from the parallel R-C model:

$$Y^*(\omega) = \frac{1}{R} + jC\omega \quad (25)$$

The following system of equations is obtained from eq. 24 and 25, allowing determination of  $R$  and  $C$ :

$$\begin{cases} \frac{1}{R} = Y(\omega) \cos \phi \\ C\omega = Y(\omega) \sin \phi \end{cases} \Leftrightarrow \begin{cases} R = \frac{1}{Y(\omega) \cos \phi} \\ C = \frac{1}{\omega Y(\omega) \sin \phi} \end{cases} \quad \begin{matrix} \text{(a)} \\ \text{(b)} \end{matrix} \quad (26)$$

Once  $R$  and  $C$  are determined, the real and imaginary part of the complex permittivity (i.e. the dielectric “constant” and the losses, respectively) are deduced from the following equations:

$$\begin{cases} C = \frac{\varepsilon_0 \varepsilon' S}{e} \\ \varepsilon'' = \varepsilon' \tan \phi \end{cases} \quad (27)$$

The equation giving the real part of the permittivity assumes that the sample is a parallel plane capacitor. The voltage frequency used in this study spans from  $10^{-1}$  to  $10^6$  [Hz]. In this frequency range, according to Figure 0-10, only relaxations related to interfacial and orientation polarization should be observed.

### III.1.b. Experimental setup

Dielectric spectroscopy is relatively easy to achieve for solids; the electrodes can be deposited and material thickness can be measured. On the other hand, dielectric spectroscopy for liquids is a bit more difficult. As the material to characterize is a liquid, the experimental cell must fulfil certain functions, namely to:

- Provide electrodes
- Control the distance between the electrodes
- Be able to retain the liquid
- Two experiments must be distinguished: one in which the material remains liquid during characterization; and the other, in which the material is hard at the end of the characterization (polymer resin + hardener). For the first category, the characterization cell can be washed and reused. Disposable cells must be used for the second category. Disposable cells are described in chapter IV. The characterization cell for liquids is shown in Figure III-2. The liquid to be characterized is poured in the center of the cell, and the distance between the electrodes is controlled by alumina spacers. The role of the PTFE cylinder is to separate the body electrode from the contact electrode so that the characterized area corresponds to the measure electrode. The O-rings seals the cell, thus preventing the liquid from evaporating.

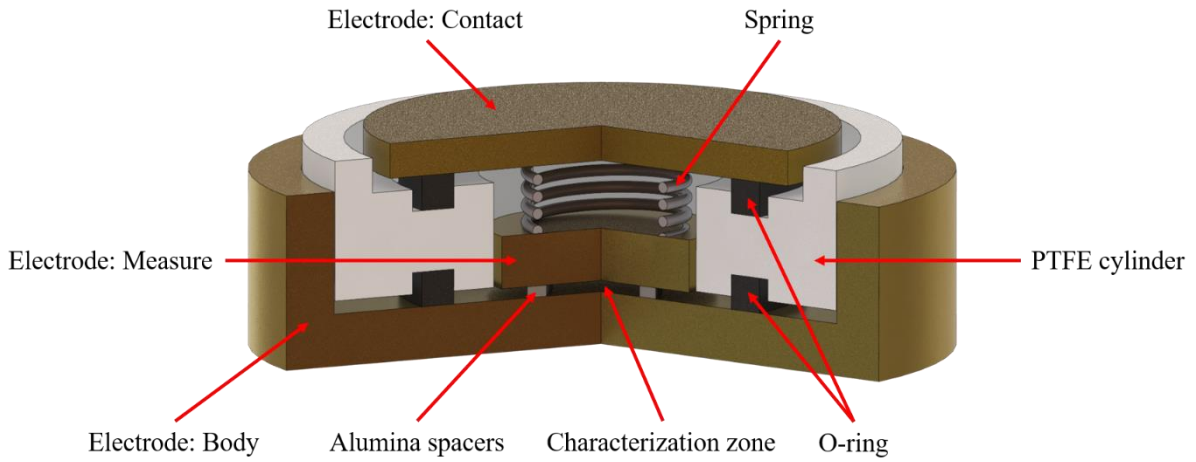


Figure III-2: Characterization cell for dielectric spectroscopy on liquids.

The characterization cell is connected to a dielectric spectrometer (Novocontrol Alpha-A). The permittivity of the liquids is measured using this device, following the principle described in III.1.a from  $10^{-1}$  to  $10^6$  Hz under 1 Vrms, at room temperature.



Figure III-3: Dielectric spectrometer with a temperature head mounted. The zoomed image on the right shows the location (1) where the characterization cell is placed.

Before characterizing the liquid, the cell must be calibrated with the cell filled with air to estimate the surface of the alumina spacers. The equivalent circuit is that given in Figure III-4.

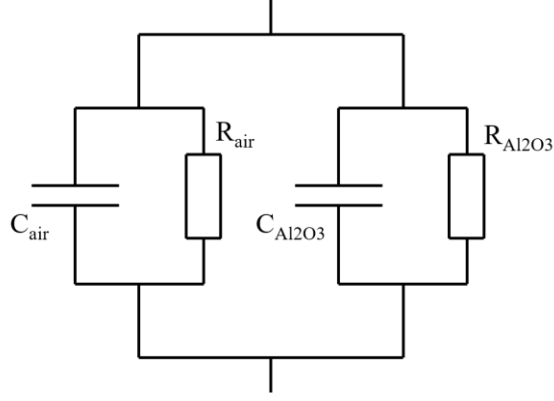


Figure III-4: Equivalent circuit of air with alumina spacers.

The following equation gives the surface of the alumina spacers:

$$C_{equivalent} = C_{air} + C_{Al_2O_3} = \frac{\epsilon_0 [(S_{total} - S_{Al_2O_3})\epsilon_{air} + S_{Al_2O_3}\epsilon_{Al_2O_3}]}{e} \quad (28)$$

With the surface known, capacitance due to the alumina can be calculated and subtracted from the measurement of the liquids. The effective measurement surface can also be calculated.

As alumina resistivity is very high compared to the resistivity of the liquids being measured (at least  $10^5$  times greater), the resistance formed by the alumina is very high compared to the one of the liquids. The impact of the alumina can therefore be neglected.

$$R_{eq} = \frac{R_{liquid} \times R_{Al_2O_3}}{R_{liquid} + R_{Al_2O_3}} \approx \frac{R_{liquid} \times R_{Al_2O_3}}{R_{Al_2O_3}} = R_{liquid} \quad (29)$$

### III.1.c. Dielectric spectroscopy on liquids

Matrix permittivity is of great importance in DEP experiments, with the DEP force being proportional to it (Eq. 1). However, great care must be taken when measuring the permittivity of liquids due to the parasitic effects of interfacial polarization.

Three different resins were studied. Table III-1 shows the characteristics provided by the suppliers.

Table III-1: Characteristics of the resins used

Name	Resin designation	Hardener	Supplier	Resin viscosity [mPa.s]	Temp. (°C)
A	Epikote 816B	Epicure 113	Mitsubishi Chemical Co.	Data not provided	
				170	20
B	SR 5311	SD 7820	Sicomin	120	25
				90	30
				9800	20
C	SR 8500	SZ 8525	Sicomin	4500	25
				2300	30

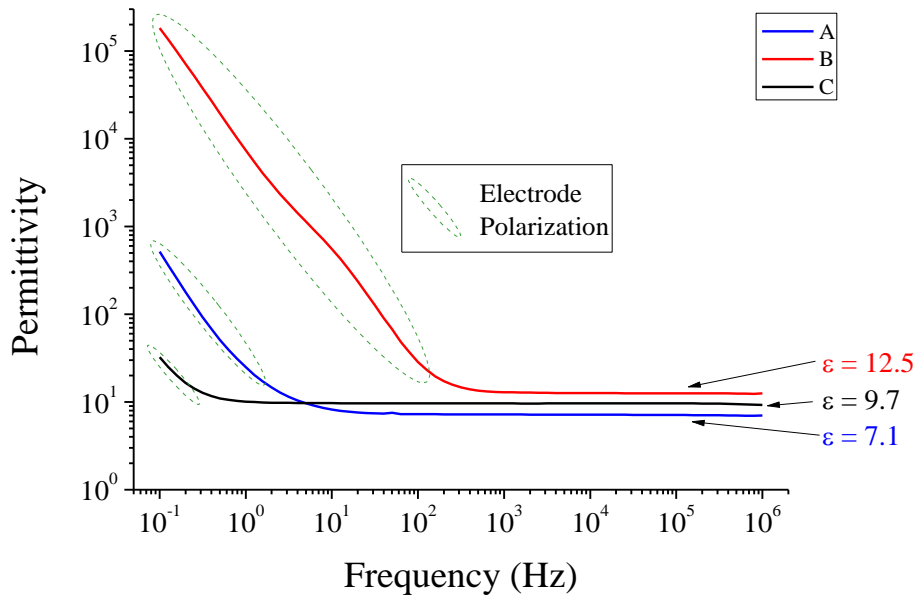


Figure III-5: Real part of the permittivity of three epoxy resins without hardener at 30 °C.

As it can be observed in

Figure III-5 for three different epoxies, the permittivity measured can be separated into two parts: a plateau at high frequencies and a sharp rise of permittivity at low frequencies. The low-frequency part is actually not related to the intrinsic permittivity of the liquid, but rather to an electrode polarization effect [125]. This effect is caused by the formation of a double layer at the interface between the liquid and the electrode due to the blocking of charges. From a circuit point of view, this can be seen as if a large capacitor was placed in series with the sample, inducing the apparent large increase in the permittivity. The theoretical treatment of this phenomenon is attributed to Warburg [126] and Fricke [127]. This effect can be corrected via numerical treatment or a hardware modification. These methods were summarized in a review by Ishai *et al.* [128]. Correction is not applied in our case, as the working



---

frequency for DEP experiments (above 1 kHz) is far above the frequency range at which electrode polarization occurs.

The plot of losses (imaginary part of complex permittivity) reveals that the predominant mechanism is ohmic conduction characterized by the -1 slope in log-log scaling. The right-hand part of the three curves shown below seems to be associated with a relaxation mechanism. However, this would need to be confirmed by a study in temperature. It is interesting to note that the more viscous the resin, respectively 0.1, 0.48 and 2.3 Pa.s, the lower the losses. Such behavior may be related to the total charge mobility.

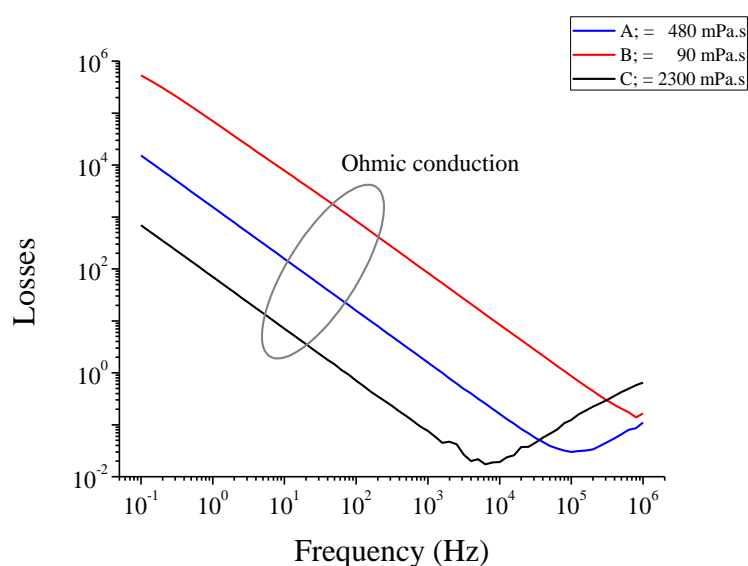


Figure III-6: Imaginary part of the permittivity of three epoxy resins without hardener, at 30°C.

According to Wilson *et al.* [129], measurement of the losses also makes it possible to determine the frequency above which EHD flow no longer occurs. However, his description is rather vague: “*it corresponds to a range where, due to relaxation, the loss approaches its high-frequency value*”. The fact that they plotted the losses in linear scale might actually be misleading, as high-frequency values are negligible compared to low-frequency values (Figure III-7).

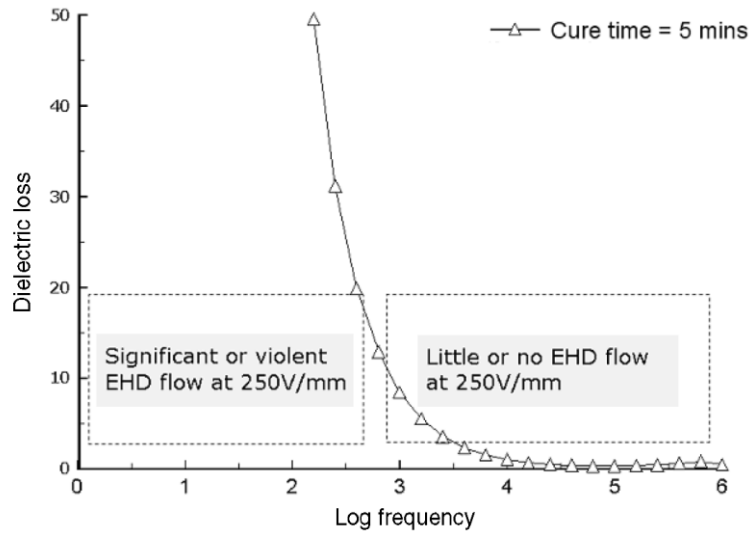


Figure III-7: Dielectric loss of Epotek 302-3M epoxy at 20°C [129].

This effect is clear in Figure III-8. Taking the description of Wilson *et al.*, one would conclude that the three resins present exactly the same behavior, reaching their high-frequency value around 1 Hz. However, at a given frequency, the SR 5311 resin is three orders of magnitude above the SR 8500 resin, as can be observed in Figure III-6. Furthermore, an experiment at 1 Hz showed that EHD flow was still observable.

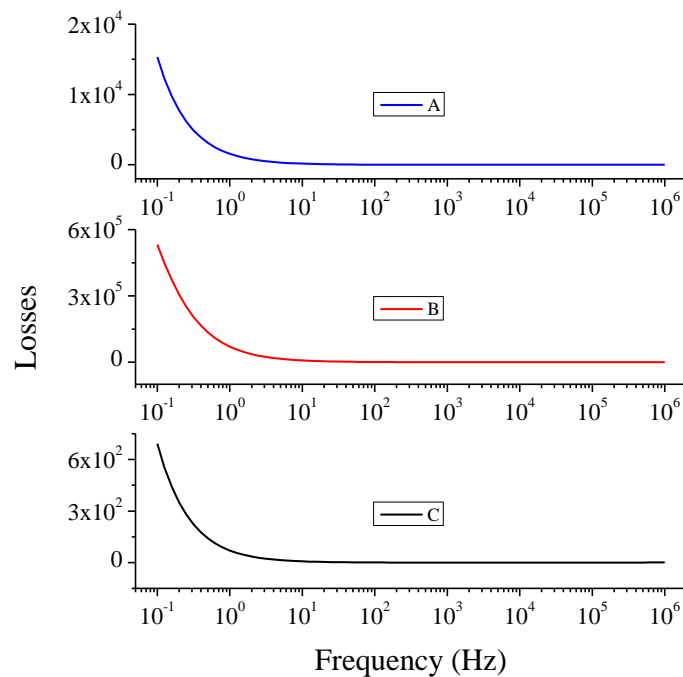


Figure III-8: Imaginary part of permittivity of the three epoxy resins plotted in linear scale.

Perhaps, a better explanation is that there is a given threshold of losses at which EHD flow strongly decreases.

Deionized water (DI water) is another liquid that is important to characterize for further study. DI water is water that has been treated to remove the mineral ions naturally present, down to  $2 \mu\text{S}/\text{cm}$ . This liquid has been proved to be “convenient” for DEP characterization (more appropriate for biological material, as the low viscosity and density mismatch lead to fast sedimentation for ceramics). The accurate measurement of the dielectric properties of DI water is necessary for DEP characterization in order to derive powder permittivity.

The real and imaginary parts of DI water are plotted in Figure III-9. The general characteristics are very similar to those of the resins. The real part presents a plateau at high frequency, around 83 in permittivity, and the electrode polarization effect at low frequency (under 1 kHz). The imaginary part has a -1 slope at high frequency and  $\approx -0.9$  at lower frequencies. Again, this is a marker of electrode polarization [125].

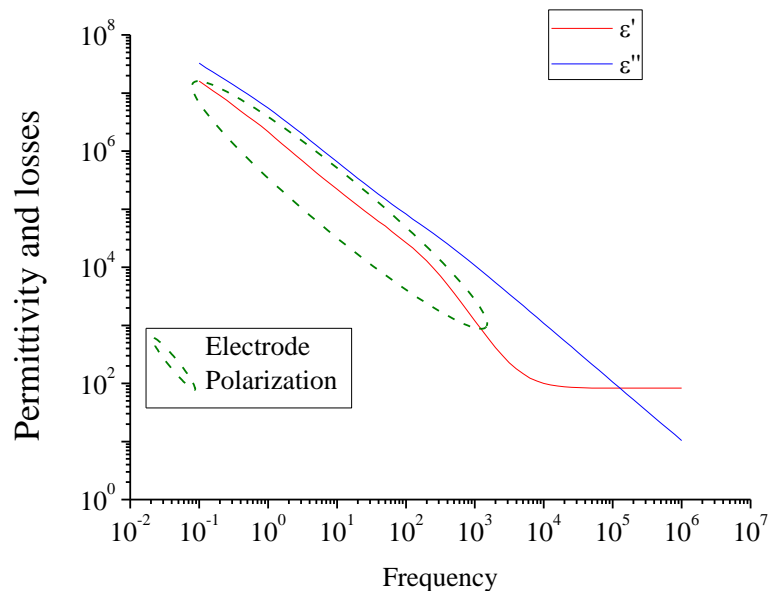


Figure III-9: Measured real and imaginary parts of DI water permittivity at ambient temperature.

#### III.1.d. Measurement of the polymer resin viscosity

The measurement of resin viscosity is an important parameter, and crucial for several aspects in DEP experiments. The higher the viscosity, the slower the particles sediment, but on the other hand, a higher electric field is necessary to move particles. Viscosity is also an inevitable input parameter for numerical modeling of DEP experiments.

Some suppliers of polymer resin give the viscosity of the resin, and even viscosity evolution over time and temperature. This property must be measured when the data is not available.

For two of the resins used in our experiments (B and C), detailed data was given by the supplier, but no data was available for resin A. Viscosity measurement was performed using a RVDV-II rheometer from

Brookfield, with mobile type CP 51. Viscosity was measured at three temperatures for the resin without hardener. At each temperature, the mobile speed was changed to verify whether the resin had non-Newtonian behavior. Non-Newtonian behavior is characterized by a change in measured viscosity when mobile speed is increased. Thanks to the device's design, increasing mobile speed also improves the measurement accuracy.

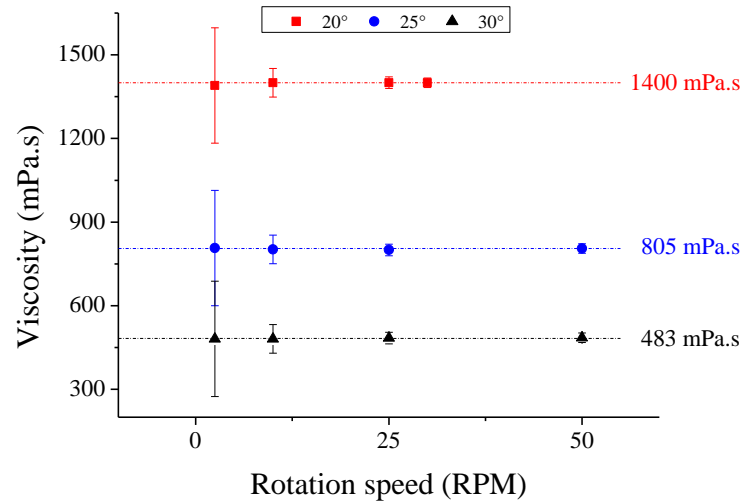


Figure III-10: Viscosity of the resin A between 2 and 50 RPM at different temperatures.

From the results plotted in Figure III-10, it appears that the fluid did not behave as non-Newtonian fluid, as the viscosity is constant with rotation speed. Resin viscosity decreases rapidly with increasing temperature.

Resin A viscosity was measured in this work without hardener. However, measurement of the change in resin viscosity with hardener was measured by Kozako *et al.* [130].

### III.2. Measurement of the powders properties

According to the definition given in section I.1.b.2, a composite is made of at least two compounds: a matrix and a filler. Determination of matrix properties is rather easy, as presented in the previous section. However, when it comes to filler properties, the problem is far more complex. Indeed, it is very difficult to measure the electrical properties of a single particle. Up until now, the filler properties have been determined mainly by two methods. The first method considers that powder properties are the same as those of bulk (i.e. large, dense, and often polycrystalline solid) materials. The second method is to estimate filler (or powder) permittivity by extracting it from mixing rules.

Knowledge of filler permittivity is a key element for predicting experimental behavior from numerical modeling.

---

### III.2.a. Estimation from bulk permittivity

While it seems reasonable to estimate powder permittivity from bulk permittivity for polymers because the structure from large sample should not differ from that of a small particle, assimilating a ceramic microparticle to bulk ceramic is less reasonable. The microstructure of a sintered polycrystalline ceramic can typically be described by two phases: grains and the interface between grains, called the grain boundary. These two phases can be observed in Figure III-11 for a sintered  $\text{BaTiO}_3$  ceramic ([131]).

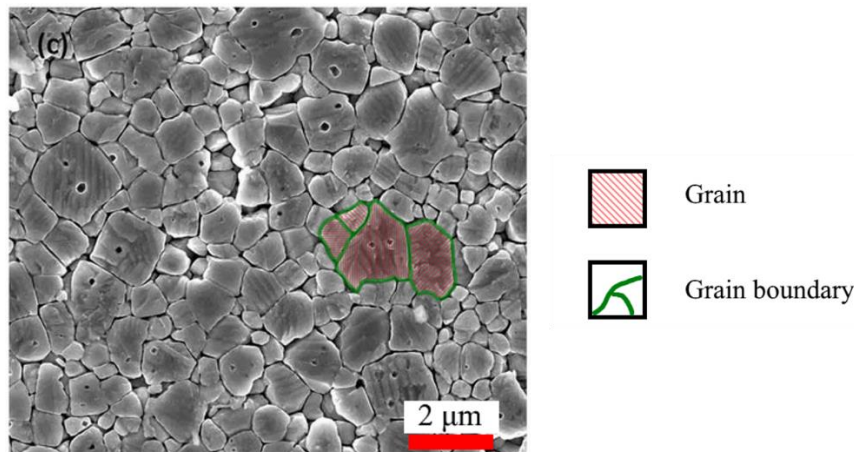


Figure III-11: SEM image of  $\text{BaTiO}_3$  domain structure [131].

The first difference between bulk ceramic and an individual powder particle is therefore due to the possible absence of grain boundaries for the particles. Moreover, depending on the process used to obtain the particles, the particles may be composed of a unique domain or several domains. The second difference can also be observed in Figure III-11: some interfaces between grains are not filled, forming voids. This is related directly to the sintering process, with the bulk material sometimes being porous.

If one chooses to take the properties from the bulk ceramic, other issues would have to be taken into account, depending on the material. It has been shown that material properties depends strongly on the grain and powder (before sintering) sizes as well as the process, as can be observed in Figure III-12 for a high permittivity ceramic.

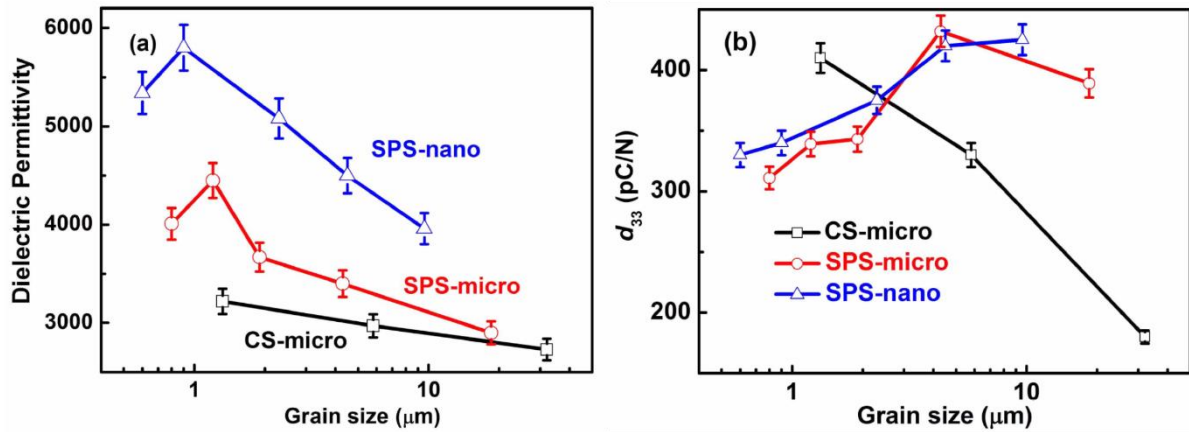


Figure III-12: Dependence of BaTiO<sub>3</sub> ceramic properties on grain size and sintering technique. CS stands for Conventional Sintering, SPS for Spark Plasma Sintering. (a) permittivity, (b) piezoelectric coefficient [131].

The property change upon grain size is not monotonous, as it also depends on the powder size used and the sintering technique. This example illustrates the potential difficulty of taking a single particle property from a bulk ceramic. With the results from Figure III-12 (a), for a particle with diameter around one micron. If one takes an unproven assumption that the powder properties correspond to bulk properties with an equivalent grain size, then particle permittivity would be estimated between 3000 and 6000.

Another aspect that must be taken into account is the dependence of material structure on particle size. This is known to be important for BaTiO<sub>3</sub>, which exhibits a cubic crystal phase for small particles (<100 nm) and a tetragonal phase for bigger particles. The impact for composites was shown by Dang [132] (Figure III-13).

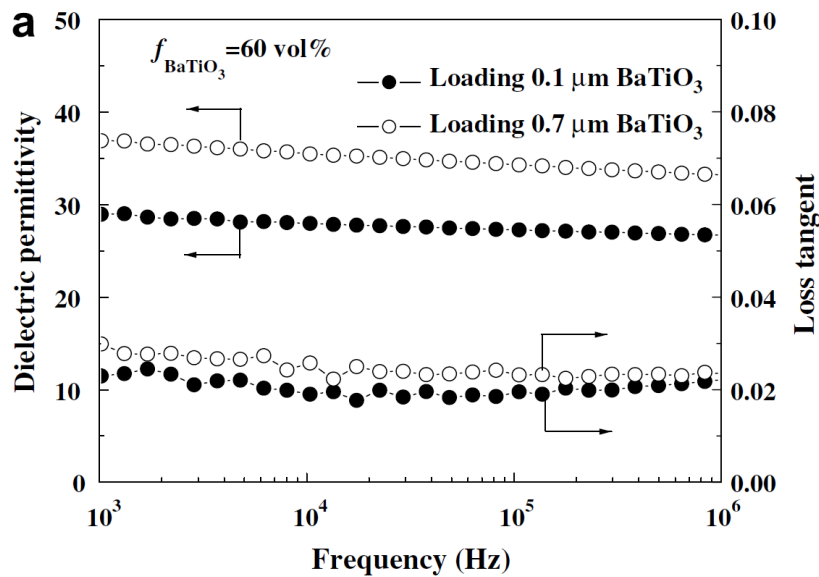


Figure III-13: Dependence of the permittivity and loss tangent of epoxy/BaTiO<sub>3</sub> composite on filler size and frequency [132].

### III.2.b. Estimation from mixing rules

Based on the above reasoning, the choice of using bulk ceramic to determine particle properties might not be entirely appropriate. There is another way to try to determine the particle properties: by using mixing laws [133], [134]. The principle is to measure the properties of a composite for different filler contents, then, the matrix properties being known, to adjust the particle property in the mixing law equation. The best fit would give the particle property. However, the main issue is that there are many mixing rules and they will all give a different value for particle permittivity. The main mixing rules and their equations are given in Table III-2. We adapted this technique to different datasets measured in our laboratory and taken from the literature, to observe the distribution in permittivity values (Figure III-14).

Table III-2: Main mixing rules and their equations

Mixing rule	Equation	Ref.
Maxwell-Garnett	$\varepsilon_{eff} = \varepsilon_m + 2f\varepsilon_m \frac{\varepsilon_p - \varepsilon_m}{\varepsilon_p + \varepsilon_m - f(\varepsilon_p - \varepsilon_m)}$	[135]
Bruggeman	$(1 - f) \frac{\varepsilon_m - \varepsilon_{eff}}{\varepsilon_m + \varepsilon_{eff}} + f \frac{\varepsilon_p - \varepsilon_{eff}}{\varepsilon_p + \varepsilon_{eff}} = 0$	[136]
Power laws	$\varepsilon_{eff}^\beta = f\varepsilon_p^\beta + (1 - f)\varepsilon_m^\beta$	[137]
		[138]
Lichtenecker	$\ln(\varepsilon_{eff}) = f\ln(\varepsilon_p) + (1 - f)\ln(\varepsilon_m)$	[139]

In the above equations,  $f$  is the volume fraction of fillers. For power-laws, the  $\beta$  parameter ranges from 0 to 1. Some specific values correspond to known laws. For instance,  $\beta = 1/3$  corresponds to the Looyenga formula [137] and  $\beta = 1/2$  to the Birchak formula [138]. The Lichtenecker formula is also derived from power-laws where  $\beta \rightarrow 0$ .

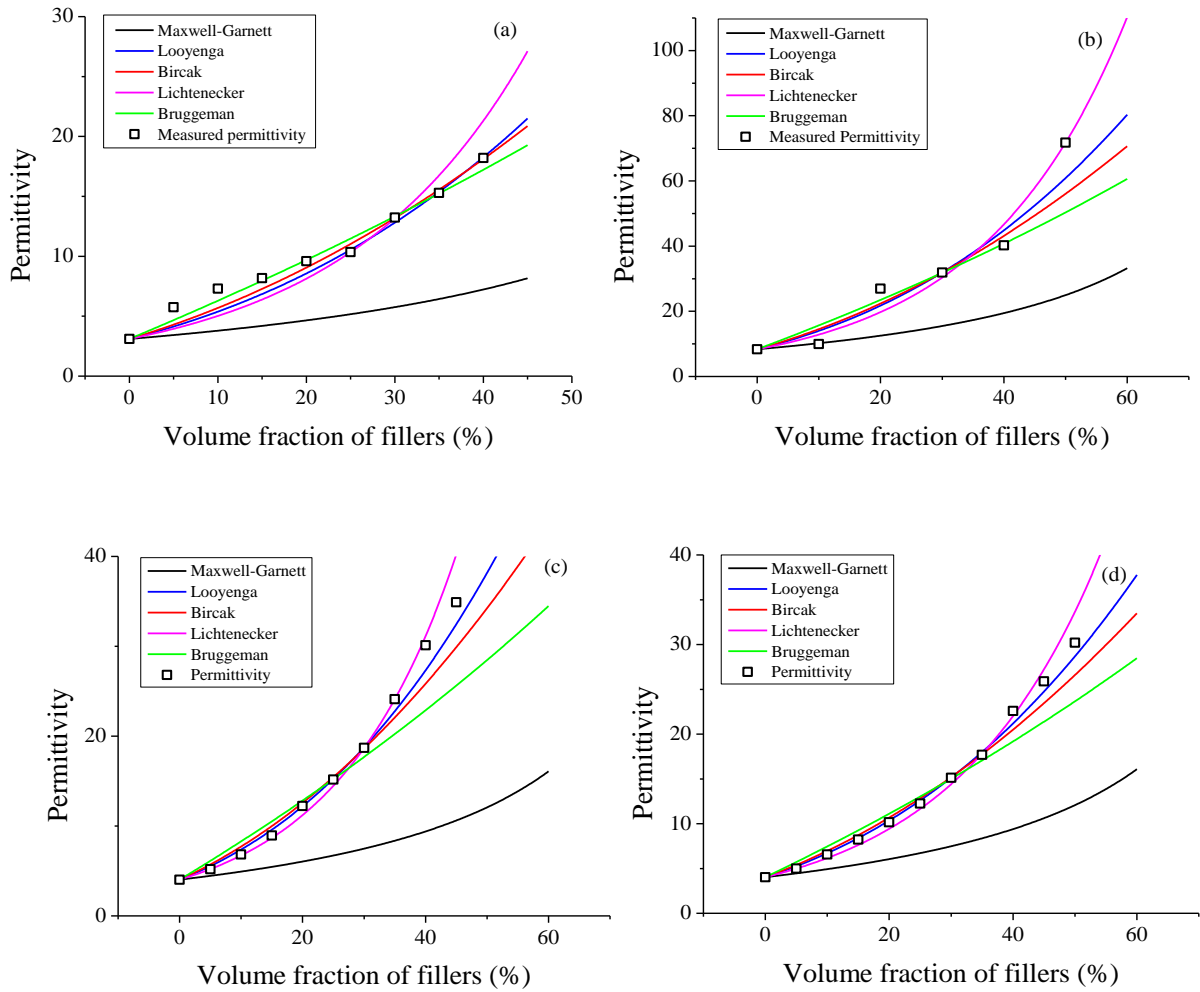


Figure III-14: Estimation of the permittivity of (a) BaTiO<sub>3</sub> nanoparticles embedded in PI at 1 kHz [140], (b) BaTiO<sub>3</sub> microparticles in PVDF at 100 Hz [141], (c) BaTiO<sub>3</sub> microparticles embedded in epoxy at 1 kHz and (d) SrTiO<sub>3</sub> microparticles in epoxy at 1kHz. The latter two materials were made and characterized in the Laplace laboratory by Louis L  v  que.

Table III-3: Estimation of powder permittivities from mixing rules.

Mixing law	Fitted permittivity			
	(a) BaTiO <sub>3</sub>	(b) BaTiO <sub>3</sub>	(c) BaTiO <sub>3</sub>	(d) SrTiO <sub>3</sub>
Maxwell-Garnett	>5000	>5000	>5000	>5000
Looyenga	85	199	136	93
Bircak	64	146	94	69
Lichtenecker	384	616	668	281
Bruggeman	48	111	64	52



From Figure III-14 and Table III-3, the Maxwell-Garnett mixing rule appears unable to correctly match the data. This is probably due to the fact that it is normally valid only for very low filler contents. The other mixing laws fit the data to much lower values of permittivity compared to the bulk (at least for BaTiO<sub>3</sub> particles).

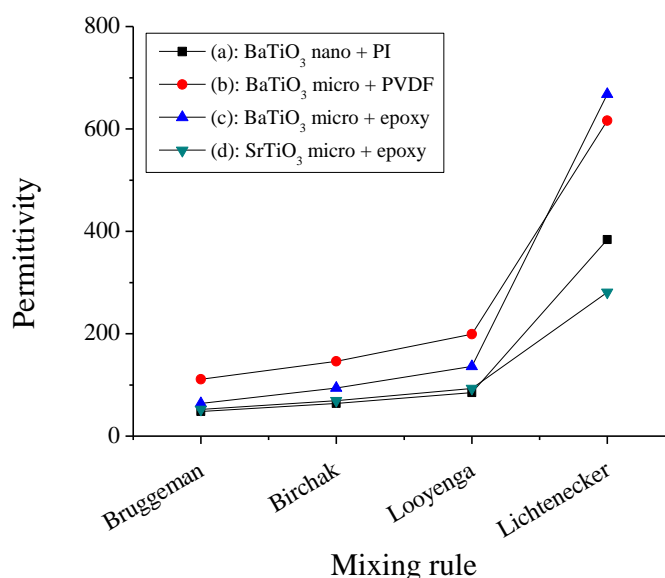


Figure III-15: Estimated permittivity as a function of the mixing law for the three samples. (b) at 100 Hz, (a), (c) and (d) at 1 kHz.

The estimated permittivities present wide distribution (e.g. from 64 to 668 for the sample (c)) as can be seen in Figure III-15. Except for the Lichtenecker formula, the predicted permittivities are relatively low compared to that which can be expected for bulk BaTiO<sub>3</sub>.

The method presented above for estimating permittivity exhibits high variability. This method implies that accuracy is related to the choice of the mixing rule to fit its experimental data. Yet, each mixing law is more or less valid according to composite characteristics (filler content, particle size, size distribution, shape, etc.). Furthermore, this method is likely to be sensitive to the material process (dispersion [142], sedimentation).

It is worth noting that the variation of estimated permittivity could be even larger. Five mixing laws were examined here, but other mixing rules are described in literature. The Jaysundere-Smith equation [143], Wiener's bounds [144] (which are in fact special cases of the Power Laws with  $\beta = -1$  and 1), Sillars equation [145] are a few examples of the numerous existing equations. To quote Shivola: "The multitude of mixing formulae presented in the literature is a reflection of the randomness in the structure of these heterogeneous materials of interest. There is no exact solution for the electromagnetic problem with random parameters and boundaries and therefore rivaling mixing theories that receive experimental confirmation can coexist." [146].

It is the author's belief that the two methods presented in III.2.a and b are not satisfactory, as they give a wide distribution of particle permittivities and they rely on weak hypotheses. Neither of them is based on direct measurements of the particle property, but rather on indirect macroscopic measurements. In the next section, a direct method is presented to try to estimate a particle's permittivity based on its dielectrophoretic response.

### III.2.c. Theoretical description of the crossover frequency

The nDEP and pDEP behaviors of particles were introduced in section III.3.c. However, in that introduction, the particle and the medium were considered as pure dielectrics without losses. When the losses are no longer negligible, eq. 1 becomes:

$$\mathbf{F}_{DEP} = 4\pi\epsilon_m R^3 \text{Re}[K^*(\omega)] \nabla E^2 \quad (30)$$

where the asterisk \* stands for complex notation. The sign of the DEP force is driven by the sign of the real part of the complex Clausius-Mossoti function. The word “function” stresses the fact that  $K^*(\omega)$  depends strongly on the electric field's instantaneous frequency.

The Clausius-Mossoti function is given by:

$$K^*(\omega) = \frac{\epsilon_p^* - \epsilon_m^*}{\epsilon_m^* + 2\epsilon_m^*} \quad (31)$$

It is possible to determine the real part of  $K^*(\omega)$ :

$$K^*(\omega) = \frac{\epsilon_p' + j\epsilon_p'' - \epsilon_m' - j\epsilon_m''}{\epsilon_p' + j\epsilon_p'' + 2(\epsilon_m' + j\epsilon_m'')} \quad (32)$$

The equation will now be developed based on the following hypothesis  $\epsilon_p'' \ll \epsilon_m''$ . This hypothesis is explained later. It is worth noting that the sign of the complex part of the permittivity depend on the convention chosen, but doesn't impact the final result.

$$\begin{aligned} K^*(\omega) &= \frac{\epsilon_p' - \epsilon_m' - j\epsilon_m''}{\epsilon_p' + 2\epsilon_m' + 2j\epsilon_m''} \times \frac{\epsilon_p' + 2\epsilon_m' - 2j\epsilon_m''}{\epsilon_p' + 2\epsilon_m' - 2j\epsilon_m''} \\ \text{Re}[K^*(\omega)] &= \frac{\epsilon_p'^2 - 2\epsilon_m'^2 + \epsilon_p'\epsilon_m' - 2\epsilon_m''^2}{(\epsilon_p' + 2\epsilon_m')^2 + 4\epsilon_m''^2} \end{aligned} \quad (33)$$

For a specific frequency, called the crossover frequency, the Clausius-Mossoti function is null. This corresponds to the change from nDEP to pDEP, or vice versa. From eq. 33 we obtain:

$$\text{Re}[K^*(\omega)] = 0 \quad \Rightarrow \quad \epsilon_p'^2 + \epsilon_p'\epsilon_m' - 2\epsilon_m'^2 - 2\epsilon_m''^2 = 0 \quad (34)$$

We now understand that without the hypothesis presented above, the system would have two unknowns and only one equation, thus making resolution impossible. This hypothesis is a key point for developing

this method into a characterization technique. If we intend to use the crossover frequency to characterize a ceramic particle, the latter should have low losses compared to medium conductivity and dielectric losses. However, care should be taken, as its surface conductivity could also have a non-negligible contribution. Its effect was demonstrated clearly by examining the crossover frequency of latex particles for different particles sizes [147].

Eq. 34 is a 2<sup>nd</sup> degree polynomial. The roots can be calculated easily, enabling the extraction of particle permittivity. The discriminant is:

$$\Delta = b^2 - 4ac = \varepsilon'_m{}^2 + 8(\varepsilon'_m{}^2 + \varepsilon''_m{}^2) > 0 \quad (35)$$

The two roots are:

$$\varepsilon'_{p_1} = \frac{-\varepsilon'_m + \sqrt{\varepsilon'_m{}^2 + 8(\varepsilon'_m{}^2 + \varepsilon''_m{}^2)}}{2} \quad (a) \quad (36)$$

$$\varepsilon'_{p_2} = \frac{-\varepsilon'_m - \sqrt{\varepsilon'_m{}^2 + 8(\varepsilon'_m{}^2 + \varepsilon''_m{}^2)}}{2} \quad (b)$$

Being negative, the second root can be excluded. Thus, eq. (36) (a) makes it possible to determine the value of particle permittivity based on knowledge of the matrix's electrical properties at the crossover frequency.

The concept of characterizing particle permittivity from DEP experiments is well known, but until now mostly used to characterize cells or living matter. However, many examples can be found with polymers such as latex. Among the numerous examples, we can cite the work of Green [147], Marszalek [148], Gascoyne [149], Hughes [150], and Ermolina [151]. To our knowledge, this work is the first attempting to use DEP to characterize the permittivity of high-permittivity ceramic particles.

### III.2.d. Method and experimental results

The dielectrophoretic characterization of particles has been widely used for cells and some polymers (mainly latex beads/spheres). The study of ceramic particles is challenging, as it raises new issues. In most studies, particles present lower permittivity than the medium (i.e. around 80 for deionized water (DI water)), so nDEP is expected to occur at high frequencies and pDEP at low frequencies (for homogeneous particles). High- $\kappa$  ceramic particles should behave oppositely, with pDEP at high frequencies and nDEP at low frequencies. Intuitively, the behavior of ceramic particles should be simpler than that of cells with a core-shell structure, and should present only one crossover. The main issue encountered in experiments with ceramic particles may be the density mismatch between the particles and the medium. For example, water has a density of 1 g/cm<sup>3</sup>, whereas BaTiO<sub>3</sub> is close to 6

$\text{g/cm}^3$ ,  $\text{SrTiO}_3$  is about  $5.1 \text{ g/cm}^3$ , and alumina is about  $4 \text{ g/cm}^3$ . This large difference between the matrix and filler densities leads to fast sedimentation, reducing the time available for DEP characterization.

The geometry chosen for the DEP characterization cell is rather basic, corresponding to a quadrupolar electrode (Figure III-16). The experimental cells were realized by evaporating 150 nm of metal (silver or aluminum) onto a microscope slide, with the pattern made by photolithography. A first series of cells was made of silver and the electrode shape was squared. They were then replaced by aluminum to decrease water electrolysis. The electrode design was also replaced by that shown in Figure III-16. The distance between diagonal electrodes was  $220 \mu\text{m}$ .

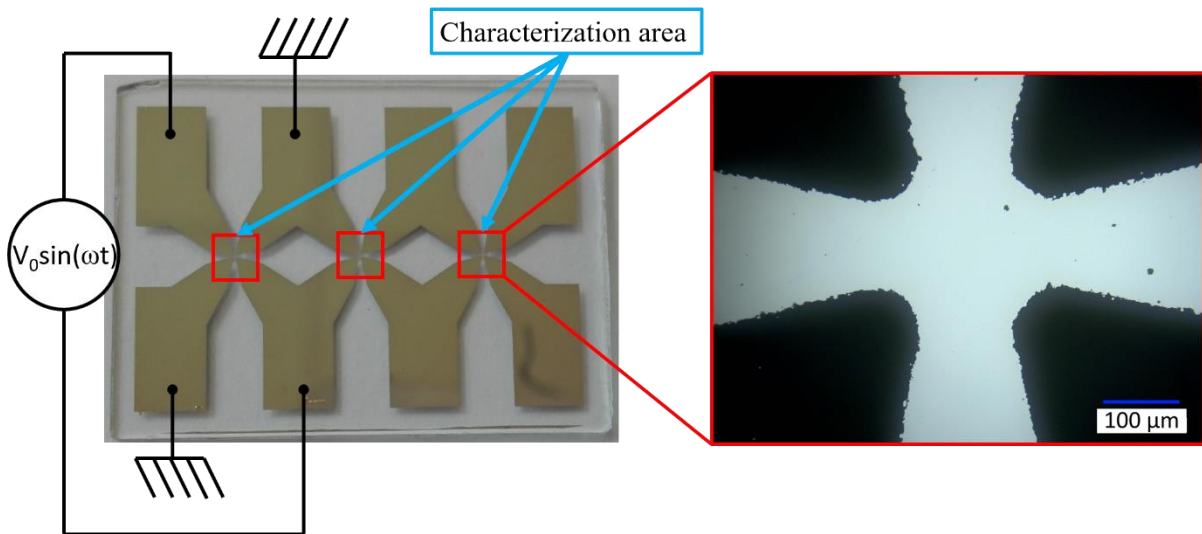


Figure III-16: DEP characterization cell. (left) 3 cells on a microscope slide, (right) zoom on one cell.

The strong electric field gradients are located near the electrodes. The weak electric field gradient area is at the center, as can be observed from the numerical simulation performed with [47] in Figure III-17.

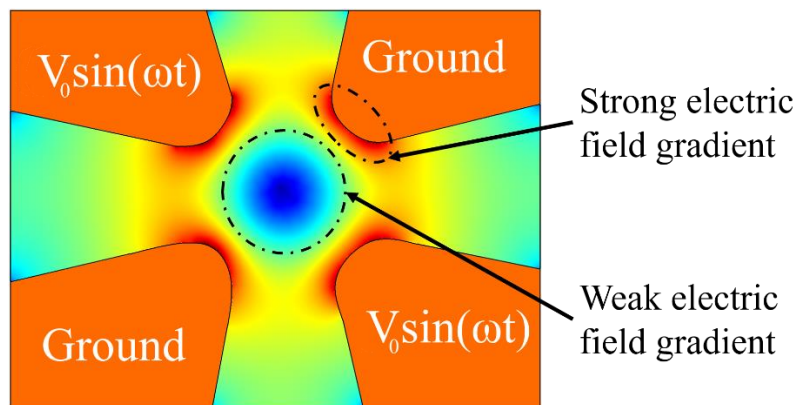


Figure III-17: Electric field distribution, DEP characterization cell.

The experimental setup is presented in Figure III-18. Particle movement is monitored using transmitted light optical microscopy with magnification ranging from  $\times 500$  to  $\times 5000$  (Keyence VHX-5000).

Sinusoidal voltage is generated by a waveform generator (TTi TGA12104). The signal is then amplified by a homemade power amplifier (160 V<sub>rms</sub> –gain ×100 – from DC to 1 MHz).

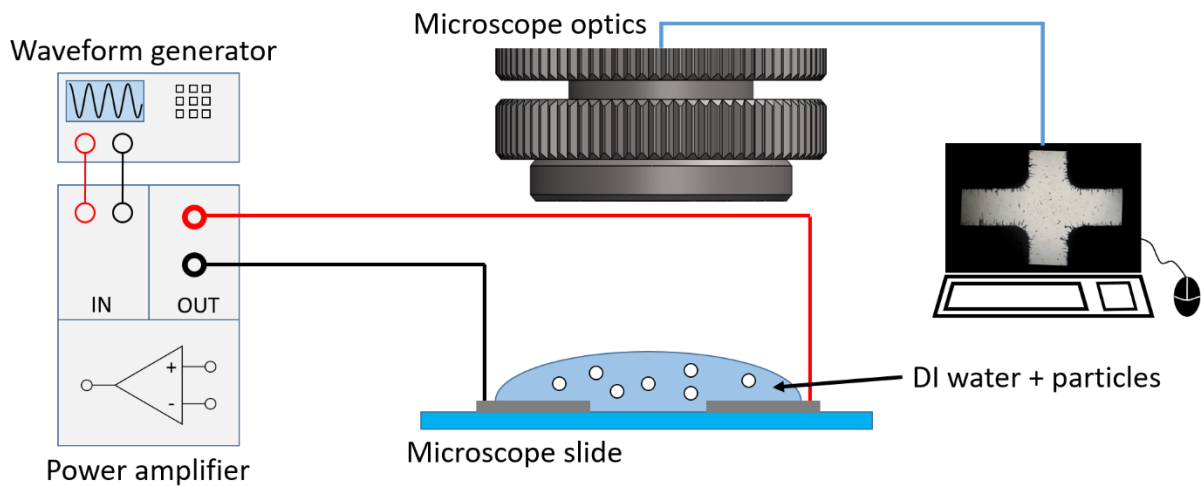


Figure III-18: Experimental setup for DEP characterization.

In nDEP, particles are expected to agglomerate at the center and, in pDEP, to be attracted to the edges of the electrodes. The best way to determine the crossover frequency would be to place a drop of DI water filled with particles, then make a frequency sweep and determine the frequency at which no movement is visible. However, as stated above, the low viscosity of DI water and the density mismatch between the particle and the medium preclude following this method, as particles sediment too rapidly. The solution found to overcome this issue was to use the following procedure to find the crossover frequency:

- Set the signal frequency
- Apply voltage across the electrodes
- Place a drop of DI water with particles on the characterization cell
- Observe particles distribution to conclude whether it was pDEP or nDEP
- Wash the characterization cell and repeat the procedure at a different frequency
- This procedure has the disadvantage of being very slow due to the numerous washing phases. Another disadvantage is that it is less accurate compared to other methods.

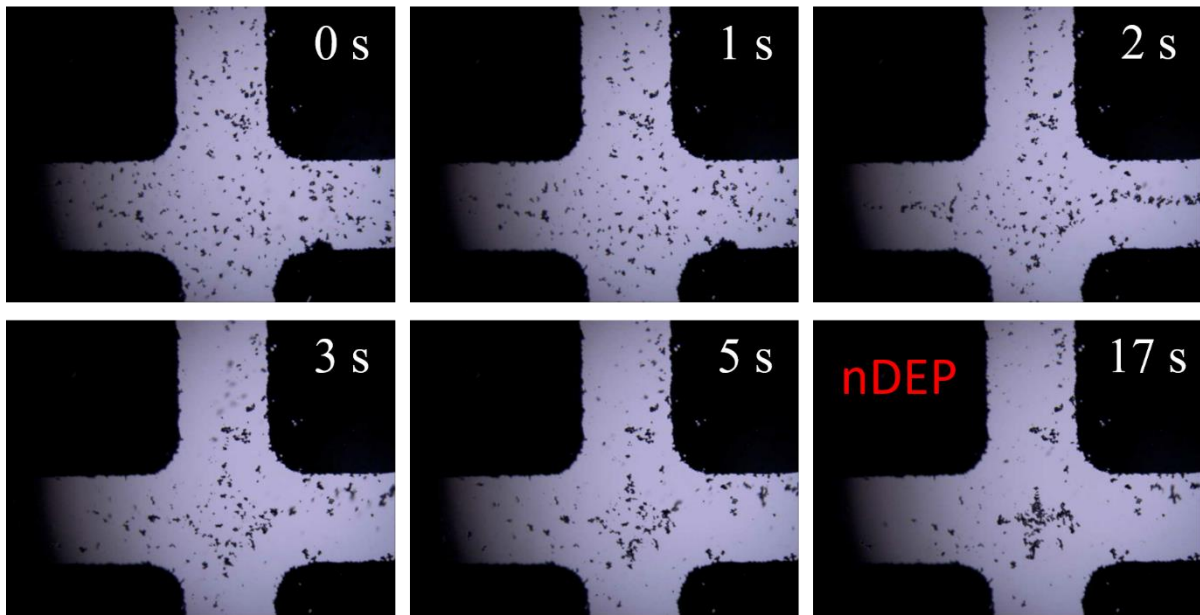


Figure III-19: BaTiO<sub>3</sub> particles in DI water undergoing nDEP. Initially, the particles are dispersed randomly. At  $t = 0$  s, 7 Vrms are applied, the particles are repelled from the electrodes.

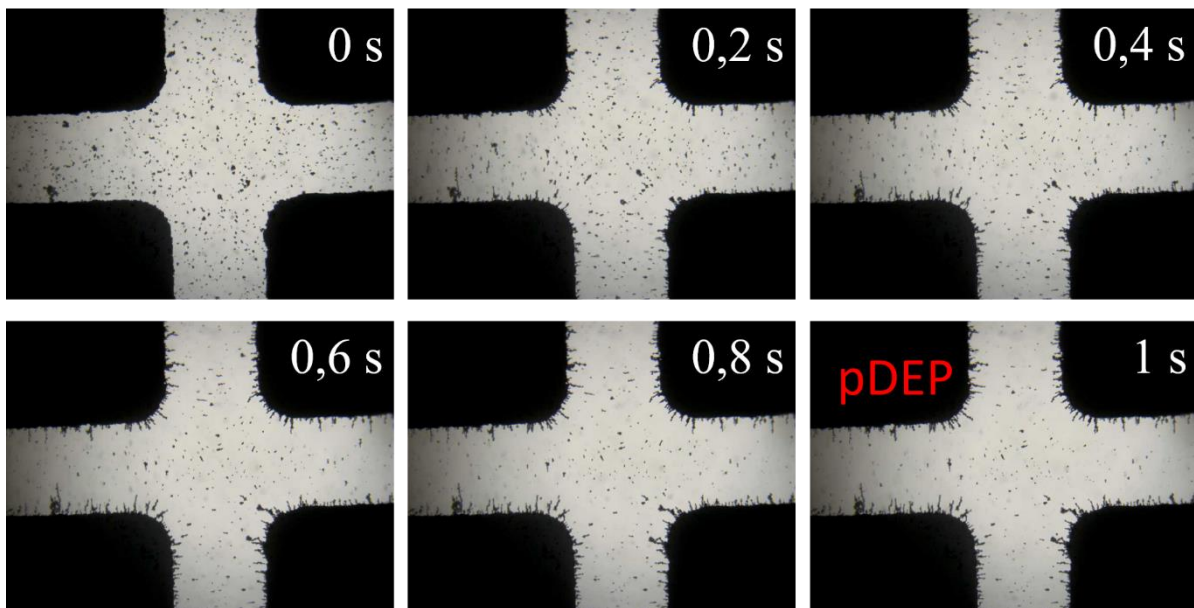


Figure III-20: BaTiO<sub>3</sub> particles in DI water undergoing pDEP. Initially, the particles are randomly dispersed. At  $t = 0$  s, 30 Vrms are applied, the particles are attracted to the electrodes.

Particles undergoing nDEP are shown in Figure III-19, and pDEP in Figure III-20. In nDEP, the particles tend to concentrate in the area at the center of the cell while, in pDEP, the particles are attracted toward the electrodes. Small particle chains are formed attached to the electrodes, directed along electric field lines. The presence of chains is detrimental, as they add particle-to-particle interactions that might interfere with the electric field configuration by adding attracting areas. This confirms that it is better to use a mixture with low filler content. Another difficulty with DEP characterization is EHD flow. Indeed,

it can be difficult to differentiate particles moving under DEP force or pushed by liquid flow. This EHD flow is frequency- and voltage-dependent. Generally the lower the frequency and the higher the voltage, the stronger the EHD flow.

The crossover frequency was found for two different types of particles, BaTiO<sub>3</sub> and SrTiO<sub>3</sub> microparticles in DI water. The resulting particle permittivities using eq.36 (a) are summarized in the following table:

Table III-4: Measured crossover frequencies and computed permittivity

<b>Particle nature</b>	<b>Crossover frequency</b>	<b>DI water permittivity</b>	<b>Di water losses</b>	<b>Computed permittivity</b>
BaTiO <sub>3</sub>	30 kHz	84.8	363	633
SrTiO <sub>3</sub>	55 kHz	83.7	185	346

The DI water permittivity and losses in the table above are given at the corresponding crossover frequencies taken from Figure III-9.

It is worth noting that the value of the permittivity calculated is only valid at the crossover frequency. This means that if one needs the dependence of the permittivity vs frequency, it is necessary to vary the medium conductivity as shown by Green [147]. However, it might not be necessary for ceramic materials for which permittivity is constant over a wide frequency range.

The value of the BaTiO<sub>3</sub> is much lower than classic values for bulk ceramic (633 and between 3000 to 6000).

To conclude: all the missing matrix and powder parameters for feeding the model developed in section II.4.b have been measured. Enough elements are available to target the experimental parameters for particle chaining, which is the topic of chapter IV.

### III.3. Perspectives

Measuring particle permittivity using the DEP characterization method was presented in this chapter. The value of permittivity we obtain agrees well with published literature. However, even though measurement was successful, this attempt is still a work in progress. Several issues still need to be resolved to obtain a better measurement technique.

The current setup is difficult to use due to fast powder sedimentation. One way to solve this problem could be to work with a continuous flow of particles.

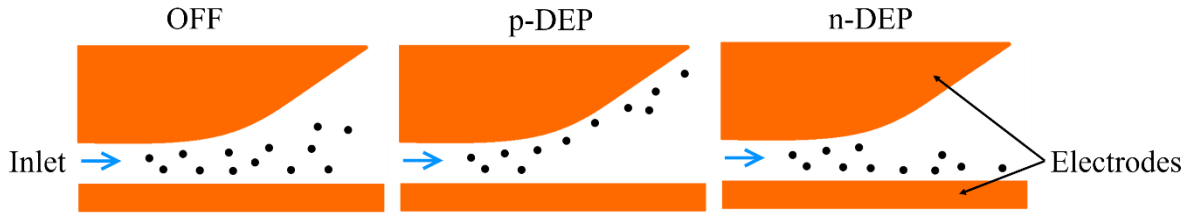


Figure III-21: Design for continuous flow DEP characterization.

The design presented in Figure III-21 could reduce the impact of sedimentation if the fluid velocity and cell length are chosen appropriately. Without sedimentation, frequency sweep would be possible, enhancing the accuracy of the measurement.

Determination of the crossover frequency is not the only characterization method relying on the DEP force. Particle levitation is an interesting alternative based on measuring particle levitation height induced by DEP forces [152]. However, both levitation and the technique presented earlier depend on optical microscopy. This leads to a severe limitation regarding particle size. It means that nanoparticles could not be characterized using these methods. Another issue is that the presented methods are not easy to automate and depend on the experimenter's expertise. A possible way to overcome these limitations would be to implement local impedance measurement to detect the presence of particles (Figure III-22).

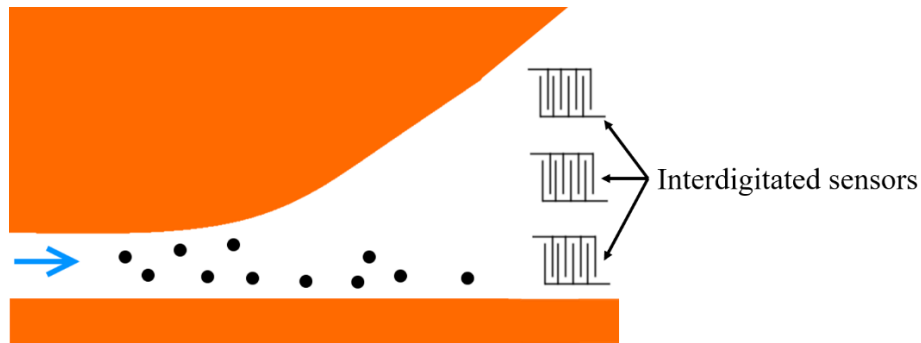


Figure III-22: Design for continuous flow DEP characterization with interdigitated sensors to detect the presence of particles.

However, even if this method could allow nanoparticle characterization, the impact of surface conductivity might not be negligible. Green and Morgan proposed a way to compute surface conductivity by measuring particle mobility, then using the Helmholtz-Smoluchowski equation to calculate the  $\zeta$  potential. The surface charge density is evaluated from the Gouy-Chapman/Grahame double-layer theory. Lastly, surface conductivity is given by the O'Konski equation [153]:

$$\sigma_{surf} = \rho_{surf} \times \mu \quad (37)$$

with  $\rho_{surf}$  being the surface charge density and  $\mu$  the associated counterion mobility.



---

Lastly, DEP characterization is not the only method able to measure the properties of single particles. A study is currently in progress on the potential of local electrical measurements using Electrostatic Force Microscopy [154].

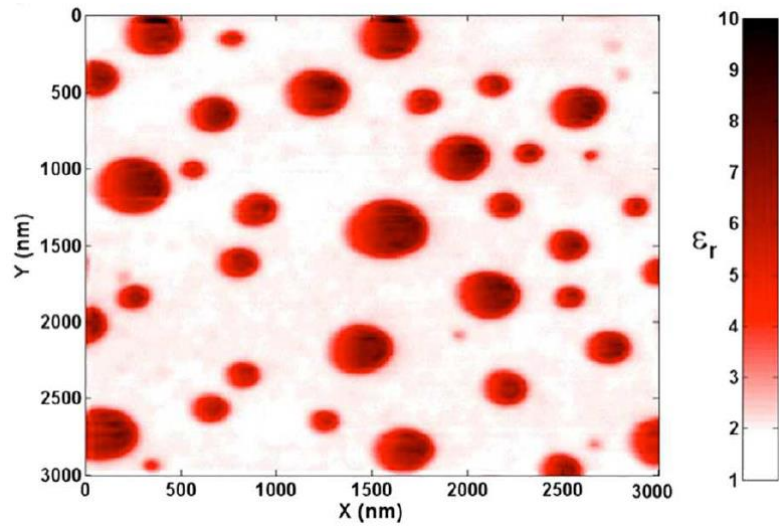


Figure III-23: Mapping of the permittivity of polystyrene/poly(vinyl-acetate) composite at 70 °C [154].

It is worth noting that the compound properties were measured, allowing their use as input for the model presented in section II.4.



# Chapter IV

Experimental Study Of  
Anisotropic Composite Formation:  
Aligned Fillers

## IV. EXPERIMENTAL STUDY OF ANISOTROPIC COMPOSITE FORMATION: ALIGNED FILLERS

This chapter reports on the study of composite material tailored by an electric field. This tailoring is achieved by chaining the fillers from the DEP interaction between particles. While several authors have reported the elaboration of such composites using this technique [59], [95], we focus here on controlling the composite properties based on knowledge of chaining dynamics. Chaining dynamics is monitored through on-line measurement of the change in permittivity. One advantage of this electrical marker of the composite structure is the possibility to compute it from numerical simulations, allowing the comparison of experimental and numerical results.

The purpose of these studies is to develop tools to enhance optimization of the electric-field-assisted elaboration process. In this context, the first part of the chapter focuses on the correlation of the chain formation and on the changes in dielectric properties using optical microscopy and online, real-time dielectric measurements. Based on knowledge of chaining dynamics, various composites are elaborated, and control of the final composite properties is evaluated by dielectric spectroscopy.

### IV.1. Description of the setups and protocols

The properties of anisotropic composites are related directly to filler structure. When the electric field is applied while the composite is still in a liquid state, the particles generally start to form chains aligned in the direction of the electric field (under certain circumstances, perpendicular orientation of non-spherical filler can occur, which is discussed in chapter VI), due to dielectrophoretic interactions between particles. The specific structures obtained enhance the composite properties in a preferential direction. In order to control the final composite properties, it is essential to understand chain formation dynamics and their correlation with the composite properties. In the following section, particle chaining is observed using real-time optical microscopy.

#### *IV.1.a. Preparation of the epoxy/ceramic powder mixtures*

The first step in observing chain formation is to prepare the epoxy/ceramic particle mixture. Preparation follows 8 successive steps:

- The ceramic powder is added to the resin (the amount of powder and resin are calculated to obtain the desired volume fraction)
- The mixture is heated for 5 minutes at 70 °C to degas and decrease viscosity
- The mixture is then stirred by hand
- The mixture is placed under vacuum to be degassed until the bubbles disappear
- Hardener is added to the mixture, respecting the hardener/resin ratio
- Once again, the mixture is heated at 70 °C, but for a shorter period of time (2 minutes)
- The mixture is stirred by hand

- The mixture is placed under vacuum to be degassed until the bubbles disappear

This procedure is summarized in Figure IV-1.

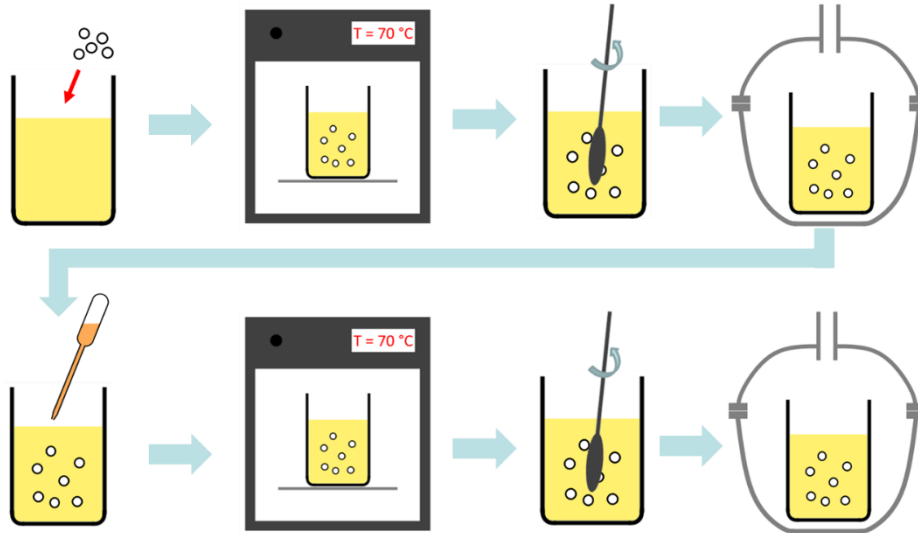


Figure IV-1: Procedure for preparing epoxy/ceramic particle mixtures.

The same procedure is applied prior to measuring dielectric property changes and optical observations during chain formation.

#### IV.1.b. Experimental setup and protocol for optical observations

The sample cell used for the optical observation is described in Figure IV-2. The copper electrodes are glued to the microscope slides and the distance between the electrodes is controlled by adding 1 mm thick glass spacers. The glass spacers also serve to seal the pool formed with the electrodes.

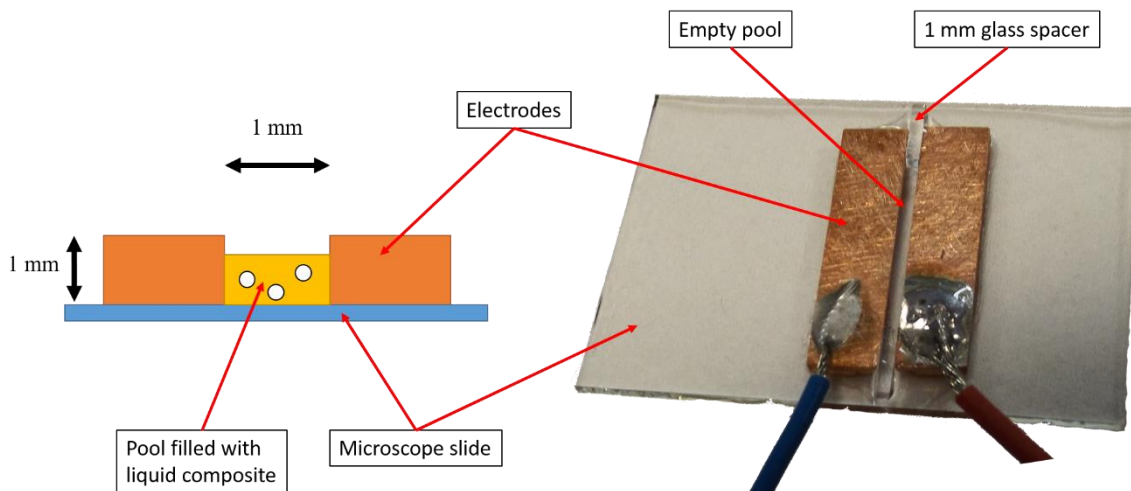


Figure IV-2: Scheme (left) and picture (right) of the sample cell.

Based on the electrode configuration in Figure IV-2 and Figure IV-3 (a), the electric field distribution was simulated (Figure IV-3 (c)), and the electric field along the cut lines in Figure IV-3 (d) was plotted (Figure IV-3 (b)). The electric field along cut line 2 in Figure IV-3 (b) presents a +17 % to -8 % deviation from the equivalent uniform electric field. Deviation is reduced to about  $\pm 1$  % along cut line 1.

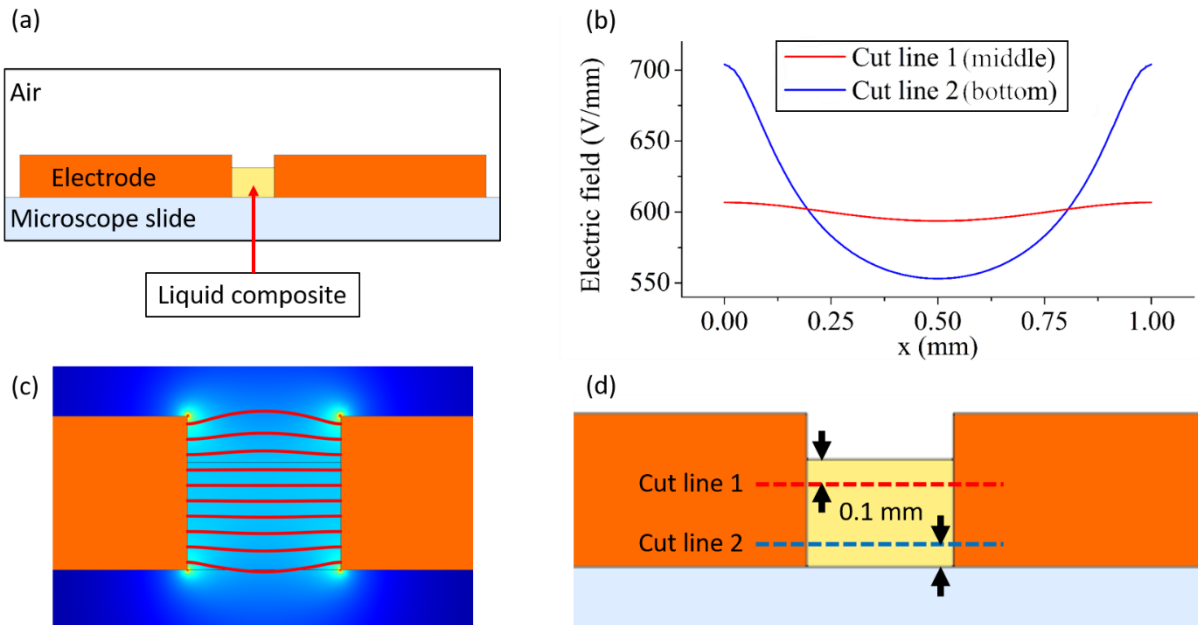


Figure IV-3: Electric field distribution evaluated by FEM, with 600 V applied across the electrodes. (a) Simulated geometry, (b) plot of the electric field along cut lines 1 and 2, (c) electric field distribution and electric field lines in the area between the electrodes, (d) plot of cut lines 1 and 2.

A small amount of the mixture, prepared as described in the previous section, is poured between the electrodes with a syringe. The space between the electrodes should not be entirely filled with the liquid, only half to avoid the DEP forces induced by the electrodes, in agreement with the simulations. In addition, the location where the chains are observed with the microscope is taken close to the liquid surface to avoid observing the areas near the bottom of the electrodes.

To observe the chain formation and allow curing the composite, the sample cell is placed on a heating plate under a Keyence VHX-5000 digital optical microscope (magnification range from  $\times 500$  to  $\times 5000$ ) as shown in Figure IV-4. A hole in the heating plate allows working with transmitted light microscopy. Transmitted light was chosen rather than reflected light because it shows better contrast for observing particles. However, both transmitted and reflected light have limitations in term of the composite volume fractions of fillers that can be studied. The images present good contrast under 0.25 vol%, but observation was impossible above 1 vol%.

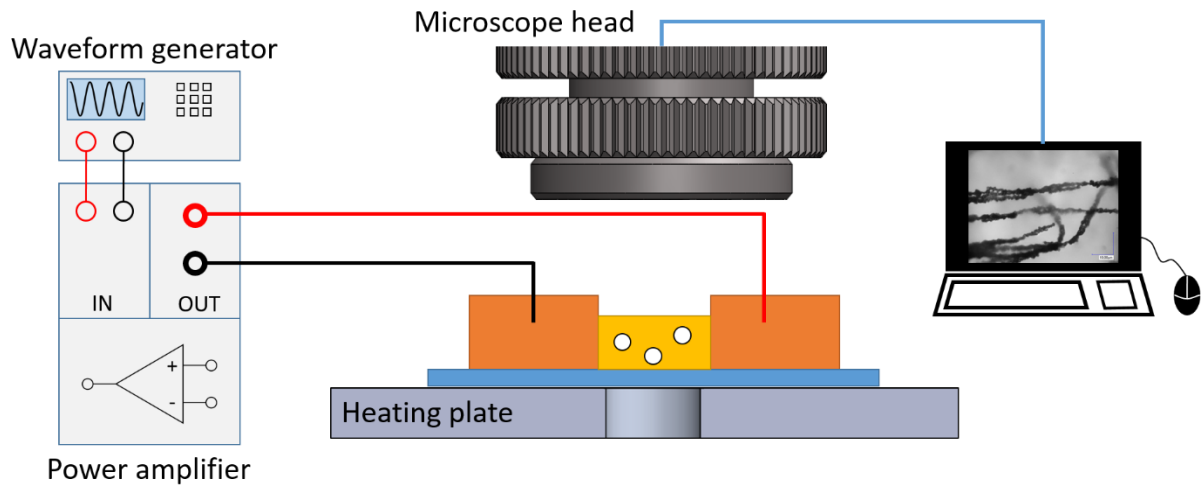


Figure IV-4: Scheme of the experimental setup for the microscopic observation of the chain formation.

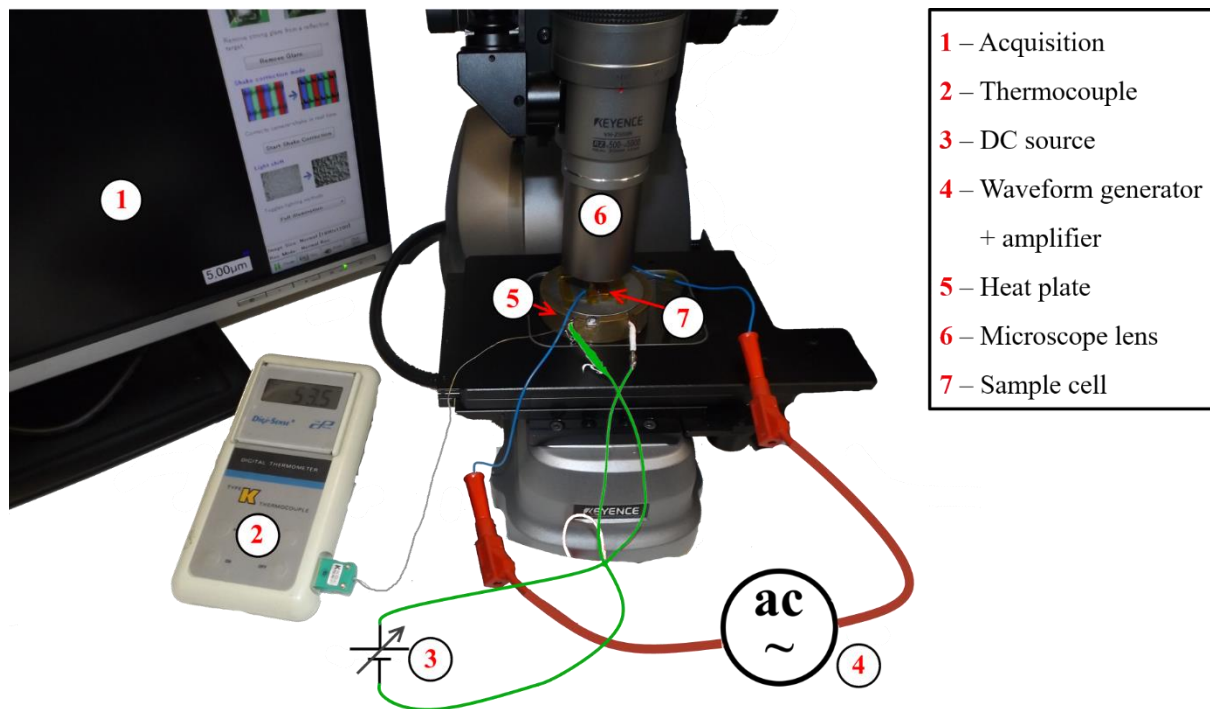


Figure IV-5: Experimental setup for microscope observation of chain formation.

The sample cell filled with liquid composite was placed under the microscope. An alternative voltage was then applied across the electrodes using a power amplifier (Trek 30 – 20A) connected to a waveform generator (TTi TGA12104). In the initial state, the fillers are randomly dispersed, and at  $t = 0$  s the voltage was applied (and therefore the electric field). Chain formation started and pictures were taken with the microscope.

The experimental protocol follows two distinct steps. In a first step, an ac electric field of 600 V/mm is applied on the sample at room temperature. In order to find the proper electrical parameters, i.e. targeting

the minimum frequency with no visible fluid turbulence (which could degrade the chaining process), we proceeded as proposed by Wilson *et al.* [129] by direct optical observation. As a result, a frequency of 1 kHz was chosen to avoid electrohydrodynamic effects. After 600 s, the temperature was increased to 70 °C to start the curing process.

#### IV.1.c. Experimental setup and protocol for dielectric monitoring of the chaining

The sample cell for the measurement of the composite dielectric properties is composed of two flat stainless steel substrates (0.8 mm thick, 33 × 33 mm) that serve as electrodes. A polyimide tape (Kapton) (two layers of 50 μm) placed at the four corners controls the inter-electrode gap. A diagram of the cell is presented in Figure IV-6.

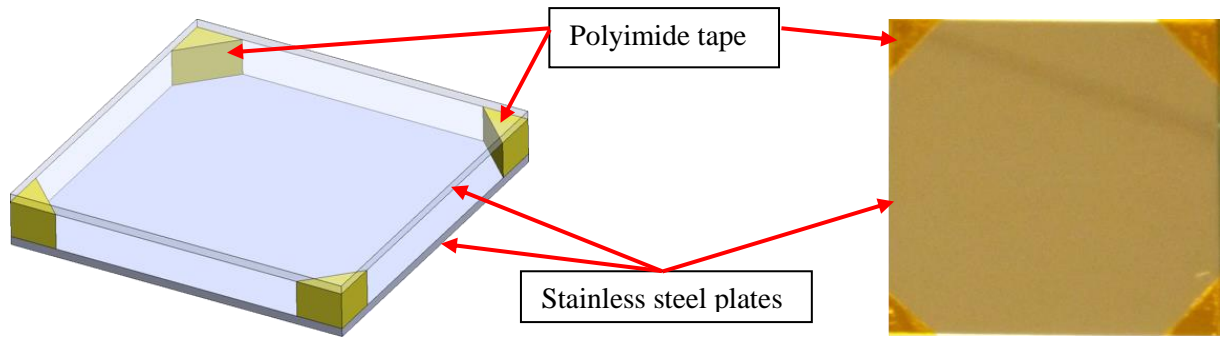


Figure IV-6: Sample cell diagram (left) and picture (right). The dimensions of the stainless-steel plates are 33×33 mm.

Theoretically, the total polyimide tape thickness is 100 μm. Nevertheless, among several samples an average dispersion in the inter-electrode distance of 7.5% was observed. For a correct extraction of permittivity, it is necessary to know the precise distance between the electrodes. This was achieved by calibrating each sample cell before filling the inter-electrode gap with the epoxy/BaTiO<sub>3</sub> mixture. The capacitance of the cell is given by:

$$C = \frac{\epsilon_0 \epsilon_{air} S}{e} \quad (38)$$

where  $\epsilon_0$  is the vacuum permittivity,  $\epsilon_{air}$  the relative permittivity of air ( $\epsilon_{air} = 1$ ),  $S$  the electrode area (33×33 mm), and  $e$  the inter-electrode gap. As the electrode area is known, the capacitance value leads directly to the accurate distance between the electrodes. Two hypotheses were drawn: the field fringing at electrode edges is negligible (the estimated error is less than 0.5% for a permittivity range from the neat epoxy to the highest filler content investigated ( $\epsilon = 15$ )), and the polyimide tape spacer capacitance was not considered (due to their small area). The polyimide spacers induce a reproducible error of 3.5% in permittivity measurement.



Once calibration is performed, the mixture is poured directly on the bottom electrode, then the sample cell is sealed with the second stainless steel plate. To avoid the presence of bubbles which would alter the results (especially with high viscosity resin) the protocol technique to close the cell was used:

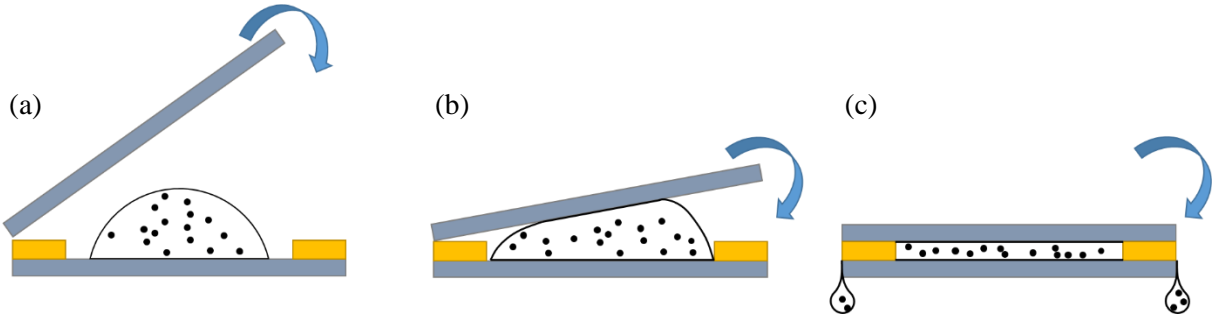


Figure IV-7: Method for closing the cell to avoid bubbles. (a) The liquid composite is poured on the middle of the bottom plate, (b) the upper plate is positioned with an angle on top of the bottom one, (c) the sample cell is closed and some of the liquid composite flows out of the cell from the sides.

In the last step, when closing the cell, is it important for some mixture to flow from all four sides of the cell to ensure that it is entirely filled.

When the sample cell is filled and closed, it is placed into a sample cell holder providing the electric contact for the dielectric spectroscopy measurements. It also ensures that the cell remains closed during the experiment, thanks to springs holding the cell in position. The sample cell holder was placed into an oven set to 30 °C and connected to an HVB 300 high voltage dielectric spectrometer from Novocontrol Technologies. An ac electric field of 600 V/mm at 1 kHz was applied to the samples. Simultaneously, the dielectric properties (i.e. complex permittivity) were measured versus time, before and during the curing. The experimental setup is shown in Figure IV-8.

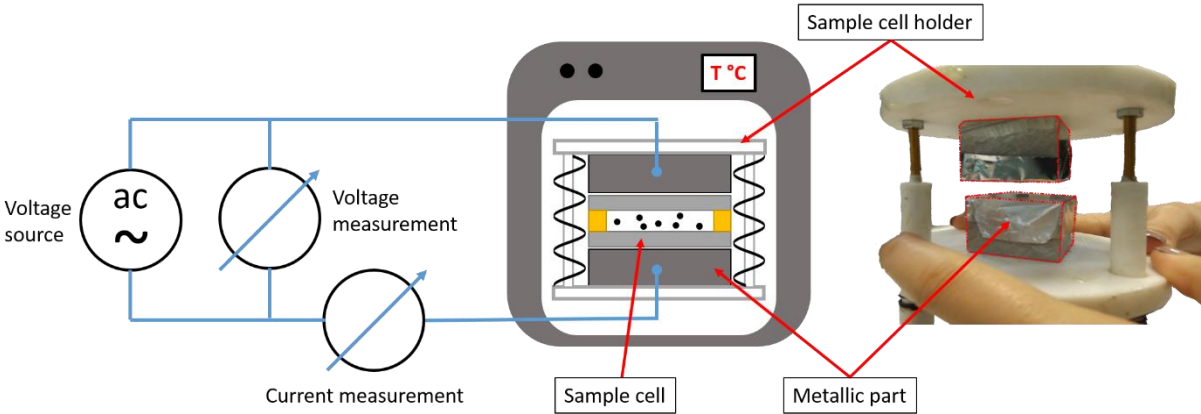


Figure IV-8: Experimental setup for on-line dielectric spectroscopy (left) and sample cell holder (right). The metallic parts of the sample cell holder allow electric contact and pressing the sample cell.

## IV.2. Monitoring the chain formation

### IV.2.a. Evolution of the dielectric properties of the neat epoxy

The neat epoxy curing without filler was monitored thanks to dielectric property measurements to obtain the reference characteristics of the matrix. It is important to know the behavior of the neat resin to distinguish the effect of chaining from curing. Figure IV-9 shows the permittivity and dielectric loss changes of the neat epoxy (resin: Epikote 816B, hardener Epicure 113, Mitsubishi Chemical Co.) during the curing process at 70 °C. This typical profile can be found in literature for several epoxies [155], [156].

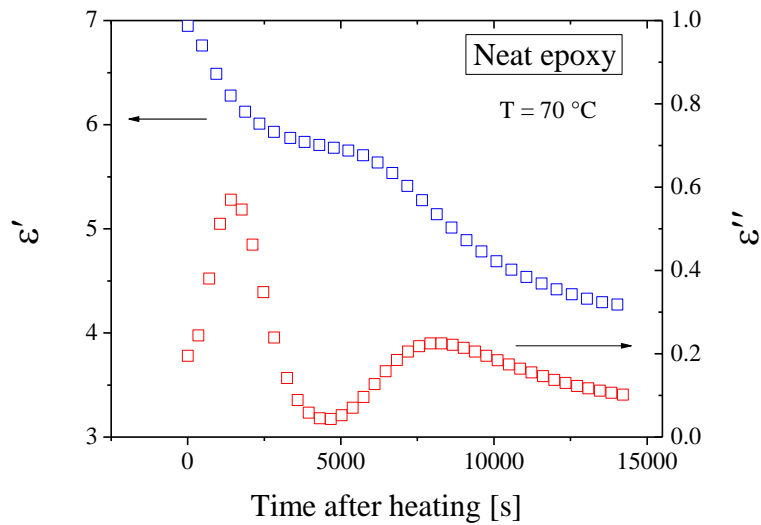


Figure IV-9: Permittivity and dielectric losses changes of neat epoxy during curing, after setting the temperature to 70 °C.  $E = 600 \text{ Vrms/mm}$  and  $f = 1 \text{ kHz}$ .

The first peak of dielectric losses around 1500 s is most likely related to viscosity changes, with its maximum corresponding to the viscosity minimum. The minima of the dielectric losses occurring at 4800 s most likely corresponds to matrix vitrification [155]. According to Kortaberria [157], the second peak around 8150 s is due to  $\alpha$  relaxation (glass transition) of the network-forming epoxy system.

### IV.2.b. Combined optical and dielectric monitoring of particle chaining at low filler content

In order to correlate chain formation to changes in the composite's dielectric properties, optical observation of chain growth is performed in parallel to monitoring the composite dielectric properties. As discussed in section V.1.b, the major drawback of optical observation is its limitation to low filler contents. Due to this limitation, the mixture studied here had 0.25 vol% of filler content. Figure IV-10 shows the optical images and Figure IV-11 the associated measured permittivity at 30 °C. At 600 s, a few tens of  $\mu\text{m}$ -long chains were observable, which is relatively short compared to the 1 mm gap

between the electrodes. Here also, the impact of chain formation is observable through the slight increase in permittivity. It is remarkable that this measurement is accurate enough even at very low filler content.

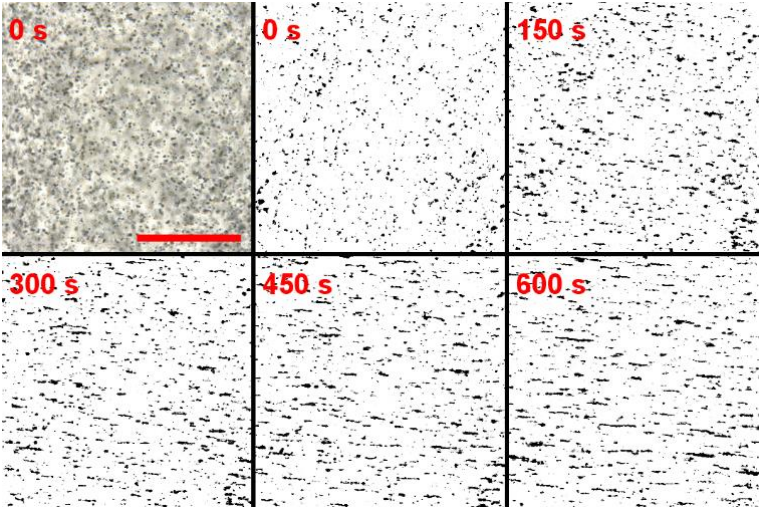


Figure IV-10: Optical microscopy images during chain formation under electric field before heating.  $E = 600\text{V/mm}$ ,  $f = 1\text{ kHz}$ ,  $\text{BaTiO}_3$  filler content = 0.25 vol%. The top left image corresponds to the untreated image at  $t = 0\text{ s}$ . The scale bar is 100  $\mu\text{m}$  long.

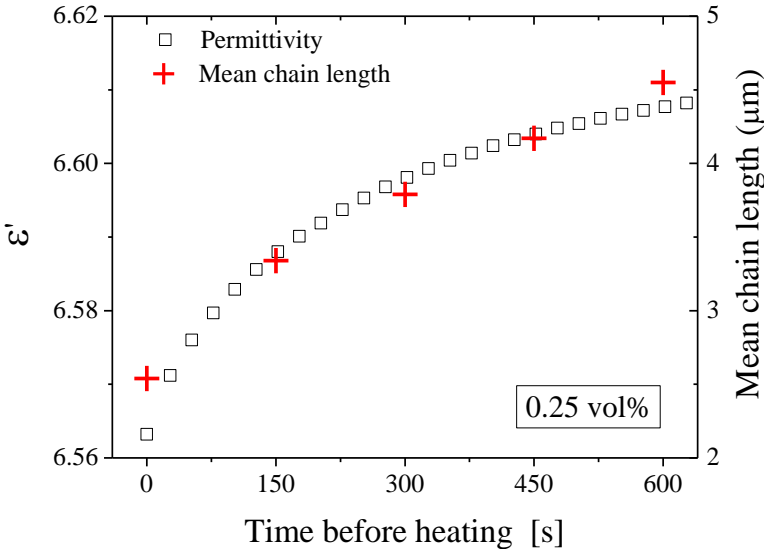


Figure IV-11: Permittivity evolution and mean chain length of epoxy/ $\text{BaTiO}_3$  (0.25 vol%) during chain formation at  $30^\circ\text{C}$ .  $E = 600\text{ V/mm}$ ,  $f = 1\text{ kHz}$ . The crosses correspond to the times when images were taken in Figure IV-10.

The temperature is set to  $70^\circ\text{C}$  after 600 s; the system reached the setpoint in about 2000 s. The results of optical and dielectric measurements are presented in Figure IV-12 and Figure IV-13, respectively. Between 120 and 660 s after the temperature increase, the longest chains reach more than 300  $\mu\text{m}$ . It is most likely that the chains grew faster due to a decrease in epoxy viscosity. Permittivity behavior does not reflect chain formation because the decrease in the effective permittivity is controlled by the dynamics of matrix dielectric permittivity during curing. This change corresponds to that of the neat epoxy, as shown in Figure IV-9. After 1380 s, the interaction between chains starts to deform them,

leading to the formation of columns of particles. Some chains are thus no longer perfectly aligned in the direction of the electric field. Between 4560 s and 9360 s, the epoxy resin crosslinks and no further particle movement is visible.

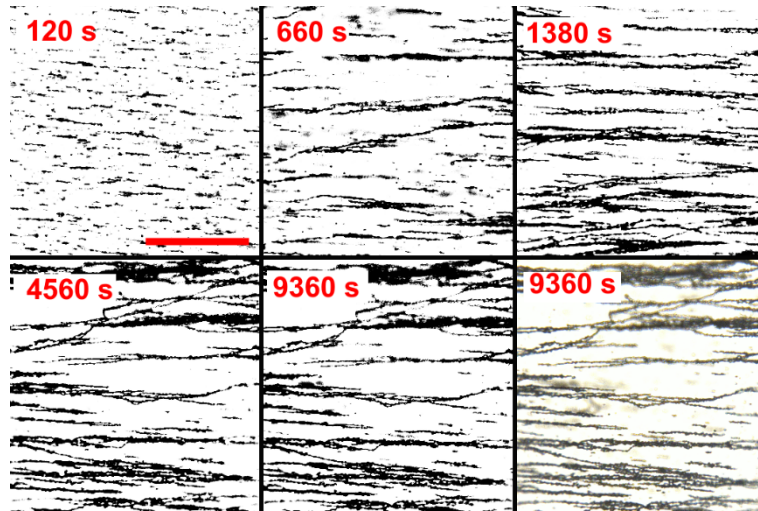


Figure IV-12: Optical microscopy images during BaTiO<sub>3</sub> chain formation under electric field after setting the temperature to 70 °C. The bottom right image corresponds to the untreated image. The scale bar is 100 μm long.

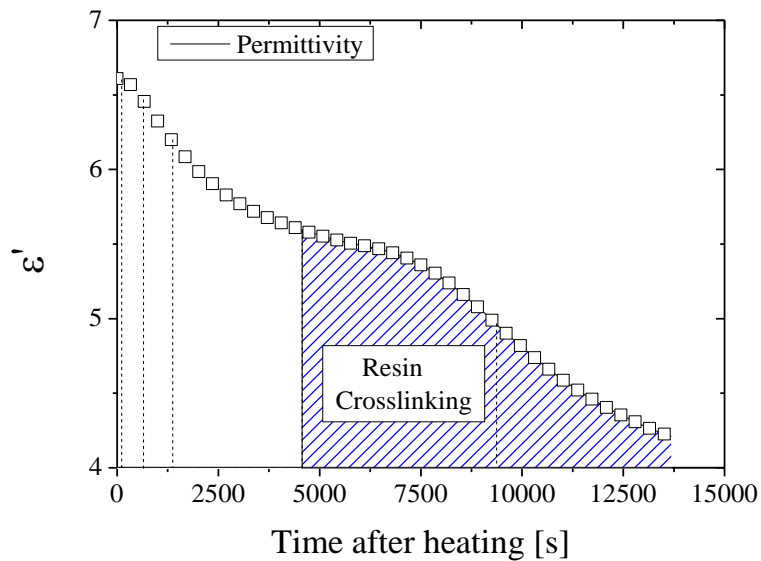


Figure IV-13: Permittivity changes during chain formation versus time after heating to 70 °C.  $E = 600$  V/mm,  $f = 1$  kHz. Epoxy filled with BaTiO<sub>3</sub> (0.25 vol%). The dashed lines correspond to the times when images were taken in Figure IV-12.

#### IV.2.c. Dielectric monitoring at high filler contents

It is worth noting that dielectric losses could be a relevant marker for chain formation. Like permittivity, dielectric losses are a contribution of both the matrix and the fillers. However, during curing, the changes in matrix dielectric losses are highly related to the ongoing chemical reactions, and vary strongly. Since

the epoxy presents higher dielectric losses than the ceramic particles during curing, the main contribution to the total losses comes from the polymer, thus preventing the extraction of particle chaining impact from this property. Consequently, chain formation through electric cure monitoring has focused only on the changes in the real part of permittivity. Permittivity results are presented in Figure IV-14 and Figure IV-16. At  $t = 0$  s, before electric field application, the higher volume fraction leads to increased permittivity values. This is a well-known result, even if most studies are performed for higher filler volume fractions [158]. The impact of chaining is visible in Figure IV-14. Under the ac electric field, permittivity dynamics differ according to the volume fraction. In fact, the more “loaded” the mixture, the faster the increase in permittivity. This is related to two phenomena: i) the particles being closer to each other when the volume fraction increases, thus leading to stronger dielectrophoretic forces; and ii) the distance for a particle to reach the neighbor one is shorter, so the chains can grow faster. These results agree well with the results in literature [70], when monitoring the current density.

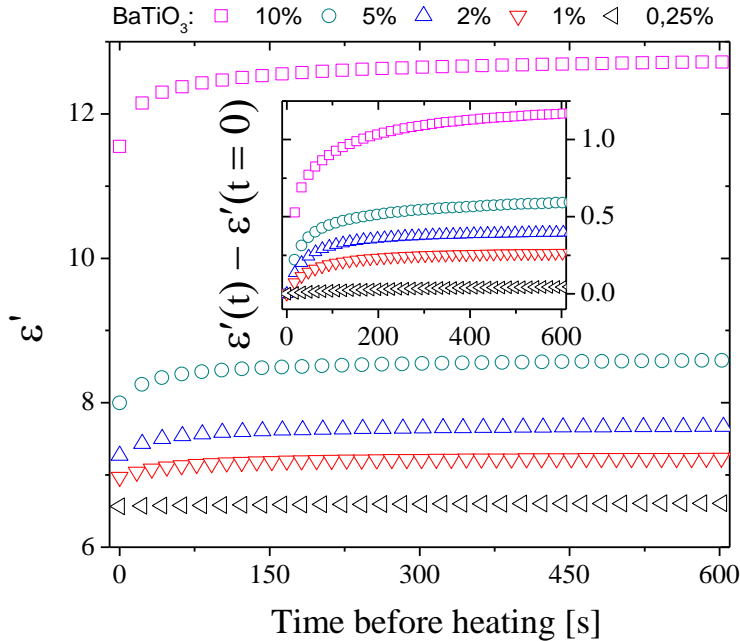


Figure IV-14: Permittivity changes of the composite as a function of time under electric field at 30 °C. The inset shows the difference between measured permittivity and initial permittivity.

In order to study the impact of particle permittivity on chaining dynamics and dielectric property changes, the same measurements were performed with  $\text{SrTiO}_3$  particles as fillers. The results are shown in Figure IV-15 (a). The quantitative impact is clear: the particle with the highest permittivity ( $\text{BaTiO}_3$ ) leads to higher permittivity for the composites. However, this representation does not allow accurate comparison of the dynamics due to the large shift in permittivity. This is why the normalized permittivity is plotted in Figure IV-15 (b). From that figure, we can observe that permittivity changes are slightly faster in the case of  $\text{BaTiO}_3$  composites. The inset, showing the derivative of normalized permittivity, also confirms the faster rise of permittivity. Intuitively, this can be explained by the higher permittivity

(and so a higher Clausius-Mossotti factor) of this particle compared with SrTiO<sub>3</sub> particles. However, other factors are involved, such as particle size and density. Further development in the chapter describing the particle chaining model seeks to answer this question (section V.2).

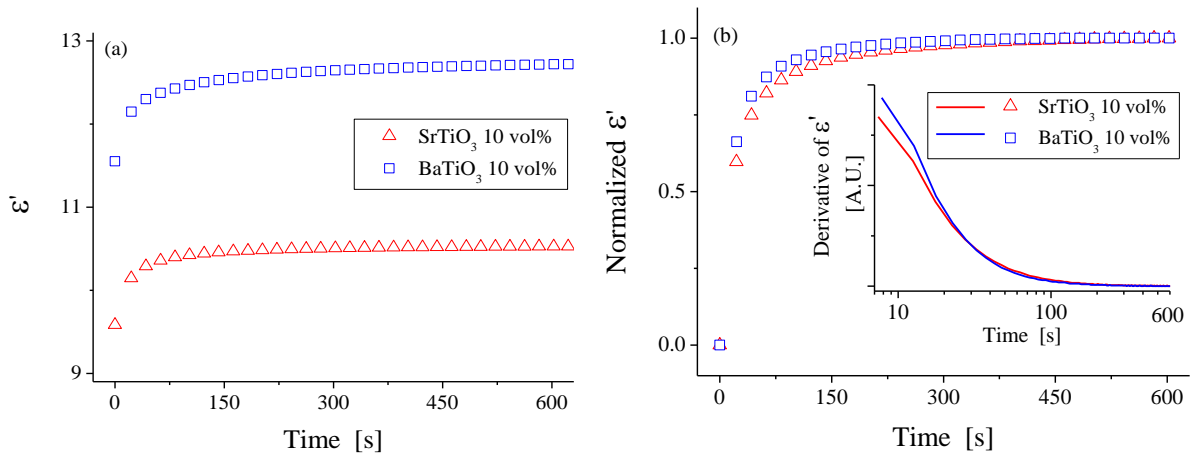


Figure IV-15: Permittivity changes of epoxy/BaTiO<sub>3</sub> and epoxy/SrTiO<sub>3</sub> composites as a function of time under field at 30 °C: (a) plot of absolute permittivity and (b) plot of normalized permittivity. The inset shows the derivative of normalized permittivity.

Figure IV-16 shows that, when increasing the temperature to solidify the composite, the same dynamics are observed as for neat epoxy. An initial decrease in permittivity is followed by a plateau and finally, a decrease when reticulation is complete. The plateau is reached after approximately 4000 s, which corresponds to mixture vitrification, as observed with optical microscopy.

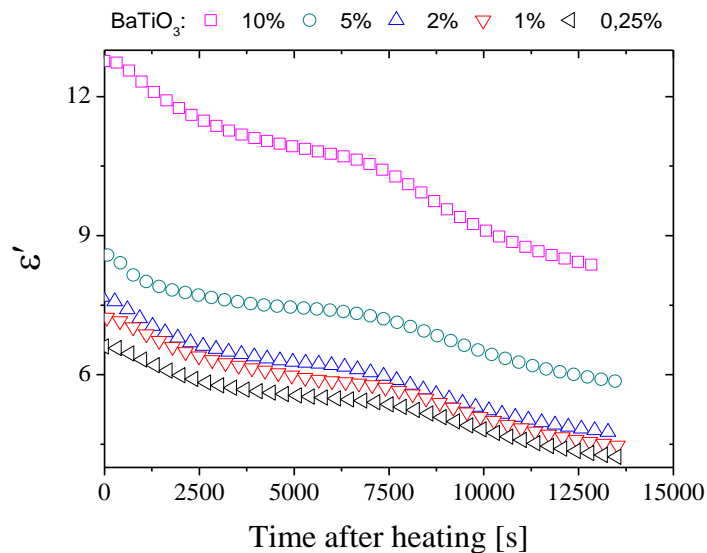


Figure IV-16: Permittivity changes of the composite as a function of time under electric field after setting the temperature to 70 °C.

These results on dielectric properties changes while chaining point out the chaining time as a key parameter for controlling final composite properties. Control should be achievable if the other

parameters (matrix viscosity, electric field, frequency and filler content) remain unchanged. In order to verify this assumption, we studied the impact of chaining duration on final composite permittivity. A set of experiments is proposed in the next section to verify these statements.

### IV.3. Characterization of the impact of the chaining

#### IV.3.a. Influence of the process on the dielectric properties

It was discussed in the previous section that permittivity is a relevant marker to follow particle chain formation. The main interest of monitoring chain formation is to enable optimizing and tailoring composite properties by controlling the curing process and electric field application. As seen in Figure IV-14, the main impact of chaining on permittivity occurs at the very beginning. Moreover, the permittivity change is non-linear with respect to chaining time. In order to verify this assumption, the four different processes shown in Figure IV-17 were investigated. Process 1 provides a reference isotropic material; processes 2, 3, and 4 are intended to study the impact of short, medium, and long chaining durations, respectively. The characterization results plotted in Figure IV-18 are in good agreement with our assumptions. After only 60 s of chaining under an electric field, an increase of 22 % in permittivity was already obtained, while it is necessary to chain over 19,000 s (without increasing the temperature) to obtain a gain of 37%. Increasing the chaining duration leads to increased permittivity of the solid material.

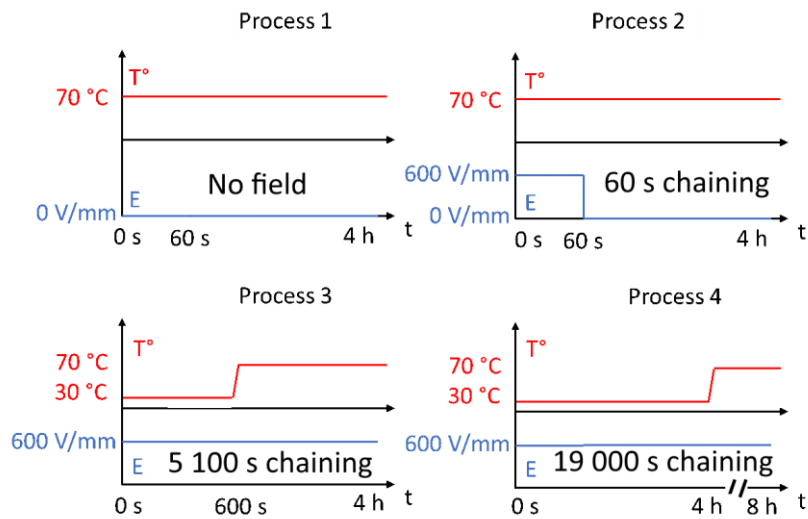


Figure IV-17: Process characteristics. The base mixture is epoxy filled with BaTiO<sub>3</sub> (10 vol%). The first process corresponds to the homogeneously dispersed composite where no field was applied.



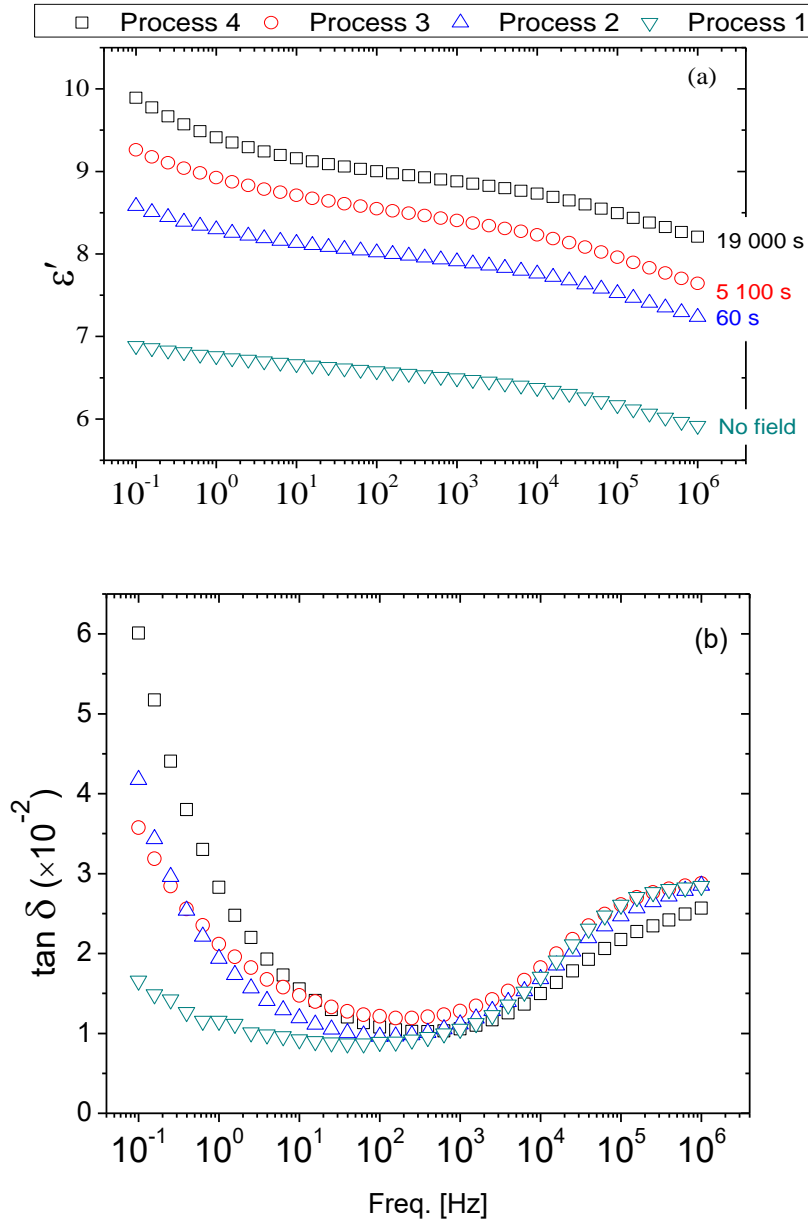


Figure IV-18: Permittivity (a) and loss factor (b) versus frequency measured for the different processes.

It is interesting to note that the losses are not modified significantly above 10 Hz. The impact of chaining on the loss factor is only observable at low frequencies ( $< 10$  Hz), whereas it increases compared to the homogeneously dispersed composite. At these low frequencies, the increase in losses is most likely related to the DC conduction in the material. It is possible that the chains of BaTiO<sub>3</sub> particles increase the DC conduction phenomenon due to the possible formation of a “percolation-like” network. From 200 Hz to 1 MHz, the loss factor of the four different processed materials is nearly the same, ranging from  $1 \times 10^{-2}$  to  $3 \times 10^{-2}$  at room temperature.

Two preliminary conclusions may be drawn from sections IV.2.c and V.3.a. The first is that process optimization may be achieved thanks to the online monitoring of permittivity where the increase in



permittivity is non-linear. Note that only a small gain in permittivity is obtained by applying the electric field for much longer times. The second is that by adjusting the chaining time, even empirically, one can also tailor the permittivity of the final material. The latter is true as long as the curing process does not affect filler structure within the composite, meaning that two conditions should be fulfilled simultaneously: the permittivity of the fillers and the matrix are to be different ( $K \neq 0$ ), and the electrohydrodynamic effects (field-induced turbulence) should be negligible compared to dielectrophoretic forces.

*IV.3.b. Influence of the filler content on the dielectric properties*

As seen in the previous section, the electric field allows controlling final composite properties. Filler content is another key parameter for tailoring these properties. In order to study this dependence on the dielectric properties on the volume fraction of particles, composites were prepared following the processes 1 and 3 (described in section IV.3.a), and from 0 to 20 vol% of BaTiO<sub>3</sub> particles. The measured permittivity spectrum of the composites is plotted in Figure IV-19.

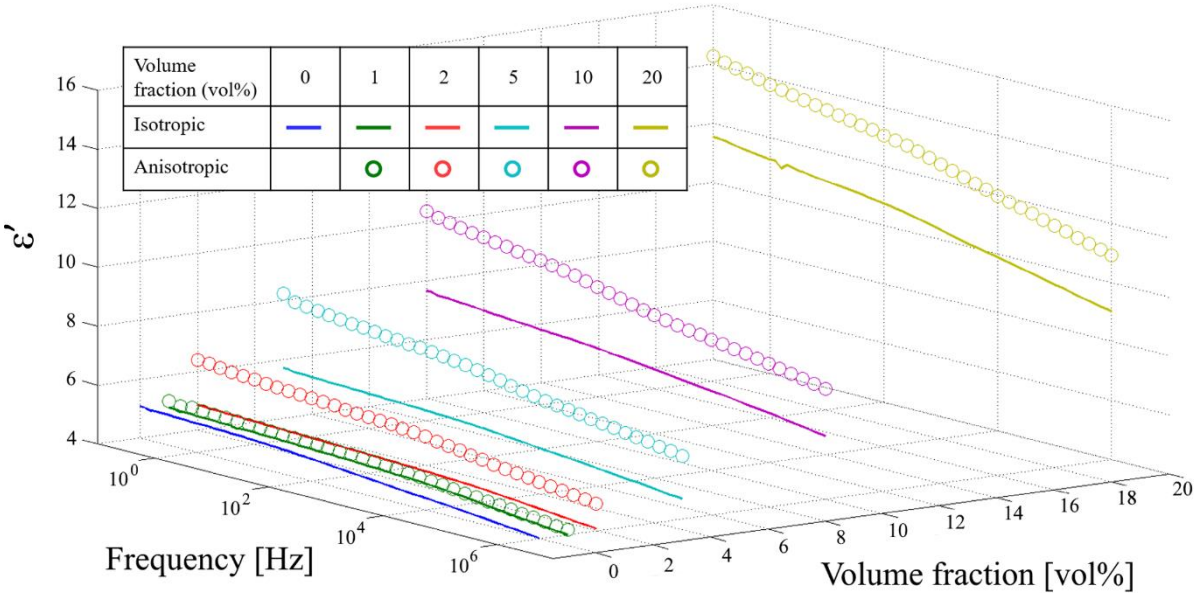


Figure IV-19: Dielectric permittivity spectra of isotropic and anisotropic epoxy/BaTiO<sub>3</sub> composites elaborated using process 3.

As expected, the higher the volume fraction, the higher the permittivity. This holds over the full range of frequency measured ( $10^{-1} - 10^6$  Hz) for both isotropic and anisotropic composites. The beneficial impact of chaining is also visible on permittivity for composites above 2 vol%. The plots of permittivity and losses at 1 kHz in Figure IV-20 (a) and (b) offer a finer comparison between isotropic and anisotropic composites.

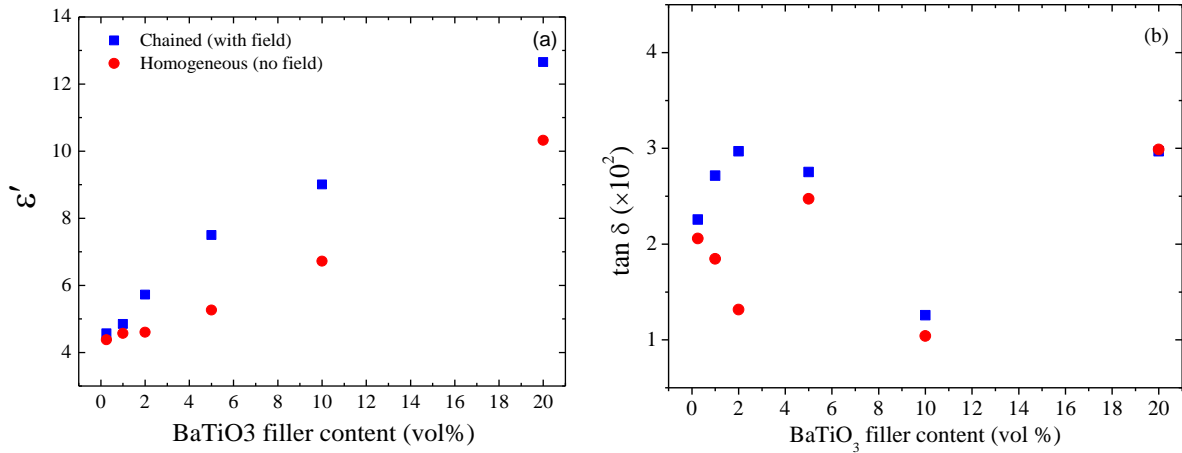


Figure IV-20: (a) Dielectric permittivity and (b) loss factor of homogeneous and chained (process 3) epoxy BaTiO<sub>3</sub> composites at 1 kHz versus BaTiO<sub>3</sub> filler content.

For a given volume fraction, all the anisotropic composites present higher permittivity than their isotropic equivalents. Measured losses are quite encouraging (especially for the case of energy storage applications), as particle chaining does not seem to have much impact. All the composite losses are below  $3 \times 10^{-2}$ . However, it seems that particle chains increase the losses compared to the isotropic composites. A more detailed study of composite losses can be found in Appendix B. Investigations on the composites dielectric strength are reported in Appendix C.

#### IV.3.c. Observation of the composite structures

The optical microscopy images performed on cured composites are shown in Figure IV-21. The difference between composites with and without aligned fillers is visible from the top-view images (cf. Figure IV-21 (a)). The anisotropic composites present transparent areas around the chains. The presence of chains is clear from the cross-section views. Moreover, it is possible to observe a difference in the structure between the 10 vol% composite and the less-filled composites.

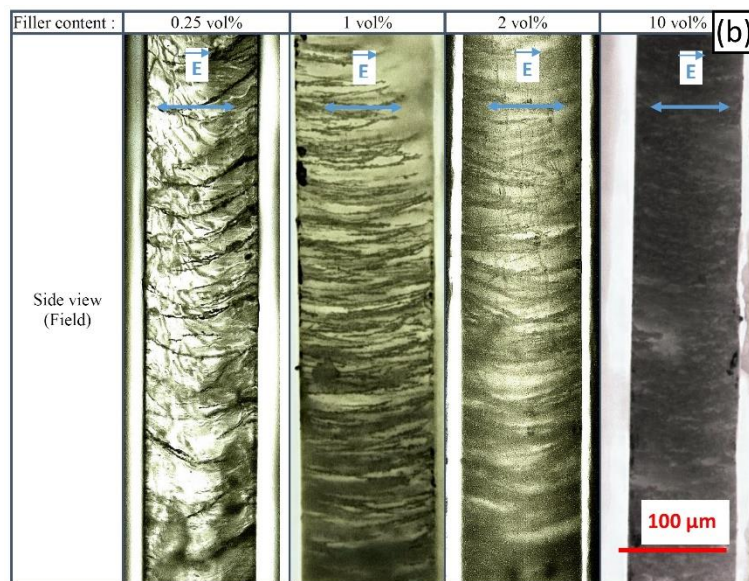
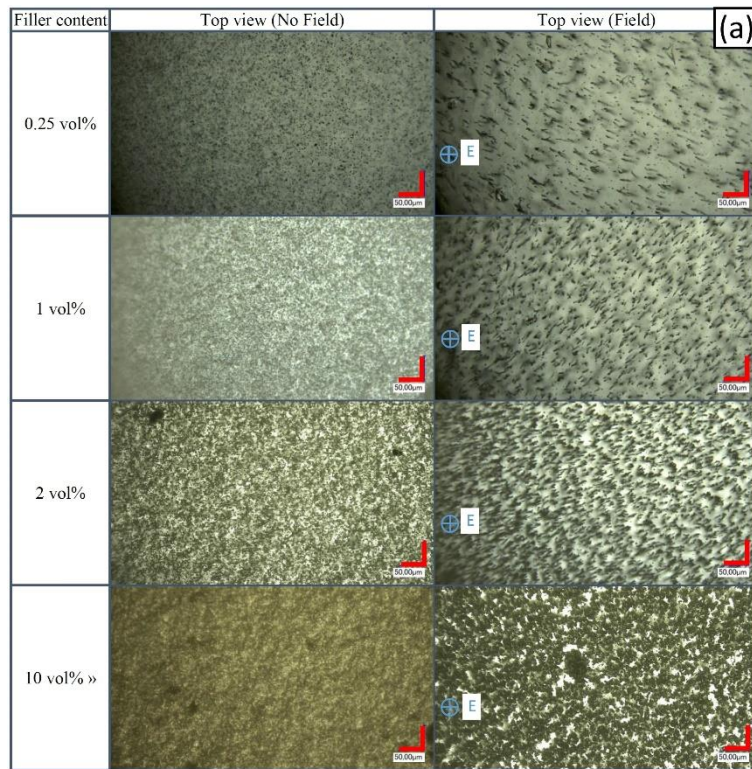


Figure IV-21: Optical microscopy images on cured composites. Crossed scale bars correspond to 50  $\mu\text{m}$ . Samples with field prepared with process 3.

The images of the 0.25, 1 and 2 vol% composites in Figure IV-21 (b) present bent chains, not perfectly aligned in the direction of the electric field. To confirm this behavior, the 1 vol% sample was observed by X-ray tomography (Nanotom - GE Sensing).

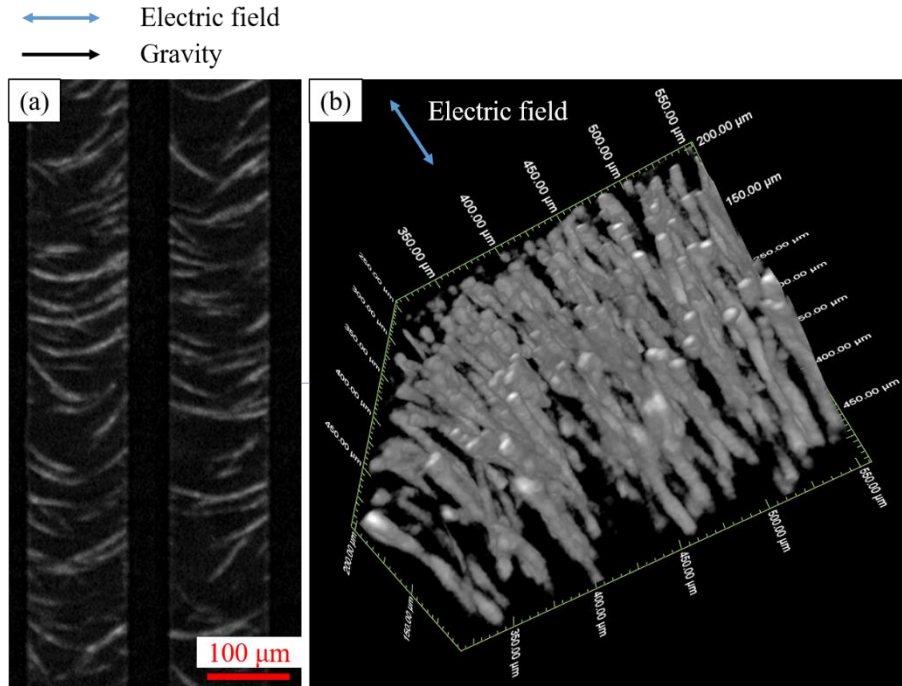


Figure IV-22: X-ray tomography images of epoxy/BaTiO<sub>3</sub> composite at 1 vol%, made with process 3. (a) Cross-sections of the composite at two different locations, (b) 3D image of the chains.

The tomography images in Figure IV-22 (a) confirm the chain structures observed with optical microscopy. The gravity force could explain the chain bending. This image also confirms the absence of sedimentation during the process, as there is no layer of particles visible on the sides of the sample. The three-dimensional image of the composite in Figure IV-22 (b) gives a good representation of how the chains are located inside the matrix. Globally, it can be seen that the chains are spaced and do not touch each other. This type of image provides a very interesting point of comparison when we corroborate the structure obtained experimentally and by simulation in section V.1. However, it should be pointed out that the particle size is very close to the tomograph resolution limits ( $\approx 0.7 \mu\text{m}/\text{voxel}$ ). This leads to imprecision in the chain imaging. That is why the chains appear thicker, which is easily noticeable on the 3D plot. The effect is also observable by comparing the chain thickness from the X-ray tomography images in Figure IV-22 (a) with the microscope image in Figure IV-21 (b).

An attempt was also made to observe a composite filled with 10 vol% of BaTiO<sub>3</sub>. However, digital processing did not render usable images.

#### IV.4. Conclusions and perspective

A novel, non-optical, and concentration-independent method for the online monitoring of chain formation is presented in this chapter. The measurement of the changes in the dielectric properties during the composite structuration proved that permittivity is closely correlated to chain formation, validating

---

dielectric permittivity as a relevant marker. This marker is used as a comparison tool for the experimental results and model outcomes.

It was also demonstrated that the control of final composite properties was possible by adapting the process on the basis of the knowledge regarding permittivity change dynamics. The impact of anisotropy on composite dielectric properties was measured, showing an increased permittivity and comparable losses. Moreover, the agreement between the structure and the properties was confirmed thanks to optical microscope images and a 3D X-ray tomography imaging method. The tomography mainly provides interesting information about chain structure at low filler content. It also enables observation of the three-dimensional chain distribution inside the matrix.

The importance knowing chaining dynamics is confirmed. A predictive model, which would give access to that knowledge, would certainly be of great interest for optimizing the elaboration process. The next chapter studies the development and outputs of a particle-chaining model. We aim to develop a model that makes it possible to describe chaining dynamics. This would open the path to the predictive tailoring of field-assisted anisotropic composites.

The inspiration for forthcoming enhancement of anisotropic composites might be found in the field of electrorheological fluids. Research works on this topic effectively reached a dead-end when no solution was found to improve liquid performance, but recently, the so-called “giant electrorheological effect” paved the way for exciting perspectives [62]. This solution is based on a urea treatment of the filler surface for better handling at the particle interfaces.



# Chapter V

Modeling The Chain Formation

And The Structure Impact On The Composite Properties

## V. MODELING THE CHAIN FORMATION AND THE STRUCTURE IMPACT ON THE COMPOSITE PROPERTIES

This chapter models particle chaining under an electric field. The purpose of this model is to predict the chaining dynamics based on measurable experimental parameters as input. The proposed model is based on calculating the DEP force from dipolar interactions as described in section II.4. First, the simulated filler structures are studied and compared to experimental results. Then, a method to estimate the simulated composite permittivity and changes based on FEM are reported. Lastly, the simulated permittivity is compared to experimental results to verify model accuracy and robustness.

### V.1. Dynamics of particle chaining

As chaining dynamics is the enabling factor for tailoring anisotropic composites, we intend to predict it through the modeling of chain formation.

#### *V.1.a. Study of the chain structure as a function of the filler content*

In our work, changes in chain structure were tracked and compared to experiments. The numerical model has an initial state where the fillers are randomly dispersed within the medium, corresponding to an isotropic composite. The parameters taken for the fillers are those of BaTiO<sub>3</sub>, and for the matrix, those of the epoxy resin A (i.e.  $\nu = 480$  mPa.s,  $\epsilon = 7.2$ ). The ac electric field is set at 600 V/mm, the frequency of the measurement of the dielectric parameters was 1 kHz. The random distribution of particles in the initial state for 1 vol% (500 particles) is represented in Figure V-1. At  $t_0$ , chain formation starts as soon as the electric field is applied. The particle positions over time are represented in Figure V-2, Figure V-3, and Figure V-4 for 1, 5, and 10 vol% of BaTiO<sub>3</sub> fillers, respectively. The system shows rapid evolution between 0 and 5 s, the period during which most of the chains are formed. This rapid evolution of filler structure is in agreement with observations and measurements reported in Section IV.2. In the last stage, only chain movements are observed, rather than isolated particle migration.



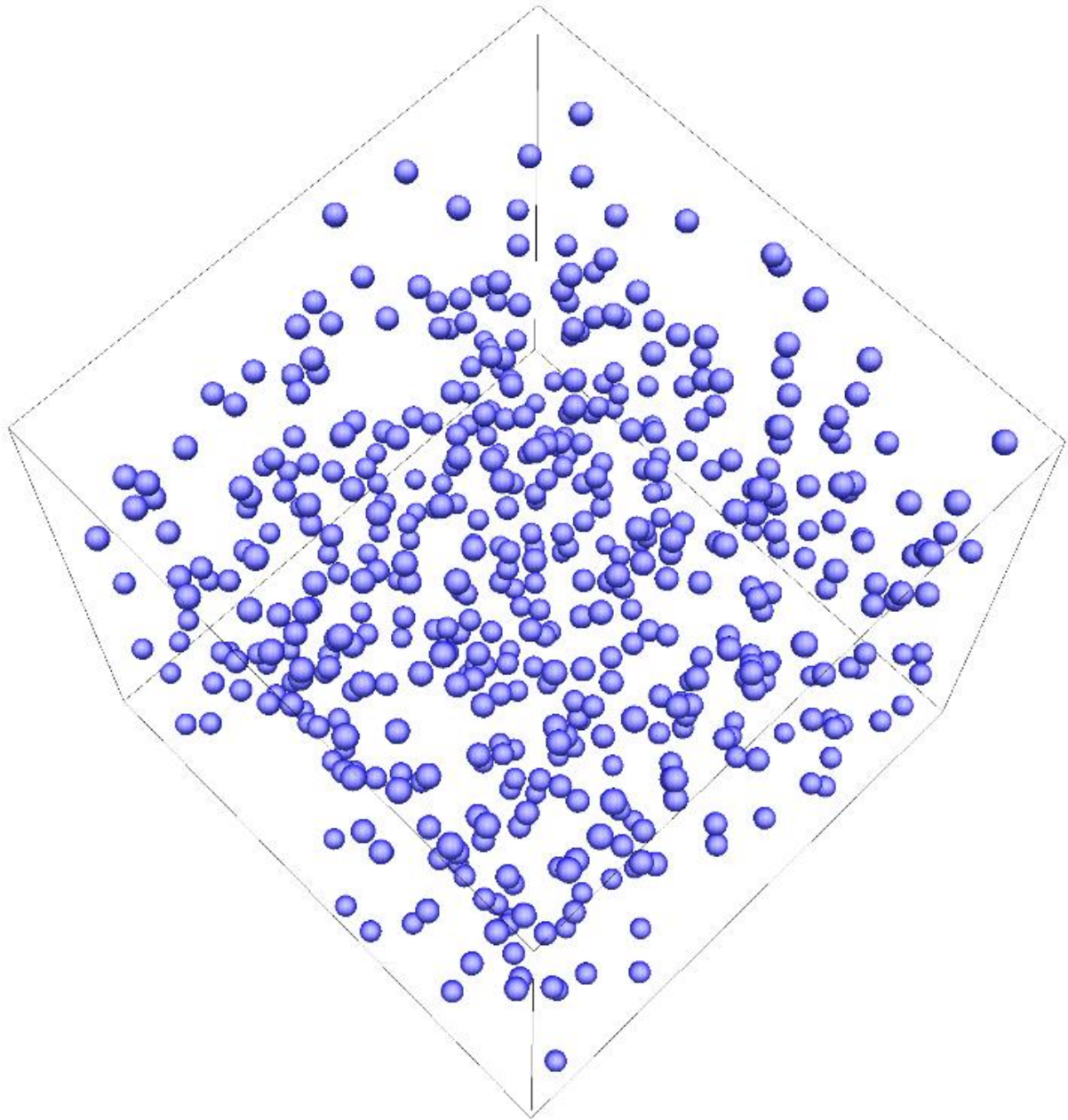


Figure V-1: Initial state 1 vol%, randomly dispersed BaTiO<sub>3</sub> particles of 0.66 μm in diameter in liquid epoxy resin. The number of particles simulated is 500 (n = 500).

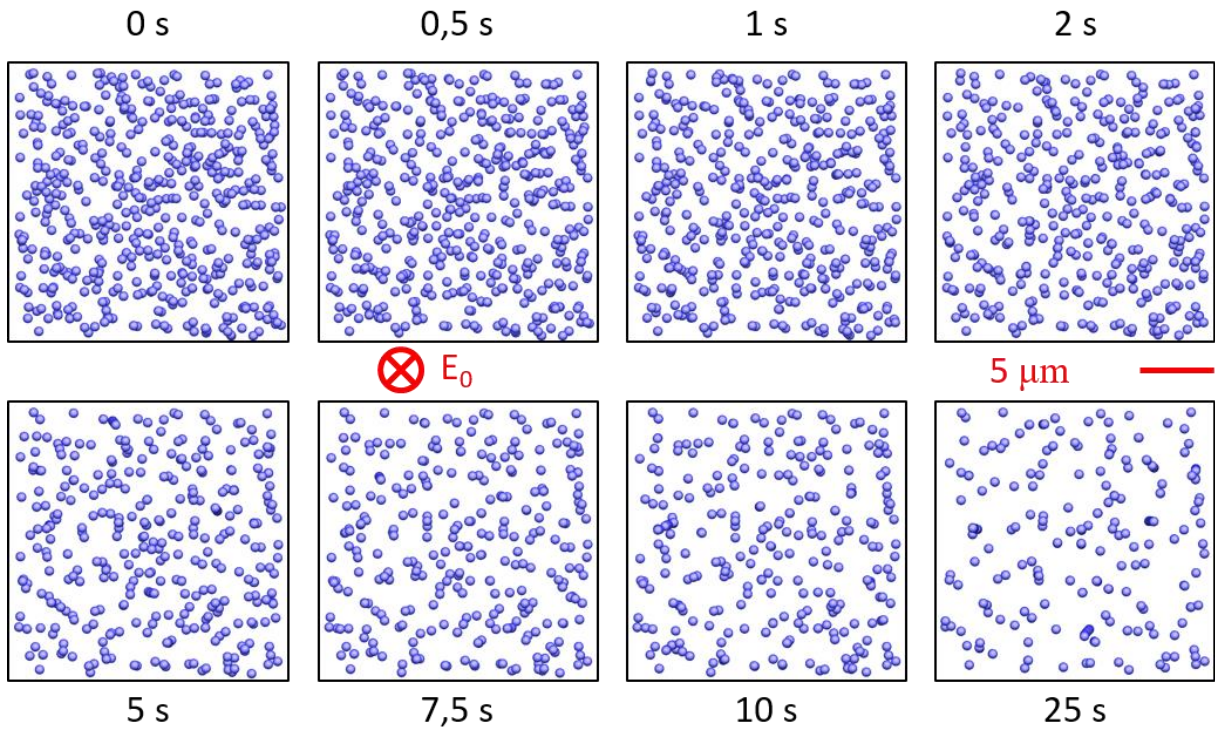


Figure V-2: Top view of filler structure evolution for 1 vol% of BaTiO<sub>3</sub> in epoxy resin no. 2.

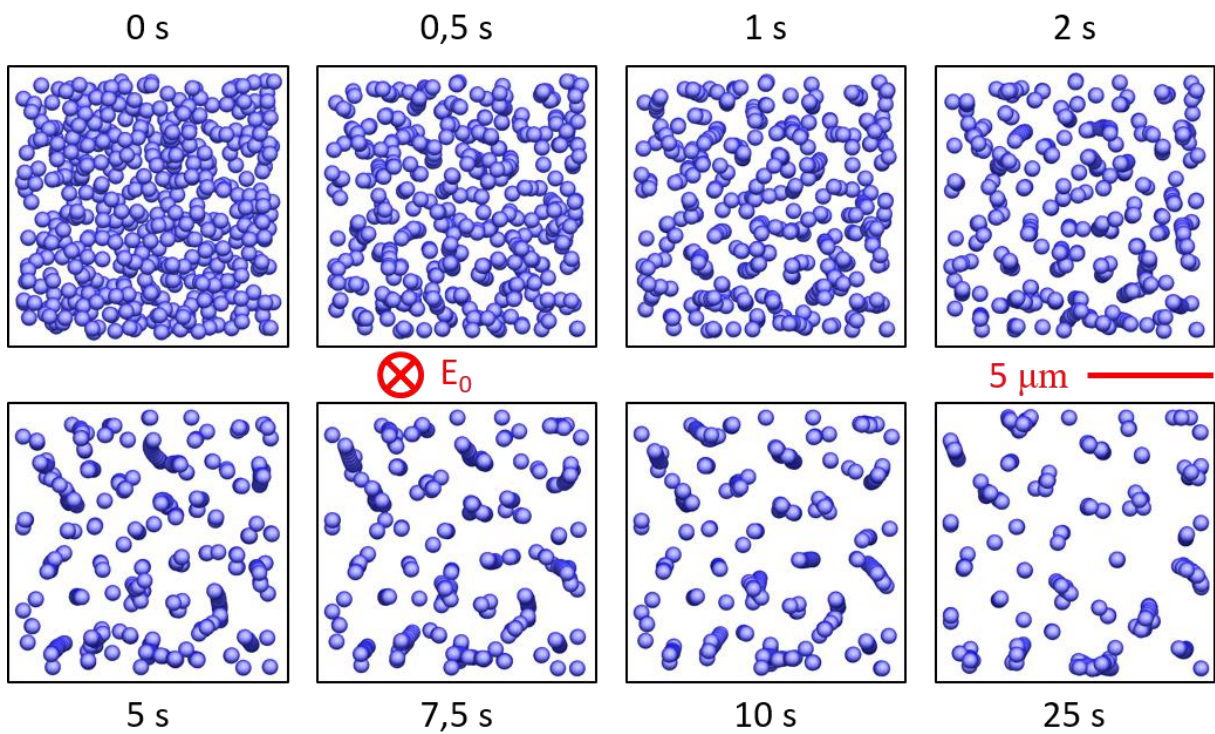


Figure V-3: Top view of filler structure evolution for 5 vol% of BaTiO<sub>3</sub> in epoxy resin no. 2.



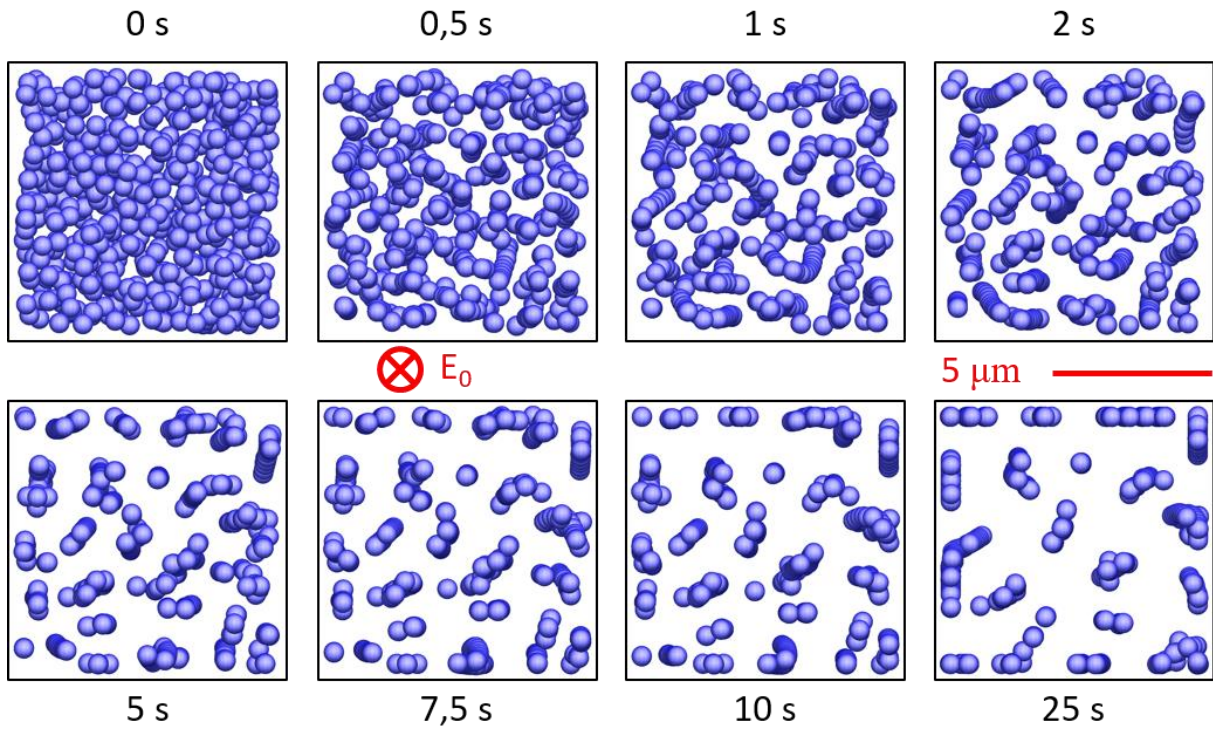


Figure V-4: Top view of filler structure evolution for 10 vol% of BaTiO<sub>3</sub> in epoxy resin no. 2.

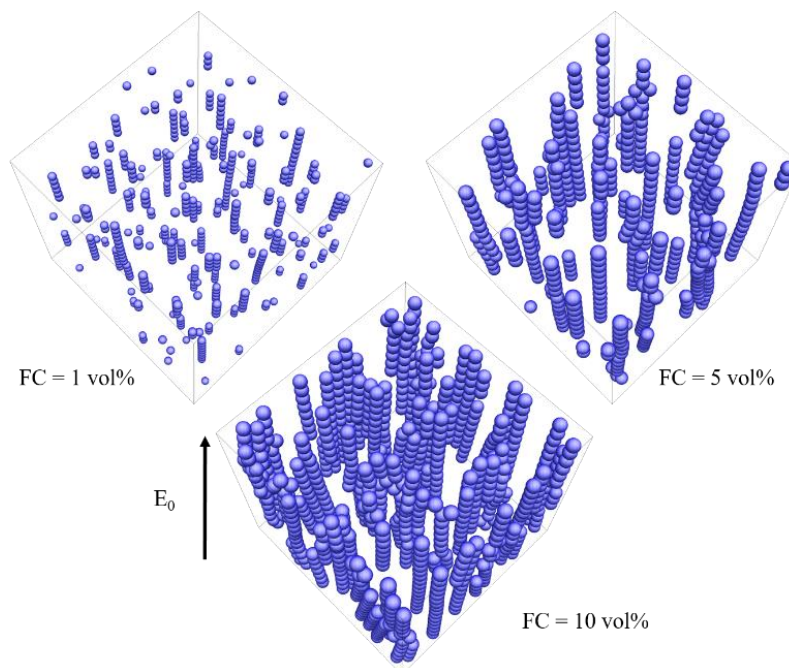


Figure V-5: Filler structures after 25 s of electric field for different initial filler contents. Particles are spherical BaTiO<sub>3</sub> of 0.66 μm in diameter. Resin has a viscosity value of 480 mPa.s and permittivity of 7.2. The applied ac electric field is 600 V/mm and  $n = 500$ .

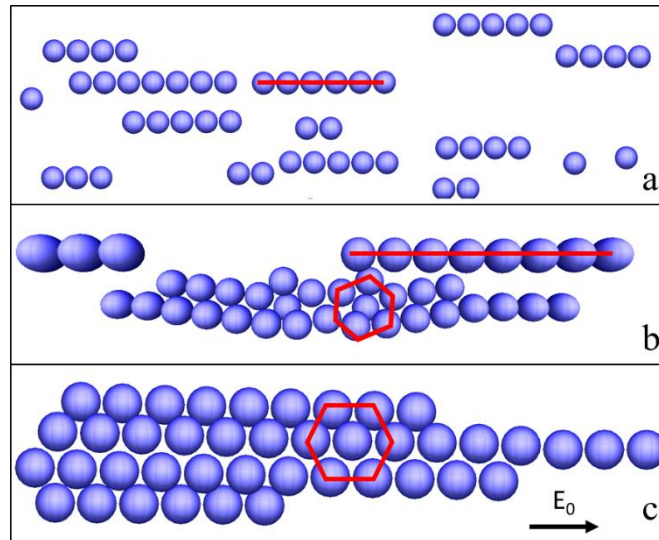


Figure V-6: Extraction of structures formed after 25 s for different filler contents: (a) 1 vol%, (b) 5 vol% and (c) 10 vol%.

After 25 s, significant differences between the filler structures can be observed in Figure V-5 and Figure V-6, according to the volume fraction. For the lowest volume fractions (i.e. 1 vol%), particles form isolated chains 1 particle thick. For 10 vol%, the structure is composed of sheets and columns of particles. In these particular structures, the particles are stacked in hexagonal close-packing corresponding to a more stable configuration. The 5 vol% case shows structures composed of both isolated chains and small “sheet-like” structures. Some structures are not perfectly aligned in the direction of the electric field, as they are distorted due to the interaction with neighboring sheets and columns. This dependence of structure as a function of volume fraction has already been pointed out experimentally in our own observations with optical microscopy, by Dassanayake [159], and numerically by Park [160]. Experimental verification of the structure’s volume fraction dependence is shown in Figure V-7, the numerical in Figure V-8.

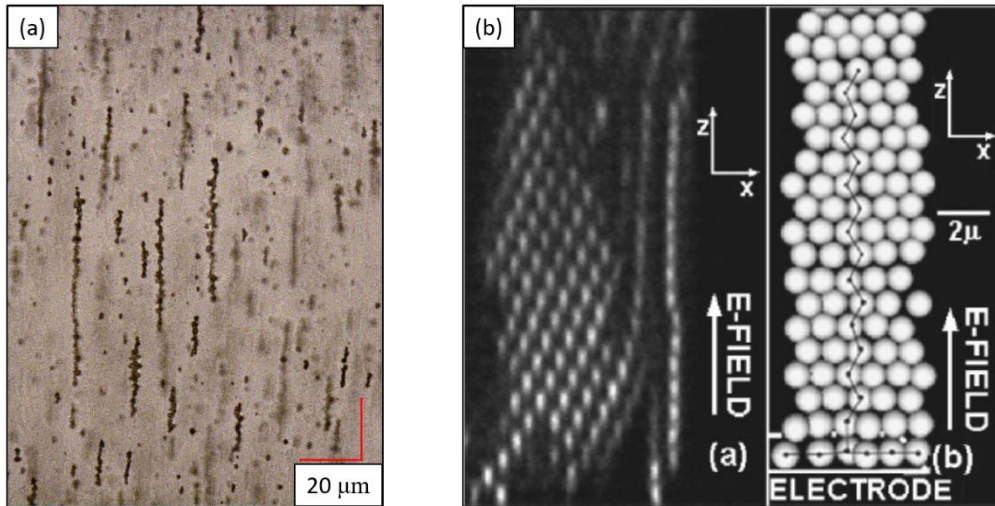


Figure V-7: Dependence of filler structure on volume fraction in experiments. (a) optical microscopy image of epoxy/BaTiO<sub>3</sub> composite after 40 s under ac electric field (600 V/mm) at 0.25 vol%, (b) confocal micrograph of water and glycerol/silica ER fluid after 30 min. under ac electric field (1.2 kV/mm) at 10 vol% [159].

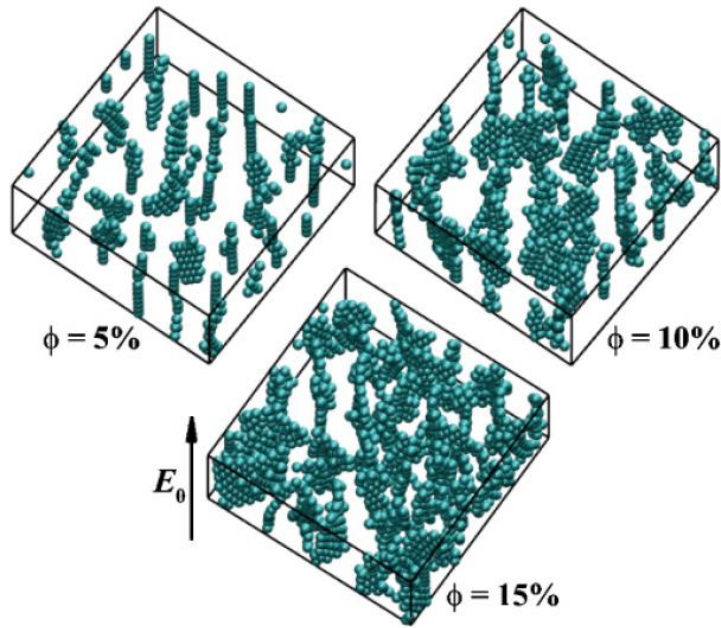


Figure V-8: Simulated dependence of filler structure for different volume fractions [160].

This level of correspondence between our simulation results to the reports comforts our model of electric field induced chaining. Confirmation that the obtained structures were compatible with those observed in literature, as well as with our own experimental observation, was a first step towards validating our model. In a second step, the model validity is verified by estimating a marker of chain formation, that is, the permittivity.

## V.2. Computation of the composite dielectric properties: comparison with the experimental measurements

The model's validity was studied by confronting simulated outcomes with experimental results. In order to test the whole model, all the simulation's input parameters were tested over defined ranges. These parameters can be found by rewriting eq. 22 as:

$$m\mathbf{a} = \mathbf{F}_{DEP} \left( \varepsilon_m, \varepsilon_p, R^3, \frac{1}{d^4}, E_0^2 \right) + \mathbf{F}_{drag}(v, R) + \mathbf{F}_g(m) + \mathbf{F}_{coll} \quad (39)$$

The impact of the parameter  $d$  corresponding to the relative positions between particles is studied by working at different filler contents. The parameters  $\varepsilon_p$ ,  $m$ , and  $R$  are varied by using different particles. The medium parameters,  $\varepsilon_m$  and  $v$ , are checked using different epoxy resins. Lastly, the impact of the electric field,  $E_0$ , is studied by varying its amplitude and waveform.

### V.2.a. Method to compute the composites dielectric properties

Once the coordinates of the particles are known as a function of time, the local electric field and electric displacement field are estimated through the finite element method (a detailed description of this method can be found in Myroshnychenko's work [161]). In that work, the author also explains the method used to randomly place particles in the initial state.

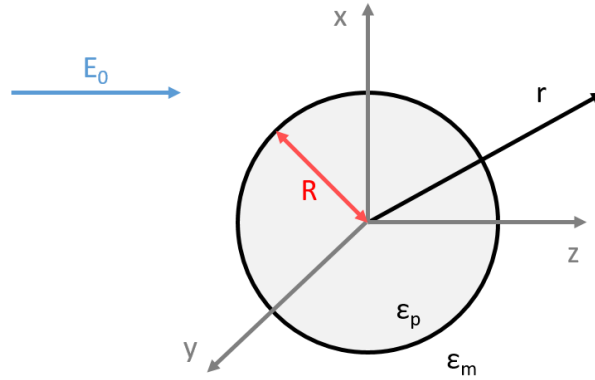


Figure V-9: Dielectric particle embedded in matrix under an external electric field.

It is assumed that there are no free charges in the system. Consequently, the problem is reduced to solving the Laplace equation with the appropriate boundary conditions at the particle/matrix interface. As a reminder, the Laplace equation is:

$$\Delta\varphi = \frac{\partial^2\varphi}{\partial x^2} + \frac{\partial^2\varphi}{\partial y^2} + \frac{\partial^2\varphi}{\partial z^2} = 0 \quad (40)$$

There are two boundary conditions at the particle/matrix interface, with electrostatic potential continuity given by:

---


$$\varphi_{inside}|_{r=R} = \varphi_{outside}|_{r=R} \quad (41)$$

and since there is no free charge, the continuity of the normal component of the electric displacement field is:

$$\varepsilon_p \frac{\partial \varphi_{inside}}{\partial r} \Big|_{r=R} = \varepsilon_m \frac{\partial \varphi_{outside}}{\partial r} \Big|_{r=R} \quad (42)$$

These equations are solved by FEM with a commercial solver [47]. Once the electric field and the electric displacement field are computed, the total energy of the system is then calculated from the following equation:

$$W = \iiint_{volume} E \cdot D \cdot dr^3 \quad (43)$$

where  $W$  is the total energy,  $E$  the local electric field, and  $D$  the local electric displacement field. Eq. 43 is valid as long as the materials present linear behavior. System capacitance is evaluated as:

$$C = \frac{2W}{V^2} \quad (44)$$

where  $C$  is the system capacitance and  $V$  the voltage. The value of permittivity is then:

$$\varepsilon = \frac{C \cdot l}{\varepsilon_0 S} \quad (45)$$

with  $l$  the distance between the electrodes and  $S$  the electrode surface.

While this method relies on a solid theoretical foundation, the domain discretization needs a huge number of tetrahedrons for a large number of particles, dramatically increasing computational costs. Early results of computed permittivity showed a shift of the values compared to measured values. Improvements might be possible through the use of immersed boundary, or boundary element, methods [162].

Permittivity computation was performed with the FEM environment [47]. The computation of 14 time steps of permittivity took approximately 900 s for 500 particles on an Intel® Core™ i7-4810MQ processor.

### *V.2.b. Normalization of the permittivity*

The plot of the evolution of the measured permittivity in Figure V-10 (a) gives rise to a large absolute numerical change. Initial permittivity depends strongly on medium permittivity, which leads to large differences between measurements, thus making it difficult to analyze the impact of the chaining dynamics. In order to remove this “scale effect”, permittivity was normalized between 0 and 1 according to eq. 46:



$$Normalized \varepsilon'(t) = \frac{\varepsilon'(t) - \varepsilon_{min}'}{\varepsilon_{max}' - \varepsilon_{min}'} \quad (46)$$

This representation, shown in Figure V-10 (b), allows a close comparison between two different cases.

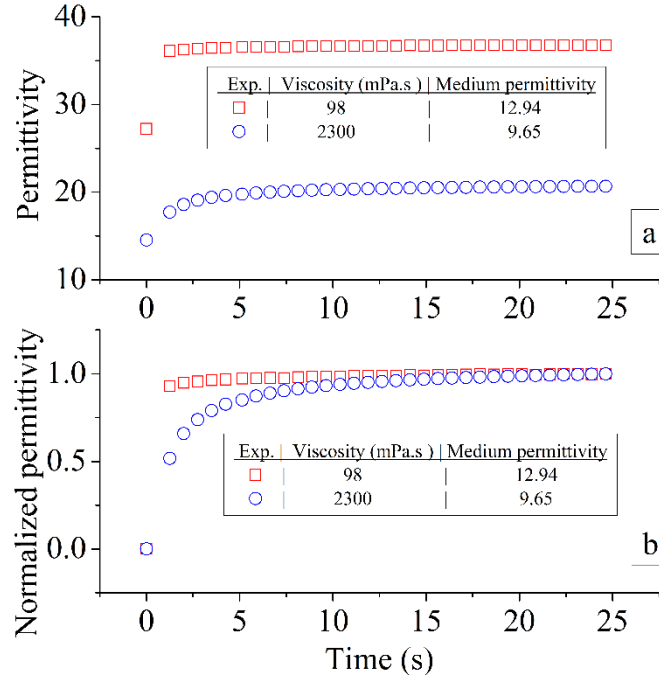


Figure V-10: Time evolution of (a) permittivity and (b) normalized representation of permittivity during chain formation for two different epoxy resins (B and C). The ac electric field is 600 V/mm and the filler content is 10 vol% of BaTiO<sub>3</sub>.

### V.2.c. Impact of the volume fraction of particles

A key parameter for controlling the final properties of a composite material is the volume fraction of fillers. The range of filler contents can be very wide, depending on the application and, especially, on the particle used. For example, very high volume fractions of ceramic particles are used to increase thermal conductivity (up to 70 or 80 vol%), while few percent of filler content is enough to reach percolation for graphene and carbon nanotubes to increase electrical conductivity. The parameter tested from the model point of view is  $d$ :

$$m\mathbf{a} = \mathbf{F}_{DEP} \left( \varepsilon_m, \varepsilon_p, R^3, \frac{1}{d^4}, E_0^2 \right) + \mathbf{F}_{drag}(v, R) + \mathbf{F}_g(m) + \mathbf{F}_{coll} \quad (43)$$

Three cases were investigated: 1, 5, and 10 vol% of BaTiO<sub>3</sub> in epoxy resin no. 2 under an ac electric field step with 600 V/mm in magnitude. As expected, the permittivity changes, plotted in Figure V-11, occur faster when increasing the volume fraction. This is due to the shorter distance that a particle has to travel to reach its nearest neighbor.



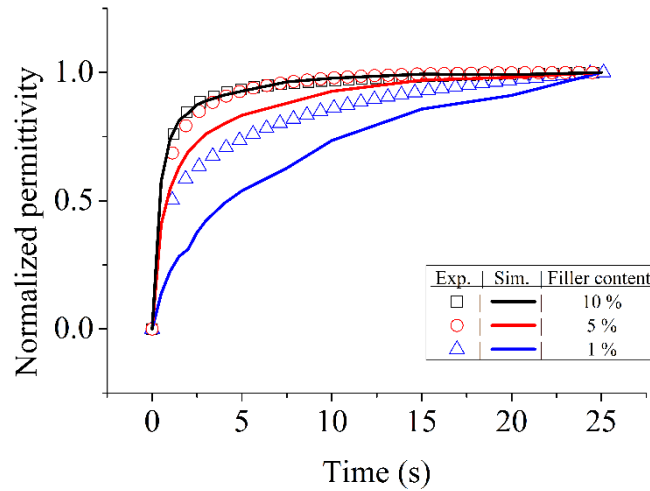


Figure V-11: Normalized permittivity measured and simulated for different filler contents. Resin viscosity of 480 mPa.s, permittivity of 7.2, ac electric field amplitude 600 V/mm and  $n = 500$ .

The model's accuracy tends to decrease with low filler contents. Several reasons could explain this result, such as the real size distribution of the particles (in contrast to simulated particles having unique size).

The relation between the filler structuration and the changes in permittivity are clear on the plot of mean particle velocity in Figure V-12.

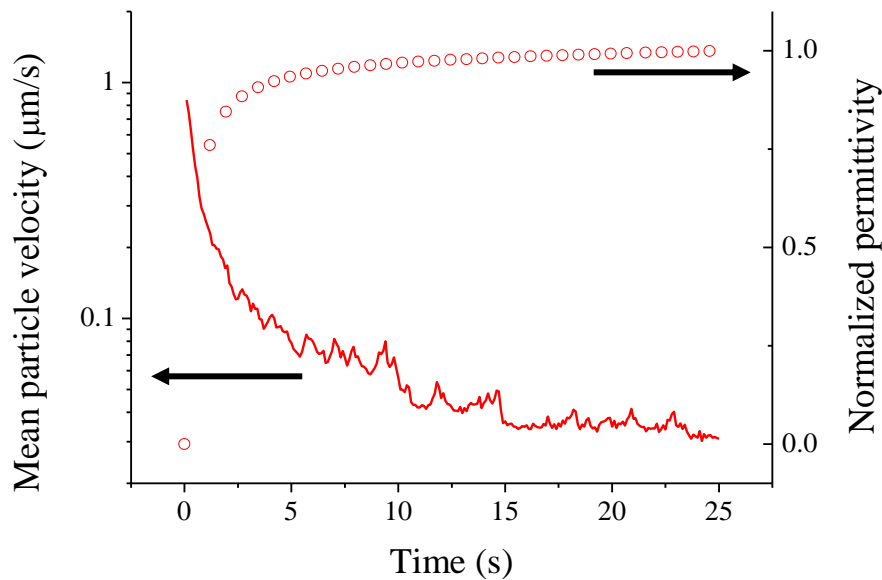


Figure V-12: Mean particle velocity and normalized permittivity plotted over time for the 5 vol% case.

The mean particle velocity is high just after application of the electric field, which can be related to the fast formation of chains observed in Figure V-3, and as well as to permittivity changes, with most of the increase taking place in the first 5 seconds. Computation of velocity is interesting, not only because it is very easy to obtain, but because it offers another marker of filler structure.

V.2.d. *Impact of the particle properties*

The choice of the particle nature is perhaps the most important consideration when elaborating anisotropic composites. The first concern is to choose the particle having properties adapted to the target application. These properties include particle electrical conductivity, thermal conductivity, permittivity etc. Another important aspect is the particle size, which can lead to entirely unexpected properties (e.g. nanoparticles can have a beneficial impact on dielectric strength whereas microparticles cause a degradation). The final choice is the particle shape, or aspect ratio, which enhances the anisotropic effect. These aspects will not be studied here.

While the selection of particle type depends on the application, particle properties also affect chain formation. The worst scenario would be a particle having dielectric properties too close to those of the matrix, leading to very weak DEP forces. The impact of particle properties was studied with two different particles: BaTiO<sub>3</sub> and SrTiO<sub>3</sub> at 10 vol% in epoxy resin no. 2 under an ac electric field step with amplitude of 600 V/mm. Permittivity changes are plotted in Figure V-13. The parameters impacted here are  $\epsilon_p$ ,  $m$ , and  $R$ .

$$m\mathbf{a} = \mathbf{F}_{DEP} \left( \epsilon_m, \epsilon_p, R^3, \frac{1}{d^4}, E_0^2 \right) + \mathbf{F}_{drag}(v, R) + \mathbf{F}_g(m) + \mathbf{F}_{coll} \quad (43)$$

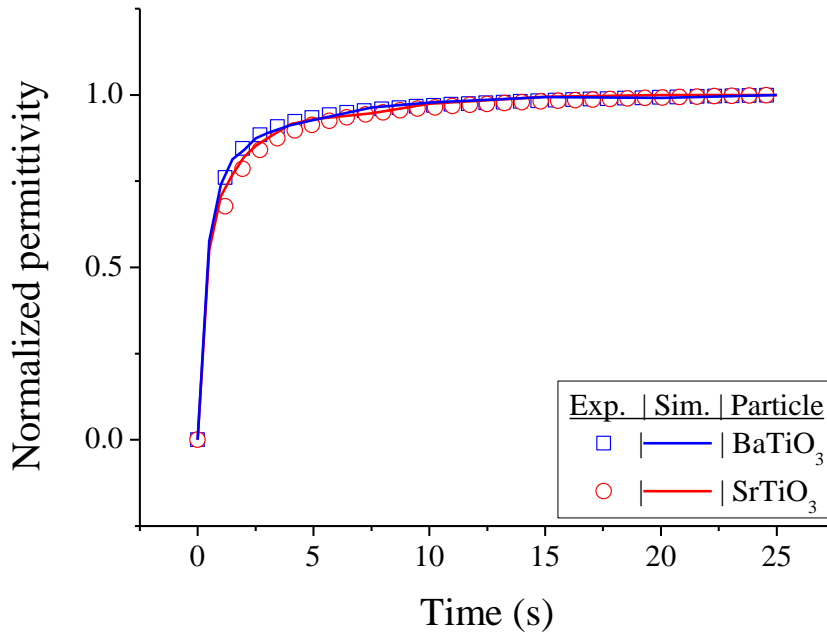


Figure V-13: Normalized permittivity measured and simulated for different particles at 10 vol%. Resin viscosity of 480 mPa.s, permittivity of 7.2. ac electric field amplitude of 600 V/mm, and  $n = 500$ .

The difference in the behavior between the two particles is very small. The dynamics with SrTiO<sub>3</sub> is slightly slower, which can be explained by its lower permittivity, as shown in section III.2.d. The model

---

seems to predict the same behavior with the red curve just under the blue curve. This very small difference might be explained by the small difference in the Clausius-Mossotti factor when using SrTiO<sub>3</sub> or BaTiO<sub>3</sub>. Indeed, the difference in the computed factor is less than 3 %, meaning that the DEP force magnitude with BaTiO<sub>3</sub> is only 3 % higher than with SrTiO<sub>3</sub>. Interestingly, in the simulations performed, the difference in filler size did not seem to impact global permittivity. It would be interesting to work with particles with a larger difference in permittivity.

### V.2.e. *Impact of the resin properties*

The resin type is another crucial choice for the correct elaboration of an anisotropic composite. This choice is usually consistent with the desired final composite specifications based on the properties of pure resins, such as dielectric strength, operating temperature range, dielectric losses, mechanical/chemical compatibility, etc. However, the resin's mechanical and electrical properties greatly impact chaining dynamics when elaborating anisotropic composites. The parameters checked in this section are  $\varepsilon_m$  and  $\nu$ .

$$m\mathbf{a} = \mathbf{F}_{DEP}\left(\boldsymbol{\varepsilon}_m, \varepsilon_p, R^3, \frac{1}{d^4}, E_0^2\right) + \mathbf{F}_{drag}(\mathbf{v}, R) + \mathbf{F}_g(m) + \mathbf{F}_{coll} \quad (43)$$

This influence is described in eqs. (18), (20), and (22). We can see from eqs. (18) and (20) that the DEP force increases linearly with medium permittivity (while  $\varepsilon_m \ll \varepsilon_p$ ), and from the eq. (22), the drag force increases linearly with medium viscosity. This complex relationship between the physical properties and the acting forces is observed in Figure V-14, where the chaining process is accelerated for the resin with the lowest viscosity and highest permittivity. On the other hand, the resin with the highest viscosity presents the slowest chaining process, while its dielectric permittivity is higher than the resin with a viscosity of 480 mPa.s. In that case, viscosity has a greater influence on chaining dynamics than medium permittivity.

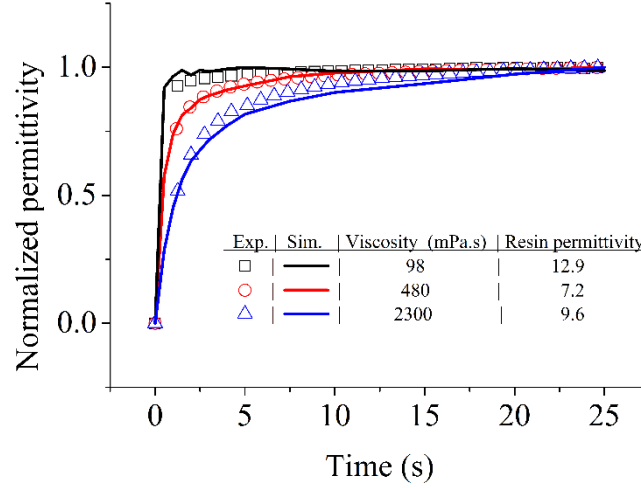


Figure V-14 Normalized permittivity measured and simulated for different epoxy resins. The ac electric field is 600 V/mm, the filler content is 10 vol% of BaTiO<sub>3</sub>, and n = 500.

As a result, from the plots in Figure V-14, the model gives a fair description of the chaining dynamics over a wide range of combined properties (viscosity and medium dielectric permittivity).

#### V.2.f. Impact of the electric field magnitude and waveform

Another parameter for electric-field-induced chaining to form anisotropic composites is the applied electric field magnitude. Because the DEP force is proportional to the square of the electric field (Eqs. (18) and (20)), its magnitude has a very strong influence on the dynamics of chaining. The parameter checked here is  $E_0$ .

$$m\mathbf{a} = \mathbf{F}_{DEP} \left( \varepsilon_m, \varepsilon_p, R^3, \frac{1}{d^4}, \mathbf{E}_0^2 \right) + \mathbf{F}_{drag}(v, R) + \mathbf{F}_g(m) + \mathbf{F}_{coll} \quad (43)$$

Figure V-15 compares experimental measurements to the model's prediction for the time-dependent change in permittivity. For the three presented cases, BaTiO<sub>3</sub> at 10 vol% in resin no. 2 for ac electric field step at 600 and 300 V/mm, and ac electric field sweep with 21 V/mm.s slope, the simulation results are in reasonable agreement with experimental measurements. This result is encouraging because it suggests that the chaining process can be controlled by the voltage magnitude and waveform. This predictive aspect of the model is crucial for elaborating anisotropic composites since, for a given voltage source, the minimum electric field to chain determines the maximum distance possible between the electrodes. On the other hand, the electric field waveform gives the possibility to modulate magnitude over time, which can be important to fight against the effects of a change in medium viscosity and/or dielectric permittivity.

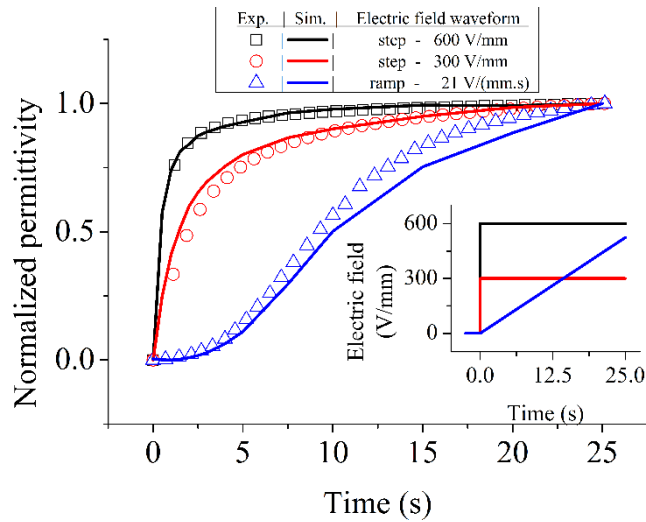


Figure V-15: Normalized permittivity measured and simulated for different ac electric field waveforms. The inset represents the different ac electric field waveforms used. The resin viscosity is 480 mPa.s and permittivity is 7.2. The filler content is 10 vol% of BaTiO<sub>3</sub>, and  $n = 500$ .

This case demonstrates the model's robustness when describing permittivity changes for time-dependent parameters, opening the way to simulation taking into account the real polymerization process.

### V.3. Conclusion and perspectives

The filler structures obtained from numerical simulations were compared to previous experimental and numerical investigations and appear to follow the same trend function of the filler content.

In order to validate the model and its predictive aspect, a common marker for filler structuration between experimental and numerical study was needed. As permittivity proved to be a relevant marker of chain formation in the previous chapter, we decided to compute permittivity from the simulated structure. Permittivity computation was obtained using FEM to solve electrostatic equations.

The model's robustness was proven over all the input parameters, even if a larger error was present for lower volume fractions.

While the control of composite properties was shown in chapter IV to be possible from the process parameters and the knowledge of chaining dynamics, we demonstrated here that information on chain formation dynamics can be obtained through numerical simulation.

There are many perspectives for improvement and further studies with this model. The model's accuracy could be improved by taking into account particle size distribution, the particle's real shape, or by simulating more particles. The first aspect has already been computed (Figure V-16: example with more than 2,600 particles simulated); the second one would be much more complex to develop, first requiring to determine a random generation of the particle shape according to the powder characteristics and then modifying the code to handle collisions. Handling collisions would certainly be very challenging.

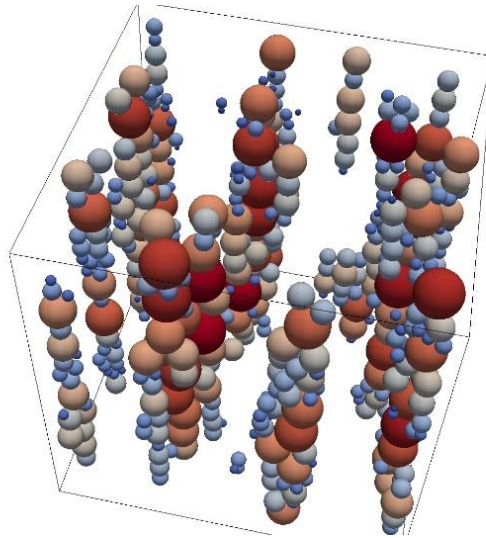


Figure V-16: Structure of particle chains taking into account real particle size distribution.

The third aspect (i.e. working with more particles) would be interesting to investigate, giving information on the interactions between large structures. Currently, the maximum number of particles simulated was larger than 4,600 particles, on a laptop computer. This could certainly be largely increased working with clusters. However, the current coding method is “brute force”, implying that all particle interactions are computed. Methods exist to compute only neighboring interactions and approximate long range interactions. This would make it possible to avoid increasing model complexity in  $O(n^2)$ , resulting in  $O(n \log(n))$  evolution [163]. However, the number of particles is not currently the limiting factor. Limitation arises from the method used to compute permittivity. While FEM is a powerful tool, its weakness is the complexity of the structure to mesh. In the present case, domain meshing is very complex. When particles are in close contact, the tetrahedrons are very small (tens of nm), while the length of the side of the simulation cube can reach a few tens of microns. In addition, the domain is three-dimensional. We were not able to compute permittivity for more than 700 particles in the present work. The case of particles with size distribution is even harder to handle. However, possible improvement could come from using boundary element methods [162] or immersed boundary methods.

As a conclusion, the developed model remains simple yet it proved its robustness and provides a powerful predictive tool for optimizing the elaboration process of anisotropic composites. The content of Chapters II to V confirms that it is possible, based on predictive approach, to tailor the structure of a composite from isotropic to anisotropic when applying a given electric field.







# Chapter VI

Prospective Study Of Anisotropic Composite

With Perpendicularly Oriented Fillers

## **VI. PROSPECTIVE STUDY OF ANISOTROPIC COMPOSITE WITH PERPENDICULARLY ORIENTED FILLERS**

In the previous chapters, we investigated the possibility to make anisotropic composites with fillers chained in the direction of the electric field. Another possibility to induce anisotropy comes with the electro-orientation of particles with a high aspect ratio. Generally, when an ac or dc electric field is applied, non-spherical particles tend to orient their longest axis in the direction of the electric field. This leaves the following question open: is it possible to design anisotropic composites with non-spherical fillers oriented perpendicularly to the electric field? That question is studied in the present chapter. The study will follow the main lines of the roadmap presented at the end of chapter I, in three steps: theoretical identification of the forces and parameters involved; modeling of the phenomenon; and trying to achieve experimental validation. However, it should be noted that the fillers used were not characterized as in detail as for the chain formation.

As an introduction, we examine the benefits of these types of composites, and then describe the theory of electro-orientation. An effort to determine the experimental parameters from numerical investigations is reported, regarding the material used. In a first step, perpendicular orientation is studied with epoxy resin in a liquid state (without hardener); then hard composite is prepared and studied. Lastly, we investigate the elaboration of a three-phase composite with fillers orientated both perpendicularly and parallel to the direction of the electric field.

### **VI.1. Context, theory and numerical study**

#### *VI.1.a. Context*

The elaboration of anisotropic composites was studied in chapter IV and V, both experimentally and numerically. The beneficial impact of filler structuration is ensured but, until now, the improvement of a specific property was only made possible in the direction of the applied electric field. This can be a limit for two main cases: (i) the property to improve is parallel to the electrodes, (ii) two different properties must be improved in different directions. The first case can be illustrated in the example of heat spreading. If the size of a component generating heat is small compared to the size of the heat sink, it could be beneficial to allow the heat flux to spread over a larger area. The figure below shows three different kinds of composite materials that could be used to improve the thermal conductivity of the interface material. The material A presents isotropic properties. Both the material B with fillers chained in the direction of the electric field, and the material C with fillers aligned perpendicularly, present anisotropic properties, but with increased thermal conductivity in different directions.

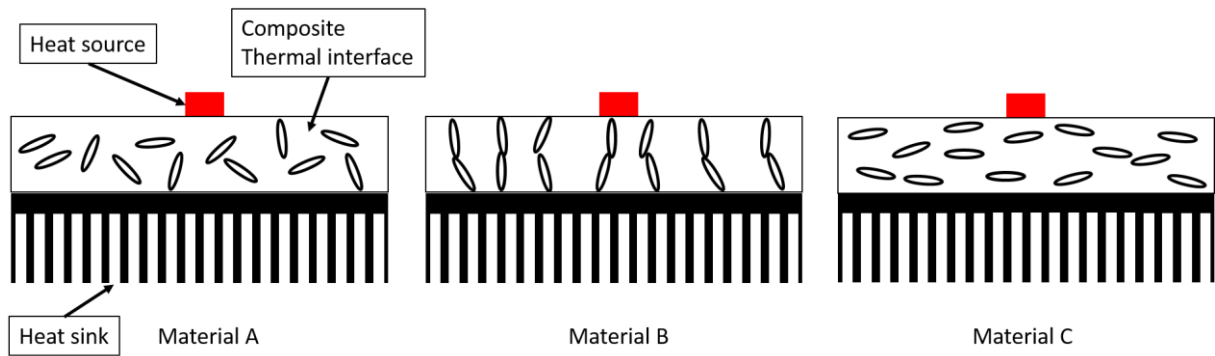


Figure VI-1: Illustration of thermal interface materials between the heat source and the heat sink.

As expected, the numerical computation of temperature distribution differs strongly between the three cases, as can be observed in Figure VI-2.

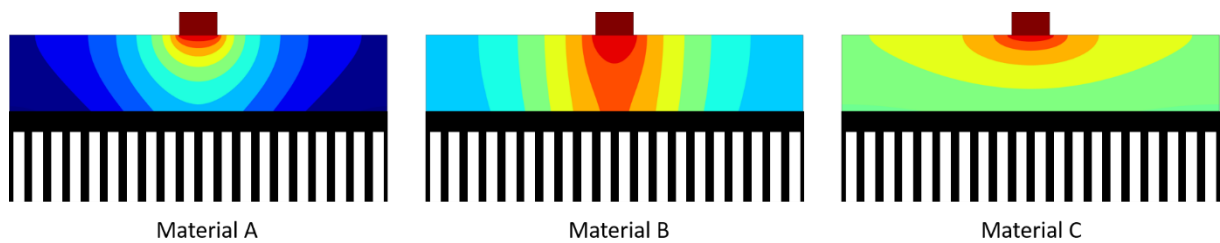


Figure VI-2: Simulation of temperature distribution according to material properties.

The temperature distribution in the  $x$  direction is far more uniform with material C than for the two other materials. The plot of the temperature at the interface in Figure VI-3 confirms better distribution of the temperature to be dissipated in the case where the composite with fillers are aligned perpendicularly.

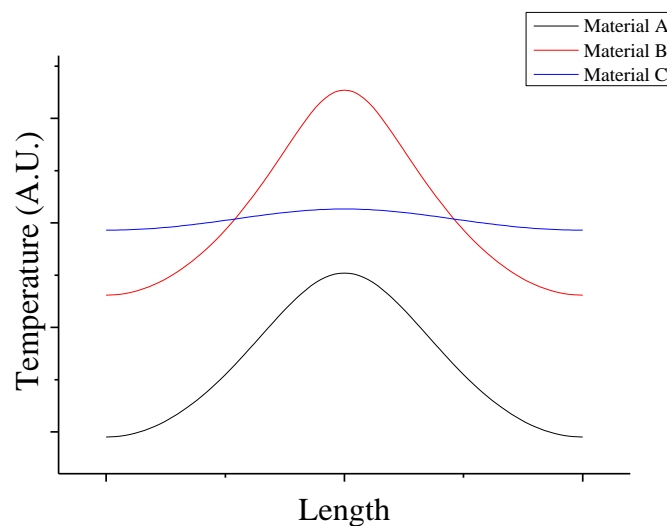


Figure VI-3: Temperature at the material/heat sink interface for the different materials.

Another application example that could be enabled by controlling filler orientation would be *switchable material*, i.e. a liquid composite in which properties could be controlled by applying an electric field. Regarding the illustration in Figure VI-1, case B would correspond to the ON property, at its higher value. Oppositely, case C would correspond to the OFF property, at its lower value.

The first intuition for elaborating composites such as material C would be to rotate the electric field in the appropriate direction. However, in many systems, this action would not be convenient and might be impossible to achieve for various reasons. First, it might not be possible to add electrodes other than the existing ones. Furthermore, the dimension of the inter-electrode spacing can be very large, resulting in the need for very high voltage to achieve chaining. That is why there is a need for a new solution to elaborate such materials.

The method we adopted was to continue working with the same electrode configuration as that in the previous chapters, and trying to determine the appropriate electric parameters to achieve perpendicular alignment. This has indeed been proven to be possible by several studies in the field of biomedical sciences [164]–[166]. To the best of the author’s knowledge, the only example of non-living particles aligned perpendicularly was given by Miller in her thesis work with TiO<sub>2</sub> particles [167].

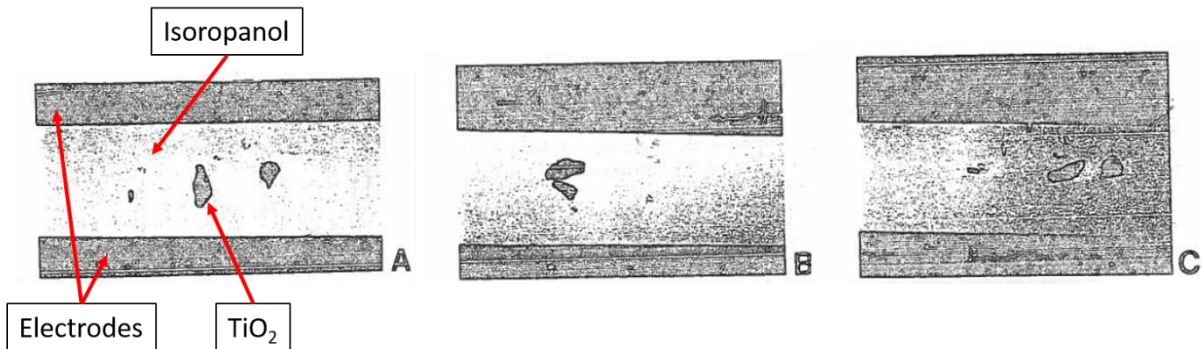


Figure VI-4 : Electroorientation of TiO<sub>2</sub> in isopropanol. (A) long axis aligned with the electric field at 1 kHz, (B) middle axis aligned with electric field at 100 kHz, (C) short axis aligned with electric field at 30 kHz.

This surprising orientational behavior comes from the fact that the particle presents different Maxwell-Wagner relaxation time constants along each axis. These particles orient one of their axes in the direction of the electric field due to a phenomenon called electroorientation. This phenomenon is related to the torques induced by the electric field on the particles.

### VI.1.b. Mathematical model

An anisotropic particle subjected to an electric field always tends to align one of its axis parallel to the electric field direction. Generally, stability is reached when the particle has its longest axis aligned with the electric field. While the other axes are aligned with the electric field, the particle is in an unstable equilibrium. However, when specific conditions are met, the longest axis might not be the stable one, but rather the short or medium axis. The conditions for this to occur depend on the particle and medium’s

dielectric properties, as well as on the particle shape. The first attempts to theorize the phenomenon of electro-orientation started in the 1960s with [168]–[170], and more recently by Jones in the 1980s [73]. A particle (here assimilated to an ellipsoid) subjected to an electric field undergoes three torques: one on each axis, named “*orientational torque*”. The torque signs are frequency dependent, and the stable equilibrium position can be determined from the set of signs. The particle is assumed to be homogeneous with isotropic properties. Both the particles and the medium are lossy dielectrics.

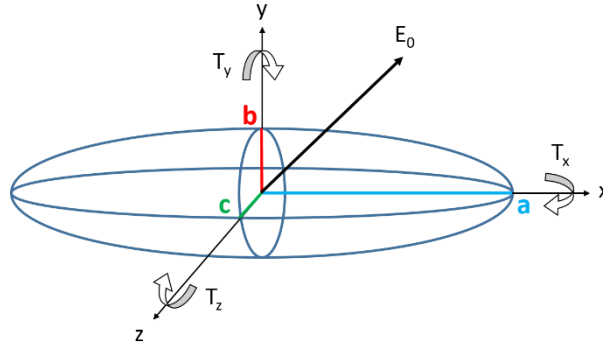


Figure VI-5: Ellipsoidal particle subjected to an electric field

The general expression of the time average torque is:

$$\langle T \rangle_\alpha = \frac{2}{3} \pi abc \epsilon_m (L_\gamma - L_\beta) E_{0,\beta} E_{0,\gamma} \text{Re}[K_\beta^* K_\gamma^*] \quad (47)$$

with  $\alpha, \beta$ , and  $\gamma$  the  $x, y$ , and  $z$  axis;  $a, b$ , and  $c$  the major, middle, and short axis of the ellipsoid;  $L_\gamma$  the  $\gamma$  coordinate of the depolarization factor of the ellipsoid;  $E_{0,\beta}$  the  $\beta$  coordinate of the external electric field; and  $K_\beta^*$  the  $\beta$  coordinate of the complex Clausius-Mossoti factor. It is important to note that the above expression is correct as long as the particle responds to time average torque, that is, it is no longer true at very low frequency. The depolarization factors are determined thanks to the following equations [171]:

$$L_x = \frac{abc}{2} \int_0^\infty \frac{ds}{(s+a^2)R_s} \quad (48)$$

$$R_s = \sqrt{(s+a^2)(s+b^2)(s+c^2)} \quad (49)$$

The expression for the two other axes can be determined by appropriate substitution of  $x, y$ , or  $z$  and  $a, b$ , or  $c$ . The Clausius-Mossoti factor is given by:

$$K_\beta^* = \frac{\epsilon_p^* - \epsilon_m^*}{3[\epsilon_m^* + (\epsilon_p^* - \epsilon_m^*)L_\alpha]} \quad (50)$$

It is worth noting that, for a spherical particle,  $L_\alpha = L_\beta = L_\gamma = \frac{1}{3}$ , and one would obtain the classic equation for the Clausius-Mossoti factor. The frequency dependence of the torques can be found in eq. 50, as  $\epsilon_p^*$  and  $\epsilon_m^*$  vary as a function of the frequency. Once the expression of the torques is determined,

the stable orientation can be obtained thanks to their relative signs, according to the following table, where a, b, and c denote the ellipsoid side aligned in the direction of the electric field:

Table VI-1: Stable orientation as a function of the torque component signs.

$\langle T \rangle_x$	$\langle T \rangle_y$	$\langle T \rangle_z$	<b>Orientation</b>
+	+	+	None
+	+	-	<i>b</i>
+	-	+	<i>a</i>
+	-	-	<i>b</i>
-	+	+	<i>c</i>
-	+	-	<i>c</i>
-	-	+	<i>a</i>
-	-	-	None

The first and the last lines of the table, where no stable orientation exists, are mathematically impossible. It now appears that, if one knows the particle geometry and the dielectric properties of the particle and the medium, it would be possible to determine the stable orientation for a given frequency.

*VI.1.c. Determination of the experimental parameters through simulation*

The particles used in these experiments are alumina platelet, prepared by Sato Chemical Engineering (Japan). The properties of the particles and their elaboration process were not given by the supplier. In order to attempt to determine the frequency range in which c orientation is possible, the distribution of sizes along a, b, and c axes was measured. The results are plotted in Figure VI-6.

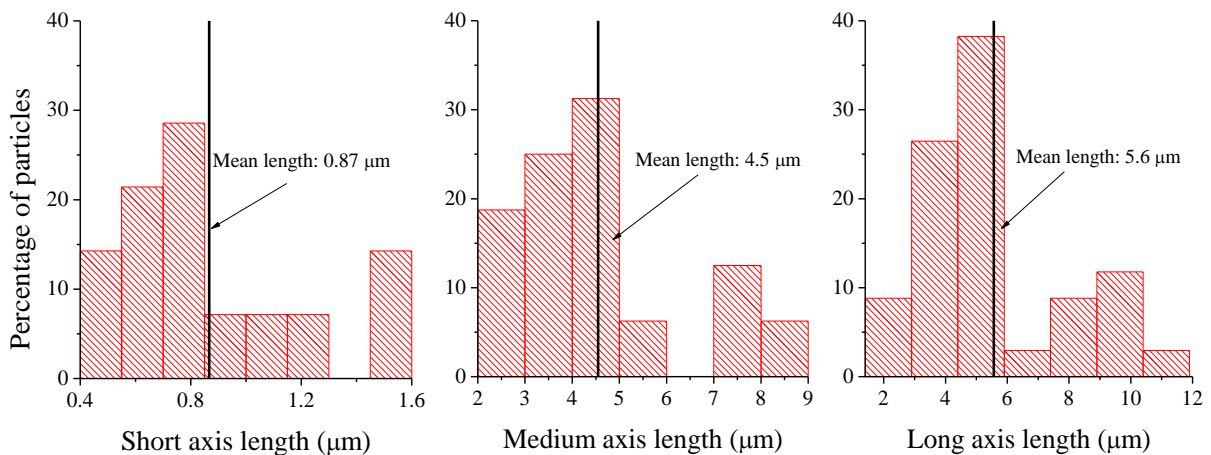


Figure VI-6: Distribution of the particle sizes along short, medium, and long axes.

The size distribution of the particles appears to be wide, which could result in a dispersion of the turnover frequencies depending on the particle form factor. In view of investigating the impact of the aspect ratio,

turnover frequencies are computed while varying particle shape parameters. The extrema and mean values of  $a$ ,  $b$  and  $c$  sides of the particles are summarized in the table below, along with the associated aspect ratios.

Table VI-2: Extrema and mean values of  $a$ ,  $b$  and  $c$  sides of particles and associated aspect ratio.

	$a$ [ $\mu\text{m}$ ]	$b$ [ $\mu\text{m}$ ]	$c$ [ $\mu\text{m}$ ]	$b/a$	$c/a$
Minimum	2.7	2.3	0.5	0.2	0.04
Mean	5.6	4.5	0.87	0.8	0.16
Maximum	11.4	8.2	1.5	0.85	0.56

We computed the turnover frequencies (Figure VI-7) using the aspect ratio values in The size distribution of the particles appears to be wide, which could result in a dispersion of the turnover frequencies depending on the particle form factor. In view of investigating the impact of the aspect ratio, turnover frequencies are computed while varying particle shape parameters. The extrema and mean values of  $a$ ,  $b$  and  $c$  sides of the particles are summarized in the table below, along with the associated aspect ratios.

Table VI-2. The black areas correspond to the frequency range of  $a$ -orientation, red to  $b$ -orientation, and blue to  $c$ -orientation. Four cases were investigated, fixing an axis aspect ratio to a minimum or maximum value and varying the other value. From the numerical estimation plotted in Figure VI-7, it seems that, in this range of particle aspect ratio, the impact on turnover frequency is rather small from  $a$  to  $c$ -orientation and quasi-null for the other transitions. This should mean that if the particles are of the same nature, they would all behave in the same manner at a given frequency.

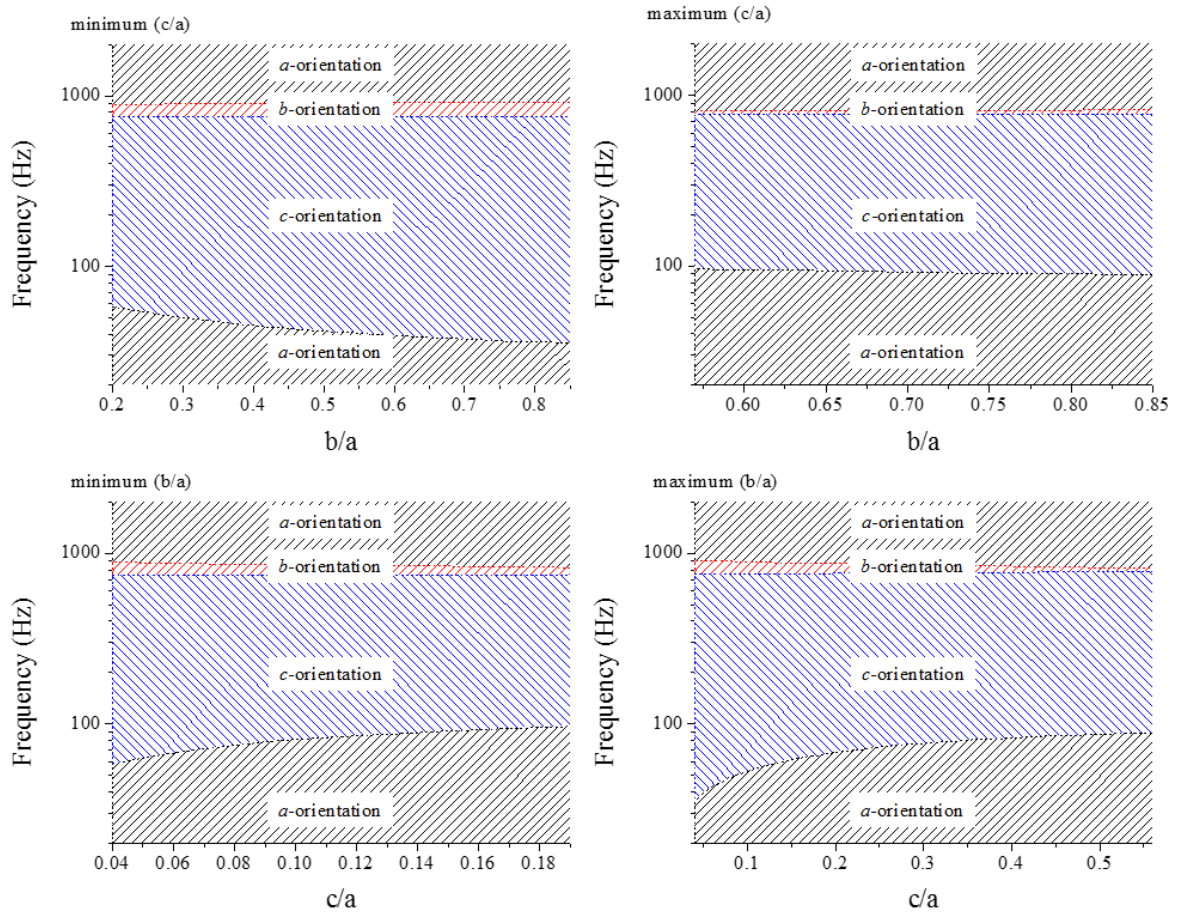


Figure VI-7: Turnover frequencies as a function of the particle aspect ratio. Particle permittivity is 10 and conductivity is  $10^{-12}$  S/m.

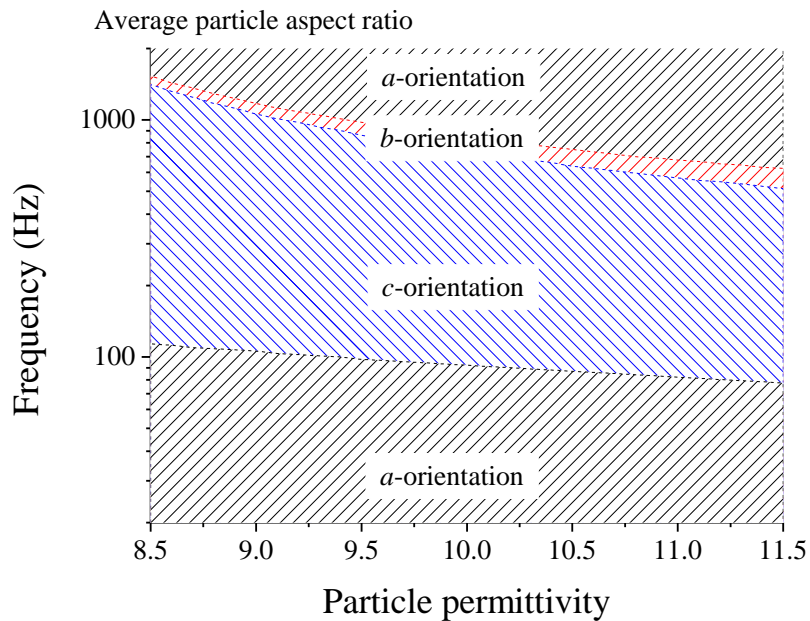


Figure VI-8: Turnover frequencies as a function of particle permittivity. Particle conductivity is  $10^{-12}$  S/m.

Since the particle permittivity is not known exactly, we studied its impact on the turnover frequencies. The particle permittivities were taken according to the range of values found in literature. The results



plotted in Figure VI-8 show low impact of particle permittivity on the crossover frequency, with a slight increase when particle permittivity tends toward that of the resin (7 – 7.5 above 20 Hz).

## VI.2. Formation of the composites

### VI.2.a. Perpendicular orientation in liquid state

The first step toward perpendicularly-aligned particles was to achieve alignment inside the epoxy resin without hardener to verify whether it was possible to determine the appropriate conditions, and to compare with the parameters deduced theoretically. The experimental setup for these experiments was the same as that described in section V.1.b. With microscope observation, it is quite easy to determine a particle's perpendicular alignment. When a particle has one of its sides aligned with the electric field, it still has one rotational degree of freedom (along the axis of stable orientation). This means that the particle can be observed as follows for the three stable orientations:

Table VI-3: Rotations around the stability axis for stable a, b, and c positions.

Angle Axis	0 °	30 °	60 °	90 °
a				
b				
c				

From The first step toward perpendicularly-aligned particles was to achieve alignment inside the epoxy resin without hardener to verify whether it was possible to determine the appropriate conditions, and to compare with the parameters deduced theoretically. The experimental setup for these experiments was the same as that described in section V.1.b. With microscope observation, it is quite easy to determine a particle's perpendicular alignment. When a particle has one of its sides aligned with the electric field,

it still has one rotational degree of freedom (along the axis of stable orientation). This means that the particle can be observed as follows for the three stable orientations:

Table VI-3, we can observe that, for the perpendicular orientation (*c* axis), the alumina particle is always be seen from its thinner side and will thus appear darker in transmitted light, which makes these particles easy to distinguish. For the other stable orientations, as the alumina particles used are semi-transparent, they might be harder to observe when not at 90°. This effect can be observed in Figure VI-9, where all the *c*-orientation particles appear black, while the others are mostly semi-transparent and only some of them black.

The matrix used in this experiment was epoxy 816B filled with alumina particles at 0.31 vol%. The decision to work at very low filler content was made to avoid interparticle interaction, which could interfere with orientational behavior. The electric field magnitude was 600 V/mm.

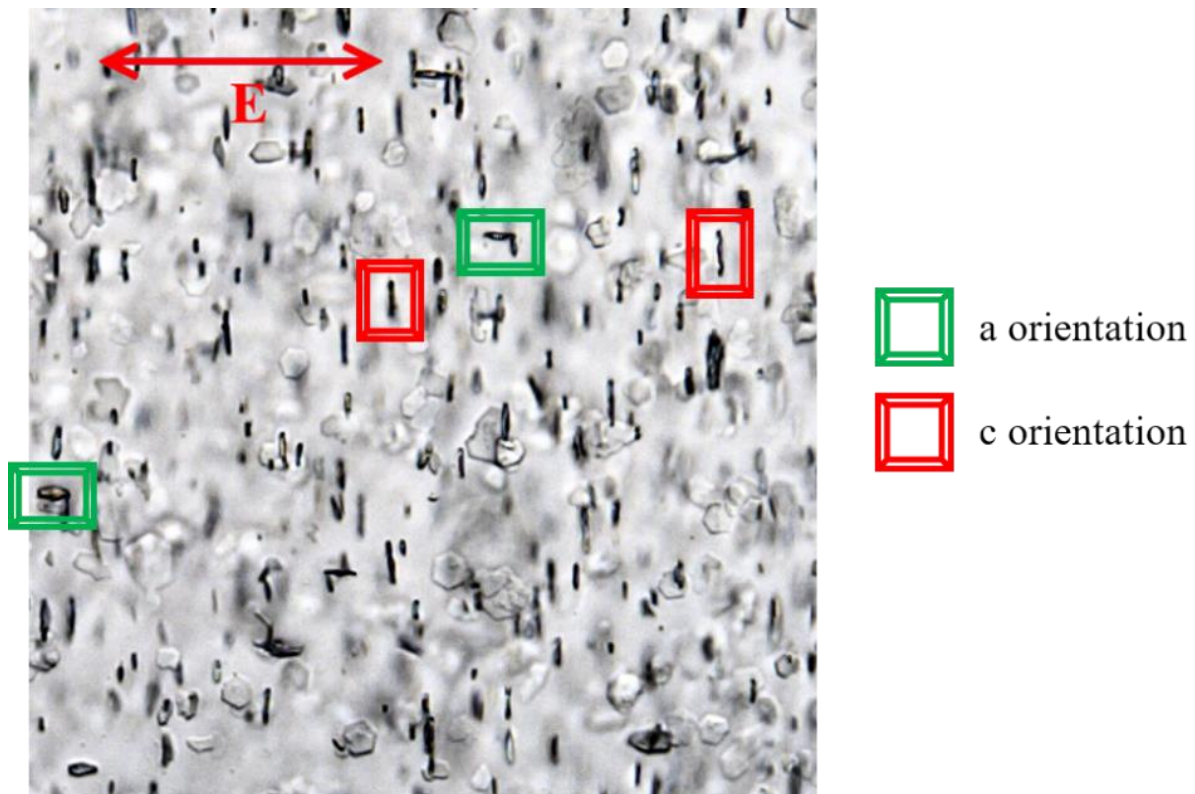


Figure VI-9: Liquid epoxy and alumina particles after 20 min under ac electric field at 30 kHz. The length of the image sides is 200  $\mu\text{m}$ .

This picture highlights two discrepancies between theoretical and experimental results. The first is that all the particles are **not** in *c*-orientation, whereas the numerical study predicted uniform orientation. The second is that the theory predicted *a*-orientation for this given frequency. The *c*-orientation was predicted roughly between 30 Hz and 2 kHz (depending on particle properties). Experimentally, *c*-orientation was observed above 3 kHz, up to 30 kHz. The change from *c*→*a* was not observed at high frequency. There is no current explanation of the difference between the theory and the experimental

results. However, several parameters are known to have possible impact: (i) even if the volume fraction is low (0.3 vol%), interparticle interactions may still have an impact; (ii) particle permittivity is taken from literature for the bulk ceramic, a lower value than those taken tends to increase the turnover frequencies. This again stresses the need for a characterization method for powder materials. As the experimental data did not fit the theoretical data, we questioned the possibility of water absorption by the particles. Consequently, the particles were dried at 350° C for 2 hours. However, the comparison of the turnover frequency with and without drying the particles did not show any differences.

Lastly, some authors have reported in literature the anisotropic behavior of alumina substrate [172], [173] and the anisotropic dielectric property of the crystal [174]. The impact of the hypothetical anisotropy of particle permittivity was not investigated theoretically. However, this study would be possible by implementing the full permittivity tensor in eqs. 47 and 50 [114].

Dynamic observation of the turnover enabled us to obtain interesting information on the involved torques. From the experimental observations, it appears that the orientational torques from  $a \rightarrow c$  and  $b \rightarrow c$  are weaker than from  $c \rightarrow b$  and  $c \rightarrow a$ . This effect can be observed in Figure VI-10 and Figure VI-11, as it takes few seconds for a particle to reorient from  $c$  to another stable orientation, while a little more than one hundred seconds was necessary to return to  $c$ -orientation.

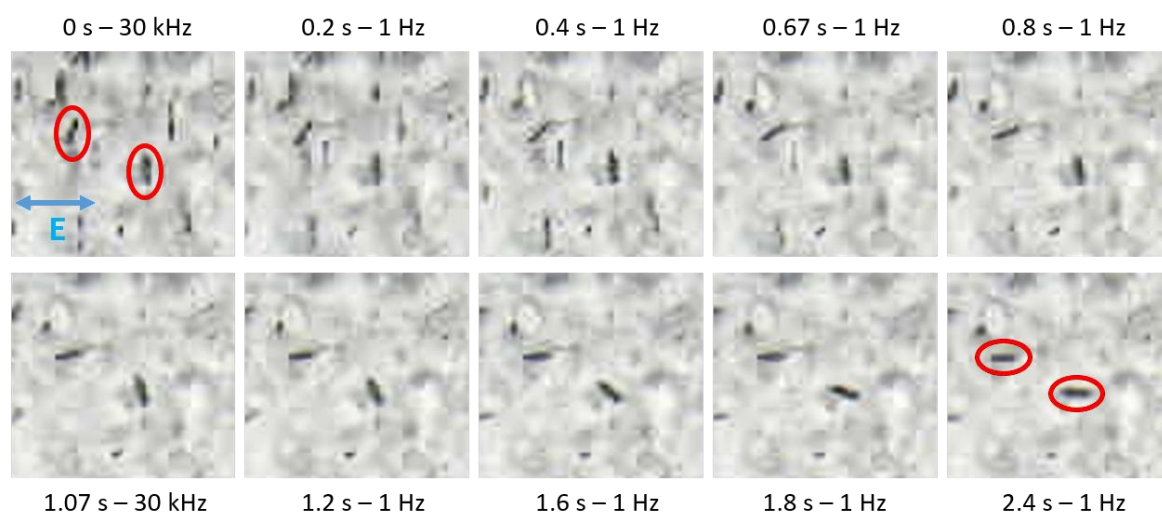


Figure VI-10: Electro-orientation of particles, changing from  $c$  to another stable orientation.

The time for particles to switch from one orientation to another is not perfectly uniform. This can be seen in Figure VI-10, where the first particle takes around 1 s to reach its stable orientation, and the second takes 2.4 s. One could argue that the first particle seems to present a slight angle at the beginning, but it is possible to observe other particles in these pictures with different times to reach stable orientation.

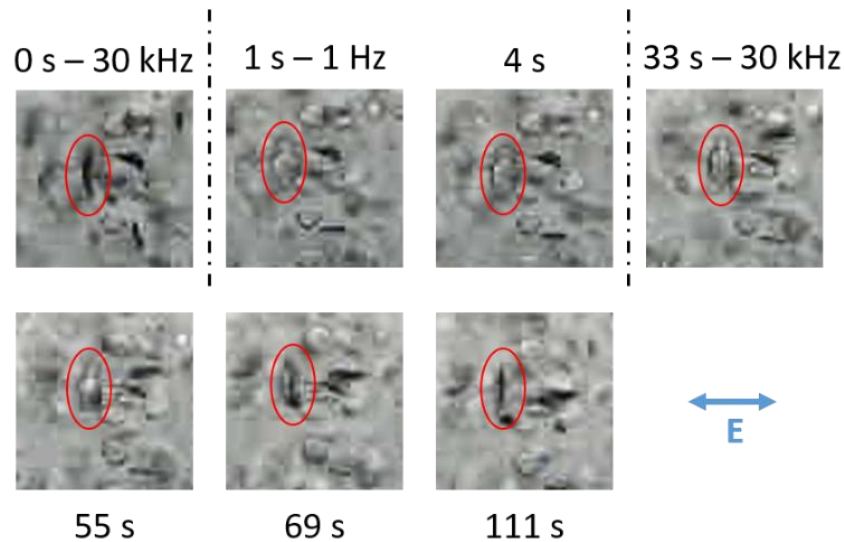


Figure VI-11: Electroorientation of particles,  $c \rightarrow b \rightarrow c$  orientation.

The electro-orientation phenomenon is fully reversible. The particle encircled in Figure VI-11 switches from  $c$  to  $b$  by decreasing the frequency, returning to its initial orientation when increasing the frequency.

This study proved that the orientation of particles perpendicular to the electric field in polymer resin was possible. However, this case was relatively easy to achieve, as resin properties are stable without the presence of hardener. The addition of hardener will increase the challenge to find the right parameters to achieve  $c$  orientation while the resin properties change over time.

### VI.2.b. Epoxy-Alumina composite

Once it was verified that particles can be aligned perpendicularly in epoxy resin without hardener, the next step was to obtain a cured composite with particles in the desired orientation. However, this appears to be far more complex than with the base resin, as the medium properties present large variations during the polymerization process. Two main strategies can be considered when tackling this issue:

- *Applying the electric field during the entire experiment and adjust the frequency for  $c$  orientation.* This possibility might lead to better alignment, as the electric constraint is present during the entire experiment. However, the conductivity of the resin used (SR8500) strongly increased during polymerization, eliminating this method. Indeed, this increase in conductivity leads to fast fluid turbulence, mixing particles, and thus preventing them from reaching stable orientation.
- *Applying the electric field briefly just before the resin crosslinks at the appropriate frequency.* In this time interval, the matrix properties are more stable and conductivity is lowered, reducing the electrohydrodynamic effects.



The difference between the composites obtained with and without an electric field is clear in Figure VI-12. It is possible to notice the presence of particles in *c*-orientation in (a) and (b), while the particles in (c) present random orientations. However, once again, the same behavior as that observed in the previous section occurred: the anisotropic composite has particles not only in *c*-orientation but also in the other orientations. It is even possible to observe particle chains in the top left corner of (a). Currently, no solution has been found to obtain only *c*-orientation. Conducting this experiment with other types of particles might yield better results.

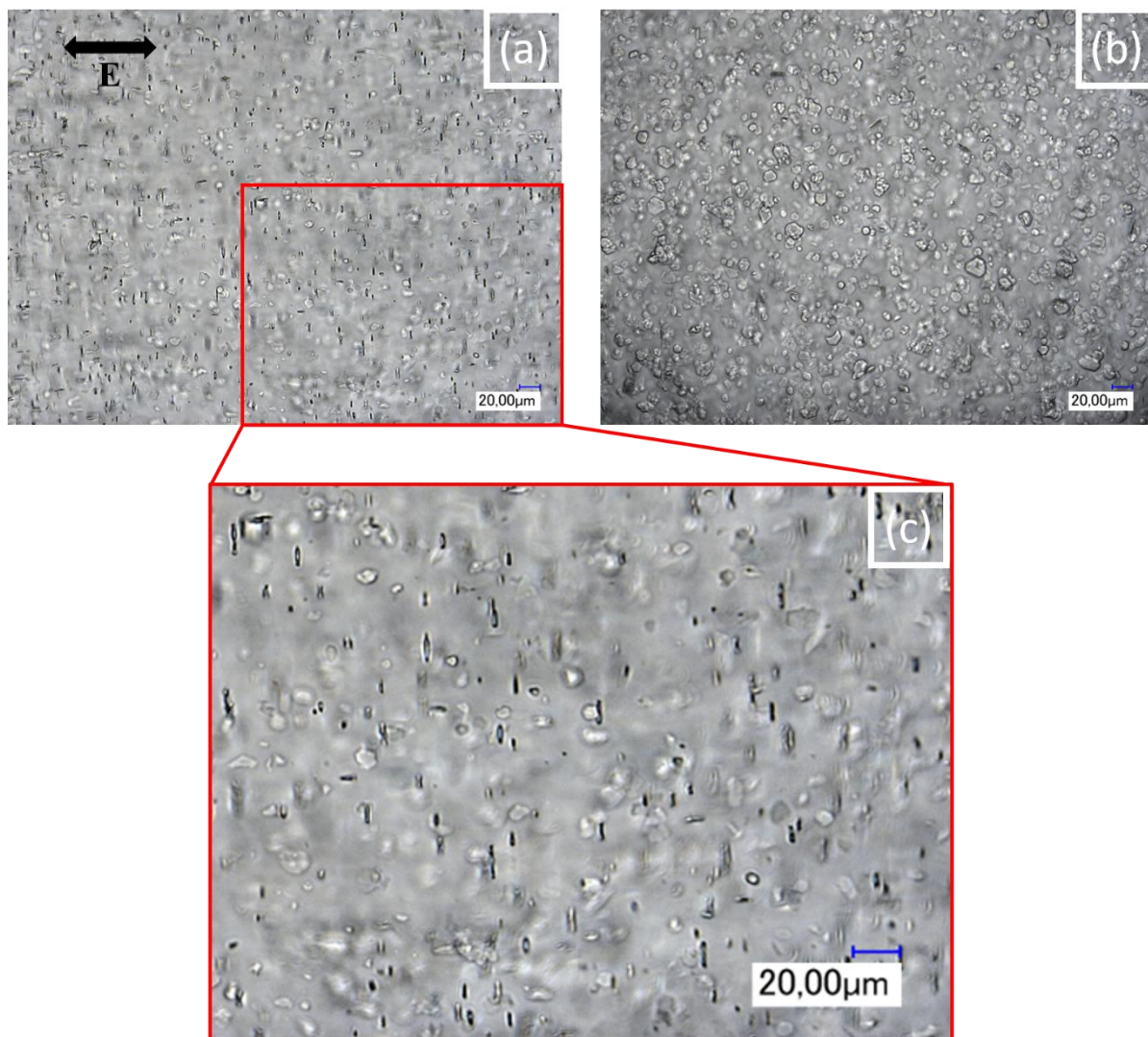


Figure VI-12: Epoxy/alumina composite after polymerization. (a) with electric field, (b) zoom, (c) without electric field.

VI.2.c. Epoxy-Alumina-BaTiO<sub>3</sub> three phase composite

In the previous section and in chapter IV, we developed the possibility of elaborating anisotropic composites. A further step toward “materials adapted to systems” is to control properties in more than one direction to obtain 3D anisotropic composites. The idea to achieve this kind of material was to combine the methods presented in chapters IV and VI. By adding two types of filler responding differently at a given frequency, it might be possible to chain one type of filler in the direction of the electric field and orient the second filler perpendicularly to the electric field.

The experiment performed was the same as that presented in VI.2.b, with the addition of BaTiO<sub>3</sub> fillers.

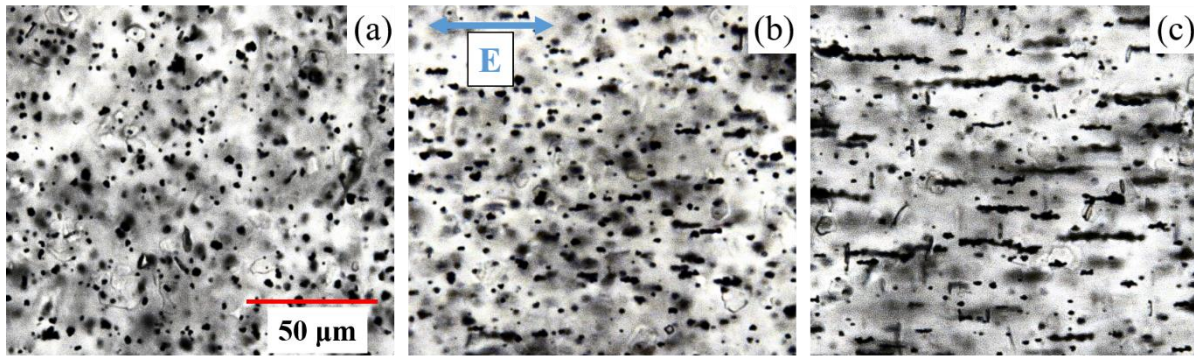


Figure VI-13: Epoxy/Al<sub>2</sub>O<sub>3</sub>/BaTiO<sub>3</sub> composite. The matrix is filled with 0.27 vol% of alumina and 0.29 vol% of BaTiO<sub>3</sub>. ac electric field is 400 V/mm. (a) before electric field application, (b) 1 min of electric field and (c) 5 min.

Before applying the electric field in Figure VI-13 (a), the alumina and BaTiO<sub>3</sub> particles are randomly dispersed; alumina is less visible than BaTiO<sub>3</sub> due to its semi-transparency. After 1 min of electric field, small chains of BaTiO<sub>3</sub> are formed, while there are no *c*-oriented particles. After 5 min under electric field (Figure VI-13), the BaTiO<sub>3</sub> chains have grown and it is possible to observe alumina particles in *c*-orientation. This result is very encouraging, as it is the first time that anisotropic composites with two different orientations were observed. In order to study how the particles interact with each other, a second attempt was performed with 3 times the amount of alumina and half the amount of BaTiO<sub>3</sub>. Interesting particle configurations were observed with this specific filler content (Figure VI-14 and Figure VI-15).

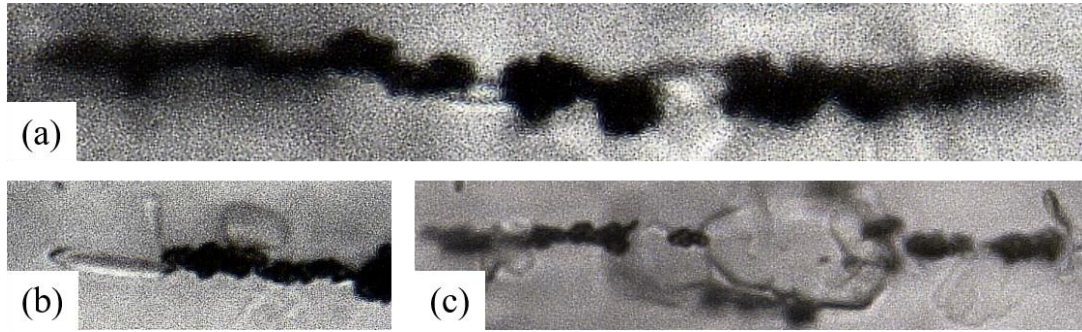


Figure VI-14: alumina particles inserted in BaTiO<sub>3</sub> chains, in *a*-orientation. (a) and (c) inside the chain, (b) at the end of the chain.

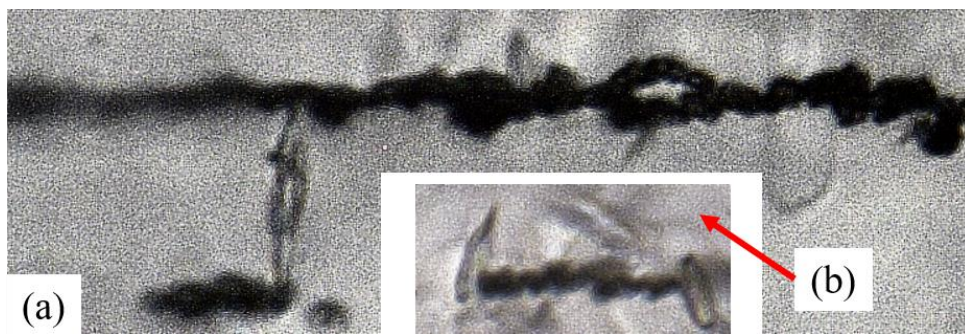


Figure VI-15: (a) alumina particle in *c*-orientation connecting to BaTiO<sub>3</sub> chain, (c) alumina.

Some BaTiO<sub>3</sub> chains presented alumina particles inside (Figure VI-14 (a) and (c)) or at the end (Figure VI-14 (b)) of the chain in *a*-orientation. Other chains had alumina in *c*-orientation (Figure VI-15 (b)); and in some cases, two chains were connected side by side with an alumina particle in *c*-orientation (Figure VI-15 (a)). These different configurations show the complexity of the structures that can exist in such composites. Some of these behaviors might be beneficial for composite properties, but some might, on the contrary, degrade performance in comparison to a one-phase composite. For example, when an alumina particle is inserted in a BaTiO<sub>3</sub> chain, as it has lower permittivity, it should decrease the overall impact of the chain on composite permittivity. This is verified from the curve plotted in Figure VI-16. When the permittivity of the ellipsoid inserted in the chain decreases, global permittivity also decreases. However, it is worth noting that permittivity is stable over a wide range, and the drop in the permittivity is probably related to the difference between the matrix and the ellipsoid permittivity rather than the difference between the ellipsoid and the sphere permittivity.



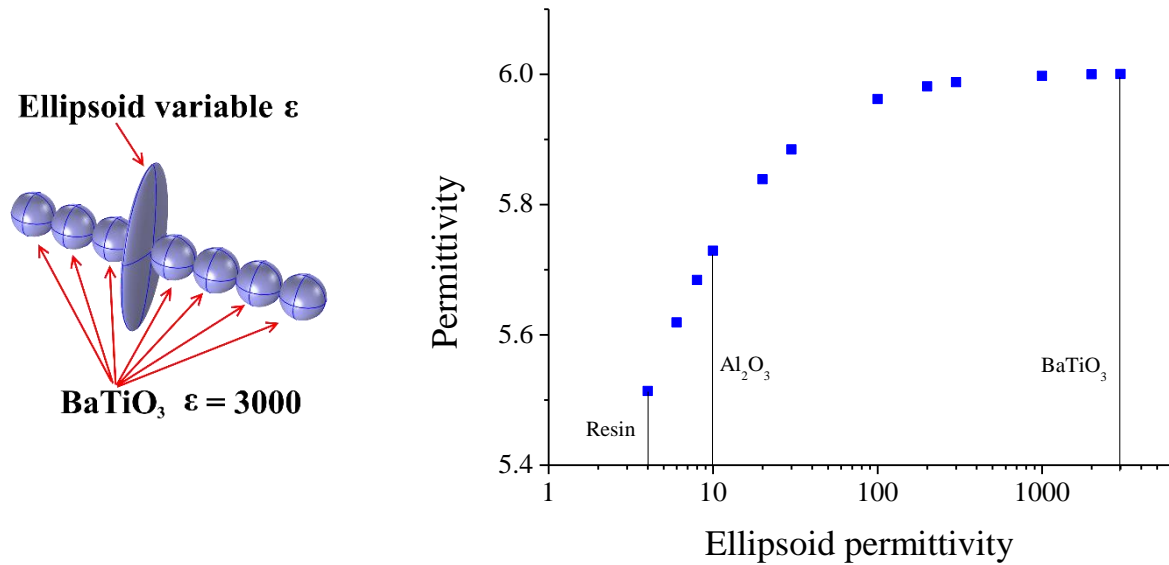


Figure VI-16: Computation of the change in permittivity for a composite with a chain of BaTiO<sub>3</sub> with an ellipsoid inserted.

### VI.3. Conclusion

This early work on the possibility of controlling the orientation of anisotropic particles perpendicular to the electric field highlights great opportunities as well as great challenges to tackle.

The ability to orient a particle perpendicularly relative to the electric field direction allows the elaboration of anisotropic composites in a direction which was until now never foreseen.

### VI.4. Perspectives

#### VI.4.a. Perspectives for anisotropic composite with perpendicular orientation

In the last section, we elaborated a three-phase anisotropic composite with controlled anisotropy in two directions. This proof-of-concept is an important step for multifunctional materials, opening the path to controlling material properties in every direction. However, as seen in this chapter, there are still many improvements to come before controlling every aspect of this kind of anisotropic composite. The first step will be to figure out why all the particles did not have the same orientation. If this is due to the nature of the fillers, it will be necessary to study a different type of particle to find the appropriate fillers. Local characterization on hard composite could be performed, such as chemical analysis with SEM or TEM in diffraction, to determine if differences exist between particles in *c*- and in *a*-orientation.

The interaction between the two kinds of particles leads to mixed chains. The impact of these configurations will have to be studied. This might emphasize the “law” in composites which states that



---

there is always a trade-off between the matrix and filler properties, and so for these specific materials, between the matrix and the different filler properties.

Many perspectives of this study are being considered to work at higher filler content, which will undoubtedly lead to strong interparticle interactions. In order to obtain better results, the particles used for *c*-orientation should present a high aspect ratio [175]–[177]. This is important, because particles in *c*-orientation will not form chains in the direction of their longest axis, but they will preferentially stack in the direction of the electric field.

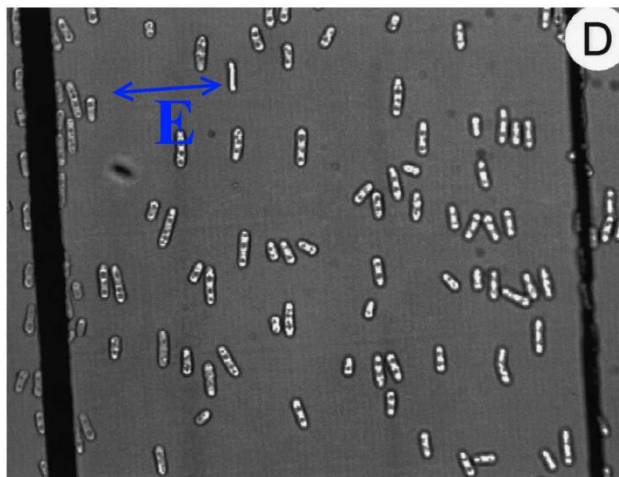


Figure VI-17: Cells in *c*-orientation, with some laterally stacked [166].

It was shown in chapter IV that the online characterization method enables us to understand, and thus to optimize, the elaboration of anisotropic composites. However, for materials with particles orienting perpendicularly, the properties in the direction of the applied electric field do not increase; it should actually result in a slight decrease in permittivity [48]. Consequently, the method shown in chapter IV might not be the best method for monitoring the structure evolution of this type of material, so new markers should be sought.

To the best of the author's knowledge, *c*-orientation of metallic or conductive particles (CNT) has never been shown. The conditions for *c*-orientation might not be met with these particles, however, appropriate surface modification might enable it.

Many innovative applications could be achieved thanks to electro-orientation, such as materials with switchable properties.

#### *VI.4.b. General Perspective*

Throughout this thesis dissertation, we demonstrated the ability to control the structuration of anisotropic composites. Chapters IV and V focused on refining the methods for tailoring anisotropic composites with fillers chained in the direction of the electric field. These materials have been known for two

decades, and the intended applications developed today have been (in most cases) predicted by Randall *et al.* in the diagram we presented in section II.1, Figure 0-7 [95].

In the last chapter, a proof-of-concept enabling composite tailoring perpendicularly to the direction of the electric field was presented. Inspired by the Randall diagram, we attempted to give clues, in the following scheme, of what could be done with this new structuring tool.



Figure VI-18: Potential applications of anisotropic, solid, and liquid composites. The inner circle corresponds to liquid composites, the outer circles to solid composites.





# Conclusion

---

## CONCLUSION

The starting point of this thesis was the following question: “Is it possible, based on a predictive approach, to tailor the structure of a composite from isotropic to anisotropic when applying an electric field?” In order to answer to this question, a roadmap, at the crossover between theoretical, numerical, and experimental studies, was proposed to enable the fine-tuning of anisotropic composite properties.

- i) The first step toward our goal was to approach the problem from a theoretical angle to point out the forces and parameters involved in material tailoring, and then to propose a model making it possible to simulate the structuration of those composites.
- ii) The main parameters being identified, the second step was to measure them and develop characterization methods, if necessary.
- iii) Once the parameters were fully characterized, the materials were elaborated while monitoring structuration by measuring a relevant marker. The chosen marker had to be accessible both experimentally and numerically to allow further comparison.
- iv) Once obtained, the materials were characterized to confirm the accurate control of composite properties.
- v) The last step was to verify the predictive nature and the robustness of the developed model by comparing experimental and numerical results.

Following this roadmap, the work accomplished resulted in several contributions for the elaboration of anisotropic composites. After identifying the key parameters and developing the chaining model, the need to characterize particle permittivities was apparent. As the existing methods for measuring powder material permittivity were not fully satisfactory, a new way, adapted from biomedical field, was adapted to ceramic particles. This method proved able to measure the permittivity of BaTiO<sub>3</sub> and SrTiO<sub>3</sub> particles. Regarding the current limitations of this method, further adjustments are still to be developed to solve sedimentation issues and to allow measurement for nanoparticles.

Another important contribution was to identify an appropriate marker for online monitoring structure evolution during elaboration of the anisotropic composite. We were able to link this marker experimentally to the chaining dynamics by optical observation. This marker, for high permittivity ceramic fillers, was found to be the permittivity of the composite. This enabled us to develop a method that numerically bridges the simulated chaining dynamics to the macroscopic permittivity derived from solving the Laplace equation by FEM at each time-step. The latter development unlocked the possibility to compare the numerical results to experimental results to verify the model’s robustness and ability to integrate the key process parameters, namely matrix and filler permittivity, filler content, viscosity, and electric field magnitude and waveform.

---

Lastly, in a forward-looking work, we offered a proof-of-concept for a new way to tailor materials perpendicularly in the direction of the electric field.

The author hopes that this thesis sheds some light on the understanding of the complex phenomena occurring in the electric field tailoring of materials. The methodology of coupling on-line monitoring to numerical predictive tools in material elaboration is seen as an example of our research team motto: “understanding for design”.





# References

---

**REFERENCES**

- [1] M. Ciappa, “Selected failure mechanisms of modern power modules,” *Microelectron. Reliab.*, vol. 42, no. 4–5, pp. 653–667, April 2002.
- [2] D. L. Saums, “Thermal Interface Materials: Purpose, Classification, Applications,” presented at the ECPE Workshop: Advances in Thermal Materials, Components and Systems, Nüremberg, Dec-2015.
- [3] J. W. Kolar, “Vision - Power Electronics 2025.”, available at <http://tinyurl.com/Kolar-Vision>.
- [4] G. C. Montanari, C. Laurent, G. Teyssedre, A. Campus, and U. H. Nilsson, “From LDPE to XLPE: investigating the change of electrical properties. Part I. space charge, conduction and lifetime,” *IEEE Trans. Dielectr. Electr. Insul.*, vol. 12, no. 3, pp. 438–446, Jun. 2005.
- [5] Z.-M. Dang, J.-K. Yuan, J.-W. Zha, T. Zhou, S.-T. Li, and G.-H. Hu, “Fundamentals, processes and applications of high-permittivity polymer–matrix composites,” *Prog. Mater. Sci.*, vol. 57, no. 4, pp. 660–723, May 2012.
- [6] D. W. van Krevelen and K. te Nijenhuis, *Properties of polymers: their correlation with chemical structure: their numerical estimation and prediction from additive group contributions*, 4th, completely ed. Amsterdam: Elsevier, 2009.
- [7] L. Zhang, Q.-Q. Ni, A. Shiga, Y. Fu, and T. Natsuki, “Synthesis and mechanical properties of polybenzimidazole nanocomposites reinforced by vapor grown carbon nanofibers,” *Polym. Compos.*, vol. 31, no. 3, pp. 491–496, Mar. 2010.
- [8] M. F. Ashby, *Materials selection in mechanical design*. Amsterdam; Boston: Butterworth-Heinemann, 2005.
- [9] “Summary of properties of Kapton - Dupont, available at <http://www.dupont.com/content/dam/dupont/products-and-services/membranes-and-films/polyimide-films/documents/DEC-Kapton-summary-of-properties.pdf>, 2016.” .
- [10] U. Gaur and B. Wunderlich, “The Glass Transition Temperature of Polyethylene,” *Macromolecules*, vol. 13, no. 2, pp. 445–446, Mar. 1980.
- [11] R. Balint, N. J. Cassidy, and S. H. Cartmell, “Conductive polymers: Towards a smart biomaterial for tissue engineering,” *Acta Biomater.*, vol. 10, no. 6, pp. 2341–2353, June 2014.
- [12] A. R. Blythe, “Measurement Techniques for Polymeric Solids Electrical resistivity measurements of polymer materials,” *Polym. Test.*, vol. 4, no. 2, pp. 195–209, Jan. 1984.
- [13] H. K. Kim and F. G. Shi, “Thickness dependent dielectric strength of a low-permittivity dielectric film,” *IEEE Trans. Dielectr. Electr. Insul.*, vol. 8, no. 2, pp. 248–252, avril 2001.
- [14] G. Maier, “Low dielectric constant polymers for microelectronics,” *Prog. Polym. Sci.*, vol. 26, no. 1, pp. 3–65, Feb. 2001.
- [15] Z. Zhang, Q. Meng, and T. C. M. Chung, “Energy storage study of ferroelectric poly(vinylidene fluoride-trifluoroethylene-chlorotrifluoroethylene) terpolymers,” *Polymer*, vol. 50, no. 2, pp. 707–715, Jan. 2009.
- [16] P. Boch and J.-C. Nièpce, Eds., *Ceramic materials: processes, properties and applications*. London: ISTE, 2007.
- [17] K. E. Spear, “Diamond—Ceramic Coating of the Future,” *J. Am. Ceram. Soc.*, vol. 72, no. 2, pp. 171–191, Feb. 1989.
- [18] R. Zhang, T.-R. Wei, B.-P. Zhang, K. Wang, D. Ichigozaki, and J.-F. Li, “Low thermal conductivity of Bi<sub>2</sub>Mo<sub>2</sub>O<sub>9</sub> ceramics,” *J. Alloys Compd.*, vol. 646, pp. 298–302, Oct. 2015.
- [19] M. A. Subramanian, D. Li, N. Duan, B. A. Reisner, and A. W. Sleight, “High Dielectric Constant in ACu<sub>3</sub>Ti<sub>4</sub>O<sub>12</sub> and ACu<sub>3</sub>Ti<sub>3</sub>FeO<sub>12</sub> Phases,” *J. Solid State Chem.*, vol. 151, no. 2, pp. 323–325, May 2000.
- [20] T. Lebey, V. Bley, S. Guillemet, M. Boulos, and B. Durand, “Origin of the colossal permittivity and possible application of CCT ceramics,” 2005, vol. 2, pp. 1248–1253.
- [21] Y. Xu, D. D. L. Chung, and C. Mroz, “Thermally conducting aluminum nitride polymer-matrix composites,” *Compos. Part Appl. Sci. Manuf.*, vol. 32, no. 12, pp. 1749–1757, Dec. 2001.

- 
- [22] H. Ishida and S. Rimdusit, "Very high thermal conductivity obtained by boron nitride-filled polybenzoxazine," *Thermochim. Acta*, vol. 320, no. 1–2, pp. 177–186, Nov. 1998.
- [23] K. Yu, H. Wang, Y. Zhou, Y. Bai, and Y. Niu, "Enhanced dielectric properties of BaTiO<sub>3</sub>/poly(vinylidene fluoride) nanocomposites for energy storage applications," *J. Appl. Phys.*, vol. 113, no. 3, p. 34105, Jan. 2013.
- [24] J. Li, P. Khanchaitit, K. Han, and Q. Wang, "New Route Toward High-Energy-Density Nanocomposites Based on Chain-End Functionalized Ferroelectric Polymers," *Chem. Mater.*, vol. 22, no. 18, pp. 5350–5357, Sep. 2010.
- [25] E. Venkatragavaraj, B. Satish, P. R. Vinod, and M. S. Vijaya, "Piezoelectric properties of ferroelectric PZT-polymer composites," *J. Phys. Appl. Phys.*, vol. 34, no. 4, p. 487, 2001.
- [26] B.-H. Xie, X. Huang, and G.-J. Zhang, "High thermal conductive polyvinyl alcohol composites with hexagonal boron nitride microplatelets as fillers," *Compos. Sci. Technol.*, vol. 85, pp. 98–103, Aug. 2013.
- [27] M. Roy, J. K. Nelson, R. K. MacCrone, L. S. Schadler, C. W. Reed, and R. Keefe, "Polymer nanocomposite dielectrics—the role of the interface," *IEEE Trans. Dielectr. Electr. Insul.*, vol. 12, no. 4, pp. 629–643, Aug. 2005.
- [28] T. Tanaka, A. Nose, Y. Ohki, and Y. Murata, "PD Resistance Evaluation of LDPE/MgO Nanocomposite by a Rod-to-Plane Electrode System," in *2006 IEEE 8th International Conference on Properties applications of Dielectric Materials*, 2006, pp. 319–322.
- [29] T. Tanaka and T. Iizuka, "Generic PD resistance characteristics of polymer nanocomposites," in *2010 Annual Report Conference on Electrical Insulation and Dielectric Phenomena (CEIDP)*, 2010, pp. 1–4.
- [30] Y.-Y. Wang, T.-E. Hsieh, I.-C. Chen, and C.-H. Chen, "Direct Encapsulation of Organic Light-Emitting Devices (OLEDs) Using Photo-Curable co-Polyacrylate/Silica Nanocomposite Resin," *IEEE Trans. Adv. Packag.*, vol. 30, no. 3, pp. 421–427, Aug. 2007.
- [31] J. K. Nelson, Y. Hu, and J. Thiticharoenpong, "Electrical properties of TiO<sub>2</sub> nanocomposites," in *Conference on Electrical Insulation and Dielectric Phenomena, 2003. Annual Report*, 2003, pp. 719–722.
- [32] K. R. Reddy, K.-P. Lee, Y. Lee, and A. I. Gopalan, "Facile synthesis of conducting polymer–metal hybrid nanocomposite by in situ chemical oxidative polymerization with negatively charged metal nanoparticles," *Mater. Lett.*, vol. 62, no. 12–13, pp. 1815–1818, Apr. 2008.
- [33] H. S. Tekce, D. Kumlutas, and I. H. Tavman, "Effect of Particle Shape on Thermal Conductivity of Copper Reinforced Polymer Composites," *J. Reinf. Plast. Compos.*, vol. 26, no. 1, pp. 113–121, Jan. 2007.
- [34] E. T. Thostenson, C. Li, and T.-W. Chou, "Nanocomposites in context," *Compos. Sci. Technol.*, vol. 65, no. 3–4, pp. 491–516, Mar. 2005.
- [35] G. Gao, T. Çagin, and W. A. G. III, "Energetics, structure, mechanical and vibrational properties of single-walled carbon nanotubes," *Nanotechnology*, vol. 9, no. 3, p. 184, 1998.
- [36] C. Lee, X. Wei, J. W. Kysar, and J. Hone, "Measurement of the Elastic Properties and Intrinsic Strength of Monolayer Graphene," *Science*, vol. 321, no. 5887, pp. 385–388, Jul. 2008.
- [37] J.-U. Lee, D. Yoon, and H. Cheong, "Estimation of Young's Modulus of Graphene by Raman Spectroscopy," 08-Aug-2012. [Online]. Available: <http://pubs.acs.org/doi/abs/10.1021/nl301073q>. [Accessed: 23-Aug-2016].
- [38] J. Hone, M. Whitney, C. Piskoti, and A. Zettl, "Thermal conductivity of single-walled carbon nanotubes," *Phys. Rev. B*, vol. 59, no. 4, pp. R2514–R2516, Jan. 1999.
- [39] J. Wang, J. Huang, R. Yan, F. Wang, W. Cheng, Q. Guo, and J. Wang, "Graphene microsheets from natural microcrystalline graphite minerals: scalable synthesis and unusual energy storage," *J. Mater. Chem. A*, vol. 3, no. 6, pp. 3144–3150, Jan. 2015.
- [40] C. L. Kane, E. J. Mele, R. S. Lee, J. E. Fischer, P. Petit, H. Dai, A. Thess, R. E. Smalley, A. R. M. Verschueren, S. J. Tans, and C. Dekker, "Temperature-dependent resistivity of single-wall carbon nanotubes," *EPL Europhys. Lett.*, vol. 41, no. 6, p. 683, Mar. 1998.
- [41] W.-T. Hong and N.-H. Tai, "Investigations on the thermal conductivity of composites reinforced with carbon nanotubes," *Diam. Relat. Mater.*, vol. 17, no. 7–10, pp. 1577–1581, July 2008.

- [42] S. Stankovich, D. A. Dikin, G. H. B. Dommett, K. M. Kohlhaas, E. J. Zimney, E. A. Stach, R. D. Piner, S. T. Nguyen, and R. S. Ruoff, "Graphene-based composite materials," *Nature*, vol. 442, no. 7100, pp. 282–286, Jul. 2006.
- [43] L. Tao, E. Cinquanta, D. Chiappe, C. Grazianetti, M. Fanciulli, M. Dubey, A. Molle, and D. Akinwande, "Silicene field-effect transistors operating at room temperature," *Nat. Nanotechnol.*, vol. 10, no. 3, pp. 227–231, Feb. 2015.
- [44] K. F. Mak, C. Lee, J. Hone, J. Shan, and T. F. Heinz, "Atomically Thin MoS<sub>2</sub>: A New Direct-Gap Semiconductor," *Phys. Rev. Lett.*, vol. 105, no. 13, p. 136805, Sep. 2010.
- [45] T. Tanaka, "Dielectric nanocomposites with insulating properties," *IEEE Trans. Dielectr. Electr. Insul.*, vol. 12, no. 5, pp. 914–928, Oct. 2005.
- [46] "Web of Science [v.5.22.3] - Web of Science," 2016. [Online]. Available: [https://apps.webofknowledge.com/WOS\\_GeneralSearch\\_input.do?product=WOS&search\\_mode=GeneralSearch&SID=S1cvR3eOWbLM6Y2HgT1&preferencesSaved=](https://apps.webofknowledge.com/WOS_GeneralSearch_input.do?product=WOS&search_mode=GeneralSearch&SID=S1cvR3eOWbLM6Y2HgT1&preferencesSaved=). [Accessed: 16-Sep-2016].
- [47] *COMSOL Multiphysics®*, Version 4.2, COMSOL, Inc., Burlington, MA, USA, 2011. .
- [48] Y. U. Wang and D. Q. Tan, "Computational study of filler microstructure and effective property relations in dielectric composites," *J. Appl. Phys.*, vol. 109, no. 10, p. 104102, May 2011.
- [49] L. F. Chen, Y. P. Hong, X. J. Chen, Q. L. Wu, Q. J. Huang, and X. T. Luo, "Preparation and properties of polymer matrix piezoelectric composites containing aligned BaTiO<sub>3</sub> whiskers," *J. Mater. Sci.*, vol. 39, no. 9, pp. 2997–3001.
- [50] H. Tang, Y. Lin, and H. A. Sodano, "Enhanced Energy Storage in Nanocomposite Capacitors through Aligned PZT Nanowires by Uniaxial Strain Assembly," *Adv. Energy Mater.*, vol. 2, no. 4, pp. 469–476, Jan. 2012.
- [51] M. Saito, T. Daian, K. Hayashi, and S. Izumida, "Fabrication of a polymer composite with periodic structure by the use of ultrasonic waves," *J. Appl. Phys.*, vol. 83, no. 7, pp. 3490–3494, Apr. 1998.
- [52] S. Yamahira, S. Hatanaka, M. Kuwabara, and S. Asai, "Orientation of Fibers in Liquid by Ultrasonic Standing Waves," *Jpn. J. Appl. Phys.*, vol. 39, no. 6R, p. 3683, Jun. 2000.
- [53] M.-S. Scholz, B. W. Drinkwater, and R. S. Trask, "Ultrasonic assembly of anisotropic short fibre reinforced composites," *Ultrasonics*, vol. 54, no. 4, pp. 1015–1019, Apr. 2014.
- [54] T. Prasse, J.-Y. Cavallé, and W. Bauhofer, "Electric anisotropy of carbon nanofibre/epoxy resin composites due to electric field induced alignment," *Compos. Sci. Technol.*, vol. 63, no. 13, pp. 1835–1841, Oct. 2003.
- [55] V. Tomer, C. A. Randall, G. Polizos, J. Kostelnick, and E. Manias, "High- and low-field dielectric characteristics of dielectrophoretically aligned ceramic/polymer nanocomposites," *J. Appl. Phys.*, vol. 103, no. 3, p. 34115, Feb. 2008.
- [56] R. B. Ladani, S. Wu, A. J. Kinloch, K. Ghorbani, J. Zhang, A. P. Mouritz, and C. H. Wang, "Multifunctional properties of epoxy nanocomposites reinforced by aligned nanoscale carbon," *Mater. Des.*, vol. 94, pp. 554–564, Mar. 2016.
- [57] E. C. Sengezer, G. D. Seidel, and R. J. Bodnar, "Phenomenological characterization of fabrication of aligned pristine-SWNT and COOH-SWNT nanocomposites via dielectrophoresis under AC electric field," *Polym. Compos.*, vol. 36, no. 7, pp. 1266–1279, July 2015.
- [58] A. I. Oliva-Avilés, F. Avilés, V. Sosa, A. I. Oliva, and F. Gamboa, "Dynamics of carbon nanotube alignment by electric fields," *Nanotechnology*, vol. 23, no. 46, p. 465710, 2012.
- [59] V. Tomer and C. A. Randall, "High field dielectric properties of anisotropic polymer-ceramic composites," *J. Appl. Phys.*, vol. 104, no. 7, p. 74106, Oct. 2008.
- [60] V. Tomer, G. Polizos, C. A. Randall, and E. Manias, "Polyethylene nanocomposite dielectrics: Implications of nanofiller orientation on high field properties and energy storage," *J. Appl. Phys.*, vol. 109, no. 7, p. 74113, Apr. 2011.
- [61] S. Wu, R. B. Ladani, J. Zhang, E. Bafekrpour, K. Ghorbani, A. P. Mouritz, A. J. Kinloch, and C. H. Wang, "Aligning multilayer graphene flakes with an external electric field to improve multifunctional properties of epoxy nanocomposites," *Carbon*, vol. 94, pp. 607–618, Nov. 2015.
- [62] K. Ushijima, M. Kozako, and M. Hikita, "Orientation effect of nano-alumina coated conductive fillers on dielectric properties of epoxy composites," in *Proceedings of 2014 International Symposium on Electrical Insulating Materials (ISEIM)*, 2014, pp. 323–326.
- [63] S. Gangwal, O. J. Cayre, and O. D. Velev, "Dielectrophoretic Assembly of Metallodielectric Janus Particles in AC Electric Fields," *Langmuir*, vol. 24, no. 23, pp. 13312–13320, Dec. 2008.

- 
- [64] K. H. Bhatt and O. D. Velev, "Control and Modeling of the Dielectrophoretic Assembly of On-Chip Nanoparticle Wires," *Langmuir*, vol. 20, no. 2, pp. 467–476, Jan. 2004.
- [65] H. Khanbarez, S. van der Zwaag, and W. A. Groen, "Effect of dielectrophoretic structuring on piezoelectric and pyroelectric properties of lead titanate-epoxy composites," *Smart Mater. Struct.*, vol. 23, no. 10, p. 105030, 2014.
- [66] A. P. Gast and C. F. Zukoski, "Electrorheological fluids as colloidal suspensions," *Adv. Colloid Interface Sci.*, vol. 30, pp. 153–202, Jan. 1989.
- [67] W. Wen, X. Huang, S. Yang, K. Lu, and P. Sheng, "The giant electrorheological effect in suspensions of nanoparticles," *Nat. Mater.*, vol. 2, no. 11, pp. 727–730, Nov. 2003.
- [68] M. Parthasarathy and D. J. Klingenberg, "Electrorheology: Mechanisms and models," *Mater. Sci. Eng. R Rep.*, vol. 17, no. 2, pp. 57–103, Oct. 1996.
- [69] S. Batra and M. Cakmak, "Ultra-capacitor flexible films with tailored dielectric constants using electric field assisted assembly of nanoparticles," *Nanoscale*, vol. 7, no. 48, pp. 20571–20583, Dec. 2015.
- [70] C. A. Martin, J. K. Sandler, A. H. Windle, M.-K. Schwarz, W. Bauhofer, K. Schulte, and M. S. P. Shaffer, "Electric field-induced aligned multi-wall carbon nanotube networks in epoxy composites," *Polymer*, vol. 46, no. 3, pp. 877–886, Jan. 2005.
- [71] C. Park and R. E. Robertson, "Mechanical properties of resin composites with filler particles aligned by an electric field," *Dent. Mater.*, vol. 14, no. 6, pp. 385–393, Nov. 1998.
- [72] D. A. van den Ende, B. F. Bory, W. A. Groen, and S. van der Zwaag, "Improving the d33 and g33 properties of 0-3 piezoelectric composites by dielectrophoresis," *J. Appl. Phys.*, vol. 107, no. 2, p. 24107, Jan. 2010.
- [73] T. B. Jones, *Electromechanics of particles*. Cambridge ; New York: Cambridge University Press, 1995.
- [74] S. Jin, T. N. Tiefel, and R. Wolfe, "Directionally-conductive, optically-transparent composites by magnetic alignment," *IEEE Trans. Magn.*, vol. 28, no. 5, pp. 2211–2213, Sep. 1992.
- [75] T. Nagai, N. Aoki, Y. Ochiai, and K. Hoshino, "Electric Conductivity-Tunable Transparent Flexible Nanowire-Filled Polymer Composites: Orientation Control of Nanowires in a Magnetic Field," *ACS Appl. Mater. Interfaces*, vol. 3, no. 7, pp. 2341–2348, July 2011.
- [76] E. S. Choi, J. S. Brooks, D. L. Eaton, M. S. Al-Haik, M. Y. Hussaini, H. Garmestani, D. Li, and K. Dahmen, "Enhancement of thermal and electrical properties of carbon nanotube polymer composites by magnetic field processing," *J. Appl. Phys.*, vol. 94, no. 9, pp. 6034–6039, Nov. 2003.
- [77] Z. Varga, G. Filipcsei, and M. Zrínyi, "Smart composites with controlled anisotropy," *Polymer*, vol. 46, no. 18, pp. 7779–7787, Aug. 2005.
- [78] P. Iversen and D. J. Lacks, "A life of its own: The tenuous connection between Thales of Miletus and the study of electrostatic charging," *J. Electrostat.*, vol. 70, no. 3, pp. 309–311, June 2012.
- [79] *Amber and fur*, available at: <http://www.newtonsapple.org.uk/static-electricity-triboelectric-series/>.
- [80] W. Gilbert, *De Magnete*. London: Peter Short, 1600.
- [81] J. H. Winckler, *Essai sur la nature, les effets et les causes de l'électricité*. S. Jorry, 1748.
- [82] J. Priestley, *The History And Present State Of Electricity: With Original Experiments*. Dodsley, Johnson and Davenport, Cadell, 1767.
- [83] J. C. Maxwell, *A treatise on electricity and magnetism*. Oxford : Clarendon Press, 1873.
- [84] H. Stafford Hatfield, *Means and process of separating substances one from another*. Google Patents, 1924.
- [85] H. A. Pohl, "The Motion and Precipitation of Suspensoids in Divergent Electric Fields," *J. Appl. Phys.*, vol. 22, no. 7, pp. 869–871, Jul. 1951.
- [86] H. A. Pohl, *Dielectrophoresis: the behavior of neutral matter in nonuniform electric fields*. Cambridge University Press, 1978.
- [87] E. Muth, "Ueber die Erscheinung der Perlschnurkettenbildung von Emulsionspartikelchen unter Einwirkung eines Wechselfeldes," *Kolloid-Z.*, vol. 41, no. 2, pp. 97–102, Feb. 1927.
- [88] W. Krasny-Ergen, "Nicht thermische wirkungen elektrischer schwingungen auf kolloide," *Hochfrequenztech Elektroakust.*, vol. 48, pp. 126–133, 1936.
- [89] P. Liebesny, "Athermic short wave therapy," *Arch. Phys. Ther.*, vol. 19, pp. 736–740, 1939.

- [90] R. Pethig, “Review Article—Dielectrophoresis: Status of the theory, technology, and applications,” *Biomicrofluidics*, vol. 4, no. 2, p. 22811, Jun. 2010.
- [91] H. A. Pohl and J. S. Crane, “Dielectrophoresis of Cells,” *Biophys. J.*, vol. 11, no. 9, pp. 711–727, Sep. 1971.
- [92] U. Zimmermann, “Electric field-mediated fusion and related electrical phenomena,” *Biochim. Biophys. Acta BBA - Rev. Biomembr.*, vol. 694, no. 3, pp. 227–277, Nov. 1982.
- [93] W. M. Winslow, *Method and means for translating electrical impulses into mechanical force*. Google Patents, 1947.
- [94] W. M. Winslow, “Induced Fibrillation of Suspensions,” *J. Appl. Phys.*, vol. 20, no. 12, pp. 1137–1140, Dec. 1949.
- [95] C. A. Randall, C. P. Bowen, T. R. ShROUT, G. L. Messing, and R. E. Newnham, “Dielectrophoretic assembly: a novel concept in advanced composite fabrication,” in *Proceedings of the Fourth International Conference on Electrorheological Fluids*, Austria, 1993, pp. 516–525.
- [96] S. Axelsson, E. E. B. Campbell, L. M. Jonsson, J. Kinaret, S. W. Lee, Y. W. Park, and M. Sveningsson, “Theoretical and experimental investigations of three-terminal carbon nanotube relays,” *New J. Phys.*, vol. 7, no. 1, p. 245, 2005.
- [97] S. Banerjee, B. E. White, L. Huang, B. J. Rego, S. O’Brien, and I. P. Herman, “Precise positioning of single-walled carbon nanotubes by ac dielectrophoresis,” *J. Vac. Sci. Technol. B*, vol. 24, no. 6, pp. 3173–3178, Nov. 2006.
- [98] B. R. Burg, F. Lütolf, J. Schneider, N. C. Schirmer, T. Schwamb, and D. Poulikakos, “High-yield dielectrophoretic assembly of two-dimensional graphene nanostructures,” *Appl. Phys. Lett.*, vol. 94, no. 5, p. 53110, Feb. 2009.
- [99] T. B. Jones and G. W. Bliss, “Bubble dielectrophoresis,” *J. Appl. Phys.*, vol. 48, no. 4, pp. 1412–1417, Apr. 1977.
- [100] T. B. Jones, “Liquid dielectrophoresis on the microscale,” *J. Electrostat.*, vol. 51–52, pp. 290–299, mai 2001.
- [101] A. R. Von Hippel, *Dielectrics and waves*. Wiley, 1954.
- [102] S. O. Kasap, *Principles of electronic materials and devices*. Boston: McGraw-Hill, 2006.
- [103] A. Ramos, Ed., *Electrokinetics and Electrohydrodynamics in Microsystems*. Vienna: Springer Vienna, 2011.
- [104] D. Griffiths, *Introduction to Electrodynamics*, 4 edition. Boston: Addison-Wesley, 2012.
- [105] M. Washizu and T. B. Jones, “Multipolar dielectrophoretic force calculation,” *J. Electrostat.*, vol. 33, no. 2, pp. 187–198, Sep. 1994.
- [106] O. Borges, G. Borchard, J. C. Verhoef, A. de Sousa, and H. E. Junginger, “Preparation of coated nanoparticles for a new mucosal vaccine delivery system,” *Int. J. Pharm.*, vol. 299, no. 1–2, pp. 155–166, août 2005.
- [107] R. Hayes, A. Ahmed, T. Edge, and H. Zhang, “Core-shell particles: Preparation, fundamentals and applications in high performance liquid chromatography,” *J. Chromatogr. A*, vol. 1357, pp. 36–52, août 2014.
- [108] C. Casagrande, P. Fabre, E. Raphaël, and M. Veyssié, “‘Janus Beads’: Realization and Behaviour at Water/Oil Interfaces,” *EPL Europhys. Lett.*, vol. 9, no. 3, p. 251, 1989.
- [109] X. Wang, X.-B. Wang, and P. R. C. Gascoyne, “General expressions for dielectrophoretic force and electrorotational torque derived using the Maxwell stress tensor method,” *J. Electrostat.*, vol. 39, no. 4, pp. 277–295, Aug. 1997.
- [110] C. Rosales and K. M. Lim, “Numerical comparison between Maxwell stress method and equivalent multipole approach for calculation of the dielectrophoretic force in single-cell traps,” *Electrophoresis*, vol. 26, no. 11, pp. 2057–2065, June 2005.
- [111] Y. Ai and S. Qian, “DC dielectrophoretic particle-particle interactions and their relative motions,” *J. Colloid Interface Sci.*, vol. 346, no. 2, pp. 448–454, June 2010.
- [112] M. A. Gutiérrez, H. Khanbareh, and S. van der Zwaag, “Computational modeling of structure formation during dielectrophoresis in particulate composites,” *Comput. Mater. Sci.*, vol. 112, Part A, pp. 139–146, Feb. 2016.
- [113] Y. Liu, W. K. Liu, T. Belytschko, N. Patankar, A. C. To, A. Kopacz, and J.-H. Chung, “Immersed electrokinetic finite element method,” *Int. J. Numer. Methods Eng.*, vol. 71, no. 4, pp. 379–405, July 2007.

- 
- [114] M. Washizu and T. B. Jones, "Dielectrophoretic interaction of two spherical particles calculated by equivalent multipole-moment method," in , *Conference Record of the 1994 IEEE Industry Applications Society Annual Meeting, 1994*, 1994, pp. 1483–1490 vol.2.
- [115] B. Techaumnat, B. Eua-arporn, and T. Takuma, "Calculation of electric field and dielectrophoretic force on spherical particles in chain," *J. Appl. Phys.*, vol. 95, no. 3, pp. 1586–1593, Feb. 2004.
- [116] T. B. Jones, R. D. Miller, K. S. Robinson, and W. Y. Fowlkes, "Multipolar interactions of dielectric spheres," *J. Electrostat.*, vol. 22, no. 3, pp. 231–244, Sept. 1989.
- [117] S. Hu, Y. Zhao, and Y. Yang, "Modeling of cellular pearl chain formation using a double photoconductive layer biochip," *J. Electrostat.*, vol. 77, pp. 110–115, Oct. 2015.
- [118] V. Giner, M. Sancho, R. S. Lee, G. Martínez, and R. Pethig, "Transverse dipolar chaining in binary suspensions induced by rf fields," *J. Phys. Appl. Phys.*, vol. 32, no. 10, p. 1182, 1999.
- [119] D. Komesu, M. Mori, S. Ishibe, M. Kozako, and M. Hikita, "Simulation on the microvaristor chain formation in liquid epoxy under electric field," *IEEE Trans. Dielectr. Electr. Insul.*, vol. 23, no. 1, pp. 216–221, Feb. 2016.
- [120] J. Kadaksham, P. Singh, and N. Aubry, "Manipulation of particles using dielectrophoresis," *Mech. Res. Commun.*, pp. 108–122, 2006.
- [121] D. J. Klingenberg, "Simulation of the dynamic oscillatory response of electrorheological suspensions: Demonstration of a relaxation mechanism," *J. Rheol. 1978-Present*, vol. 37, no. 2, pp. 199–214, Mar. 1993.
- [122] A. Limsimarat and B. Techaumnat, "Dynamic simulation using a multipolar model of particles under dielectrophoretic force," *J. Electrostat.*, vol. 65, no. 10–11, pp. 672–679, Oct. 2007.
- [123] *MATLAB®, Version R2013b. The MathWorks, Inc., Natick, MA, USA, 2013.* .
- [124] J. AHRENS, B. GEVECI, and C. LAW, "36 - ParaView: An End-User Tool for Large-Data Visualization A2 - Hansen, Charles D.," in *Visualization Handbook*, C. R. Johnson, Ed. Burlington: Butterworth-Heinemann, 2005, pp. 717–731.
- [125] F. Kremer and A. Schönhals, Eds., *Broadband Dielectric Spectroscopy*. Berlin, Heidelberg: Springer Berlin Heidelberg, 2003.
- [126] E. Warburg, "Ueber die Polarisationscapacität des Platins," *Ann. Phys.*, vol. 311, no. 9, pp. 125–135, Jan. 1901.
- [127] H. Fricke, "A Mathematical Treatment of the Electric Conductivity and Capacity of Disperse Systems ii. The Capacity of a Suspension of Conducting Spheroids Surrounded by a Non-Conducting Membrane for a Current of Low Frequency," *Phys. Rev.*, vol. 26, no. 5, pp. 678–681, Nov. 1925.
- [128] P. B. Ishai, M. S. Talary, A. Caduff, E. Levy, and Y. Feldman, "Electrode polarization in dielectric measurements: a review," *Meas. Sci. Technol.*, vol. 24, no. 10, p. 102001, 2013.
- [129] S. A. Wilson, G. M. Maistros, and R. W. Whatmore, "Structure modification of 0–3 piezoelectric ceramic/polymer composites through dielectrophoresis," *J. Phys. Appl. Phys.*, vol. 38, no. 2, pp. 175–182, Jan. 2005.
- [130] M. Kozako, Z. Valdez-Nava, S. Diahm, S. Dinculescu, and T. Lebey, "Fundamental investigation of dielectric phenomena in epoxy composites during curing process under a uniform electric field," in *2012 Annual Report Conference on Electrical Insulation and Dielectric Phenomena (CEIDP)*, 2012, pp. 574–550.
- [131] Y. Tan, J. Zhang, Y. Wu, C. Wang, V. Koval, B. Shi, H. Ye, R. McKinnon, G. Viola, and H. Yan, "Unfolding grain size effects in barium titanate ferroelectric ceramics," *Sci. Rep.*, vol. 5, p. 9953, May 2015.
- [132] Z.-M. Dang, Y.-F. Yu, H.-P. Xu, and J. Bai, "Study on microstructure and dielectric property of the BaTiO<sub>3</sub>/epoxy resin composites," *Compos. Sci. Technol.*, vol. 68, no. 1, pp. 171–177, Jan. 2008.
- [133] S. Wada, H. Yasuno, T. Hoshina, S.-M. Nam, H. Kakemoto, and T. Tsurumi, "Preparation of nm-Sized Barium Titanate Fine Particles and Their Powder Dielectric Properties," *Jpn. J. Appl. Phys.*, vol. 42, no. 9S, p. 6188, Sep. 2003.
- [134] D. A. Robinson and S. P. Friedman, "A method for measuring the solid particle permittivity or electrical conductivity of rocks, sediments, and granular materials: PERMITTIVITY OR ELECTRICAL CONDUCTIVITY MEASUREMENT," *J. Geophys. Res. Solid Earth*, vol. 108, no. B2, Feb. 2003.

- [135] J. C. M. Garnett, "Colours in Metal Glasses and in Metallic Films," *Philos. Trans. R. Soc. Lond. Math. Phys. Eng. Sci.*, vol. 203, no. 359–371, pp. 385–420, Jan. 1904.
- [136] D. a. G. Bruggeman, "Berechnung verschiedener physikalischer Konstanten von heterogenen Substanzen. I. Dielektrizitätskonstanten und Leitfähigkeiten der Mischkörper aus isotropen Substanzen," *Ann. Phys.*, vol. 416, no. 7, pp. 636–664, Jan. 1935.
- [137] H. Looyenga, "Dielectric constants of heterogeneous mixtures," *Physica*, vol. 31, no. 3, pp. 401–406, Mar. 1965.
- [138] J. R. Birchak, C. G. Gardner, J. E. Hipp, and J. M. Victor, "High dielectric constant microwave probes for sensing soil moisture," *Proc. IEEE*, vol. 62, no. 1, pp. 93–98, 1974.
- [139] K. Lichtenecker, "Dielectric constant of natural and synthetic mixtures," *Phys. Z.*, vol. 27, p. 115, 1926.
- [140] Z.-M. Dang, Y.-Q. Lin, H.-P. Xu, C.-Y. Shi, S.-T. Li, and J. Bai, "Fabrication and Dielectric Characterization of Advanced BaTiO<sub>3</sub>/Polyimide Nanocomposite Films with High Thermal Stability," *Adv. Funct. Mater.*, vol. 18, no. 10, pp. 1509–1517, May 2008.
- [141] Z.-M. Dang, Y. Shen, and C.-W. Nan, "Dielectric behavior of three-phase percolative Ni–BaTiO<sub>3</sub>/polyvinylidene fluoride composites," *Appl. Phys. Lett.*, vol. 81, no. 25, pp. 4814–4816, Dec. 2002.
- [142] S. Ogitani, S. A. Bidstrup-Allen, and P. A. Kohl, "Factors influencing the permittivity of polymer/ceramic composites for embedded capacitors," *IEEE Trans. Adv. Packag.*, vol. 23, no. 2, pp. 313–322, May 2000.
- [143] N. Jayasundere and B. V. Smith, "Dielectric constant for binary piezoelectric 0-3 composites," *J. Appl. Phys.*, vol. 73, no. 5, pp. 2462–2466, Mar. 1993.
- [144] O. Wiener, "Zur theorie der refraktionskonstanten," *Berichteüber Verhandlungen K.-Sächs. Ges. Wissenschaften Leipz.*, pp. 256–277, 1910.
- [145] R. W. Sillars, "The properties of a dielectric containing semiconducting particles of various shapes," *Wirel. Sect. Inst. Electr. Eng. - Proc. Of*, vol. 12, no. 35, pp. 139–155, Jun. 1937.
- [146] A. H. Shivola, "Self-consistency aspects of dielectric mixing theories," *IEEE Trans. Geosci. Remote Sens.*, vol. 27, no. 4, pp. 403–415, July 1989.
- [147] N. G. Green and H. Morgan, "Dielectrophoresis of Submicrometer Latex Spheres. 1. Experimental Results," *J. Phys. Chem. B*, vol. 103, no. 1, pp. 41–50, Jan. 1999.
- [148] P. Marszałek, J. J. Zieliński, and M. Fikus, "Experimental verification of a theoretical treatment of the mechanism of dielectrophoresis," *Bioelectrochem. Bioenerg.*, vol. 22, no. 3, pp. 289–298, Dec. 1989.
- [149] P. R. C. Gascoyne, Y. Huang, R. Pethig, J. Vykoukal, and F. F. Becker, "Dielectrophoretic separation of mammalian cells studied by computerized image analysis," *Meas. Sci. Technol.*, vol. 3, no. 5, p. 439, 1992.
- [150] M. P. Hughes and H. Morgan, "Dielectrophoretic Characterization and Separation of Antibody-Coated Submicrometer Latex Spheres," *Anal. Chem.*, vol. 71, no. 16, pp. 3441–3445, Aug. 1999.
- [151] I. Ermolina and H. Morgan, "The electrokinetic properties of latex particles: comparison of electrophoresis and dielectrophoresis," *J. Colloid Interface Sci.*, vol. 285, no. 1, pp. 419–428, May 2005.
- [152] K. V. I. S. Kaler, J.-P. Xie, T. B. Jones, and R. Paul, "Dual-frequency dielectrophoretic levitation of Canola protoplasts," *Biophys. J.*, vol. 63, no. 1, pp. 58–69, Jul. 1992.
- [153] C. T. O'Konski, "Electric properties of macromolecules. v. theory of ionic polarization in polyelectrolytes," *J. Phys. Chem.*, vol. 64, no. 5, pp. 605–619, May 1960.
- [154] C. Riedel, G. A. Schwartz, R. Arinero, P. Tordjeman, G. Lévêque, A. Alegría, and J. Colmenero, "Nanoscale dielectric properties of insulating thin films: from single point measurements to quantitative images," *Ultramicroscopy*, vol. 110, no. 6, pp. 634–638, May 2010.
- [155] S. D. Senturia and N. F. Sheppard Jr, *Dielectric analysis of thermoset cure*, vol. 80. 1986.
- [156] G. Maistros, H. Block, C. Bucknall, and I. Partridge, "Dielectric monitoring of phase separation during cure of blends of epoxy resin with carboxyl-terminated poly(butadiene-co-acrylonitrile)," *Polymer*, vol. 33, no. 21, pp. 4470–4478, Jan. 1992.
- [157] G. Kortaberria, P. Arruti, and I. Mondragon, "Dielectric monitoring of curing of liquid oligomer-modified epoxy matrices," *Polym. Int.*, vol. 50, no. 9, pp. 957–965, Jan. 2001.



- 
- [158] S. D. Cho, J. Y. Lee, J. G. Hyun, and K. W. Paik, "Study on epoxy/BaTiO<sub>3</sub> composite embedded capacitor films (ECFs) for organic substrate applications," *Mater. Sci. Eng. B*, 2004.
- [159] U. Dassanayake, S. Fraden, and A. van Blaaderen, "Structure of electrorheological fluids," *J. Chem. Phys.*, vol. 112, no. 8, p. 3851, Jan. 2000.
- [160] J. S. Park and D. Saintillan, "Electric-field-induced ordering and pattern formation in colloidal suspensions," *Phys. Rev. E*, vol. 83, no. 4, p. 41409, Apr. 2011.
- [161] V. Myroshnychenko and C. Brosseau, "Finite-element method for calculation of the effective permittivity of random inhomogeneous media," *Phys. Rev. E*, vol. 71, no. 1, p. 16701, Jan. 2005.
- [162] S. Kagami and I. Fukai, "Application of Boundary-Element Method to Electromagnetic Field Problems (Short Papers)," *IEEE Trans. Microw. Theory Tech.*, vol. 32, no. 4, pp. 455–461, Apr. 1984.
- [163] T. Darden, D. York, and L. Pedersen, "Particle mesh Ewald: An N·log(N) method for Ewald sums in large systems," *J. Chem. Phys.*, vol. 98, no. 12, pp. 10089–10092, Jun. 1993.
- [164] R. D. Miller and T. B. Jones, "Electro-orientation of ellipsoidal erythrocytes. Theory and experiment.," *Biophys. J.*, vol. 64, no. 5, pp. 1588–1595, May 1993.
- [165] M. Radu, M. Ionescu, N. Irimescu, K. Iliescu, R. Pologea-Moraru, and E. Kovacs, "Orientation Behavior of Retinal Photoreceptors in Alternating Electric Fields," *Biophys. J.*, vol. 89, no. 5, pp. 3548–3554, Nov. 2005.
- [166] M. Kriegmaier, M. Zimmermann, K. Wolf, U. Zimmermann, and V. L. Sukhorukov, "Dielectric spectroscopy of *Schizosaccharomyces pombe* using electrorotation and electroorientation," *Biochim. Biophys. Acta BBA - Gen. Subj.*, vol. 1568, no. 2, pp. 135–146, Dec. 2001.
- [167] R. D. Miller, "Frequency-dependent orientation of lossy dielectric ellipsoids in AC electric fields," University of Rochester, Rochester, New York, 1990.
- [168] A. D. Gruzdev, "Orientation of microscopic particles in electric fields," *Biophysics*, vol. 10, pp. 1206–1208, 1965.
- [169] G. Schwarz, M. Saito, and H. P. Schwan, "On the Orientation of Nonspherical Particles in an Alternating Electrical Field," *J. Chem. Phys.*, vol. 43, no. 10, pp. 3562–3569, Nov. 1965.
- [170] M. Saito, H. P. Schwan, and G. Schwarz, "Response of Nonspherical Biological Particles to Alternating Electric Fields," *Biophys. J.*, vol. 6, no. 3, pp. 313–327, May 1966.
- [171] L. D. Landau, E. M. Lifshits, L. P. Pitaevskii, and L. D. Landau, *Electrodynamics of continuous media*, 2nd ed., And enl. Oxford [Oxfordshire] ; New York: Pergamon, 1984.
- [172] U. Fritsch and I. Wolff, "Characterization of anisotropic substrate materials for microwave applications," 1992, pp. 1131–1134.
- [173] J. H. C. van Heuven and T. H. A. M. Vlek, "Anisotropy in Alumina Substrates for Microstrip Circuits (Short Papers)," *IEEE Trans. Microw. Theory Tech.*, vol. 20, no. 11, pp. 775–777, Nov. 1972.
- [174] A. K. Harman, S. Ninomiya, and S. Adachi, "Optical constants of sapphire ( $\alpha$ -Al<sub>2</sub>O<sub>3</sub>) single crystals," *J. Appl. Phys.*, vol. 76, no. 12, pp. 8032–8036, Dec. 1994.
- [175] P. Hu, Y. Song, H. Liu, Y. Shen, Y. Lin, and C.-W. Nan, "Largely enhanced energy density in flexible P(VDF-TrFE) nanocomposites by surface-modified electrospun BaSrTiO<sub>3</sub> fibers," *J. Mater. Chem. A*, vol. 1, no. 5, pp. 1688–1693, Jan. 2013.
- [176] G. Wang, X. Huang, and P. Jiang, "Tailoring Dielectric Properties and Energy Density of Ferroelectric Polymer Nanocomposites by High-*k* Nanowires," *ACS Appl. Mater. Interfaces*, vol. 7, no. 32, pp. 18017–18027, Aug. 2015.
- [177] J.-W. Zha, T.-X. Zhu, Y.-H. Wu, S.-J. Wang, R. K. Y. Li, and Z.-M. Dang, "Tuning of thermal and dielectric properties for epoxy composites filled with electrospun alumina fibers and graphene nanoplatelets through hybridization," *J. Mater. Chem. C*, vol. 3, no. 27, pp. 7195–7202, Jul. 2015.
- [178] L. A. Dissado and J. C. Fothergill, *Electrical Degradation and Breakdown in Polymers*. P. Peregrinus, 1992.
- [179] J. J. O'Dwyer, *The theory of electrical conduction and breakdown in solid dielectrics*. Oxford: Clarendon Press, 1973.
- [180] V. Tomer, G. Polizos, E. Manias, and C. A. Randall, "Epoxy-based nanocomposites for electrical energy storage. I: Effects of montmorillonite and barium titanate nanofillers," *J. Appl. Phys.*, vol. 108, no. 7, p. 74116, Oct. 2010.

- [181] Z. Li, K. Okamoto, Y. Ohki, and T. Tanaka, “The role of nano and micro particles on partial discharge and breakdown strength in epoxy composites,” *IEEE Trans. Dielectr. Electr. Insul.*, vol. 18, no. 3, pp. 675–681, Jun. 2011.
- [182] F. Saysouk, “Elaboration et caractérisation de film polyimide/nitrure de bore nanocomposites pour l’isolation électrique à haute température,” Paul Sabatier, Toulouse, 2014.





# Appendices

## Appendix A: Method to compute the impact of the dipoles on the electric field

In order to take into account the impact of the induced dipoles on the electric field, the electric field at the center of each particle now depends on the external electric field and the electric field induced by the neighboring particles. The electric field of the  $i^{\text{th}}$  particle is then given by:

$$\mathbf{E}_{p(i)} = \mathbf{E}_0 + \sum_{\substack{j=1 \\ j \neq i}}^n \mathbf{E}_{induced(j)} \quad (51)$$

Where  $\mathbf{E}_{induced(j)}$  is the electric field induced by the  $j^{\text{th}}$  particle at the center of the  $i^{\text{th}}$  particle. The expression of the electric field induced by a dipole is [104]:

$$\mathbf{E}_{induced(j)} = \frac{1}{4\pi\epsilon_m} \frac{1}{d_{ij}^3} \left( 3(\mathbf{p}_j \cdot \mathbf{d}_{ij}) \frac{\mathbf{d}_{ij}}{d_{ij}^2} - \mathbf{p}_j \right) \quad (52)$$

By putting eq. (52) in eq. (51) we obtain a set of  $n$  equations for each coordinate (a total of  $3 \times n$  equations):

$$\begin{aligned} E_{p(i)-x} &= \frac{1}{4\pi\epsilon_m} \sum_{\substack{j=1 \\ j \neq i}}^n \frac{1}{r_{ij}^3} \left( 3(p_{j-x}d_{ij-x} + p_{j-y}d_{ij-y} + p_{j-z}d_{ij-z}) \frac{d_{ij-x}}{d_{ij}^2} - p_{j-x} \right) \\ E_{p(i)-y} &= \frac{1}{4\pi\epsilon_m} \sum_{\substack{j=1 \\ j \neq i}}^n \frac{1}{r_{ij}^3} \left( 3(p_{j-x}d_{ij-x} + p_{j-y}d_{ij-y} + p_{j-z}d_{ij-z}) \frac{d_{ij-y}}{d_{ij}^2} - p_{j-y} \right) \\ E_{p(i)-z} &= E_0 + \frac{1}{4\pi\epsilon_m} \sum_{\substack{j=1 \\ j \neq i}}^n \frac{1}{r_{ij}^3} \left( 3(p_{j-x}d_{ij-x} + p_{j-y}d_{ij-y} + p_{j-z}d_{ij-z}) \frac{d_{ij-z}}{d_{ij}^2} - p_{j-z} \right) \end{aligned} \quad (53)$$

Where  $-x$ ,  $-y$  and  $-z$  correspond to the  $x$ ,  $y$  and  $z$  component of the vector. From eq. 15 we obtain:

$$\begin{aligned} p_{i-x} &= 4\pi\epsilon_m KR^3 E_{p(i)-x} \\ p_{i-y} &= 4\pi\epsilon_m KR^3 E_{p(i)-y} \\ p_{i-z} &= 4\pi\epsilon_m KR^3 E_{p(i)-z} \end{aligned} \quad (54)$$

Eq. (53) in eq. (54):

$$\begin{aligned} p_{i-x} &= KR^3 \sum_{\substack{j=1 \\ j \neq i}}^n \frac{1}{d_{ij}^3} \left( 3(p_{j-x}d_{ij-x} + p_{j-y}d_{ij-y} + p_{j-z}d_{ij-z}) \frac{d_{ij-x}}{d_{ij}^2} - p_{j-x} \right) \\ p_{i-y} &= KR^3 \sum_{\substack{j=1 \\ j \neq i}}^n \frac{1}{d_{ij}^3} \left( 3(p_{j-x}d_{ij-x} + p_{j-y}d_{ij-y} + p_{j-z}d_{ij-z}) \frac{d_{ij-y}}{d_{ij}^2} - p_{j-y} \right) \end{aligned} \quad (55)$$

$$p_{i-z} = 4\pi\varepsilon_m KR^3 E_0 + KR^3 \sum_{\substack{j=1 \\ j \neq i}}^n \frac{1}{d_{ij}^3} \left( 3(p_{j-x}d_{ij-x} + p_{j-y}d_{ij-y} + p_{j-z}d_{ij-z}) \frac{d_{ij-z}}{d_{ij}^2} - p_{j-z} \right)$$

Which can be rewritten as:

$$\begin{aligned} p_{i-x} &= KR^3 \sum_{\substack{j=1 \\ j \neq i}}^n \left[ \left( \frac{3d_{ij-x}^2 - d_{ij}^2}{d_{ij}^5} \right) p_{j-x} + \left( \frac{3d_{ij-x}d_{ij-y}}{d_{ij}^5} \right) p_{j-y} + \left( \frac{3d_{ij-x}d_{ij-z}}{d_{ij}^5} \right) p_{j-z} \right] \\ p_{i-y} &= KR^3 \sum_{\substack{j=1 \\ j \neq i}}^n \left[ \left( \frac{3d_{ij-y}^2 - d_{ij}^2}{d_{ij}^5} \right) p_{j-y} + \left( \frac{3d_{ij-x}d_{ij-y}}{d_{ij}^5} \right) p_{j-x} + \left( \frac{3d_{ij-y}d_{ij-z}}{d_{ij}^5} \right) p_{j-z} \right] \\ p_{i-y} &= 4\pi\varepsilon_m KR^3 E_{ext} \\ &\quad + KR^3 \sum_{\substack{j=1 \\ j \neq i}}^n \left[ \left( \frac{3d_{ij-z}^2 - d_{ij}^2}{d_{ij}^5} \right) p_{j-z} + \left( \frac{3d_{ij-x}d_{ij-z}}{d_{ij}^5} \right) p_{j-x} \right. \\ &\quad \left. + \left( \frac{3d_{ij-y}d_{ij-z}}{d_{ij}^5} \right) p_{j-y} \right] \end{aligned} \tag{56}$$

The following matrices and vectors are defined:

$$\begin{aligned} M_x(i, j) &= \begin{cases} -KR^3 \left( \frac{3d_{ij-x}^2 - d_{ij}^2}{d_{ij}^5} \right); j \neq i \\ 1; j = i \end{cases} \\ M_y(i, j) &= \begin{cases} -KR^3 \left( \frac{3d_{ij-y}^2 - d_{ij}^2}{d_{ij}^5} \right); j \neq i \\ 1; j = i \end{cases} \\ M_z(i, j) &= \begin{cases} -KR^3 \left( \frac{3d_{ij-z}^2 - d_{ij}^2}{d_{ij}^5} \right); j \neq i \\ 1; j = i \end{cases} \\ A_{xy}(i, j) &= \begin{cases} -KR^3 \left( \frac{3d_{ij-x}d_{ij-y}}{d_{ij}^5} \right); j \neq i \\ 0; j = i \end{cases} \\ A_{xz}(i, j) &= \begin{cases} -KR^3 \left( \frac{3d_{ij-x}d_{ij-z}}{d_{ij}^5} \right); j \neq i \\ 0; j = i \end{cases} \\ A_{yz}(i, j) &= \begin{cases} -KR^3 \left( \frac{3d_{ij-y}d_{ij-z}}{d_{ij}^5} \right); j \neq i \\ 0; j = i \end{cases} \end{aligned} \tag{57}$$

$$E(i) = 4\pi\epsilon_m KR^3 E_0$$

The equation system can be solved through a matrix approach:

$$\begin{aligned} M_x P_x + A_{xy} P_y + A_{xz} P_z &= 0 \\ M_y P_y + A_{xy} P_x + A_{yz} P_z &= 0 \\ M_z P_z + A_{xz} P_x + A_{yz} P_y &= E \end{aligned} \quad (58)$$

And so:

$$\begin{pmatrix} M_x & A_{xy} & A_{xz} \\ A_{xy} & M_y & A_{yz} \\ A_{xz} & A_{yz} & M_z \end{pmatrix} \begin{pmatrix} P_x \\ P_y \\ P_z \end{pmatrix} = \begin{pmatrix} E \\ 0 \\ 0 \end{pmatrix} \quad (59)$$

Once all the dipole moments are computed, the dielectrophoretic force can be deduced through the following equation:

$$\mathbf{F}_{D,ij} = \frac{1}{4\pi\epsilon_0\epsilon_c} \frac{3}{r^5} \left( \mathbf{r}_{ij}(\mathbf{p}_i \cdot \mathbf{p}_j) + (\mathbf{r}_{ij} \cdot \mathbf{p}_i)\mathbf{p}_j + (\mathbf{r}_{ij} \cdot \mathbf{p}_j)\mathbf{p}_i - \frac{5}{r^2} \mathbf{r}_{ij}(\mathbf{p}_i \cdot \mathbf{r}_{ij})(\mathbf{p}_j \cdot \mathbf{r}_{ij}) \right) \quad (60)$$

which is the general form of eq. 20.

It is easily understandable that this method will be much more costly in term of computation time as it requires to generate numerous matrices and to invert a matrix to compute the dipole moments. The size of the matrix to invert grows in  $3n \times 3n$  (due to the three-dimensional approach).



# Appendix B: Measurements of the electric losses of composites

In this appendix, the measurement losses of epoxy/BaTiO<sub>3</sub> isotropic and anisotropic composite is reported. The materials studied correspond to those presented in section IV.3.

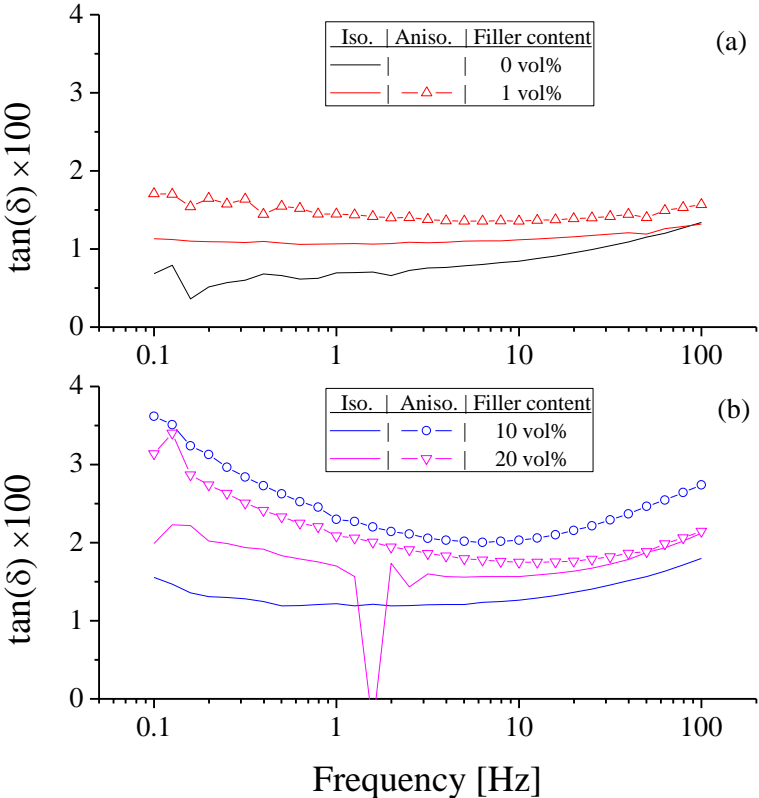


Figure B-1: Composite losses at low frequency. (a) low filler content, (b) high filler content.

Studying the frequency dependence of the losses is quite a sensitive prospect. For that reason, we divided the study into two parts: low frequencies and high frequencies. At a low frequency (Figure B-1), the isotropic composites present a higher loss factor when increasing filler content. Chaining seems to further increase the losses. At a very low frequency (i.e. under 1 Hz) for high filler content (Figure B-1 (b)), the losses might be due to a conduction phenomenon. At a high frequency (Figure B-2), the loss factor is quite independent of filler content. Some relaxation peaks are visible, though the peaks are not located at the same frequency, which remains unexplained. The impact of the chains is also less clear: at low filler content, the losses are slightly higher, while there is no direct pattern for the higher volume fractions. These puzzling results might be due to the fact that the resin and the particles have close loss factor values. The same study, but with particles presenting higher losses than the resin, would yield interesting information, especially regarding the impact of chaining. This study could be performed using CCT powder as filler, for example.

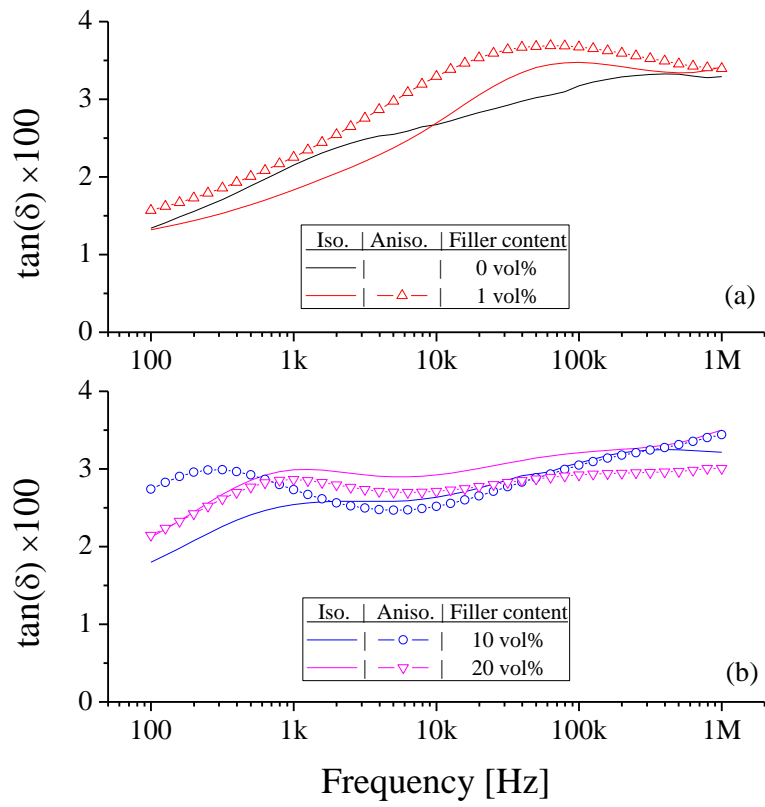


Figure B-2: Composite losses at high frequency. (a) low filler content, (b) high filler content.

---

## Appendix C: Measurements of the dielectric strength of composites

This appendix presents the results of breakdown strength of both isotropic and anisotropic composites. Dielectric strength is an important property for materials in electronic/electrical systems. With the increase in power densities, materials are expected to withstand higher electric fields, sometimes combined with high temperature. In addition, for energy storage applications, the amount of energy that can be stocked depends linearly on the permittivity, but essentially on the voltage squared. This means that an increase in the permittivity associated to a decrease of the dielectric strength is not necessarily beneficial.

Dielectric strength has been studied intensively for homogeneous materials (polymer and ceramics [178], [179]) and composite materials [180], [181]. Since, in general, ceramics present lower dielectric strength than polymers, the addition of ceramic microparticles tends to lower the breakdown voltage of the composite, compared to the neat polymer. However, it has been proven that nanoparticles could, on the contrary, enhance the dielectric strength of composites [27], even showing better results at high temperature [182], but sometimes to the detriment of the material permittivity. On the other hand, when trying to increase the permittivity of a composite by forming a chain of fillers, very few studies have been conducted on the impact on the dielectric strength. To the best of the author's knowledge, only Tomer *et al.* studied this aspect [59]. In that article, he showed a decrease in the composite strength (from 1 to 0.85 MV/cm for isotropic and anisotropic composite respectively) for epoxy/BaTiO<sub>3</sub> composite at 25 vol%. In this case, the particles were submicronic ( $\approx 0.2 \mu\text{m}$  diameter).

In order to determine whether the composite obtained could be used for storage energy applications, the impact of chaining was studied. As the particles used in this study were bigger than those used by Tomer (0.66  $\mu\text{m}$  for the BaTiO<sub>3</sub> and 0.85  $\mu\text{m}$  for the SrTiO<sub>3</sub>), we expect a more drastic decrease in the composite dielectric strength. The resin used was different from that used in the previous section (resin SR8500, hardener SZ8525 from Sicomin Epoxy Systems). The electric field and temperature were applied together from the beginning of the experiment. Once cured, one side of the sample cell (as described in Figure IV-6) was removed. The sample was then placed inside a dielectric strength test chamber (Figure C-1).

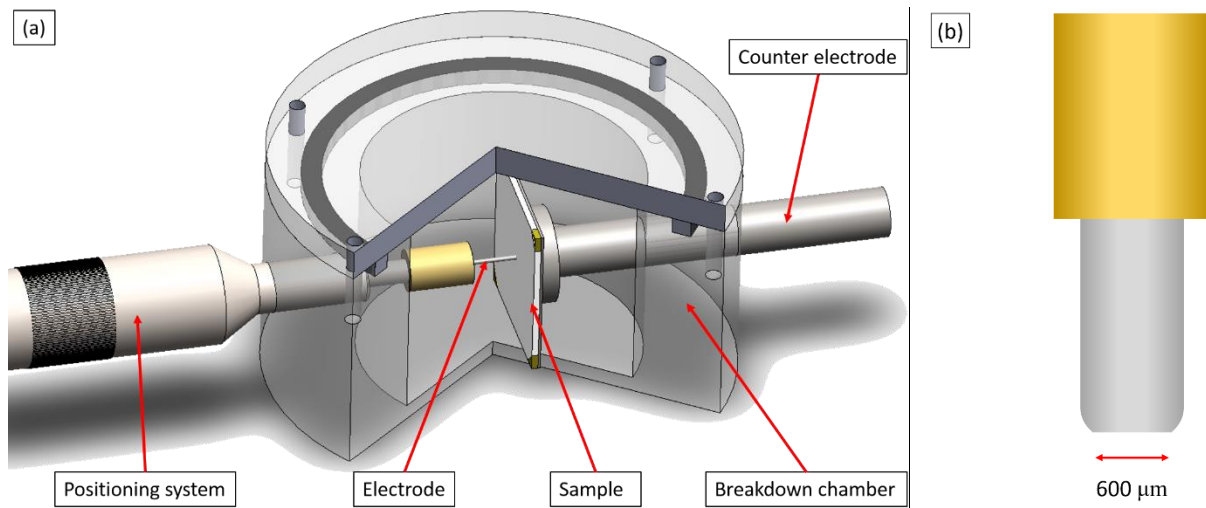


Figure C-1: (a) dielectric breakdown setup, (b) electrode shape.

The breakdown chamber was filled with insulating liquid (Galden HT 55) to avoid flashover. The counter electrode was in contact with the stainless-steel plate; the “needle” electrode was then put in contact with the composite surface. The electric field is assumed to be uniform since the thickness over the electrode diameter ratio is 1:6 (100 μm and 600 μm). For each sample, several breakdown tests were performed on different points of the composite surface. The applied voltage is an ac ramp with 500 V/s slope to reach breakdown in less than 20 s and to avoid ageing effects.

The resulting dielectric strength is plotted in Figure C-2 (a) for BaTiO<sub>3</sub>. This result follows a quite logical trend: when increasing the filler content, the dielectric strength decreases. The breakdown strength is lower in the case of anisotropic composite compared to isotropic composites.

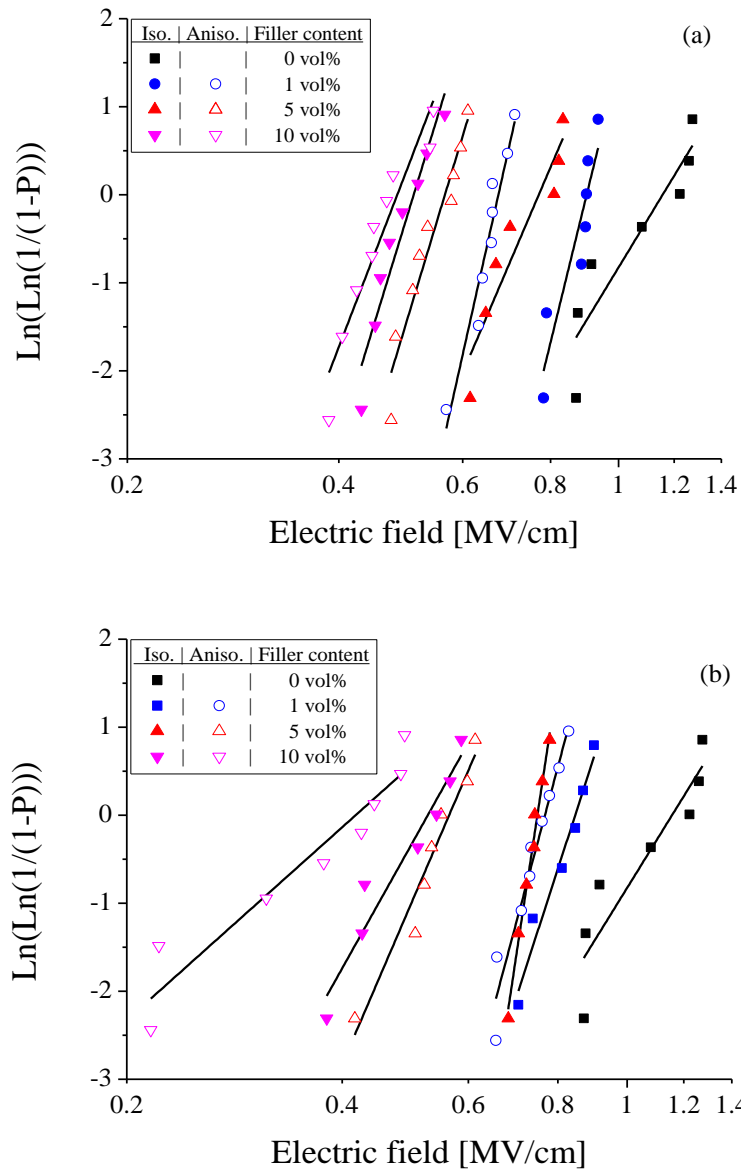


Figure C-2: Weibull plot of the failure distribution for (a) epoxy/BaTiO<sub>3</sub>, (b) epoxy/SrTiO<sub>3</sub> composites from neat to 10 vol%.

The results for the SrTiO<sub>3</sub> composites plotted in Figure C-2 (b) are comparable to those for BaTiO<sub>3</sub>. These two plots confirm the previous assumption, namely that the addition of microparticles has a negative impact on the breakdown, and chaining tends to further lower its value. Several aspects could explain this decrease: the lower dielectric strength of the bulk ceramics and the local increase of the electric field due to the high permittivity of the particles.

In order to study the impact of the particle nature, the alpha parameter from the Weibull plot is calculated and plotted in Figure C-3. The decrease in dielectric strength appears clearly with increasing volume fraction and particle chaining. However, the impact of chaining is lower than the impact of volume fraction, and seems to be even lower at high filler content. Yet, the anisotropy of the structure seems to increase the conduction phenomenon. Indeed, when the breakdown test was performed, the anisotropic

composites presented higher conduction currents for high electric fields. This might highlight the non-linear behavior of these composites, which could be investigated by I-V measurements and/or dielectric spectroscopy under a high electric field (the results presented in V-3.a and b were measured for  $E = 100$  V/cm, far from the breakdown electric fields).

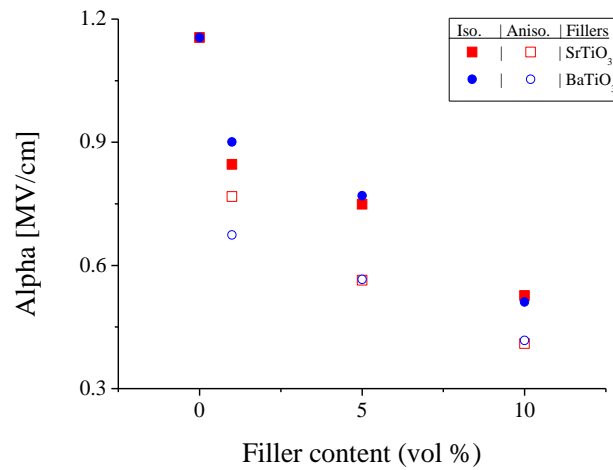


Figure C-3: alpha parameter calculated from the Weibull plot for SrTiO<sub>3</sub> and BaTiO<sub>3</sub> composites.

It is interesting to note that there is no clear impact of the particle nature on the breakdown strength of the composites, even if the bulk ceramic SrTiO<sub>3</sub> present a higher dielectric strength than the bulk ceramic BaTiO<sub>3</sub>.

**AUTEUR :** Guillaume BELIJAR

**DIRECTEUR DE THESE :** Thierry LEBEY

**LIEU ET DATE DE SOUTENANCE :** Toulouse, le 05 Décembre 2016

**DISCIPLINE ADMINISTRATIVE :** Génie Electrique

---

**TITRE :** Elaboration et modélisation de composites anisotropes: vers des matériaux adaptés aux systèmes

**RESUME :** L'objectif de ces travaux de thèse a été de démontrer la possibilité, en se basant sur une approche prédictive, de contrôler avec précision la fonctionnalisation d'un matériau composite, d'isotrope à anisotrope, sous l'application d'un champ électrique. Ces derniers matériaux présentent en effet un fort potentiel pour des applications futures telles que des condensateurs intégrés ou bien encore des composites conducteurs thermiques.

Une première approche théorique des différentes forces et mécanismes entrant en jeux lors de l'élaboration de composites anisotropes par chaînage a permis d'identifier les paramètres impactant le procédé d'élaboration. A la suite de cette étude théorique, un modèle de formation de chaînes de particules sous champ électrique a été développé afin de prédire la dynamique de chaînage. Le modèle choisi (méthode moment dipolaire effectif) a permis la simulation de plus de 4500 particules. Les paramètres ayant au préalable été identifiés ont ensuite été mesurés. Pour la permittivité des particules, une méthode de mesure diélectrophorétique a été développée, ce qui est une première dans le cas de particules céramiques.

L'élaboration des composites anisotropes a été couplé avec un suivi novateur, en temps réel, d'un marqueur (permittivité) de la formation de chaînes, permettant d'obtenir la dynamique de structuration des particules. Afin de valider l'aspect prédictif du modèle numérique, une comparaison a été effectuée entre la dynamique mesurée et simulée. Les résultats obtenus ont démontré une très bonne fiabilité des prédictions du modèle, même si des progrès sont encore réalisables aux faibles taux de chargement.

Dans un dernier temps, une preuve de concept a été démontrée, de la réalisation de composites anisotropes dont les particules sont alignées perpendiculairement au champ électrique.

**MOTS-CLEFS :** Composites anisotropes, Diélectrophorèse, Diélectriques, Elaboration, Modélisation

---

**TITLE:** Anisotropic composite elaboration and modeling: toward materials adapted to systems

**ABSTRACT:** This study was aimed to demonstrate the possibility, based on a predictive approach, to tailor the structure of a composite from isotropic to anisotropic when applying an electric field. This composites have great potential for future applications such as embed capacitors or thermally conductive composites.

A theoretical approach of the forces and mechanisms acting in the elaboration of anisotropic composites by chaining allowed identifying the key parameters. Based on this approach a model of particle chaining under electric field was established to predict the structuration dynamics. This model (effective dipole moment) allowed simulating more than 4500 particles.

The parameters previously identified were then measured, and for the particle permittivity, a dielectrophoretic measurement method was developed, which was a first for ceramic particles.

The elaboration of anisotropic composites was coupled to a novel on-line monitoring of a chaining marker (permittivity), allowing to obtain the structuration dynamics. To validate the predictive aspect of the model, experimental and numerical dynamics were compared showing the robustness and accuracy of the model, even if improvement is still possible at low filler content.

In the last part, a proof of concept was demonstrated of the elaboration of anisotropic composites with fillers oriented normally to the direction of the electric field.

**KEYWORDS :** Anisotropic composites, Dielectrophoresis, Dielectrics, Elaboration, Modeling

---